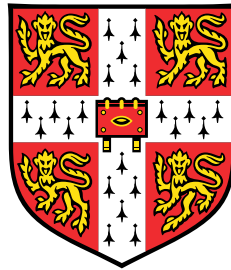


Modelling the effects on building temperatures of phase change materials



Rachael Helen Bonnebaigt

Department of Applied Mathematics and Theoretical Physics
University of Cambridge

This dissertation is submitted for the degree of
Doctor of Philosophy

Sidney Sussex College

September 2016

For my Lord and Saviour Jesus Christ.

“For from him and through him and for him are all things. To him be the glory for ever!

Amen.” Romans 11:36, NIV

Declaration

This dissertation is the result of my own work and includes nothing which is the outcome of work done in collaboration except as declared in the Preface and specified in the text. Specifically, this work was done under the supervision of Prof. Colm-cille Caulfield, with Prof. Paul Linden as advisor, and Dr Gavin Davies as industrial supervisor. A manuscript based on the third chapter of this thesis has been submitted to *Environmental Fluid Mechanics*, with myself, Prof. Caulfield, and Prof. Linden as co-authors.

It is not substantially the same as any that I have submitted, or, is being concurrently submitted for a degree or diploma or other qualification at the University of Cambridge or any other University or similar institution. I further state that no substantial part of my dissertation has already been submitted, or, is being concurrently submitted for any such degree, diploma or other qualification at the University of Cambridge or any other University or similar institution.

Rachael Helen Bonnebaigt
September 2016

Acknowledgements

Many people have supported and encouraged me in this work, and I am grateful to all of them. Here, I have tried to thank a few of those people.

First, I would like to thank my supervisor, Colm Caulfield, for all his work in supervising me, and for his encouragement. When I was a third year undergraduate, wanting to do a PhD but unsure whether I had the ability, Colm believed in me, encouraging me that I could do a PhD. That support and encouragement has carried on throughout my PhD, and I am truly grateful to have had such an excellent supervisor.

I would also like to thank those in the GK Batchelor lab, especially Paul Linden (my advisor), Alexis Kaminski, Tom Eaves, Jason Olsthoorn for helping me to set up my conductivity probe, Stuart Dalziel, Mark Hallworth and Megan Stamper for helping me to transport a peristaltic pump to and from the BP Institute, and the amazing technicians for all their help with my experimental setup. It has been a privilege being part of such an amazing group of people. I would also like to thank Lotty Gladstone, at the BP Institute, for useful conversations, and for her generosity in lending me equipment.

The work was generously funded by an EPSRC CASE award with Laing O'Rourke. At Laing O'Rourke, I would particularly like to thank Gavin Davies (my industrial supervisor) for sharing his insight in how this work relates to industry, and Greg Bond for helping set up the real life data collection equipment.

Throughout my PhD studies, I have been blessed to have been surrounded by many kind, supportive people outside the department too. In particular, I would like to thank those in the Christian Graduate Society and at Holy Trinity Church who have upheld me in prayer, cared about me, and supported me in practical ways. In particular, I'd like to thank Ben Woodhams, Clara Lloyd, John & Di Lister, Tom & Ellie Button, and Allen & Edwina Swann. I would also like to thank my parents, for all their love and support over the years. A big thank you must also go to my husband, Chris Warrington, for his love, kindness, support, and encouragement - I love you!

Finally, and most importantly, I want to thank my Lord and Saviour, Jesus Christ, for everything.

Abstract

In this thesis, three problems motivated by the possibility of use of phase change materials in buildings are presented.

First, a model for the response of phase change material (PCM) to a varying room temperature is extended, and applied to realistic situations in a building. For a spatially varying distribution of PCM through a wall, an equation estimating the appropriate depth for PCM inclusion is found. For cooling at the exterior surface of the wall, a wall thickness and a PCM mass fraction that give a low maximum daily interior surface temperature, without redundant PCM, are identified. The hot upper layer for a displacement ventilated space is cooler but deeper when a PCM ceiling interacting with the exhaust from an air heat pump is used. During hot weather, the maximum daily interior surface temperatures are reduced when using two PCMs with different, appropriate, melting ranges. In each extension, PCM reduces temperature fluctuations substantially when used in appropriate quantities and locations.

Second, experimental results are presented, demonstrating that, for a buoyancy source vertically distributed over a full wall, detrainment qualitatively changes the shape of the ambient buoyancy profile in a sealed space. Theoretical models with one-way entrainment predict stratifications that are qualitatively different from the stratifications measured in experiments. A peeling plume model, where density and vertical velocity vary linearly across the plume, so that plume fluid “peels” off into the ambient at intermediate heights, more accurately captures the shape of the ambient buoyancy profiles measured in experiments than a one-way-entrainment model does. For a half wall source, however, detrainment is not observed in the experiments, and a one-way-entrainment model is appropriate.

Third, experimental results are presented for a time-varying, vertically distributed buoyancy source. For a source whose buoyancy flux decreases linearly with time, the peeling plume model is appropriate, as it was for a constant flux source. For a source providing a buoyancy flux that increases linearly with time, however, the one-way-entrainment model is the most appropriate model for predicting the stratification that develops in a sealed space. A PCM wall solidifying provides a buoyancy source which decreases linearly with time, then is constant, then again decreases linearly with time. Experiments show that, in a space with such a buoyancy source, the first front moves quickly through the space, so the whole space

is stratified for most of the experiment. The shape of the stratification changes only slightly after this point, with heat being added uniformly throughout the space, so that the ambient buoyancy profile simply translates, with little change in its shape.

Table of contents

List of figures	xv
List of tables	xxvii
1 Introduction	1
1.1 Thermal comfort in buildings	1
1.2 Storing heat	3
1.3 Phase change materials (PCMs)	4
1.3.1 Types of PCM	4
1.3.2 Measuring a PCM's properties	5
1.3.3 Containing PCMs	6
1.3.4 Ways to use PCMs in buildings	7
1.3.5 Modelling PCMs	10
1.4 Modular construction of buildings	11
1.5 Models for temperature stratification in rooms	12
1.5.1 Plumes	12
1.5.2 Filling boxes with point or line sources of buoyancy	13
1.5.3 Natural ventilation	15
1.5.4 Time-varying buoyancy sources	16
1.5.5 Distributed sources	17
1.6 Outline	21
2 Phase change material thermal mass reducing fluctuations in building temperature	23
2.1 Introduction	23
2.2 PCM thermal mass model of Richardson and Woods (2008)	25
2.3 Optimisation of the properties of PCM	31
2.3.1 Optimising wall thickness and PCM mass fraction	31

2.3.2	Spatially varying PCM distributions	36
2.4	Interaction of PCM with surrounding conditions	40
2.4.1	Time varying cooling at the exterior surface of the thermal mass	40
2.4.2	A PCM ceiling in a naturally ventilated room	42
2.4.3	A period of hot weather	46
2.4.4	Long hot days with short cool nights	48
2.5	Discussion and Conclusions	48
3	Detrainment of plumes from vertically distributed sources	51
3.1	Introduction	51
3.2	Experiments	54
3.2.1	Methods	54
3.2.2	Horizontal line source	55
3.2.3	Full wall source	55
3.2.4	Half wall source	59
3.3	Theoretical models	61
3.3.1	Horizontal line source	61
3.3.2	Full wall source	66
3.3.3	Half wall source	74
3.4	Conclusions	77
4	Time-varying vertically distributed buoyancy sources	81
4.1	Introduction	81
4.2	Experiments	82
4.2.1	Setup	82
4.2.2	Selecting a source buoyancy flux that mimics the solidification of PCM	84
4.2.3	Results: “ramp down” in source buoyancy flux	90
4.2.4	Results: “ramp up” in source buoyancy flux	92
4.2.5	Results: source buoyancy flux that mimics the solidification of PCM	95
4.3	Theory	95
4.3.1	Top-hat plume with a vertically distributed, time varying source	95
4.3.2	Analytic solutions for a plume in a uniform, unconfined ambient	102
4.3.3	Peeling plume with a vertically distributed, time varying source	107
4.4	Comparing theory with experiments	111
4.4.1	“Ramp down” in source buoyancy flux	111
4.4.2	“Ramp up” in source buoyancy flux	116
4.4.3	A source buoyancy flux that mimics the solidification of PCM	121

4.5	Using the PCM mimicking source model to inform design decisions	123
4.6	Conclusions	129
5	Conclusions	133
5.1	Summary	133
5.1.1	PCM thermal mass reducing fluctuations in building temperature . .	133
5.1.2	Detrainment of plumes from vertical sources	136
5.1.3	Time-varying, vertically distributed buoyancy sources	137
5.1.4	Overall key points of this thesis	139
5.2	Future work	139
5.2.1	PCM thermal mass reducing fluctuations in building temperature . .	140
5.2.2	Detrainment of plumes from vertical sources	141
5.2.3	Time-varying, vertically distributed buoyancy sources	141
	References	143
	Appendix A PCM wallboard field tests	153
A.1	Motivation	153
A.2	Review of studies that use PCM in walls	153
A.3	Setup	154
A.3.1	Apartments	154
A.3.2	PCM wallboard	156
A.3.3	Equipment for measuring temperatures	159
A.4	Results and discussion	159
A.4.1	Autumn data	159
A.4.2	Winter data	162
A.5	Conclusions	163

List of figures

1.1	Examples of thermal mass in buildings: the thick walls of (a) Carmel Mission Basilica, California, and (b) a house in North Wales, and (c) exposed concrete thermal mass at the Centre for Mathematical Sciences, Cambridge, UK.	4
1.2	A schematic showing what the phase change temperature, latent heat, thermal conductivity, and heat transfer coefficient mean for a PCM.	5
1.3	Knauf Comfortboard, a wallboard containing microencapsulated PCM. Figure (a) shows the front of the wallboard, and figure (b) shows the side view (two sheets of wallboard have been used together in this picture).	9
1.4	An apartment block that was constructed using modular manufacturing, by Laing O'Rourke, at Explore Industrial Park, in Steetley, near Worksop.	11
1.5	A schematic showing the method of Germeles (1975).	14
1.6	Schematics of two types of ventilation: displacement and mixing	15
2.1	Schematic showing: (left) the asymmetric melting temperature of a PCM relative to a sinusoidally varying room temperature, (right) the uniform distribution of encapsulated PCM within a concrete wall, insulated at its outer surface $x = l_{tm}$, and subject to heat transfer with the room air at its inner surface $x = 0$	24
2.2	Room temperature (dashed) and interior surface temperature (solid) for: a) and b) different wall thicknesses; c) and d) different PCM mass fractions. H_+ and Ω are given in table 2.3, s is given in table 2.4, $U_{min} = -0.6$, and $U_{max} = 0$	33
2.3	Measures of PCM effectiveness: the maximum interior surface temperature $U_{hottest}$ (2.3a, 2.3c, 2.3e, 2.3g) and the energy storage D (2.3b, 2.3d, 2.3f, 2.3h), as defined in (2.16). When parameters are constant, they are taken from tables 2.3 and 2.4. When parameters are varying, they are calculated using equations (2.7), (2.8), and (2.9), with properties given in table 2.2.	35

2.4	Variation of interior surface temperature with time for the three different PCM distributions: uniform (thick solid line), linear (dashed line), and step (thin solid line) for a) 1cm wallboard and b) 10cm wallboard. The three curves overlap in a).	37
2.5	Variation with dimensionless depth into the wall X of dimensionless temperature U , as defined in equation (2.6), for various time steps at intervals 0.02π (each represented with a distinct solid line).	38
2.6	Numerical results for a wallboard ceiling with cooling at the exterior surface.	42
2.7	Temperatures and interface height for a room with displacement ventilation and a PCM ceiling, as shown schematically in figure 2.7a. Parameter values, as defined in equations (2.7 – 2.10), (2.38), and (2.41), are $U_e = 3.5, H_+ = 15.7, H_- = 6.85, \Omega = 3.85, U_{\min} = 4.2, U_{\max} = 4.5, s = 4.25, E = 180.6, F = 3.7, G = 4.0, J = 0.5$	43
2.8	Time variation of interior surface temperature with a) one PCM and parameters $H_+ = 1.06, \Omega = 0.2, U_{\min} = -0.1, U_{\max} = 0.1, s = 5$. For b), two PCMs are used, with parameters $H_+ = 1.06, \Omega = 0.2, U_{\min_1} = -0.1, U_{\max_1} = 0.1, U_{\min_2} = 0.9, U_{\max_2} = 1.1$, and for the two PCMs, $s_1 = 2.5, s_2 = 2.5$ (as defined in (2.44)), whilst for the one PCM $s = 5$ with the melting range $U_{\min_1} = -0.1$ to $U_{\max_1} = 0.1$	47
2.9	Variation with time of interior surface temperature. Parameters are $H_+ = 1.06, \Omega = 0.2, U_{\min} = -0.1, U_{\max} = 0.1$, with $s = 5$ for the PCM thermal mass and $s = 0$ for the thermal mass with no PCM.	49
3.1	The experimental setup (left), including details of the source (right).	54
3.2	Dimensionless ambient buoyancy profiles for line source experiment N_{line} (which has a flow rate of 0.9ml/s and a dimensionless density difference $\Delta\rho = 0.13$). The four subplots show the experimental results at four different times: 375s, 855s, 1335s, and 1815s after starting. When nondimensionalised by the timescale $W\alpha^{-2/3}f_0^{-1/3}$, where α is the entrainment coefficient, f_0 is the source buoyancy flux per unit source width, and W is the tank width, these times are 1.6, 3.7, 5.7, and 7.8. Grey crosses show the original data and a black line shows the filtered data (filtered using a median filter).	57

3.3	Dimensionless ambient buoyancy profiles (median filtered data) for full wall source experiment N_{full} (which has a flow rate of 3.8ml/s and a dimensionless density difference $\Delta\rho = 0.10$). The four subplots show the experimental results at four different times: 120s, 360s, 600s, and 840s after starting. When nondimensionalised by the timescale $W\alpha^{-2/3}b_{s_0}^{-1/3}H^{-1/3}$, where α is the entrainment coefficient, b_{s_0} is the source buoyancy flux per unit source area, and W is the tank width, these times are 0.4, 1.3, 2.2, and 3.1.	59
3.4	Left: source fluid (dyed red 3 minutes into the experiment) detrains – it intrudes into the ambient at intermediate heights. Shown at 4 minutes into experiment T_{full} . Right: source fluid (dyed green 7 minutes into the experiment) detrains. Shown at 10 minutes into experiment T_{full} . The contrast has been enhanced, for clarity. The approximate location of the first front is shown by the dashed line.	60
3.5	Source fluid (dyed red 3 minutes into the experiment) detrains at similar heights towards the bottom of the tank for each experiment. Experiment C_{full} at 6 minutes is shown on the left, and experiment T_{full} at 4 minutes is shown on the right. The contrast has been enhanced, for clarity. The approximate location of the first front is shown by the dashed line.	60
3.6	The half wall source.	61
3.7	Dimensionless ambient buoyancy profiles (median filtered data) for half wall source experiment N_{half} (which has a flow rate of 1.8ml/s and a dimensionless density difference $\Delta\rho = 0.14$). The four subplots show the experimental results at four different times: 375s, 855s, 1335s, and 1815s after starting.	62
3.8	Dimensionless ambient buoyancy profiles for line source experiments B_{line} , H_{line} , N_{line} , and T_{line} . Solid black lines show filtered experimental results, the dashed lines show the model results. Each subplot shows profiles at times 375s, 855s, 1335s, and 1815s after starting, as in figure 3.2. The corresponding dimensionless times are listed on each plot.	64
3.9	RMS error between theoretical and experimental dimensionless ambient buoyancy profiles, divided by maximum theoretical dimensionless ambient buoyancy, against dimensionless time, for each of the 20 line source experiments listed in table 3.1, apart from experiment A which has a large RMS error, and is not shown.	65

-
- 3.10 The distance from the source to the first front for experiment N_{line} (crosses), from line source theory (solid line), and from half axisymmetric source theory (dashed line), with $\alpha = 0.04$ for both. The line source theory and the half axisymmetric source theory give very different first front speeds. 66
- 3.11 Dimensionless ambient buoyancy profiles for full wall source experiments B_{full} , H_{full} , N_{full} , and T_{full} . Solid black lines show filtered experimental results, the dashed lines show the model results. Each subplot shows profiles at times 120s, 360s, 600s, and 840s after starting. The corresponding dimensionless times are listed on each plot. 68
- 3.12 RMS error between theoretical (Cooper and Hunt (2010) one-way-entrainment model, with $\alpha = 0.018$, chosen to give a low RMS error over all the experiments) and experimental dimensionless ambient buoyancy profiles, divided by the maximum theoretical dimensionless ambient buoyancy, against dimensionless time for each of the 20 full wall source experiments listed in table 3.3. 69
- 3.13 Numerical solutions to the full wall source plume equations with wall drag. Dimensionless ambient buoyancy profiles are shown for four different values of dimensionless wall drag D : 0, 0.1, 0.2, and 0.3. Changing the value of D does not qualitatively change the shape of the ambient buoyancy profile. . . 69
- 3.14 In the peeling plume model, density and vertical velocity vary linearly across the width of the plume, allowing parts of the plume to peel off into the ambient at intermediate heights. 70
- 3.15 Dimensionless ambient buoyancy profiles for full wall source experiments B_{full} , H_{full} , N_{full} , and T_{full} . Solid black lines show filtered experimental results, the dashed lines show the peeling plume model results with $\alpha = 0.018$. Each subplot shows profiles at times 120s, 360s, 600s, and 840s after starting. The corresponding dimensionless times are listed on each plot. . . 75
- 3.16 RMS error between theoretical (peeling plume model shown by the thick orange lines marked with circles, and the Cooper and Hunt (2010) one-way-entrainment model shown by the thin grey lines marked with crosses, both models using $\alpha = 0.018$, which was chosen to give a low RMS error over all the experiments) and experimental dimensionless ambient buoyancy profiles, divided by the maximum theoretical dimensionless ambient buoyancy, against dimensionless time for each of the 20 full wall source experiments listed in table 3.3. Darker colours are experiments with larger source densities. 75

3.17	RMS error between theoretical (peeling plume model shown in the thick orange lines marked with circles, and the Cooper and Hunt (2010) one-way-entrainment model shown in the thin grey lines marked with crosses) and experimental dimensionless ambient buoyancy profiles, divided by the maximum theoretical dimensionless ambient buoyancy, against dimensionless time for each of the 20 full wall source experiments listed in table 3.3. For a flow rate of 1.6ml/s, $\alpha = 0.011$, for a flow rate of 2.7ml/s, $\alpha = 0.011$, for a flow rate of 3.8ml/s, $\alpha = 0.018$, and for a flow rate of 4.8ml/s, $\alpha = 0.020$. Darker colours are experiments with larger source densities.	76
3.18	Different source flow rates lead to different variations in vertical velocity across the width of the plume, leading to different amounts of peeling. . . .	76
3.19	Dimensionless ambient buoyancy profiles for half wall source experiments B_{half} , H_{half} , N_{half} , and T_{half} . Solid black lines show filtered experimental results, the dashed lines show the model results. Each subplot shows profiles at times times 375s, 855s, 1335s, and 1815s after starting. The corresponding dimensionless times are listed on each plot.	78
3.20	RMS error between theoretical (extension of the Cooper and Hunt (2010) one-way-entrainment model) and experimental dimensionless ambient buoyancy profiles, divided by the maximum theoretical ambient buoyancy, against dimensionless time for each of the 20 half wall source experiments listed in table 3.4.	78
4.1	The experimental setup (left), including details of the source (right).	83
4.2	The form of source buoyancy flux that mimics the solidification of PCM. . .	87
4.3	Dimensionless ambient buoyancy profiles (median filtered data) for “ramp down” experiment G_{down} (which has an initial flow rate of 6.3ml/s and a dimensionless density difference $\Delta\rho = 0.14$). The six subplots show the experimental results at six different times: 235s, 475s, 715s, 955s, 1195s, and 1435s after starting, which correspond to dimensionless times of 0.9, 1.8, 2.7, 3.6, 4.5, and 5.4. A value of $\alpha = 0.012$ is used, consistent with table 4.6.	91
4.4	False colour (enabling the intrusions to be more clearly seen) photographs of experiment J_{down} , taken 11 minutes (left) and 22 minutes (right) after the start of the experiment, showing dyed plume fluid (left: orange, right: blue) intruding into the ambient (left: undyed but stratified, right: orange at the bottom of the tank, undyed above) at several intermediate heights.	91

-
- 4.5 False colour (enabling the intrusions to be more clearly seen) photographs of experiments E_{down} (left, taken at 11 minutes 40s after the start of the experiment) and J_{down} (right, taken at 11 minutes after the start of the experiment). In both photographs, plume fluid (orange) intrudes into the ambient over approximately the same range of heights. 92
- 4.6 Dimensionless ambient buoyancy profiles (median filtered data) for “ramp up” experiment G_{up} (which has an initial flow rate of 6.3ml/s and a dimensionless density difference $\Delta\rho = 0.14$). The six subplots show the experimental results at six different times: 235s, 475s, 715s, 955s, 1195s, and 1435s after starting, corresponding to dimensionless times of 0.7, 1.3, 2.0, 2.7, 3.4, and 4.0 (using the value of α for the one-way-entrainment model, $\alpha = 0.008$, from table 4.7). Note that, unlike the constant flux experiments of chapter 3, there is no “flick” – a large change in curvature – near dimensionless height 0. 93
- 4.7 A (false colour, to enable the intrusions to be clearly seen) photograph of experiment K_{up} , taken 21 minutes after the start of the experiment, showing dyed plume fluid (pink) detraining, that is, intruding into the ambient (purple at the bottom of the tank, and grey above that) at intermediate heights. . . . 94
- 4.8 Dimensionless ambient buoyancy profiles (median filtered data) for a PCM mimicking experiment, with the source buoyancy flux as described in section 4.2.2. The four subplots show the experimental results at four different times: 235s, 715s, 1195s, and 1675s after starting, which, when nondimensionalising by the timescale $\tau = 217\text{s}$, correspond to 1.1, 3.3, 5.5, 7.7, 9.9, 12.1, and 14.4. 95
- 4.9 Schematic showing how, in a modified version of the Germeles (1975) method, the layer thickness and buoyancy are adjusted to account for the non-zero source volume flux present in the experiments of section 4.2. . . . 102
- 4.10 The first front height, from theory, for 4 types of source: a “ramp down” in source buoyancy flux, a “ramp up” in source buoyancy flux, a constant source buoyancy flux, and a PCM mimicking source. All are shown up to a dimensionless time of 3, which is when the “ramp down” source and PCM mimicking source have reached zero source buoyancy flux, and so their first front height does not change beyond this point. 106

- 4.11 The experimental first front height divided by the theoretical first front height from (4.67) for the 12 “ramp down” experiments. Each experiment is shown by a different marker shape. The experimental first front height (measured from the base of the tank upwards) is systematically slightly too large, compared with the theoretical first front height, because the theoretical first front height neglects the extra volume flux added by the source in experiments. 108
- 4.12 The experimental first front height divided by the theoretical first front height from (4.68) for the 12 “ramp up” experiments. Each experiment is shown by a different marker shape. The experimental first front height (measured from the base of the tank upwards) is systematically slightly too large, compared with the theoretical first front height, because the theoretical first front height neglects the extra volume flux added by the source in experiments. 108
- 4.13 Dimensionless ambient buoyancy profiles shown at 8 different times: 115s, 355s, 595s, 835s, 1075s, 1315s, 1555s, and 1795s (the 8 lines of each line style on each subplot) through each of 4 “ramp down” experiments (the 4 different subplots) with an initial flow rate of 3.7ml/s. Experimental profiles are shown by the thin, solid, black lines, and theoretical profiles using the peeling plume model are shown by the thicker, dashed, grey lines. 113
- 4.14 Dimensionless ambient buoyancy profiles shown at 8 different times: 115s, 355s, 595s, 835s, 1075s, 1315s, 1555s, and 1795s (the 8 lines of each line style on each subplot) through each of 4 “ramp down” experiments (the 4 different subplots) with an initial flow rate of 6.3ml/s. Experimental profiles are shown by the thin, solid, black lines, and theoretical profiles using the peeling plume model are shown by the thicker, dashed, grey lines. 114
- 4.15 Dimensionless ambient buoyancy profiles shown at 8 different times: 115s, 355s, 595s, 835s, 1075s, 1315s, 1555s, and 1795s (the 8 lines of each line style on each subplot) through each of 4 “ramp down” experiments (the 4 different subplots) with an initial flow rate of 9.5ml/s. Experimental profiles are shown by the thin, solid, black lines, and theoretical profiles using the peeling plume model are shown by the thicker, dashed, grey lines. 114
- 4.16 RMS error between the theoretical and the experimental profiles, divided by the maximum dimensionless ambient buoyancy from theory at each timestep, for the “ramp down” experiments. Each subplot is for one slope of ramp, and each line is one experiment, with lighter coloured lines corresponding to experiments with smaller source densities. The crosses on each line are for each time that a profile is taken and compared. 115

4.17	Schematic showing why the model and experiments give different stratifications near the first front.	116
4.18	Dimensionless ambient buoyancy profiles shown at 8 different times: 115s, 355s, 595s, 835s, 1075s, 1315s, 1555s, and 1795s through each of 4 “ramp up” experiments (one subplot for each experiment) with a final flow rate of 3.7ml/s. Experimental profiles are shown by the thin, solid, black lines, and theoretical profiles using the peeling plume model are shown by the thicker, dashed, grey lines.	117
4.19	Dimensionless ambient buoyancy profiles shown at 8 different times: 115s, 355s, 595s, 835s, 1075s, 1315s, 1555s, and 1795s through each of 4 “ramp up” experiments (one subplot for each experiment) with a final flow rate of 6.3ml/s. Experimental profiles are shown by the thin, solid, black lines, and theoretical profiles using the peeling plume model are shown by the thicker, dashed, grey lines.	118
4.20	Dimensionless ambient buoyancy profiles shown at 8 different times: 115s, 355s, 595s, 835s, 1075s, 1315s, 1555s, and 1795s through each of 4 “ramp up” experiments (one subplot for each experiment) with a final flow rate of 9.5ml/s. Experimental profiles are shown by the thin, solid, black lines, and theoretical profiles using the peeling plume model are shown by the thicker, dashed, grey lines.	118
4.21	Dimensionless ambient buoyancy profiles shown at 8 different times: 115s, 355s, 595s, 835s, 1075s, 1315s, 1555s, and 1795s through each of 4 “ramp up” experiments (one subplot for each experiment) with final source flow rate 3.7ml/s. Experimental profiles are shown by the thin, solid, black lines, and theoretical profiles using the one-way-entrainment model are shown by the thicker, dashed, grey lines.	119
4.22	Dimensionless ambient buoyancy profiles shown at 8 different times: 115s, 355s, 595s, 835s, 1075s, 1315s, 1555s, and 1795s through each of 4 “ramp up” experiments (one subplot for each experiment) with final source flow rate 6.3ml/s. Experimental profiles are shown by the thin, solid, black lines, and theoretical profiles using the one-way-entrainment model are shown by the thicker, dashed, grey lines.	119

- 4.23 Dimensionless ambient buoyancy profiles shown at 8 different times: 115s, 355s, 595s, 835s, 1075s, 1315s, 1555s, and 1795s through each of 4 “ramp up” experiments (one subplot for each experiment) with final source flow rate 9.5ml/s. Experimental profiles are shown by the thin, solid, black lines, and theoretical profiles using the one-way-entrainment model are shown by the thicker, dashed, grey lines. 120
- 4.24 RMS error between theoretical and experimental profiles for the “ramp up” experiments, looking at the bottom tenth of the tank, where the difference between the two models is located. The thick grey lines with circles are for the one-way-entrainment model, and the thin orange lines with crosses are for the peeling plume model. Each subplot is for one slope of ramp, and each line is one experiment. The crosses/circles on each line are for each time that a profile is taken and compared. 120
- 4.25 RMS error between theoretical and experimental profiles for the “ramp up” experiments, divided by the maximum dimensionless ambient buoyancy from theory at each timestep - each circle - that a profile is taken and compared. Each subplot is for one slope of ramp, and each line is one experiment, with lighter shaded lines corresponding to smaller source densities. Values of the entrainment coefficient α are taken from table 4.7. 121
- 4.26 Schematic showing that, although some peeling occurs, entrainment in the stratified region is still important. 122
- 4.27 Dimensionless ambient buoyancy profiles for the PCM mimicking experiment shown at 14 different times, starting at 115s = 0.5τ , and shown every $240s = 1.1\tau$. Experimental profiles are shown by the thin, solid, black lines, and theoretical profiles using the peeling plume model are shown by the thicker, dashed, grey lines. The entrainment coefficient used is $\alpha = 0.012$ 124
- 4.28 RMS error between theoretical (peeling plume model) and experimental profiles, divided by maximum dimensionless ambient buoyancy at each time profiles were compared, for the PCM mimicking experiment. Each circle corresponds to a time at which a profile is measured and compared with the theory. 124
- 4.29 Three cases to be studied using the PCM mimicking source model. Case A has solidification time $t_s \ll \tau$, case B has $t_s = \tau$, and case C has $t_s \gg \tau$ 125
- 4.30 The final dimensionless ambient buoyancy profiles for case A (dot-and-dash line), case B (dashed line), and case C (solid line). 126

4.31	The final dimensionless ambient buoyancy profiles for case A (dot-and-dash line), case B (dashed line), and case C (solid line). The new model, with the source buoyancy flux varying with the ambient temperature, is shown by the thick lines, while the old model, with a source buoyancy flux that depends on the initial ambient temperature only, is shown by the thin lines.	128
4.32	The final temperature profiles for case A (dot-and-dash line), case B (dashed line), and case C (solid line). The green rectangle indicates temperature 1°C either side of the melting range. These temperatures are considered comfortable temperatures, and we aim to maintain temperatures in the occupied region of the room within this range. This is a preliminary result, and is by no means perfect. The wall thickness should be tuned to give comfortable temperatures over a wider range of heights in the room. This example shows, however, that the wall thickness needs to be such that the solidification time t_s is much greater than the timescale τ , as in case C, but just how much bigger is yet to be determined.	130
A.1	A winter garden, a space mostly enclosed by glass, apart from a small gap in the exterior glass wall, allowing for ventilation. Viewed from the bedroom of one of the test apartments (left), and from the exterior (right).	155
A.2	The two bedrooms: the apartment with PCM wallboard (left), and the apartment without PCM wallboard (right).	155
A.3	PCM wallboard mounted on the wall of one apartment. A double thickness of wallboard is used, as evident from the side view (right).	156
A.4	Wall surface temperature for PCM wallboard (thick solid line) and wallboard without PCM (thin solid line), responding to a sinusoidally varying room temperature (thin dashed line), using the five dimensionless parameter values listed in table A.1.	158
A.5	Thermocouples measuring temperatures of (left) PCM wallboard, and (right) a wall without PCM wallboard.	160
A.6	Thermocouples measuring room temperatures are placed on a free standing pole. The pole in the apartment with PCM (left), the pole in the apartment without PCM (centre), and detail of the thermocouple holders on the pole (right).	160
A.7	Wall (green lines) and room (orange lines) temperatures in the apartment with PCM wallboard (left) and in the apartment without PCM (right), measured during September 2015. Darker shades correspond to temperatures measured at lower heights.	161

A.8 Wall (green lines) and room (orange lines) temperatures in the apartment with PCM wallboard (left) and the apartment without PCM (right), measured from the 28th October 2015 to the 23rd November 2015. Darker shades correspond to temperatures measured at lower heights. 162

List of tables

2.1	Symbols used, the quantities they refer to, and their units. Dimensionless variables and parameters are shown in brackets on the same line as the corresponding physical quantity.	27
2.2	Typical values of the relevant physical properties, values for wallboard taken from the paper by Richardson and Woods (2008), and for concrete taken from The Engineering ToolBox.	30
2.3	Values of H_+ , as defined in (2.7), and Ω , as defined in (2.8), for three different wall thicknesses, for both concrete and wallboard.	30
2.4	Values of Stefan number s , as defined in (2.9), for three different PCM mass fractions, for both concrete and wallboard.	31
3.1	The 20 line source experiments, including the dimensionless density difference $\Delta\rho$ between the source and the initial ambient. These give the source buoyancy fluxes listed in table 3.2.	56
3.2	The source buoyancy flux per unit source width (line source) or source area (full wall and half wall sources), $g\Delta\rho$, multiplied by the volume flux (in m^3s^{-1}), divided by the source width (line source) or source area (full wall and half wall sources).	56
3.3	The 20 full wall source experiments, including the dimensionless density difference $\Delta\rho$ between the source and initial ambient. These give the source buoyancy fluxes listed in table 3.2.	58
3.4	The 20 half wall source experiments, including the dimensionless density difference $\Delta\rho$ between the source and initial ambient. These give the source buoyancy fluxes listed in table 3.2.	60
3.5	The timescales $W\alpha^{-2/3}f_0^{-1/3}$ for the 20 line source experiments.	63
3.6	The timescales $W\alpha^{-2/3}b_{s0}^{-1/3}H^{-1/3}$ for the 20 full wall source experiments, with $\alpha = 0.018$	67
3.7	The timescales $W\alpha^{-2/3}b_{s0}^{-1/3}H^{-1/3}$ for the 20 half wall source experiments.	77

4.1	The three ramps used for the “ramp down” experiments. The “ramp up” experiments start from zero flow rate and reach the values listed in the “Initial flow rate” column of the table after 30 minutes, so the magnitude of the slope of the ramp is the same as for the “ramp down” experiments, but with the opposite sign.	83
4.2	The ramp and dimensionless source density difference for each of the 12 “ramp down” experiments and each of the 12 “ramp up” experiments. . . .	84
4.3	The maximum source buoyancy flux for each of the 12 “ramp down” experiments and each of the 12 “ramp up” experiments. Source buoyancy flux is $g\Delta\rho$ multiplied by the source flow rate, divided by the source area.	85
4.4	The timescale $W\alpha^{-2/3}b_{s_{0\max}}^{-1/3}H^{-1/3}$ for each “ramp down” and “ramp up” experiment. Since the one-way-entrainment and peeling plume models have different values of α that minimise total RMS error, timescales calculated using both values of α are listed.	85
4.5	Parameter values for Knauf Comfortboard. Convection coefficient from Richardson and Woods (2008); thermal expansion coefficient, density of air, specific heat capacity of air from The Engineering ToolBox, and melting temperature, thermal mass density, thermal mass thickness, and latent heat from Knauf (2014).	88
4.6	The value of the entrainment coefficient α that minimises total RMS error between the experimental and theoretical (peeling plume) profiles, for each “ramp down” experiment.	115
4.7	The value of the entrainment coefficient that minimises total RMS error between the experimental and theoretical profiles, for each “ramp up” experiment, for both the one-way-entrainment model and the peeling plume model.	122
A.1	Dimensionless parameter values for Knauf Comfortboard.	157

Chapter 1

Introduction

Reducing energy consumption in the built environment is a key concern in the face of costly energy bills and the threat of climate change. Fuel poverty was a reality for approximately 10.4% of, or 2.35 million, households in England in 2013. Fuel poverty means that their required fuel costs are above the national average and, were they to spend this amount on fuel, the income remaining would leave them below the official poverty line (Department of Energy & Climate Change, 2015). While the fuel poverty gap has decreased in recent years, for the 2.34 million households that were projected to be fuel poor in 2015 (Department of Energy & Climate Change, 2015), the cost of energy bills remains a real concern.

Anthropogenic emissions of greenhouse gases are extremely likely to be the main cause of warming that has been observed since the middle of the 20th century (IPCC, 2014). Rising sea levels as snow and ice melt (increasing the risk of flooding), more heat waves, and more extreme precipitation events are just some potential effects of this warming climate (IPCC, 2014). Greenhouse gases, which are likely to be the main cause of anthropogenic climate change, are produced when burning fossil fuels to, for example, produce electricity or to provide heating. By reducing our energy consumption, we also reduce our greenhouse gas emissions and our contribution to climate change.

1.1 Thermal comfort in buildings

Heating the buildings that we live and work in contributes significantly to our total energy consumption. Approximately 48% of the energy used (excluding transport) in the UK in 2013 was used for space heating, and when considering just domestic buildings, this amount increases to approximately 65% (DECC, 2012, updated in 2014). Since heating buildings accounts for such a large proportion of our energy use, when looking to reduce our energy consumption, heating is a natural place to seek improvements.

Cooling the buildings that we live and work in is increasingly required, particularly in modern, well-insulated buildings, which may be at risk of overheating. Modern (after 1990) buildings in England, when monitored by Beizaee et al. (2013) in the summer of 2007 (a study of 207 homes), had higher bedroom temperatures than those of older (before 1919) buildings. Despite 2007 being a cool summer, Beizaee et al. (2013) found that 21% of the bedrooms exceeded the recommended limit of more than 5% of nighttime hours over 26°C, highlighting the importance of cooling, even in the UK. Lomas and Kane (2013) measured temperatures in the living rooms and bedrooms of 268 homes in Leicester, UK. They find that, compared with other types of house, flats tend to be significantly warmer. One-person households (who may choose to live in a smaller flat rather than a house) in England are projected to increase by 72,000 per year (Department for Communities and Local Government, 2015), and, in 2014/2015, over a quarter of new builds in England were flats (Department for Communities and Local Government, 2016). If flats, then, are significantly warmer than other house types, and heat waves are likely to occur more often, because of climate change (IPCC, 2014), then preventing overheating in flats will become increasingly important. In 18 social housing flats in Coventry, UK, built to the Passivhaus standard (BRE, 2011), Sameni et al. (2015) found that more than two thirds of the flats exceeded a fixed benchmark temperature, so have a high risk of summer overheating. With the risk of summer overheating, cooling in buildings, with its associated energy consumption, is set to become increasingly important.

Heating and cooling are often used to achieve thermal comfort for a building's occupants. Thermal comfort depends on both environmental (air temperature, mean radiant temperature, relative air velocity, relative humidity) and personal (metabolic rate, clothing thermal resistance) factors (Hensen, 1990). In some situations, however, these six classical factors in thermal comfort are insufficient, and other factors, such as culture, behaviour, age, gender, space layout, thermal history, an individual's preferences, and, particularly, control over the environment (for example, whether windows are openable), also play a role (Rupp et al., 2015). Different measures of thermal comfort may lead to different conclusions. For example, Sameni et al. (2015) find that, when using an adaptive benchmark rather than a fixed benchmark (the Passivhaus criteria), normal (rather than vulnerable) occupants of the social housing flats studied have a lower overheating risk, but vulnerable occupants (those who are particularly sensitive and fragile, for example, the elderly) have a higher overheating risk. Thermal comfort is complex, and depends on more than just the air temperature in a room.

1.2 Storing heat

Temperatures, which affect comfort, vary from day to night. Beizaee et al. (2013) measured temperatures varying by approximately 2 – 4°C between day and night in an unheated home in Leicestershire, UK, during the summer of 2007. Storing heat during the day and “coolth” during the night, to be used at a later time, smooths out temperature fluctuations, reducing the need for additional heating or cooling.

Thermal energy storage (TES) tanks store heat or “coolth”, to use at a later time. These tanks often consist of a solid to store the heat (for example, rocks), and a fluid for heat transfer (for example, water or air). One phase models, which combine the solid and liquid rather than treating them separately, have been used to model thermal energy storage. Schütz et al. (2015) present four such one-phase models for stratification in the TES tank. These models more accurately calculate the system’s efficiency than models that assume the TES tank has no stratification, so is all at the same temperature. The perturbation model presented by Votyakov and Bonanos (2014) goes beyond one-phase models and represents the solid temperature as the fluid temperature plus a small perturbation. This perturbation model agrees well with the full two-phase model, which accounts for both solid and fluid, but the perturbation model is simpler.

Another way to store heat or “coolth” is in the fabric of the building. This idea, thermal mass, has been used from ancient times, in the form of buildings made of adobe and stone, for example, to modern times, in the form of buildings made of concrete, brick, and rammed earth, for example (Rempel and Rempel, 2013). Examples of thermal mass are shown in figure 1.1. Holford and Woods (2007) use a “lumped” model for thermal mass in a naturally ventilated space. The ventilation rate is key: they find that if it is small, the thermal mass buffers indoor temperatures from outdoor temperature fluctuations, but if the ventilation rate is large, then the indoor temperature fluctuates with the outdoor temperature. Two time scales matter: the time for ventilating the room, and the time for the thermal mass temperature to adjust. Careful design of thermal mass, with these timescales in mind, will help ensure its effectiveness. With a gradual change in heat load or wind forcing, the important time scales are the time over which the ventilation flow adjusts and the time over which the thermal mass temperature adjusts. These time scales control how room temperatures evolve (Lishman and Woods, 2009). Many modern buildings, however, have little thermal mass and are thermally lightweight.



Fig. 1.1 Examples of thermal mass in buildings: the thick walls of (a) Carmel Mission Basilica, California, and (b) a house in North Wales, and (c) exposed concrete thermal mass at the Centre for Mathematical Sciences, Cambridge, UK.

1.3 Phase change materials (PCMs)

Thermally lightweight modern buildings may have thermal mass added to them by using phase change materials (PCMs). These PCMs store heat as latent heat by melting and solidifying in a melting range selected to be around room temperature. During the day, when a room is hot, the PCM melts, storing heat as latent heat, and then during the night, when a room is cold, the PCM solidifies, releasing heat. This storing and releasing heat smooths out fluctuations in building temperatures; PCM acts as thermal mass. Only a small volume of PCM is needed to store heat, compared with a concrete wall, so PCMs are ideal for use in modern, lightweight buildings to increase the thermal mass.

1.3.1 Types of PCM

PCMs are of three main types: organics, salt hydrates, and eutectic mixtures (Tyagi and Buddhi, 2007). Organic PCMs, including both paraffins and non-paraffins (such as fatty acids, esters, and glycols) (Baetens et al., 2010), are chemically stable, undergo little supercooling, are non-corrosive, are non-toxic, and are available in a large temperature range (Baetens et al., 2010), (Kuznik et al., 2011), (Abhat, 1983). They have, however, low thermal conductivity, low latent heat, and are flammable (Kuznik et al., 2011). Salt hydrates have a high latent storage density, a high thermal conductivity, are non-flammable, and are typically cheaper than organic PCMs. However, they undergo supercooling, undergo phase segregation (they melt into a solid and a liquid part, which separate), and have a large volume change (Baetens et al., 2010), (Kuznik et al., 2011), (Abhat, 1983). Eutectic mixtures, which are mixtures of

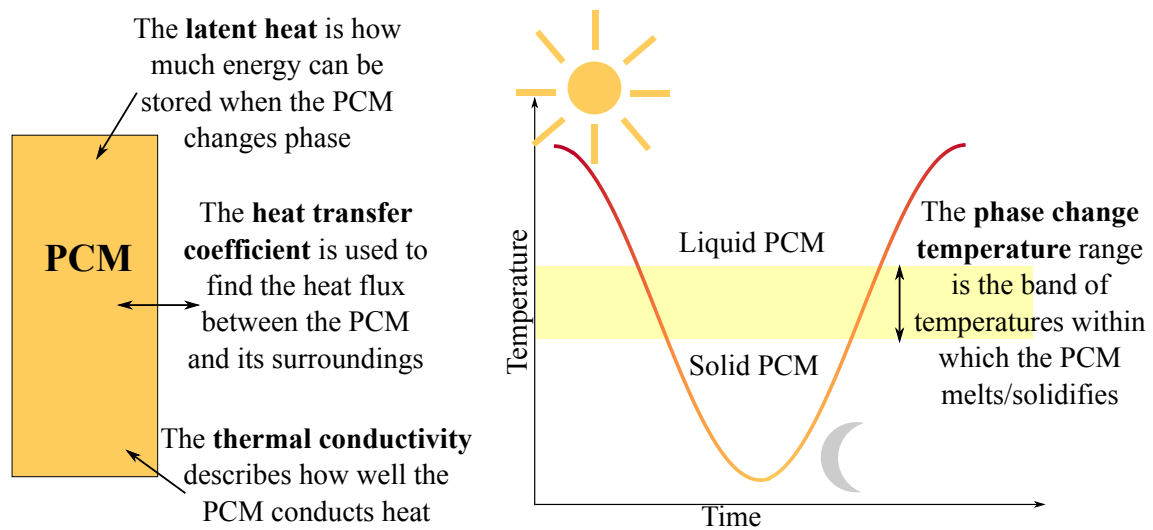


Fig. 1.2 A schematic showing what the phase change temperature, latent heat, thermal conductivity, and heat transfer coefficient mean for a PCM.

components in proportions that give the lowest possible single melting temperature (Baetens et al., 2010), (Kuznik et al., 2011), have sharp melting points and higher storage density than organic PCMs. However, only limited data is available about them (Pasupathy et al., 2008). Different PCMs have different values of melting temperature and other key properties. The ideal values of these PCM properties depend on the climate that the PCM is used in. In the US alone, Poudel and Blouin (2013) identify 15 climate types for which they find optimal PCM properties.

1.3.2 Measuring a PCM's properties

To assess a PCM's suitability, its properties must be measured. Important parameters for determining the effectiveness of a PCM are, according to Zhou et al. (2014), phase change temperature, latent heat, thermal conductivity, and heat transfer coefficients. These properties are shown schematically in figure 1.2. Zhou et al. (2014) find that a narrow melting range with large latent heat is best. Techniques used to measure PCM properties include differential scanning calorimetry, the T-history method (Günther et al., 2006), an impulse method (Pavlík et al., 2013), a water bath method, differential thermal analysis (Xie et al., 2013), and a transient guarded hot plate technique (Karkri et al., 2015).

Differential scanning calorimetry is used to find the phase change temperature and the latent heat storage capacity (Shilei et al., 2007). It works by heating a sample and a reference, and measuring the difference in heat absorbed between the two (Xie et al., 2013). Two modes are available: a dynamic mode, where the temperature is ramped up at a constant rate, and

a step mode, where the temperature is increased in discrete steps (Barreneche et al., 2013). The method is sensitive to the heating/cooling rate (Barreneche et al., 2013), so this rate must be selected carefully – Günther et al. (2006) recommend a small heating rate for accuracy.

The T-history method is used to find the heat capacity (Günther et al., 2006). As in differential scanning calorimetry, a sample and a reference are heated or cooled, but in the T-history method, the respective temperature differences from the surroundings are measured (Günther et al., 2006). The T-history method allows both large samples and PCMs with supercooling to be measured (Günther et al., 2006), but is limited by the assumption that specific heats are constant and independent of temperature (Rady and Arquis, 2010).

Differential scanning calorimetry and the T-history method are commonly used to measure PCM properties, but other methods are also available. The impulse method of Pavlík et al. (2013) is used to find thermal conductivity and thermal diffusivity. It works by analysing the temperature response of a signal to heat flow impulses. The water bath method of Xie et al. (2013) is used to find heat capacity. It works by heating a sample, raising the temperature at a constant ramp, then using an energy balance to determine the heat capacity. Differential thermal analysis is used to measure specific heat capacity and latent heat. It works by subjecting a sample and a reference to the same heat load, then measuring their temperature differences. The transient guarded hot plate technique of Karkri et al. (2015) is used to find heat storage capacity and thermal conductivity. It works by measuring temperature changes and heat fluxes when a (possibly large) sample is heated or cooled.

1.3.3 Containing PCMs

We must contain PCM in some way, if it is to be used in buildings, so that the liquid phase remains in the building fabric, rather than simply flowing away. Five main ways to include PCM in buildings are macro-encapsulation, micro-encapsulation, immersion, direct incorporation, and shape-stabilisation (Zhou et al., 2012).

Macro-encapsulation involves placing the PCM in containers, such as tubes, pouches, spheres, or panels (Pasupathy et al., 2008), that are larger than 1cm (Cabeza et al., 2011). It reduces external volume changes (the container stays the same when the PCM changes phase) (Cabeza et al., 2011) and prevents leakage of liquid phase PCM. However, macro-encapsulated PCMs have poor thermal conductivity and PCM tends to solidify at the edges of the container (reducing heat transfer) (Zhou et al., 2012). Elmozughi et al. (2014) simulate the phase change process for PCM macro-encapsulated in both spherical and cylindrical containers with an air void, finding that the void affects heat transfer rates. They also find the shape of the interface between solid and liquid PCM.

Micro-encapsulation means coating small (around $5\mu\text{m}$ (BASF, 2015)) spherical or rod-shaped PCM particles in a polymer film (Pasupathy et al., 2008). Provided the polymer film is compatible, these particles may then be mixed in with any building material. Careful selection of the type of film, based on the operating temperature, is required, to ensure that the micro-encapsulated PCM remains contained, without leaking (Konuklu et al., 2014). Micro-encapsulated PCMs are free from the problems with solidification at the container edges that macro-encapsulated PCMs experience (Pasupathy et al., 2008). When added to a building material, however, they may affect its mechanical strength (Zhou et al., 2012).

Immersion means dipping building components, made of gypsum, brick, or concrete, into liquid PCM, and direct incorporation means adding powdered solid PCM directly into building materials. Both of these methods are simple, requiring no extra equipment, but PCM may leak (Zhou et al., 2012).

Shape stabilisation means combining liquid PCM with a supporting material (Tang et al. (2015) used expanded graphite), then cooling the mixture until it solidifies (Kuznik et al., 2011). Large PCM mass fractions of up to 80% can be achieved if an appropriate supporting material is chosen, but shape-stabilised PCMs typically have low thermal conductivities (Kuznik et al., 2011).

1.3.4 Ways to use PCMs in buildings

Thermal energy storage (TES) tanks, discussed in section 1.2, are one way to use PCMs to store heat and “coolth” in modern, thermally lightweight buildings. Moreno et al. (2014) compare a TES tank filled with macro-encapsulated PCM with a TES tank filled with water. They find that, compared with the water tank, whilst the PCM tank takes longer to charge, it is able to maintain the indoor temperature within a comfortable range for longer. On combining a hollow core concrete slab with active PCM thermal mass, Whiffen et al. (2016) find that, although under peak conditions additional air conditioning is needed, under fixed occupancy and diurnal swing conditions, using PCM saves energy on cooling. To further improve the use of PCM in TES tanks, Hosseini et al. (2015) find that using fins in horizontal cylindrical tubes filled with PCM leads to more symmetric melting and better heat absorption. PCM thermal energy storage systems are also used with solar energy for heating and hot water, solving the mismatch between production and demand (Noyé, 2011), (Fiorentini et al., 2015), as well as with earth-air heat exchangers for cooling (Rodrigues and Gillott, 2013). Hybrid passive-active systems, such as that of Navarro et al. (2015) have also been developed. They put macro-encapsulated PCM in the holes of a concrete slab, and pumped air through the holes in the slab, around the macro-encapsulated PCM. On testing a prototype experimentally

at the University of Lleida, Spain, they conclude that, since the prototype was inefficient in summer, a control system is needed to make best use of the system.

For active or hybrid passive-active systems, such as those described above, to be of use, energy must be input. Passive systems, however, require no extra energy use. Not only do active systems consume more energy than passive systems, they need complex equipment, such as the control system suggested by Navarro et al. (2015). The capital costs associated with such equipment may be large, for example, for PCM thermal energy storage combined with mechanical ventilation, Udra (2015) finds that the capital cost of the system dominates, and that the system costs more than it saves. This thesis focuses on passive PCM thermal mass, since active PCM thermal storage systems require extra energy to be input, and have high capital costs.

PCM incorporated in the building fabric acts as passive thermal mass. Lecompte et al. (2015) add micro-encapsulated PCM to concretes and mortars, finding that PCM improves the thermal behaviour of walls. From a mechanical point of view, however, they find that the microcapsules act as voids, possibly affecting the strength of the concrete. By adding lightweight aggregate soaked in PCM to mortar, Sharifi and Sakulich (2015) find that, compared with mortar without PCM, the thermal mass is increased. The improved thermal behaviour of walls containing PCMs in these two studies suggests that using PCM passively in walls is a promising way to reduce the energy consumption associated with maintaining a comfortable thermal environment in buildings. Whilst using PCM in concretes and mortars is appropriate for new builds, to use PCMs in existing buildings requires retrofitting. One way to do this is to retrofit wallboard containing PCM.

PCM has been included in wallboard, often by adding microencapsulated PCM to wallboard (an example of this type of wallboard is shown in figure 1.3). Feustel and Stetiu (1997) carry out simulations for a living room with high internal loads, located in Sunnyvale, California, where, since the area is earthquake prone, many buildings are lightweight. They compare a double thickness of PCM wallboard with a double thickness of conventional wallboard and find that, with PCM, room temperature is significantly reduced. PCM wall temperatures were higher than those of other walls when the PCM was solidifying, and lower than those of other walls when the PCM was melting, in the experiments of Liu and Awbi (2009) – PCM is having the desired effect of reducing temperature fluctuations. Significant amounts of heat are stored and released in the experiments and simulations of Ahmad et al. (2006) on PCM wallboard combined with a vacuum isolation panel. The PCM external wall panel developed by Khalifa (2013) achieves a reduction of between 3°C–5°C in indoor temperature. The location of the PCM within the wall matters, Jin et al. (2014) find, and that



Fig. 1.3 Knauf Comfortboard, a wallboard containing microencapsulated PCM. Figure (a) shows the front of the wallboard, and figure (b) shows the side view (two sheets of wallboard have been used together in this picture).

having the PCM close to the side of the wall facing into the room (without being at the wall surface) is the optimal location.

Horizontal surfaces such as floors and ceilings may also have PCMs added to them. Royon et al. (2014) simulate (validated by experiments) cylindrical cavities in a floor slab filled with a polymer-PCM composite, and find that using an annulus of PCM that takes up 50% of the cross-sectional area of the cylindrical cavity is optimal. Directly incorporating PCM in ceramic floor tiles, in work by Novais et al. (2015), reduces the indoor space variation by up to 22%. Macro-encapsulated PCM reduces the maximum room temperature by 2°C when used by Weinläder et al. (2014) in a (ventilated) suspended ceiling, although the PCM regenerates poorly. PCM may also be used on roofs, as in the experiments of Guichard et al. (2015) on Reunion Island, which has a tropical and humid climate. They find that the PCM recharges without needing other appliances, thus reducing energy consumption. For PCMs on a flat roof located in Istanbul, Tokuç et al. (2015) find that a PCM thickness of 2cm is ideal.

PCM is beneficial, as shown by the studies discussed above, since it reduces temperature fluctuations, improving the thermal performance of buildings. Phase change materials have associated costs, however, including both environmental and financial costs. The environmental impact of rammed earth is increased by up to 4.5 times (using the Eco

Indicator 99 impact point) when PCM is added (Serrano et al., 2012). The financial payback period, calculated by Kosny et al. (2013), for PCM wallboard used in Phoenix, Arizona, is between 7 and 10 years. To make the best use of PCMs whilst minimising the cost (i.e. minimising the amount of PCM used), mathematical models, such as the model presented in chapter 2, can be used to optimise the amount and location of PCM. Experimental studies are restricted in the number of different PCMs, wall thicknesses, and external conditions that can be studied. In contrast, mathematical models apply to a wide range of situations: changing the wall thickness or type of PCM means simply changing parameter values, for example. Mathematical models are therefore valuable tools for designing PCM thermal mass.

1.3.5 Modelling PCMs

The phase change itself has been modelled in previous work by various authors, tracking the moving interface between the solid and liquid phases of the PCM. Goodrich (1978) presents an efficient numerical technique for solving the one-dimensional version of this problem, which accurately captures the interface position. Enthalpy methods (where latent and specific heat are combined into an enthalpy term in the governing equation (Al-Saadi and Zhai, 2013)), such as that presented by Voller and Cross (1981), work without the boundary between the solid and liquid phases needing to be accurately tracked, and they allow a phase change temperature range, rather than a single phase change temperature, to be used (a phase change temperature range is more physically realistic). Date (1991) presents a strong enthalpy formulation, which prevents the problem of “waviness” of the temperature histories that is encountered when using the weak enthalpy formulation of the Stefan problem. More recently, Gowreesunker et al. (2012) present a method that mimics melting as a heat sink and freezing as a heat source, which allows hysteresis to be included in the model. These models, however, give more detail than is needed to answer questions about how best to use PCMs in buildings.

When modelling PCMs included in building material, we can account for the phase change using other, simpler, methods. Richardson and Woods (2008), for example, use an effective specific heat capacity, which takes different values depending on the PCM temperature. They use a top hat profile for effective specific heat capacity - it takes one value whilst the material is changing phase, and another value when the material is completely solid or completely liquid, whilst Neeper (2000) uses a Gaussian profile. This heat capacity method, Al-Saadi and Zhai (2015b) find, is sensitive to the PCM’s melting range, but is less sensitive to the latent heat. Other methods include the enthalpy method (discussed above), the temperature transforming model (where the energy equation is transformed into a nonlinear equation depending only on temperature, and latent heat is included via a source

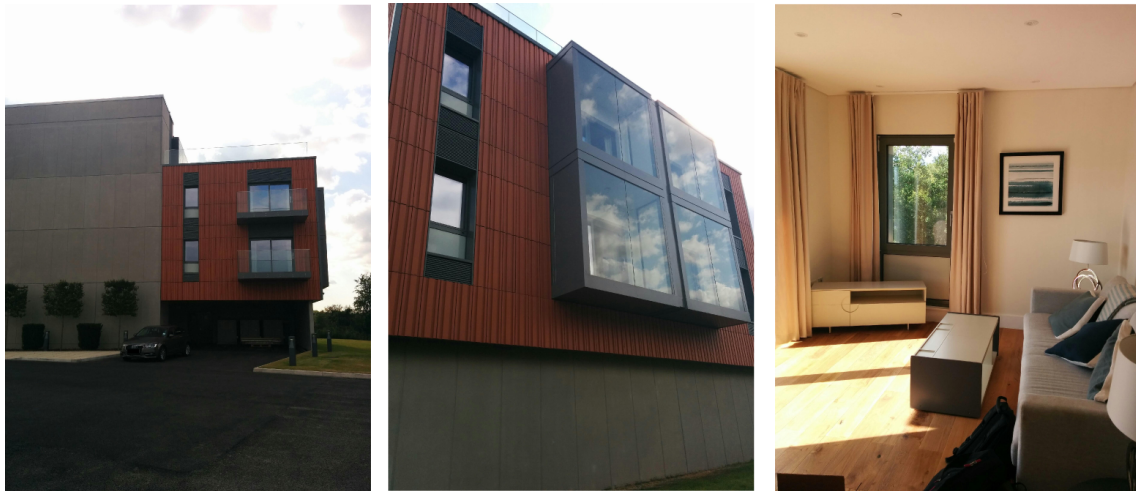


Fig. 1.4 An apartment block that was constructed using modular manufacturing, by Laing O'Rourke, at Explore Industrial Park, in Steetley, near Worksop.

term), and the heat source method (where the enthalpy is split into specific heat and a latent heat source term) (Al-Saadi and Zhai, 2013). The enthalpy method is used by Al-Saadi and Zhai (2015a) in their TRNSYS module, allowing for simulation of PCM walls. In this thesis, the Richardson and Woods (2008) model will be used (and extended to a range of realistic situations) because it is simple, while still capturing the important physics associated with the phase change.

1.4 Modular construction of buildings

Phase change materials could be used in buildings in conjunction with modular manufacturing, an approach to construction where building components are manufactured offsite, in a factory, then simply assembled onsite. Laing O'Rourke are investing in developing their capability in this area, through their Design for Manufacture and Assembly (DfMA) approach. An example of modular construction using this DfMA approach is shown in figure 1.4. When constructing new offices at Tooley Street, London, UK, using the DfMA approach meant that 80% (by volume) of the components used in construction were manufactured offsite (Laing O'Rourke, 2016). Modular components of buildings are of three types: non-volumetric, such as wall panels, volumetric, such as toilet pods, and modular buildings, where the volumetric units form the building (Gibb, 2001).

Similar manufacturing techniques are used in both modular building manufacturing and car manufacturing, as Gann (1996) points out, looking particularly at manufacturing in Japan. However, more computer-integrated-manufacturing techniques are used in car

production than in modular housing, whilst in modular housing, more customization is available. Customization is in demand, although most customers are uninterested in the production process, they are only interested in the end product (allowing for standardization of unseen parts) (Gibb, 2001). Both industries can and do learn from each other: at Toyota, production line workers are transferred between the two factories (Gann, 1996).

Modular manufacturing has both advantages and disadvantages. Improved health and safety is one advantage of modular manufacturing (Court et al., 2009). With modular manufacturing, less work takes place in the potentially dangerous conditions on a building site, and more work takes place in factories, where, for example, mechanical lifting aids can be provided to reduce the risk of injury to workers when handling heavy loads. Other advantages of modular manufacturing include an increase in quality (producing components in a factory, rather than onsite, allows for better quality control) and a shorter time needed onsite for construction, although a barrier to use of modular manufacturing is the perceived cost (Goodier and Gibb, 2007). Pan et al. (2007) suggest that another barrier is the long lead time.

When designing ways to use PCM in buildings, doing so in a way that is consistent with a modular manufacturing approach is prudent. This is because the many benefits of modular manufacturing, together with the interest in it shown by Laing O'Rourke, a large construction company, suggest that it may become an increasingly common way to construct buildings.

1.5 Models for temperature stratification in rooms

One-dimensional models for including PCMs in walls, such as that of Richardson and Woods (2008), tell us about room temperatures without giving details of the temperature stratification within a room. To find the temperature stratification, we must consider models for the stratification that results when a buoyancy source drives a turbulent plume that is contained within a room.

1.5.1 Plumes

The Morton et al. (1956) turbulent plume model underlies many models for the stratification developing in spaces containing buoyancy sources. They make three key assumptions. First, they assume that profiles of vertical velocity and buoyancy across the plume are self-similar with height. Second, they assume that ambient fluid is entrained into the plume at a rate proportional to the characteristic vertical velocity. Third, they assume that changes in density are small compared with a reference density – the Boussinesq approximation. With non-

Boussinesq effects included in the model, van den Bremer and Hunt (2014b) find that, for pure plumes, the two models lead to equivalent solutions, which, they suggest, means that their unmodified entrainment model may be invalid.

Describing entrainment is a key part of any plume model. The enhanced entrainment seen in plane pure plumes, compared with plane pure jets, Paillat and Kaminski (2014) explain, is due to buoyancy-induced vorticity generation. The entrainment coefficient for a jet with negative buoyancy depends linearly on the local plume Richardson number (to first order) (Kaminski et al., 2005). Plumes have a range of source conditions; van den Bremer and Hunt (2014a) find five classes: fountains, pure jets, forced plumes, pure plumes, and lazy plumes. In experiments with three different source conditions, Ezzamel et al. (2015) find that the entrainment coefficient varies with plume Richardson number. By using energy constraints, van Reeuwijk and Craske (2015) find restrictions on the entrainment coefficient. The Morton et al. (1956) model is a limit case of van Reeuwijk and Craske's entrainment model, as it assumes that the entrainment coefficient is independent of the plume Richardson number $Ri = \frac{b_m r_m}{w_m^2}$ (where b_m , r_m , and w_m are the characteristic plume buoyancy, width, and velocity, respectively). The other limit case is when δ_m , the contribution from the mean flow to the profile coefficient associated with turbulence production, is independent of Ri . In this thesis, the Morton et al. (1956) model is used for simplicity.

Multiple plumes form with multiple buoyancy sources, and these plumes may then merge. For two coalescing axisymmetric plumes, Cenedese and Linden (2014) find three dynamical regions: first, the plumes are separate, but are drawn together as they entrain the ambient fluid between them, then they touch each other, and finally, they are merged. The height at which the plumes merge is predicted by Kaye and Linden (2004).

1.5.2 Filling boxes with point or line sources of buoyancy

Inside a sealed space where a buoyancy source drives a turbulent plume, as the plume adds buoyant fluid to the ambient, a stratification develops. Typically, a buoyant plume rises to the ceiling of the space, where it adds buoyant fluid to the ambient, forming, from the ceiling down, a stratified region. Using the Morton et al. (1956) plume model, Baines and Turner (1969) find both the location of (depending on time) and the density step at the interface between the initial ambient and this stratified region. The time dependent ambient density profile that develops is described by approximate analytic expressions, found by Worster and Huppert (1983), which they compare with numerical solutions. To solve this type of problem numerically, a method similar to that of Germeles (1975) is sometimes used, where it is assumed that the plume lays down layers of buoyant fluid at the ceiling, then the thickness and location of these layers are tracked in time, as shown by the schematic in figure 1.5.

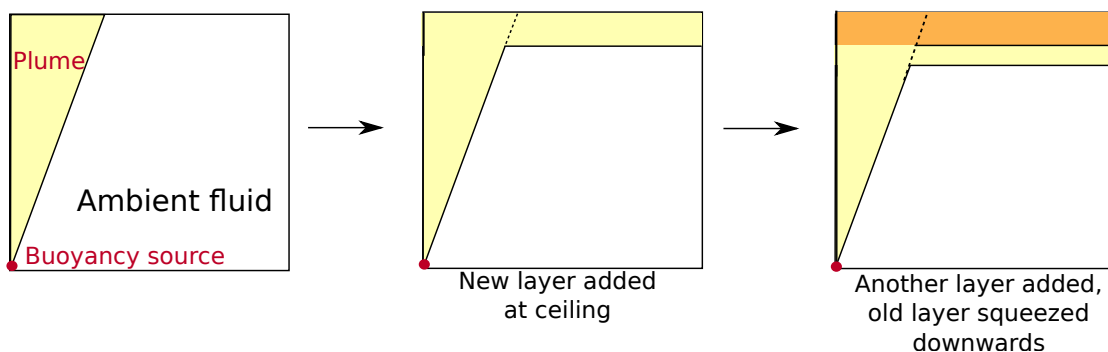


Fig. 1.5 A schematic showing the method of Germeles (1975).

Wong et al. (2001) find that, superimposed on the filling box flow, a series of shear layers are supported. Whilst these shear layers have a large effect on the transport of individual water parcels and tracers, they have little effect on the stratification. With a filling box that contains a pre-existing stable stratification, the experiments of Cardoso and Woods (1993) show that the plume can intrude into the ambient at an intermediate height.

In some spaces, a two layer stratification forms, with the two layers separated by an interface. The plume impinging on this interface can lead to entrainment across the interface. For a plume impinging on a two layer stratification, Kumagai (1984) finds that the entrainment rate depends on the Froude number $Fr = \frac{w_H}{(b_H \Delta_{12})^{1/2}}$ (where b_H and w_H are the local width and velocity, respectively, of the plume at the interface, and Δ_{12} is the buoyancy difference across the interface), and is close to Fr^3 at small values of Fr . Shrinivas and Hunt (2015) find that it also depends on a confinement parameter $\lambda_i = \frac{b_i}{H-h}$ (where b_i is the radius of the impinging fountain, H is the box height, and h is the interface height), which compares the length scale of interfacial turbulence with the depth of the upper layer. With a two layer stratification, Mott and Woods (2009) find that the plume intrudes at the interface, supplying an intermediate fluid layer. They account for the mixing in this intermediate layer using a model based on effective turbulent diffusion; compared with the Kumagai (1984) model, this model more accurately describes the density profiles. Their model assumes that there is a vertical buoyancy flux associated with mixing which scales as $\epsilon u b \frac{g}{\rho_0} \frac{\partial \rho}{\partial z} b^2$, where u is the mean velocity of the plume, b is the mean radius of the plume, $\frac{\partial \rho}{\partial z}$ is the local density gradient, and ϵ is a dimensionless parameter. They assume that the mixing decays over a distance $\frac{\beta u}{((g/\rho_0)(\partial \rho/\partial z))^{1/2}}$, where β is a constant of proportionality. Also considering a two layer stratification, Bower et al. (2008) include penetrative entrainment from the intruding plume, with an entrainment flux assumed to depend linearly (with a constant coefficient) on the volume flux of the plume when it arrives at the interface. They find that the model with penetrative entrainment is good for modelling the increased rate at which the depth of the

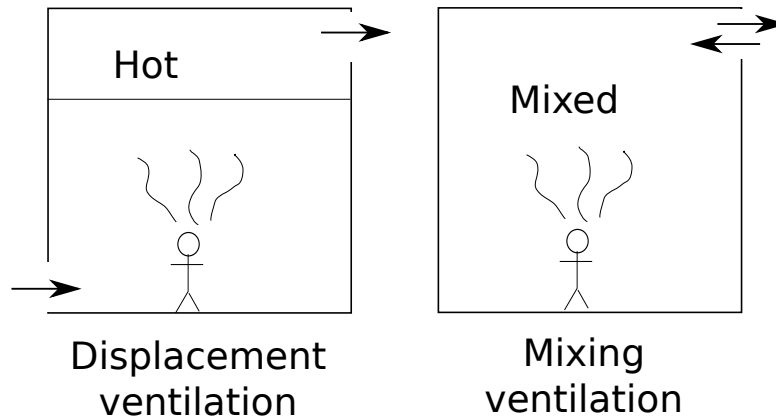


Fig. 1.6 Schematics of two types of ventilation: displacement and mixing

original upper layer decreases, but that a model with no penetrative entrainment is better for finding the density of the intermediate, intruding layer.

1.5.3 Natural ventilation

Real rooms, rather than being merely sealed spaces containing heat sources, are ventilated in some way. Some spaces are naturally ventilated, where flows through the space are driven by temperature differences or wind, and this type of ventilation is of particular interest for low energy buildings. The two types of natural ventilation are displacement ventilation, where cool air enters a space through a low level vent, with warm air leaving through a high level vent, and mixing ventilation, where, when fresh air is introduced into a space, it mixes throughout the whole space. Schematics of these two types of ventilation are shown in figure 1.6. Linden et al. (1990) model these processes, both with theoretical models and experimentally. In section 2.4.2, natural ventilation is included in a PCM thermal mass model, considering a chilled PCM ceiling that is cooled from above in a room with displacement ventilation.

There are different ways to model displacement (natural) ventilation. Perfect mixing models assume that the fluid in the hot upper layer mixes to be at a uniform temperature, whilst zero mixing models assume that plume fluid laid down at the ceiling does not mix with

the rest of the fluid in the hot upper layer. Coomaraswamy and Caulfield (2011) compare these two types of model for flows with opposing wind and buoyancy. They find that, in the situation that they study, the zero mixing model is more appropriate. The two important time scales in the perfect mixing model of Kaye and Hunt (2004) are the filling box time (the time for a plume to fill a closed box) and the draining box time (the time for a ventilated box to drain). Zero mixing models, such as the Germeles (1975) method, which Sandbach and Lane-Serff (2011a) use, assume a sharp first front, but Kaye et al. (2010) find that the interface is smeared out by diffusion.

There are many variations on naturally ventilated spaces, as highlighted by Linden (1999), including non-adiabatic walls (walls which are not totally insulating, and undergo heat exchange with the space). Lane-Serff and Sandbach (2012) find that including conduction through the ceiling lowers the temperature in a ventilated space, and radiative heat transfer between ceiling and floor gives a lower layer that is warmer than the outdoor ambient. Sandbach and Lane-Serff (2011b) also find that including heat transfer in models improves temperature predictions substantially. When PCM is included in walls, accounting for heat transfer is crucial – without it, the effect of the PCM (storing and releasing heat) is missing from the model.

1.5.4 Time-varying buoyancy sources

Some buoyancy sources vary in time - for example, PCM solidifying produces a time-varying buoyancy source - which leads to different flows in the space. Three regions of behaviour occur for a point source whose strength decreases in time: the upper region, which remains mostly unaffected, the lower region, which is, effectively, a steady plume with the new (lower) source buoyancy flux, and a transitional region, where the plume narrows (Scase et al., 2006). This result assumes a constant entrainment coefficient, meaning that the source adjustment time and the characteristic time scale of the plume are assumed to be much longer than the characteristic timescales of turbulent eddies. In the plume's transitional region, however, a shallower slope at the plume edge may modify entrainment from the assumed constant entrainment coefficient, allowing the plume to pinch off. This decreasing source strength is relevant to PCMs: when PCM solidifies, its temperature decreases towards that of the room, so it acts a buoyancy source whose strength is decreasing in time.

In a displacement-ventilated space, when the source strength steps up from a small to a large value, Bower et al. (2008) find that a new upper layer forms, which gradually depletes the old upper layer as it is entrained into the plume. If, instead, the source strength steps down, again the old upper layer is depleted, but now both because it is ventilated out of the upper opening and because of penetrative entrainment as the plume intrudes beneath

the original upper layer. Two models, with and without penetrative entrainment, provide bounds on possible flows. The model with penetrative entrainment picks up the increased rate at which the depth of the draining layer decreases, but the model without penetrative entrainment better describes the density in the intruding layer. Since PCM acts a buoyancy source whose strength is decreasing in time, the resulting plume may intrude, as Bower et al. (2008) find, and then we may need to take account of penetrative entrainment as the plume intrudes.

Some sources have a strength that varies periodically in time. This is relevant to rooms containing PCM since the diurnal temperature variations forcing the system vary periodically in time. For a periodically varying source, Killworth and Turner (1982) find that, in a confined region, fluid far from the plume asymptotically becomes stably stratified, but, when the plume goes through a statically unstable phase, it spreads horizontally. They assume that this spreading takes place over an infinitesimally thin layer, although in reality this spreading will take place over a finite thickness layer. In a naturally ventilated space with a time-periodically varying source, Bolster and Caulfield (2008) find that there are four important flow rates: the three steady state flow rates associated with the larger buoyancy flux, with the smaller buoyancy flux, and with the average of the larger and smaller buoyancy fluxes, as well as the average \bar{q} of the steady state flow rates associated with the smaller and larger buoyancy fluxes. For different spaces, with different occupancy patterns (and therefore buoyancy sources with different strengths and oscillation periods), different flow rates are appropriate for design engineers to consider as the flow rate through the space. The worst case scenario is \bar{q} , which would be appropriate for design engineers to assume. Bolster and Caulfield (2008) also find that, for small changes in source buoyancy flux, the variation in average flow rate is small, whereas for large changes in source buoyancy flux, there can be, depending on the forcing frequency, variations of 20% or larger in the average flow rate.

1.5.5 Distributed sources

Some sources are distributed, rather than just being a point or a line, for example, underfloor heating provides a distributed source, as does solidifying PCM included in floor or ceiling tiles. A source distributed over the floor of a naturally ventilated space gives, Gladstone and Woods (2001) find, lower temperatures, but greater flow rates through the space, than a point source (for a given heat flux) gives. Fitzgerald and Woods (2007) find three possible ventilation regimes: for initial room temperature below the outdoor temperature, the original air is displaced downwards; for initial room temperature between the outdoor and equilibrium temperatures, the room is well mixed; and for initial room temperature above the equilibrium temperature, the original hot upper layer is displaced upwards.

Distributed sources also appear on ceilings, for example, in chilled ceilings. With both a heat source on the floor and distributed cooling at the ceiling, a two layer stratification forms. As the strength of the cooling at the ceiling increases, the depth of the lower layer decreases, and, if the cooling is sufficiently strong, the space becomes well mixed (Livermore and Woods, 2008). When both cooling and heating are distributed, the space is well mixed, and Livermore and Woods (2008) find how much the temperature changes from its initial value by equating two expressions for the natural ventilation flow – one expression from the distributed heat source work of Gladstone and Woods (2001), the other from the displacement ventilation work of Linden (1999). When cooling is distributed, but the heat source is localised, Livermore and Woods (2008) find expressions for the dimensionless depth of the interface in the two layer stratification that develops, along with the temperature. They do this by rearranging two equations, one for volume flux, the other for heat flux. The ventilation volume flux, which is given by Linden (1999), must equal the volume flux supplied by the plume, which is found using the Morton et al. (1956) plume model, and the volume flux from penetrative entrainment at the interface. The heat flux from the heat source matches the heat flux through the heat sink (the ceiling, where there is cooling), added to the heat loss when hot air is ventilated out of the space. These equations for volume flux and heat flux are rearranged to find the dimensionless depth of the interface, along with the temperature. In section 2.4.2, this distributed cooling model of Livermore and Woods (2008) is extended to include PCM in the ceiling of a naturally ventilated room, with the PCM ceiling being chilled from above.

Distributed sources occur on vertical surfaces, such as vertical radiators or patches of wall heated by the sun. A vertical isothermal surface drives a flow, which Wells and Worster (2008) describe using an outer turbulent region with plume equations, coupled to an inner laminar region. They find that, on the laboratory scale, the laminar region gives a constant heat flux, whereas, on the geophysical scale that they are interested in, a larger heat flux is predicted. The dimensionless local Nusselt number, $Nu_z = \frac{q_w z}{\rho_\infty C_p \kappa \Delta T}$ describes the heat flux q_w , where z is distance from the leading edge of the wall, ρ_∞ is ambient density, C_p is specific heat capacity, κ is thermal diffusivity, and ΔT is the temperature difference between the wall and the ambient. Two different scalings, in two different regimes, are used to relate Nu_z to the local Rayleigh number, $Ra_z = \frac{g(\rho_\infty - \rho_w) z^3}{\rho_\infty \kappa \nu}$, where ρ_w is the density of fluid at the wall temperature, and ν is the kinematic viscosity. Specifically, there are two regimes: after transition to turbulence, the flow is buoyancy driven and $Nu_z \propto Ra_z^{1/3}$, but there is another regime, relevant for geophysical flows, where the inner flow is driven by shear, and $Nu_z \propto Ra_z^{1/2}$.

An isothermal vertical wall that is contained in an enclosure gives, Caudwell et al. (2016) find, a boundary layer that is initially laminar, and only transitions to turbulence some way up the wall. They develop a hybrid model, with similarity solutions for the laminar part, and an entrainment model for the turbulent part. They find that the models predicting the stratification that develops in the space are improved by using a variable entrainment coefficient. An exponential fit to experimental data – for the hybrid laminar-turbulent model it is $0.072 \exp(-2.05 \times 10^7 \tau) + 0.0038$, where τ is time – is used for the variable entrainment coefficient. Although this variable entrainment coefficient improves the predicted ambient density profiles somewhat, the model still does not capture the shape of the top of their experimental profiles (see figure 12 of Caudwell et al. (2016)), where the temperature gradient is steeper than in the theoretical profiles. In the wall source experiments of section 3.2.3 we observe a similar shape to the ambient density profiles, and find that this may be explained by using a peeling plume model, as used by Hogg et al. (2015). In this peeling plume model, density and vertical velocity vary across the width of the plume, allowing parts of the plume to peel off into the ambient at intermediate heights.

In a displacement ventilated space containing a vertically distributed source, Chen et al. (2001) propose a multi-layer stratification, which is smoothed out by fluid leaving the plume towards the top of a layer, then being re-entrained farther down in the layer. They extend the multi-layer stratification model of Linden et al. (1990), who use conservation of volume flux with Bernoulli's theorem to obtain an expression for the volume flux through the bottom opening of the space. By equating this to the volume flux through the plume at the interface between two layers, which is obtained from the plume equations, an expression for the number of interfaces, and thus their locations (as the layers are assumed to all have the same thickness) are found. In experiments, Chen et al. (2001) observe the outer layer of plume fluid peeling off into the ambient over a range of heights, while the core of the plume keeps rising. Fluid peeling off at a range of heights, rather than just at the interface between layers, smooths out the multi-layered stratification. Motivated by experimental results, Chen et al. (2001) approximate the room as having two parts, a lower layer and an upper part with a linear stratification. They then use volume conservation and Bernoulli's theorem to find an expression for the interface height which, as with a point source, is independent of the source strength.

In experiments with a vertical line source in a displacement ventilated space, Gladstone and Woods (2014) observe intermittent entrainment and detrainment of plume fluid. This detrainment is plume fluid leaving the plume, intruding into the ambient at intermediate heights. They observe no overall vertical motion in the ambient, so the horizontally averaged plume density at a given point must match that input from the source up to that point, giving

a reduced gravity in the plume which varies linearly with height. Then, Gladstone and Woods (2014) take the difference between the net plume density and ambient density to be independent of height, so the ambient must also be linearly stratified. Experimental measurements also show that the stratified region of the tank is approximately linearly stratified.

Cooper and Hunt (2010) study a vertically distributed source in three situations: an unconfined ambient, a sealed space, and a displacement ventilated space. In the unconfined ambient, they find similarity solutions to the plume equations – these are similar to those used by Morton et al. (1956) for a point source, but include an extra term in the conservation of buoyancy flux equation, to account for the buoyancy flux added by the vertical source. In a sealed box, an extra equation is used for the ambient stratification that develops, and the set of equations are solved numerically, using a method based on that of Germeles (1975). In a ventilated box, a steady-state stratification is reached, and Cooper and Hunt (2010) note that the plume fluid at a given height may be less buoyant than that of the ambient at the same height. In this case, the plume spreads horizontally into the ambient, and a new plume starts. Linden et al. (1990) used this idea, finding a multi-layer stratification, although their experiments, and those of Chen et al. (2001), showed only weak evidence for this layering. On solving the equations numerically, Cooper and Hunt (2010) find that the multi-layer stratification is unstable with respect to small perturbations in either the plume flow or the ambient stratification, and is thus unphysical. The problems with the multi-layer stratification arise from the assumption that the plume is uniform across its width, and so the plume is assumed to intrude at one height, and with one buoyancy. To overcome this problem, Cooper and Hunt (2010) model the plume as having a linear buoyancy profile across its width, so it intrudes into the ambient over a finite depth, and with a finite range of buoyancies. The range of buoyancies for this profile is somewhat arbitrary, however, and Cooper and Hunt (2010) note that there is “complex, and as yet unquantified physics of the detrainment process”. Although Cooper and Hunt (2010) allow for plume properties to vary across the plume width in the ventilated case, their plume model for the sealed case uses top hat profiles, which exclude the possibility of detrainment. In chapter 3, experimental results for a vertically distributed source in a sealed space show that detrainment occurs. The Cooper and Hunt (2010) model for the ambient stratification that develops in a sealed space with a vertically distributed buoyancy source is inadequate, since the shapes of the profiles it predicts are qualitatively different from those measured in experiments. Instead, a peeling plume model, as used by Hogg et al. (2015), is required, and this better captures the shape of the ambient stratification profiles measured in experiments.

The experiments of McConnochie and Kerr (2016) use a filling box containing a vertically distributed buoyancy source; the source is an ice wall (made of fresh water), and it is in a tank of salty water. They measure the velocity maximum in the plume, and their results agree with the predictions of the Cooper and Hunt (2010) model that velocity scales with height to the one-third power. McConnochie and Kerr (2016) suggest, however, that, because velocities measured in experiments are smaller than those predicted by the model of Cooper and Hunt (2010) (which has no viscous effects and predicts a velocity maximum immediately next to the wall), viscous drag also has a significant effect. Motivated by observations from previous work, they update their model to include a linear velocity profile across the width of the plume, and apply this updated model to a typical dissolving iceberg and a typical room. Although their study is more focussed on velocity measurements than the ambient stratification, they find, as Gladstone and Woods (2014) also find, that the ambient buoyancy profile above the first front is approximately linear. They note that the ambient buoyancy profile is continuous at the first front, and that this is not possible without some mechanism for detrainment. In chapter 3, we use a peeling plume model to include detrainment, and find that it better describes the ambient stratification than the one-way-entrainment model of Cooper and Hunt (2010).

1.6 Outline

In this thesis, I investigate using phase change materials to provide thermal mass in buildings. I do this by extending a simple model of PCM thermal mass to a range of realistic situations, using the model to optimise the amount of PCM and wall thickness. To investigate the effect that a PCM wall solidifying (a source of heat, and thus buoyancy) has on the temperature stratification in a room, I consider the effect that vertically distributed buoyancy sources have on the stratification in a sealed space.

Chapter 2 extends a model of PCM thermal mass, applying it to a variety of realistic scenarios. In each scenario, PCM reduces temperature fluctuations substantially when used in appropriate quantities and locations. The model may also be used as a design tool, to optimise the amount of PCM and the wall thickness. In particular, I estimate, given properties of the PCM and of the wall, the ideal depth into the wall for PCM inclusion. Considering a different PCM requires simply changing some parameter values, rather than needing to run new, expensive, and time-consuming experiments or simulations.

Since PCM (included in a wall), when it solidifies, acts as a buoyancy source, chapter 3 considers the stratification that develops with a vertically distributed buoyancy source. In experiments with a vertically distributed buoyancy source spread over the full height of a

wall, detrainment is observed - plume fluid intrudes into the ambient at intermediate heights. This detrainment is modelled using a peeling plume model, where plume density and vertical velocity vary linearly across the width of the plume, and so parts of the plume peel off at intermediate heights. This peeling plume model more accurately captures the shape of the ambient buoyancy profiles measured in experiments than a one-way-entrainment model, with top hat profiles for plume density and vertical velocity, does.

Chapter 4 extends this vertically distributed source work further, by allowing the vertically distributed source to provide a buoyancy flux that, as a PCM wall solidifying does, varies in time. Three cases are considered: ramps up in source buoyancy flux, ramps down in source buoyancy flux, and a combination of two ramps down with a constant flux section, that mimics the source buoyancy flux from a solidifying PCM wall.

Appendix A contains results from measuring temperatures in a real building, constructed using modular manufacturing, that has been fitted with PCM wallboard. I compare temperatures measured in an apartment with PCM with temperatures measured in an apartment without PCM. Autumn data suggests that PCM reduces peaks in temperature, so is useful for reducing overheating. Unfortunately, due to technical problems, summer data was unable to be collected, but the autumn data suggests that collecting the summer data is worthwhile, to test whether PCMs have a noticeable effect in reducing summer overheating. Finally, in chapter 5, I present conclusions of this work.

Chapter 2

The effect of phase change material thermal mass on reducing fluctuations in building temperatures

2.1 Introduction

The threat of climate change and rising energy prices are strong motivations to reduce energy consumption. Over 60% of the energy used in homes in 2011 was used for space heating (DECC, 2012, updated in 2014), so heating in buildings is one area where there is scope for reduction in energy consumption. One way to do this is to use thermal mass. Thermal mass is the ability of building fabric to store heat. Storing heat during a hot day to be used during the cool night reduces the need for daytime cooling and nighttime heating, saving energy, whilst keeping buildings at a comfortable temperature. Holford and Woods (2007) found that, in a naturally ventilated building with small ventilation rates, thermal mass is effective at reducing diurnal temperature fluctuations. Traditional buildings used thermal mass in various forms, such as the thick-walled, dried earth buildings in desert climates (Rempel and Rempel, 2013).

However, modern buildings are often lightweight, with little thermal mass. Phase change materials (PCMs), such as wax and salt hydrates, when installed within a building, can effectively increase thermal mass. PCMs work by changing phase – melting and solidifying – at typical temperatures found in a building. When the PCM changes phase, it absorbs or releases latent heat, without a temperature change. This latent heat is different from sensible heat, which results in a temperature change. The large amount of latent heat absorbed or released during a phase change allows even small volumes of PCM to work effectively

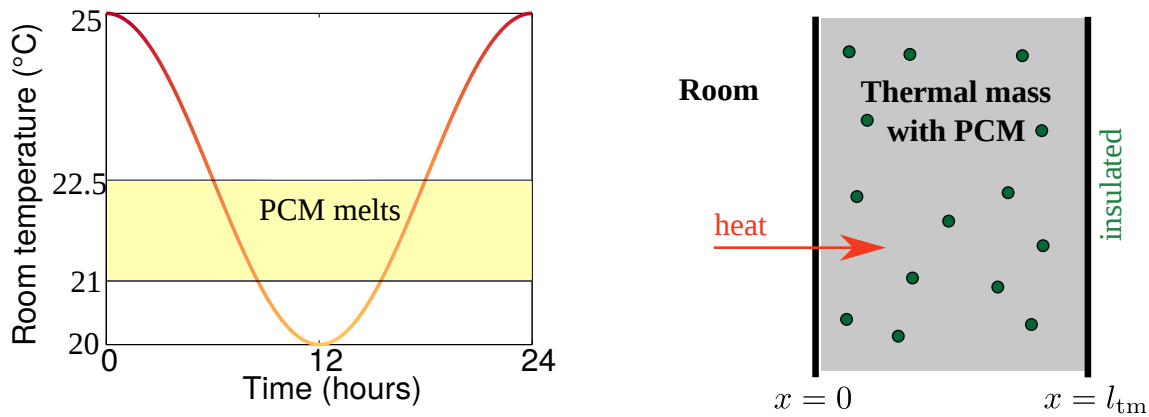


Fig. 2.1 Schematic showing: (left) the asymmetric melting temperature of a PCM relative to a sinusoidally varying room temperature, (right) the uniform distribution of encapsulated PCM within a concrete wall, insulated at its outer surface $x = l_{tm}$, and subject to heat transfer with the room air at its inner surface $x = 0$.

as thermal mass. Zhou et al. (2012) give examples of PCMs. PCM can be included in building fabric: for example, a concrete wall can contain microencapsulated PCM, as shown schematically in figure 2.1. The PCM is encapsulated in relatively small polymer spheres, then mixed into wet concrete, so that PCM is distributed throughout the finished wall (see section 4.1.2 of Zhou et al. (2012)). Typically, the PCM is distributed uniformly through the wall, but Castellón et al. (2010) consider different distributions: with the PCM concentrated near the exterior or interior face of the wall.

In this chapter, a mathematical model developed by Richardson and Woods (2008) to describe the response of PCM thermal mass temperature to a varying room temperature is used. The focus of the chapter is on generalising and applying this mathematical model to realistic circumstances in a building, with the aim of developing design guidelines using commercially realistic parameters. To achieve this aim, several specific real-world circumstances are considered, demonstrating the utility of this modelling approach. The model is briefly described in section 2.2, before being applied and developed in sections 2.3 and 2.4.

The model is first applied, in section 2.3, to two situations that explore optimising the properties and distribution of PCM thermal mass. In section 2.3.1, the wall thickness and quantity of PCM that yield the most benefit – defined as the largest reduction in daily maximum temperatures – for the cost are found. This is important because, not only must PCMs reduce temperature fluctuations, but they must also be commercially viable if they are to be widely used in the built environment. In section 2.3.2, the model is extended to different spatial distributions of PCM through the wall thickness, to see which of these distributions is

the most effective in reducing daily maximum temperatures. Again, this is to ensure that the best use is being made of the PCM, eliminating, as much as possible, redundant PCM.

Section 2.4 explores how PCM thermal mass interacts with its surroundings and in particular with convective air flow. In section 2.4.1, cooling is included at the exterior surface of the PCM thermal mass. This is motivated by exhaust air heat pumps, which may be used in low-energy buildings to recover heat from the exhaust air of a building (Fracastoro and Serraino, 2010), (NIBE Energy Systems AB, 2012). These exhaust air heat pumps output cool air, which is ordinarily wasted, but by storing the “coolth” in PCM thermal mass, it can be used usefully, to provide additional free cooling. Of course real buildings are also ventilated, and this ventilation will interact with the PCM thermal mass. Therefore, in section 2.4.2, displacement natural ventilation in a room with a PCM thermal mass ceiling is considered. As in section 2.4.1, cooling is also included at the exterior surface of the PCM thermal mass (i.e. above the ceiling). To be operationally useful, PCM thermal mass must respond well both to normal operating conditions, and to periods of hot weather that often occur over a summer. Therefore, section 2.4.3 investigates how PCM responds to such a period of hot weather. During summer, the hot days may be longer than the cool nights, so section 2.4.4 investigates how PCM responds to such an asymmetric diurnal cycle. Finally the results are discussed and conclusions are presented in section 2.5.

2.2 PCM thermal mass model of Richardson and Woods (2008)

This chapter uses the Richardson and Woods (2008) one-dimensional PCM thermal mass model, which uses a heat equation with an effective specific heat capacity to find temperatures in the PCM thermal mass. Other PCM models have been developed and used for PCM. For example, Peippo et al. (1991) found the optimal phase change temperature and wall thickness using a simple model that applies only during the phase change. The model uses only two values of the room temperature (one value when the PCM melts, another value when the PCM solidifies), rather than allowing for a room temperature that varies over the course of a day. In contrast, the Richardson and Woods (2008) model applies before, during, and after phase change, and uses a room temperature that varies over the course of the day. Peippo et al. (1991) also did numerical simulations, using a model that finds enthalpy, rather than temperature. Their model assumes an isothermal phase change, whereas the Richardson and Woods (2008) model allows for a phase change across a melting range, which is more physically realistic. The top hat profile used for the effective specific heat capacity, is, as

justified later in this section, appropriate for describing the phase change, but is simpler than that used by Feustel and Stetiu (1997), who took specific heat capacity to be proportional to the square of the hyperbolic secant function. Ahmad et al. (2006) used, like Richardson and Woods (2008), a top hat profile for effective specific heat capacity, but their numerical simulations use a model that includes multiple zones in a building. These zones, and the interactions between them, will be different for different buildings, and need to be found for each building. The model is therefore difficult to apply to a wide range of buildings, whereas Richardson and Woods's simpler, more general model can easily be applied to a wide range of buildings. So, although other models have been developed and used for PCM, this chapter will use the Richardson and Woods (2008) model because it is simple, while still capturing the important physics, and gives temperatures before, during, and after the phase change.

The Richardson and Woods (2008) model is a one wall model. Whole building models are available – see Al-Saadi and Zhai (2013, 2015a) – but in this chapter a one wall model is considered because it is relevant to one potential use of PCMs: retrofitting one wall of a room in an existing building with PCM wallboard, as is done in the real life data collection described in appendix A. For this reason, comparison with whole building simulations, which use EnergyPlus or TRNSYS, for example, is not appropriate.

The Richardson and Woods (2008) model is extended to allow for a more physically realistic asymmetric (about the average room temperature) melting range. Figure 2.1 shows an example of such a melting range: the average room temperature is 22.5°C, but the melting range is 21°C to 22.5°C. The assumption is made, as made by Richardson and Woods (2008), that the fraction of PCM that is liquid varies linearly with temperature from 0 to 1 over this melting range. The evolution of the temperature fluctuations in the PCM thermal mass satisfies a heat equation

$$\frac{\partial u}{\partial t} = \frac{K}{\rho \bar{C}(u)} \frac{\partial^2 u}{\partial x^2}, \quad (2.1)$$

where the thermal mass has thermal conductivity K (assumed uniform and including both the PCM and wall material together), density ρ , and effective specific heat capacity $\bar{C}(u)$. (Symbols are defined both in the text and in table 2.1.) Temperature fluctuations are defined as $u = \theta - \bar{\theta}$, where θ is the room temperature and $\bar{\theta} = (\theta_{\max,r} + \theta_{\min,r})/2$ is the average room temperature, where $\theta_{\max,r}$ and $\theta_{\min,r}$ are the maximum and minimum, over a 24 hour period, room temperatures. The temperature fluctuations u in the thermal mass vary with time t , and depth x (from the interior surface) into the thermal mass.

Symbol	Quantity	Units
$u, (U)$	thermal mass temperature fluctuations, (dimensionless)	K, (-)
$t, (T)$	time, (dimensionless)	s, (-)
K	thermal conductivity	$\text{Wm}^{-1}\text{K}^{-1}$
ρ	thermal mass density	kgm^{-3}
\bar{C}, C	effective specific heat capacity, specific heat capacity	$\text{Jkg}^{-1}\text{K}^{-1}$
$x, (X)$	depth into the thermal mass, (dimensionless)	m, (-)
$\theta, \bar{\theta}$	room temperature, average room temperature	K
$\theta_{\min, \max, r}, \Delta\theta$	minimum and maximum room temperatures, $\Delta\theta = \theta_{\max, r} - \theta_{\min, r}$	K
ϕ	PCM mass fraction	-
L	latent heat	Jkg^{-1}
$u_{\min, \max}, (U_{\min, \max})$	minimum and maximum melting temperatures, (dimensionless)	K, (-)
l_m, l_{pcm}	thermal mass thickness, depth up to which PCM is included	m
U_{cool}	dimensionless cool air temperature	-
$u_r, (U_r)$	room temperature fluctuations away from the average, (dimensionless)	K, (-)
u_0	maximum room temperature	K
h_+	convection coefficient: interior surface	$\text{Wm}^{-2}\text{K}^{-1}$
H_+	dimensionless convection rate: interior surface	-
$\bar{\Omega}, \Omega$	effective dimensionless diffusivity, dimensionless diffusivity	-
s	Stefan number	-
U_{hottest}	dimensionless maximum interior surface temperature	-
D	dimensionless diurnal energy storage	-
subscript U, L , or S	uniform, linear, or step distribution	-
U_m	$U_{\max} = -U_{\min}$ for a symmetric melting range	-
X_p	dimensionless penetration depth	-
Ω_m	dimensionless reduced diffusivity	-
$\psi(U)$	fraction of the PCM which is liquid at temperature U	-
h_-	convection coefficient: exterior surface	-
H_-	dimensionless convection rate: exterior surface	-
A	room convection strength parameter	-
B	number of air changes in $1/2\pi$ days	-
P	dimensionless additional power load	-
U_e	dimensionless exterior air temperature	-
l_{room}	room height	m
B_0	point buoyancy source strength	m^4s^{-3}
ζ	dimensionless interface height	-
q	volume flux	m^3s^{-1}
m	momentum flux	m^4s^{-2}
f	buoyancy flux	m^4s^{-3}
z, r	height within the room, radius	m
w	vertical velocity of the plume	ms^{-1}
$\rho_{p, a, \text{ or } 1}$	density of the plume, ambient, or reference	kgm^{-3}
g, g'	acceleration due to gravity, reduced gravity	ms^{-2}
τ	characteristic cooling time scale	s
S	ceiling surface area	m^2
A^* , and a_1, a_2	effective area, and areas of high and low level openings	m^2
c	ratio of discharge coefficients	-
E	dimensionless ventilated room convection strength	-
F	ventilated air changes	-
G	dimensionless plume buoyancy flux strength	-
J	dimensionless plume volume flux strength	-
subscript n	with no PCM and no cooling	-
$T_{\text{hot, start, end}}$	dimensionless times at which the hot period starts and ends	-
U_{hot}	dimensionless jump in temperature during a hot period	-

Table 2.1 Symbols used, the quantities they refer to, and their units. Dimensionless variables and parameters are shown in brackets on the same line as the corresponding physical quantity.

The effective specific heat capacity depends on the thermal mass specific heat capacity C , PCM mass fraction ϕ , i.e. the ratio of PCM mass to total mass, and the latent heat L . The effective specific heat capacity $\bar{C}(u)$ quantifies the energy required to change the temperature of 1kg of thermal mass by 1K. This is different inside and outside the PCM melting range. A top hat profile is assumed, so $\bar{C}(u)$ takes two different values – one for temperatures within the PCM melting range, u_{\min} to u_{\max} , and another for temperatures outside the PCM melting range.

Differential Scanning Calorimetry (DSC) can be used to find PCM properties. Figures 16 and 17 of Pavlík et al. (2013) show apparent specific heat capacity varying with temperature for plaster with added PCM. Outside the melting range, apart from a small peak at low temperatures, specific heat capacity is roughly constant. The melting range contains a peak in specific heat capacity. This peak appears approximately Gaussian, rather than top hat, but Neeper (2000) suggests that the exact shape of the peak is, for his analysis, unimportant. Note that Pavlík et al. (2013) use large heating and cooling rates (10°C per minute) for their DSC, but Günther et al. (2006) recommend small heating and cooling rates, so the results of Pavlík et al. (2013) may inaccurately represent the properties of the PCM. Therefore, for simplicity, a top hat profile is used for the effective specific heat capacity $\bar{C}(u)$, which is taken to be

$$\bar{C}(u) = \begin{cases} C, & u < u_{\min} \\ C + (\phi L / (u_{\max} - u_{\min})), & u_{\min} < u < u_{\max} \\ C, & u > u_{\max}. \end{cases} \quad (2.2)$$

In this chapter it is typically assumed that the exterior surface of the wall, where $x = l_{\text{tm}}$, is insulated, so

$$\left. \frac{\partial u}{\partial x} \right|_{x=l_{\text{tm}}} = 0. \quad (2.3)$$

If the heat flux through the exterior surface of the wall, due to, for example, solar radiation and the outdoor air temperature, is significant, it can be included in the model. This is done in sections 2.4.1 and 2.4.2 where the heat flux through the exterior surface of the wall due to cooling from an exhaust air heat pump is included.

At the interior surface, heat is transferred between the room and the wall. Room temperatures, for example, those measured by Beizaee et al. (2013) and shown in their figure 5, can be quite complicated, but the key aspect for this work is that rooms are hot during the day and cool at night. Therefore, for simplicity, in this chapter it is typically assumed that the fluctuations u_r of room temperature away from average room temperature vary sinusoidally

over 24 hours (86400s), with amplitude $u_0 = (\theta_{\max,r} - \theta_{\min,r})/2 = \Delta\theta/2$,

$$u_r = u_0 \cos \frac{2\pi}{86400}t. \quad (2.4)$$

Room temperatures that are not simply sinusoidally varying – when there is a period of hot weather, and when the hot days are longer than the cool nights – are also considered in sections 2.4.3 and 2.4.4.

Assuming that the heat flux from the room – the rate of heat transfer per unit wall area – depends on a convection coefficient h_+ (which is taken to be $7\text{Wm}^{-2}\text{K}^{-1}$ (Richardson and Woods, 2008)), the interior surface boundary condition is

$$K \left. \frac{\partial u}{\partial x} \right|_{x=0} = -h_+ (u_r - u|_{x=0}). \quad (2.5)$$

The wall thickness l_{tm} is the natural length scale of the system. The maximum room temperature u_0 is chosen to be the temperature scale, and $86400/2\pi$ to be the time scale. Dimensionless variables are therefore defined:

$$X = x/l_{\text{tm}}, \quad U = u/u_0 = 2(\theta - \bar{\theta})/\Delta\theta, \quad \text{and} \quad T = 2\pi t/86400, \quad (2.6)$$

and so $0 \leq X \leq 1$ and $-1 \leq U \leq 1$. The system under consideration has five dimensionless parameters: H_+ , Ω , s , U_{\min} , and U_{\max} .

H_+ is the dimensionless convection rate, i.e. the ratio of the energy that convection supplies in $1/2\pi$ days, to the wall heat capacity, and so

$$H_+ = \frac{86400 h_+}{2\pi \rho C l_{\text{tm}}}. \quad (2.7)$$

The parameter Ω is the dimensionless diffusivity, i.e. half the square of the ratio of the decay distance for thermal mass without PCM, $\sqrt{2K/\rho C(2\pi/86400)}$, to the wall thickness l_{tm} :

$$\Omega = \frac{86400 K}{2\pi \rho C l_{\text{tm}}^2}. \quad (2.8)$$

The parameter s is the Stefan number, i.e. the ratio of latent to sensible heat:

$$s = \frac{\phi L}{2Cu_0}. \quad (2.9)$$

U_{\min} is the dimensionless minimum melting temperature, i.e. the minimum melting temperature u_{\min} divided by the temperature scale u_0 , while U_{\max} is the dimensionless maximum

Property	Typical Value
ρ , density (concrete)	2400 kg m ⁻³
ρ , density (wallboard)	760 kg m ⁻³
C , specific heat capacity (concrete)	750 J kg ⁻¹ K ⁻¹
C , specific heat capacity (wallboard)	1200 J kg ⁻¹ K ⁻¹
K , thermal conductivity (concrete)	0.5 W m ⁻¹ K ⁻¹
K , thermal conductivity (wallboard)	0.13 W m ⁻¹ K ⁻¹

Table 2.2 Typical values of the relevant physical properties, values for wallboard taken from the paper by Richardson and Woods (2008), and for concrete taken from The Engineering ToolBox.

Wall thickness	Concrete		Wallboard	
	H_+	Ω	H_+	Ω
0.01m	5.3	38.2	10.6	19.6
0.02m	2.7	9.5	5.3	4.9
0.05m	1.1	1.5	2.1	0.8

Table 2.3 Values of H_+ , as defined in (2.7), and Ω , as defined in (2.8), for three different wall thicknesses, for both concrete and wallboard.

melting temperature, i.e. the maximum melting temperature u_{\max} divided by the temperature scale u_0 , and so

$$U_{\min} = \frac{u_{\min}}{u_0} \quad \text{and} \quad U_{\max} = \frac{u_{\max}}{u_0}. \quad (2.10)$$

Different thermal mass materials give different parameter values. Values for wallboard, and for concrete, taken from the paper by Richardson and Woods (2008) and given in table 2.2, are used. These values are used in equations (2.7) and (2.8) to find H_+ and Ω , which are given in table 2.3. For the example calculations in this chapter, a room temperature varying between 20°C and 25°C is used. To get dimensionless temperatures, the average room temperature 22.5°C is subtracted, and the answer divided by $u_0 = 2.5^\circ\text{C}$. Values for a salt hydrate PCM that has a melting range of 21°C to 22.5°C (from Ure (2013)) are used, giving, from equation (2.10), $U_{\min} = (21 - 22.5)/2.5 = -0.6$, and $U_{\max} = (22.5 - 22.5)/2.5 = 0$.

The latent heat of the PCM is taken to be 170 000 J kg⁻¹. This latent heat, and the specific heat capacity values from table 2.2 are used in equation (2.9) to find s , which is given in table 2.4.

In dimensionless variables the heat equation (2.1) becomes

$$\frac{\partial U}{\partial T} = \bar{\Omega} \frac{\partial^2 U}{\partial X^2}, \quad (2.11)$$

	Concrete	Wallboard
PCM mass fraction	s	s
0	0	0
0.3	13.6	8.5
0.5	22.6	14.2

Table 2.4 Values of Stefan number s , as defined in (2.9), for three different PCM mass fractions, for both concrete and wallboard.

which is, in general, a nonlinear equation. The effective diffusivity $\bar{\Omega}$ depends on the dimensionless melting range U_{\min} to U_{\max} :

$$\bar{\Omega}(U) = \begin{cases} \Omega, & U < U_{\min} \\ \Omega \left(1 + \frac{2s}{U_{\max} - U_{\min}}\right)^{-1}, & U_{\min} < U < U_{\max} \\ \Omega, & U > U_{\max}. \end{cases} \quad (2.12)$$

Analogously, the room temperature equation (2.4) becomes, in dimensionless form,

$$U_r = \cos T, \quad (2.13)$$

while the exterior surface boundary condition (2.3) becomes

$$\left. \frac{\partial U}{\partial X} \right|_{X=1} = 0, \quad (2.14)$$

and the interior surface boundary condition (2.5) becomes

$$\left. \frac{\partial U}{\partial X} \right|_{X=0} = -\frac{H_+}{\Omega} (U_r - U|_{X=0}), \quad (2.15)$$

where H_+/Ω is a Biot number.

2.3 Optimisation of the properties of PCM

2.3.1 Optimising wall thickness and PCM mass fraction

Equations (2.11) – (2.15) are solved numerically, using the Crank-Nicolson method, with variable effective diffusivity $\bar{\Omega}(U)$. The Crank-Nicolson method is implicit, and so to avoid solving the nonlinear system of equations, the implicit value of $\bar{\Omega}(U)$ in the forward time step is taken to be its current value. Figure 2.2 shows the response of the interior

surface temperature (solid lines) to a sinusoidally varying room temperature (dashed lines). The interior surface temperature is considered because it is a key component, along with room temperature (which is set), air velocity, humidity, clothing, and metabolic rate, in the determination of thermal comfort for occupants (Hensen, 1990). Figures 2.2a and 2.2c are for concrete, figures 2.2b and 2.2d are for wallboard, while figures 2.2a and 2.2b are for different wall thicknesses, and figures 2.2c and 2.2d are for different PCM mass fractions. The parameter values used for wallboard and for concrete are listed in table 2.2. Comparing the thin (no PCM) and thick (PCM) lines of figures 2.2c and 2.2d, the perhaps unsurprising leading order observation is found: use of PCM reduces temperature fluctuations, which improves thermal comfort. This reduction is asymmetric, in that it is greater when the room is cooler and for the early part of the period when the room is heating up, before all the PCM has melted. This central result of this simple model – that PCM reduces temperature fluctuations – agrees with the work of other authors, both in more complicated numerical simulations and in experiments. Figure 6 of Peippo et al. (1991) and figure 4 of Feustel and Stetiu (1997) show that, in both of those numerical simulations, use of PCM reduces temperature fluctuations. Figure 9 of Ahmad et al. (2006) and figures 3 and 4 of Liu and Awbi (2009) show that, in those two sets of experiments with PCM walls, use of PCM reduces temperature fluctuations.

Adding extra PCM and wall thickness leads to smaller temperature fluctuations. This leads to an important practical question: does the extra cost of PCM outweigh the benefits? In this chapter, the “ideal” PCM mass fraction and wall thickness are defined to be the smallest values that still give a substantial ($1 - 2^\circ\text{C}$) decrease in maximum interior surface temperature. The results are shown in figure 2.3. Note that the first 24 hours are ignored, so that the results are independent of the initial conditions, which have thermal mass temperature equal to average room temperature, $U(T = 0) = 0$. In temperature profiles showing several days of evolution, after the first 24 hours, the profile just repeats the 24-48 hour profile, and so 24 hours is believed to be a long enough period for the initial transients to decay in this specific case. When using different parameter values, it is important to identify the analogous period for the decay of initial transients. Figures 2.3a – 2.3d show diminishing returns. The maximum interior surface temperature U_{hottest} , and the diurnal energy storage D – the maximum dimensionless energy stored in the mass at any one time, defined in equation (2.11) of Richardson and Woods (2008) as

$$D = \max_{0 \leq T < 2\pi} \int_0^T H_+(U_r - U|_{X=0}) dT, \quad (2.16)$$

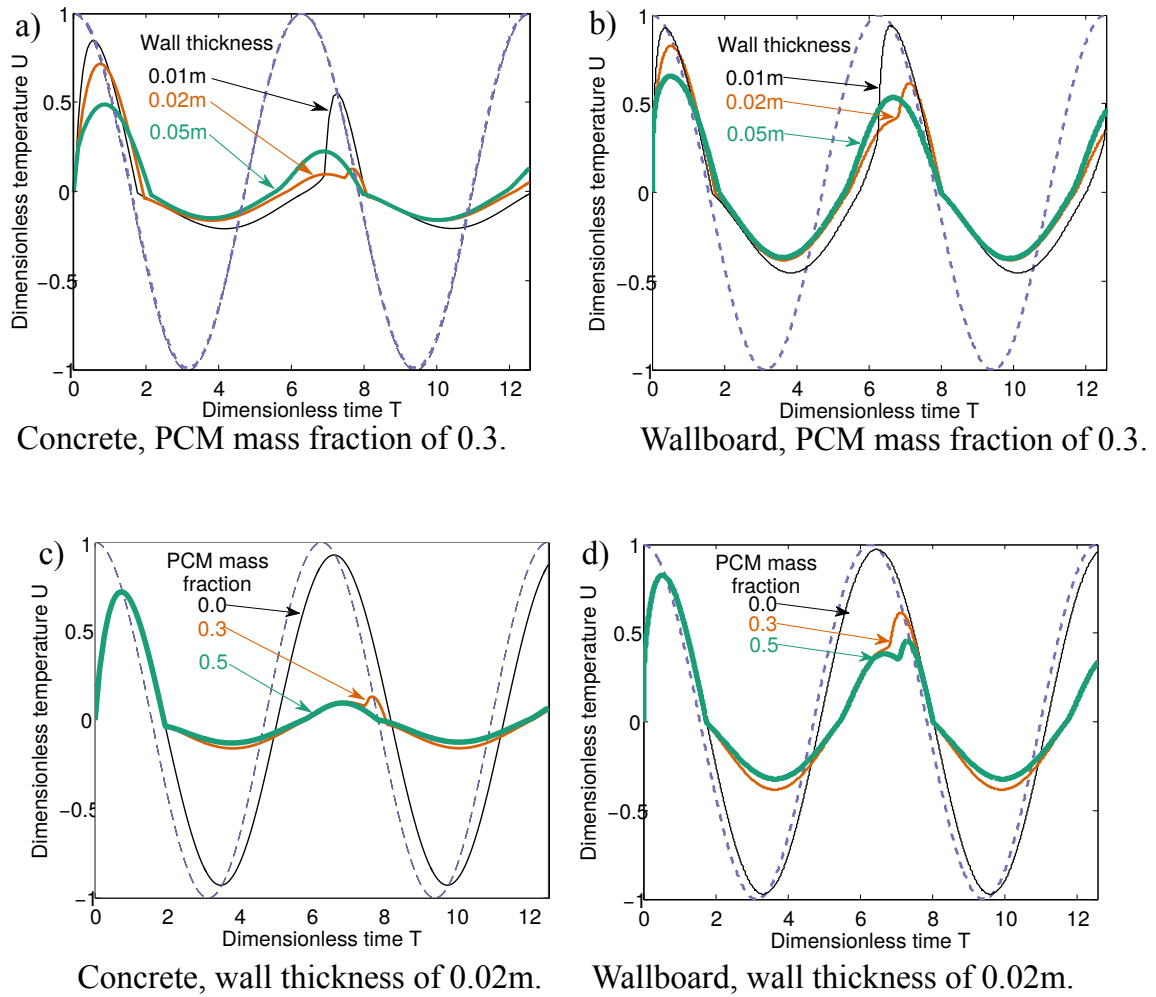
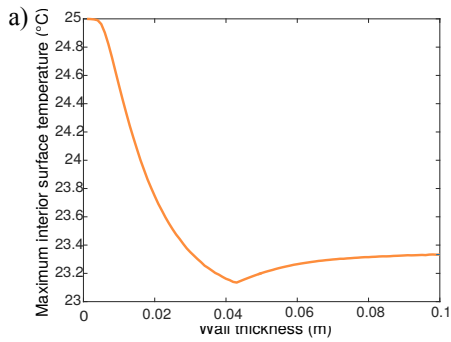
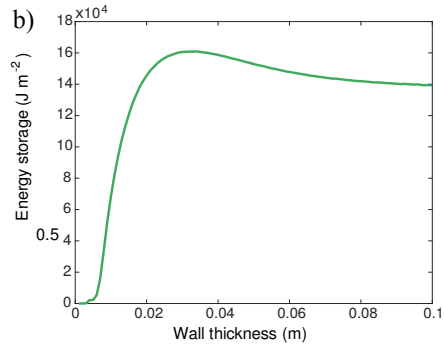


Fig. 2.2 Room temperature (dashed) and interior surface temperature (solid) for: a) and b) different wall thicknesses; c) and d) different PCM mass fractions. H_+ and Ω are given in table 2.3, s is given in table 2.4, $U_{\min} = -0.6$, and $U_{\max} = 0$.

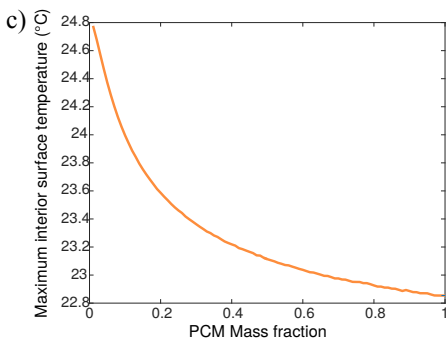
are considered. As the wall thickness or the PCM mass fraction is increased, the rates at which U_{hottest} decreases and D increases both decrease towards zero. Figures 2.3e and 2.3g show contours of constant maximum interior surface temperature, and figures 2.3f and 2.3h show contours of constant energy storage. Rates of change of maximum interior surface temperature and energy storage are inferred by considering contour separation. Close contours imply a small increase in PCM mass fraction or wall thickness yields a large return, in the sense of a relatively large decrease in maximum interior surface temperature. Widely spread contours imply that an increase in PCM mass fraction or wall thickness yields a small return, which may well be worth less than the extra cost of PCM. For example, 0.03m thick concrete thermal mass and a PCM mass fraction of 0.4 reduces the maximum interior surface temperature by 2.2°C, but extra PCM or wall thickness has little effect (see figure 2.3e). Further, for wallboard, 0.03m thick thermal mass and a PCM mass fraction of 0.3 reduces the maximum interior surface temperature by 1.3°C, but extra PCM or wall thickness again has little effect (see figure 2.3g).



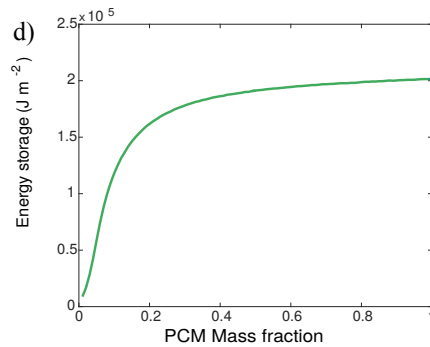
Variation of maximum interior surface temperature with wall thickness for a concrete wall with PCM mass fraction of 0.3.



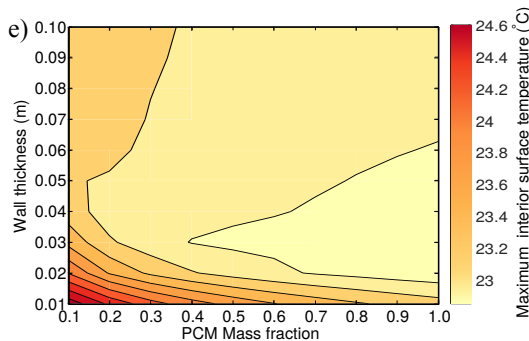
Variation of energy storage D with wall thickness for a concrete wall with PCM mass fraction of 0.3.



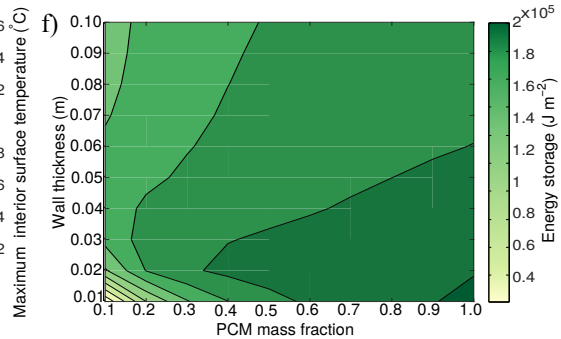
Variation of maximum interior surface temperature with PCM mass fraction for a concrete wall with wall thickness of 0.02m.



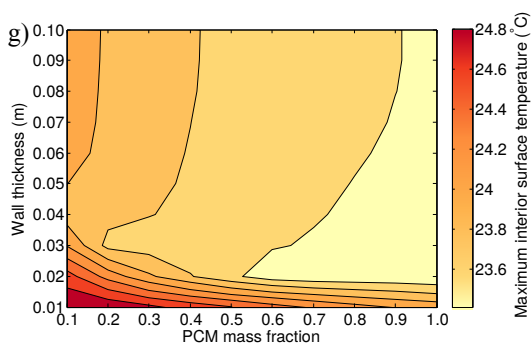
Variation of energy storage D with PCM mass fraction for a concrete wall with wall thickness of 0.02m.



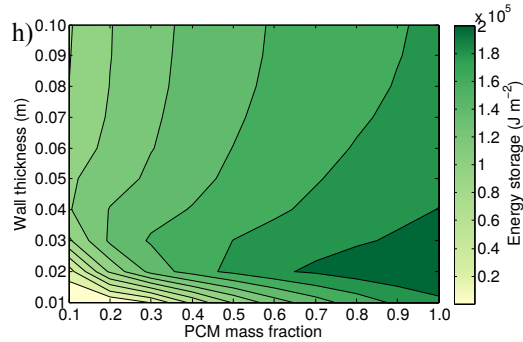
Variation of maximum interior surface temperature with wall thickness and PCM mass fraction for concrete.



Variation of energy storage D with wall thickness and PCM mass fraction for concrete.



Variation of maximum interior surface temperature with wall thickness and PCM mass fraction for wallboard.



Variation of energy storage D with wall thickness and PCM mass fraction for wallboard.

Fig. 2.3 Measures of PCM effectiveness: the maximum interior surface temperature U_{hottest} (2.3a, 2.3c, 2.3e, 2.3g) and the energy storage D (2.3b, 2.3d, 2.3f, 2.3h), as defined in (2.16). When parameters are constant, they are taken from tables 2.3 and 2.4. When parameters are varying, they are calculated using equations (2.7), (2.8), and (2.9), with properties given in table 2.2.

This estimate for the optimal wall thickness can be compared with the estimate of Peippo et al. (1991) (although they define the optimal wall thickness to be the value for which the most energy is delivered by the PCM during nights when heating is required). Assuming that the day and the night are both 12 hours long, that the difference between the daytime and nighttime temperatures is $2u_0$, then changing to the notation used in this chapter, the Peippo et al. (1991) estimate for optimal thermal mass thickness is

$$l_{tm_{opt}} = \frac{Q}{2\rho\phi L} + \frac{86400u_0h}{2\rho\phi L}, \quad (2.17)$$

where Q is the heat absorbed by a unit area of the room surface, and is taken by Peippo et al. (1991) to be $Q = 2\text{MJ m}^{-2}$. Taking this value of Q , with PCM mass fraction $\phi = 0.3$, and the parameter values used to obtain figure 2.3, namely, density of wallboard $\rho = 760\text{kg m}^{-3}$, latent heat $L = 170000\text{J kg}^{-1}$, temperature scale $u_0 = 2.5^\circ\text{C}$, and convection coefficient $h = 7\text{W m}^{-2}\text{K}^{-1}$, gives $l_{tm_{opt}} = 0.045\text{m}$, which is close to 0.03m . The estimate (from figure 2.3g) of 0.03m is thus consistent with the results of Peippo et al. (1991).

2.3.2 Spatially varying PCM distributions

The previous examples have assumed that the PCM has a uniform distribution throughout the wall, but a natural question is whether this spatial distribution is the most effective. To answer this question, in this section, three different distributions are considered: namely a uniform distribution, a linearly varying distribution, and a step-discontinuous distribution. These three different distributions are described using their PCM mass fractions, ϕ . For the uniform distribution,

$$\phi_U(X) = \phi_0, \quad (2.18)$$

while for the linear distribution,

$$\phi_L(X) = \phi_0(1 - X), \quad (2.19)$$

where X is the dimensionless depth into the wall. For the ‘‘step’’ distribution, there is a uniform distribution of PCM only up to $X = l_{\text{pcm}}/l_{\text{tm}}$, and so

$$\phi_S(X) = \begin{cases} \phi_0, & 0 \leq X \leq l_{\text{pcm}}/l_{\text{tm}}, \\ 0, & X > l_{\text{pcm}}/l_{\text{tm}}. \end{cases} \quad (2.20)$$

As $l_{\text{pcm}}/l_{\text{tm}} \rightarrow 1$, the step distribution converges to the uniform distribution.

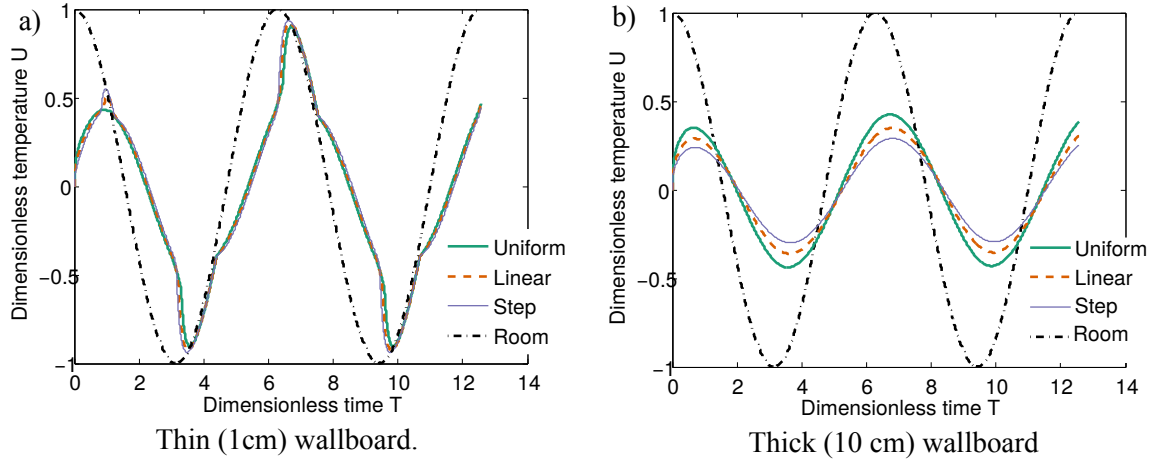


Fig. 2.4 Variation of interior surface temperature with time for the three different PCM distributions: uniform (thick solid line), linear (dashed line), and step (thin solid line) for a) 1cm wallboard and b) 10cm wallboard. The three curves overlap in a).

The effective diffusivity $\bar{\Omega}$ is given, for the uniform distribution, by equation (2.12). For the linear distribution,

$$\bar{\Omega}_L(U, X) = \begin{cases} \Omega \left(1 + \frac{2s(1-X)}{U_{\max} - U_{\min}} \right)^{-1}, & U_{\min} < U < U_{\max} \\ \Omega, & \text{otherwise,} \end{cases} \quad (2.21)$$

while for the step distribution,

$$\bar{\Omega}_S(U, X) = \begin{cases} \Omega \left(1 + \frac{2s}{U_{\max} - U_{\min}} \right)^{-1}, & U_{\min} < U < U_{\max} \\ & \text{and } 0 \leq X \leq \frac{l_{\text{pcm}}}{l_{\text{tm}}} \\ \Omega, & \text{otherwise.} \end{cases} \quad (2.22)$$

The three expressions for $\bar{\Omega}$, (2.12), (2.21), and (2.22), are used in the model described in section 2.2 to find the interior surface temperature for the three distributions. The Stefan number s as defined in equation (2.9) is adjusted in each case so that the total amount of PCM is the same for each distribution. The results in figure 2.4, show that, for sufficiently thick walls, the distribution of PCM makes a significant difference. However, for thinner walls, the distribution makes little difference. The linear distribution gives interior surface temperatures between those of the uniform and step distribution, so now only the uniform and step distributions are considered as appropriate end members.

If the depth into the thermal mass up to which PCM is included is too small, the PCM melts before all the excess heat is stored, which Richardson and Woods (2008) refer to as

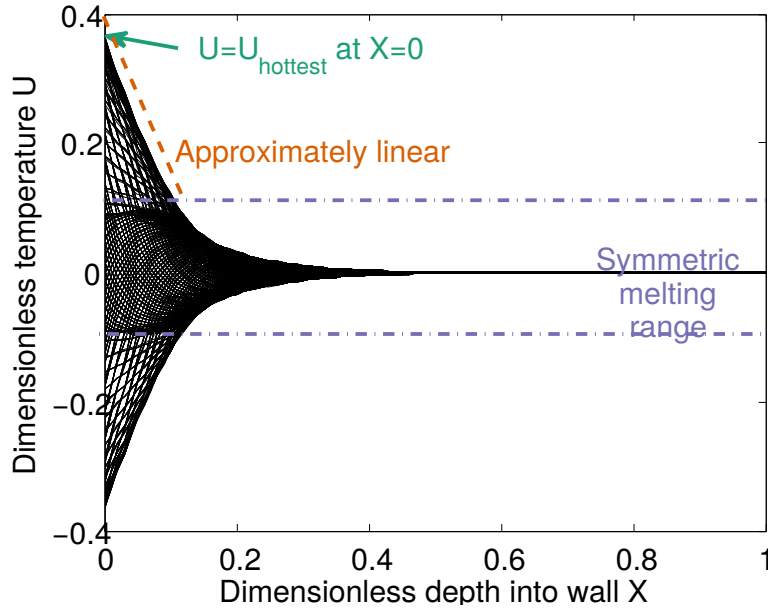


Fig. 2.5 Variation with dimensionless depth into the wall X of dimensionless temperature U , as defined in equation (2.6), for various time steps at intervals 0.02π (each represented with a distinct solid line).

the “full penetration regime”. On the other hand, if the depth containing PCM is too large, the PCM at the back stays solid, and so is redundant, which Richardson and Woods (2008) refer to as the “low penetration regime”. Operationally, the best depth for PCM inclusion is therefore the “penetration depth”, i.e. the maximum depth up to which the PCM completely melts and solidifies over the course of a day.

Estimating penetration depth

Some natural approximations are made to estimate the penetration depth. Figure 2.5 shows variation with dimensionless depth into the wall X of dimensionless temperature U for various time steps at intervals 0.02π , calculated by solving equations (2.11) – (2.15) numerically. At many time steps (i.e. for many of the black lines in figure 2.5), the graph of temperature against depth into the wall is approximately linear up to the penetration depth. Therefore, the temperature is approximated as $U = aX + b$, where a and b are constants to be determined. At the time when the temperature graph has the steepest gradient, the interior surface boundary condition (2.15) and $U = U_{\text{hottest}}$ (an unknown parameter) at $X = 0$, are used to find a, b , and so U is written as

$$U = -\frac{H_+}{\Omega} (1 - U_{\text{hottest}})X + U_{\text{hottest}}. \quad (2.23)$$

For simplicity, a symmetric (about the average room temperature, $U = 0$) melting range is assumed, with $U_{\max} = -U_{\min} = U_m$. At the penetration depth, the PCM temperature is the same as the maximum melting temperature, i.e. at $X = X_p$, $U = U_m$, and so, rearranging (2.23),

$$X_p = \frac{U_{\text{hottest}} - U_m}{\frac{H_+}{\Omega} (1 - U_{\text{hottest}})}. \quad (2.24)$$

There is now an expression for penetration depth in terms of known parameters, U_m , H_+ , and Ω , but also a parameter that is yet to be determined: U_{hottest} , which depends on the properties of the PCM thermal mass.

Estimating U_{hottest}

To estimate U_{hottest} , two further assumptions are made. First, it is assumed that the surface temperature also varies sinusoidally in phase with the room temperature, i.e.

$$U|_{X=0} = U_{\text{hottest}} \cos T. \quad (2.25)$$

Although a phase lag is observed, as is apparent in figure 2.4b, this phase lag is small (in figure 2.4b it is less than 1), and so it is set to zero. Second, it is assumed that beyond the penetration depth, the temperature decays exponentially,

$$U = U_m e^{-(X-X_p)/\sqrt{2\Omega_m}} \text{ for } X > X_p, \quad (2.26)$$

where $\Omega_m = \Omega (1 + s/U_m)^{-1}$. These assumptions are made because, as noted by Richardson and Woods (2008), beyond the penetration depth, the PCM thermal mass can be viewed as normal thermal mass with exponentially decaying temperature fluctuations and a reduced diffusivity Ω_m , forced by a temperature U_m at the penetration depth $X = X_p$.

Diurnal energy storage, the total energy stored and released by the thermal mass over a day, is given in equation (2.11) of Richardson and Woods (2008) in two ways: by equation (2.16) and by

$$D = \max_{0 \leq T < 2\pi} \int_0^1 \left(U + 2s \left(\psi(U) - \frac{1}{2} \right) \right) dX, \quad (2.27)$$

where $\psi(U)$ is the fraction of PCM which is liquid at temperature U . Using the approximations (2.25) and (2.26) in equation (2.16), with room temperature given by (2.13), gives that

$$D \approx H_+ (1 - U_{\text{hottest}}), \quad (2.28)$$

and from equation (2.27),

$$D \approx \frac{U_{\text{hottest}} - U_m}{\frac{H_+}{\Omega} (1 - U_{\text{hottest}})} \left(s + \frac{1}{2} (U_{\text{hottest}} + U_m) \right) + \sqrt{2\Omega} U_m \left(1 + \frac{s}{U_m} \right)^{1/2}. \quad (2.29)$$

Equating the two approximate expressions for diurnal energy storage, (2.28) and (2.29), gives us a quadratic for U_{hottest} in terms of known parameters,

$$U_{\text{hottest}}^2 + \frac{\frac{H_+}{\Omega} \sqrt{2\Omega} \left(1 + \frac{s}{U_m} \right) U_m - \frac{2H_+^2}{\Omega} - s}{\frac{H_+^2}{\Omega} - \frac{1}{2}} U_{\text{hottest}} + \frac{\frac{H_+^2}{\Omega} + (s + \frac{1}{2} U_m) U_m - \frac{H_+}{\Omega} \sqrt{2\Omega} \left(1 + \frac{s}{U_m} \right) U_m}{\frac{H_+^2}{\Omega} - \frac{1}{2}} \approx 0, \quad (2.30)$$

which can be solved for U_{hottest} . For example, with $H_+ = 1.06$, $\Omega = 0.2$, $U_m = 0.1$, and $s = 5$ (the parameters used when plotting figure 2.5), $U_{\text{hottest}} \approx 0.4$ (the other solution to the quadratic (2.30) has $U_{\text{hottest}} > 1$, which is unphysical), which is consistent with figure 2.5. Then, using (2.24), the penetration depth can be obtained in terms of known parameters. For example, where $U_{\text{hottest}} \approx 0.4$, the penetration depth $X_p \approx 0.1$, which is consistent with figure 2.5. Using PCM up to this penetration depth should operationally reduce temperature fluctuations without including redundant (with attendant cost) PCM.

2.4 Interaction of PCM with surrounding conditions

2.4.1 Time varying cooling at the exterior surface of the thermal mass

Exhaust air heat pumps may be used in low energy buildings. They capture heat from the exhaust air of a building (to be used for heating hot water), outputting cool air (Fracastoro and Serraino, 2010), (NIBE Energy Systems AB, 2012). Ordinarily, this cool air is exhausted to the exterior and hence wasted, but it is desirable to take advantage of it, and use it usefully, as additional (and free) cooling. So, instead of “throwing” this cool air away, this section considers circulating it over the exterior surface of PCM thermal mass (either a wall or a ceiling) to store the “coolth”, which can be used to reduce summer overheating. The thermal mass model of Richardson and Woods (2008) is extended to this realistic situation by including cooling at the exterior surface of the thermal mass.

With specified room temperature

The exterior surface boundary condition (2.14) changes, but equations (2.11), (2.12), (2.13), and (2.15), remain the same. At the exterior surface, there is now a heat flux, which depends

on a convection coefficient h_- , and the temperature of the cool air coming from the heat pump, which typically outputs air at around 0°C , which is then tempered to 15°C . Typically, the cool air is output only at certain times of the day, due to, for example, a water heating cycle. This time-varying cooling is modelled by setting the temperature at the exterior surface of the thermal mass to be 15°C for six hours, then 22.5°C for six hours, and repeating. The dimensionless temperature of the cool air, U_{cool} , is scaled as in (2.6), relative to the average room temperature. The new exterior surface boundary condition (replacing (2.14)), which involves a new dimensionless parameter, $H_- = 86400h_-/2\pi\rho Cl_{\text{tm}}$, is

$$\left. \frac{\partial U}{\partial X} \right|_{X=1} = -\frac{H_-}{\Omega} (U|_{X=1} - U_{\text{cool}}(T)) + S_{\text{sol}}(T). \quad (2.31)$$

As already noted in section 2.2, the effects of solar radiation and exterior air temperature can be included in this equation. To include the effect of exterior air, the temperature of the cool air U_{cool} would be replaced with the (appropriately scaled) exterior air temperature $U_e(T)$, while to include the effect of solar radiation the appropriate functional form would be assigned to the solar radiation term $S_{\text{sol}}(T)$. For simplicity here solar radiation is taken to be $S_{\text{sol}}(T) = 0$, i.e. the effect of solar radiation is assumed to be negligible.

Once again, the heat equation (2.11) is solved numerically, using the Crank-Nicolson method, for a range of PCM mass fractions and wall thicknesses. Figure 2.6a shows the maximum interior surface temperature for a range of PCM mass fractions and wall thicknesses for a wallboard and PCM ceiling. Note that the convection coefficients h_+ and h_- are typically different for walls and for ceilings. The cross on figure 2.6a marks a choice of PCM mass fraction that gives a substantial decrease in maximum interior surface temperature, but values larger than it give little extra benefit. Note that if the wall thickness is increased from the value marked by the cross, then the maximum interior surface temperature also starts to increase, in contrast to the case shown in figure 2.3, when there was no cooling. This is because if the thermal mass is too thick, the room temperature will be unaffected by the cooling. Figure 2.6b shows the interior surface temperature (thick solid line) for this specific “optimal” choice of PCM mass fraction and wall thickness.

With specified exterior air temperature and forced ventilation

Now, instead of having a sinusoidally varying room temperature, the room temperature in a room with forced ventilation and an additional power load is determined using an energy balance. The heat in the room changes, balanced by the heat flux from the thermal mass, heat brought into the room by ventilation, and the additional power load. This energy balance is

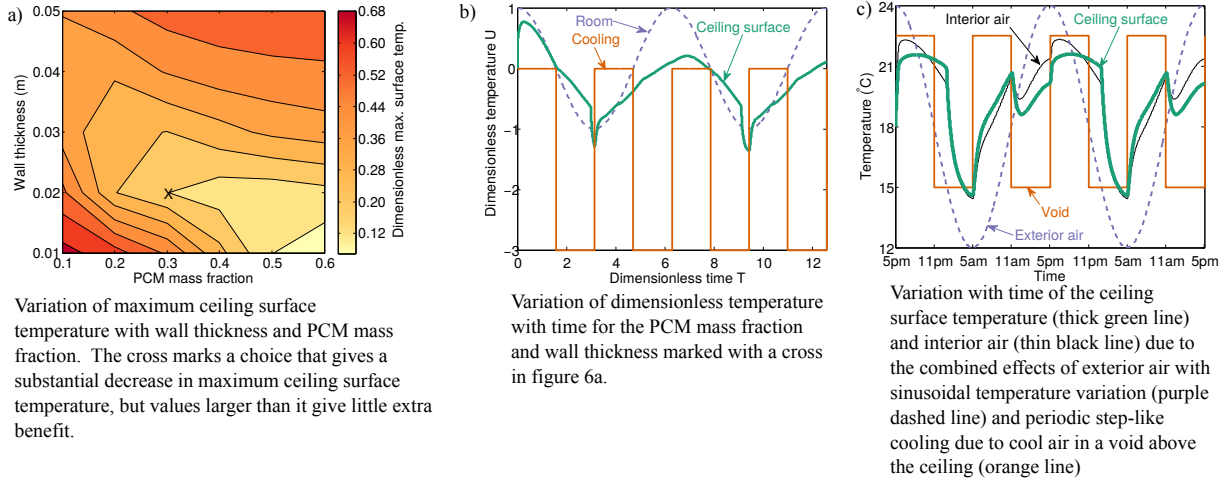


Fig. 2.6 Numerical results for a wallboard ceiling with cooling at the exterior surface.

written as

$$\frac{dU_r}{dT} = A(U|_{X=0} - U_r) + B(U_e - U_r) + P, \quad (2.32)$$

where the dimensionless exterior air temperature is

$$U_e = \cos T, \quad (2.33)$$

A is the room convection strength parameter, i.e. the energy crossing the interior surfaces over $1/2\pi$ days divided by the heat capacity of the air, B is the number of air changes in $1/2\pi$ days, and P is the dimensionless additional power load. Figure 2.6c shows the (sinusoidally varying) exterior air temperature (plotted with a dashed purple line), the cooling above the ceiling (solid orange line), and the resulting ceiling surface temperature (thick solid green line) and room temperature (thin solid black line). It can be seen that PCM does reduce temperature fluctuations: the ceiling surface and room temperatures have smaller amplitude fluctuations (by about 2°C) than the exterior air temperature fluctuations.

2.4.2 A PCM ceiling in a naturally ventilated room

Natural ventilation can also be included in the model. As an example, a chilled PCM ceiling that is cooled from above, in a naturally ventilated – specifically displacement ventilation – room is considered. Livermore and Woods (2008) study the combined effects of a chilled ceiling and a localised heat source in a room. For a constant rate of cooling at the ceiling, they find that a two-layer steady stratification develops. In this section, their ideas are extended to the time-varying cooling that results from a chilled PCM ceiling that is cooled intermittently

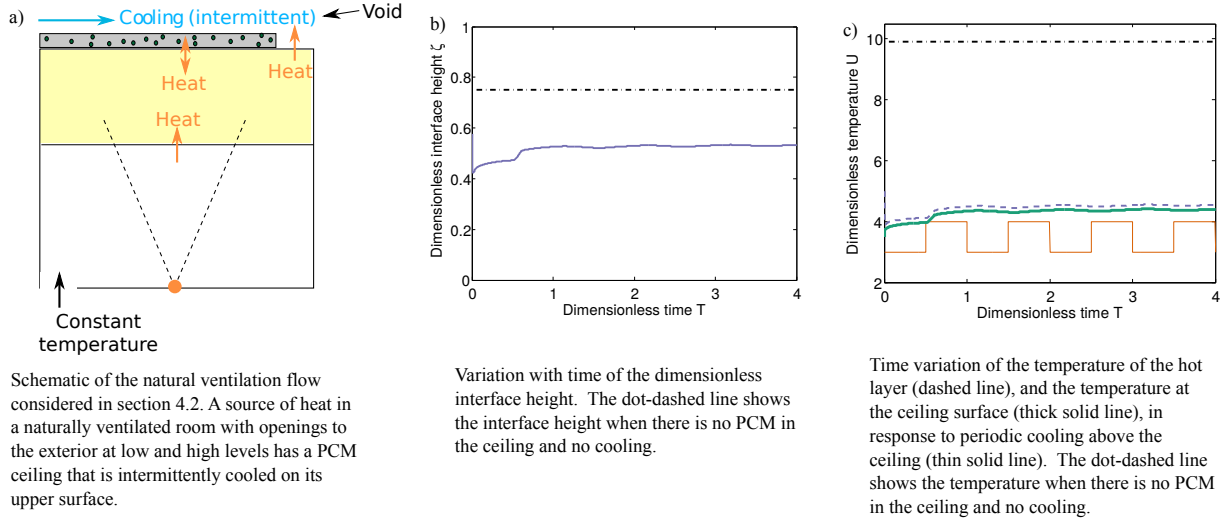


Fig. 2.7 Temperatures and interface height for a room with displacement ventilation and a PCM ceiling, as shown schematically in figure 2.7a. Parameter values, as defined in equations (2.7 – 2.10), (2.38), and (2.41), are $U_e = 3.5$, $H_+ = 15.7$, $H_- = 6.85$, $\Omega = 3.85$, $U_{\min} = 4.2$, $U_{\max} = 4.5$, $s = 4.25$, $E = 180.6$, $F = 3.7$, $G = 4.0$, $J = 0.5$.

from above. The analysis is the same as theirs, but the notation has been changed to be consistent with the rest of this chapter.

The model setup is shown schematically in figure 2.7a. The room, which has height l_{room} , contains a point source of buoyancy, of strength B_0 , on the floor. This source of buoyancy causes a turbulent plume to rise towards the ceiling, where it forms, from height ζl_{room} , a hot layer with dimensionless temperature U_r . It is assumed that the upper layer is well mixed and that the cooling at the ceiling is not so great as to mix the whole space. For simplicity, the plume is modelled using the Morton et al. (1956) plume model. The plume entrains, with entrainment coefficient α , constant temperature ambient air that enters the room through the bottom vent. It is assumed that profiles of buoyancy and vertical velocity across the plume are self similar with height, and that changes in density are small compared with a reference density – the Boussinesq approximation. Equations for conservation of volume flux, momentum flux, and buoyancy flux describe the plume, and they can be solved to find how the volume flux q , momentum flux m , and buoyancy flux f through the plume change with height z . These fluxes are defined as

$$q = 2\pi \int_0^\infty wr dr, \quad m = 2\pi \int_0^\infty w^2 r dr, \quad \text{and} \quad f = 2\pi \int_0^\infty wg \left(\frac{\rho_a - \rho_p}{\rho_1} \right) r dr, \quad (2.34)$$

where w is the vertical velocity of the plume, ρ_p is the density of the plume, ρ_a is the ambient density, ρ_1 is a reference density, g is the acceleration due to gravity, and r is the radius. The

equations describing the plume below the hot layer are:

$$\frac{dq}{dz} = 2\pi^{1/2}\alpha m^{1/2}, \quad \frac{dm}{dz} = \frac{fq}{m}, \quad \text{and} \quad \frac{df}{dz} = 0, \quad (2.35)$$

which have similarity solutions

$$q = \frac{6}{5}\alpha \left(\frac{9}{10}\alpha\right)^{1/3} \pi^{2/3} B_0^{1/3} z^{5/3}, \quad m = \left(\frac{9}{10}\alpha\right)^{2/3} \pi^{1/3} B_0^{2/3} z^{4/3}, \quad \text{and} \quad f = B_0. \quad (2.36)$$

The dimensionless temperature of the air entering through the bottom vent is U_e . Some hot air leaves the room through the top vent. It is assumed that the volume flux out of the room is the same as the volume flux into the room (i.e. the fluid is incompressible), for simplicity.

With the PCM ceiling and time dependent cooling above the ceiling, the temperature and thickness of the hot upper layer vary in time. The characteristic time scale τ is defined as the length of time (in this chapter 6 hours is used) over which the PCM ceiling is cooled from above. The PCM ceiling has surface area S and an effective area A^* , originally considered by Linden et al. (1990), is also used. It is defined as

$$A^* = \frac{a_1 a_2}{\left(\frac{1}{2}(a_1^2/c + a_2^2)\right)^{1/2}}, \quad (2.37)$$

where a_1 and a_2 are the areas of the high and low level openings, and c is a constant ratio of discharge coefficients which lies between 1/2 and 1. An energy balance is used to find the (time dependent) temperature, U_r , of the upper layer. The energy balance in this situation involves three new dimensionless parameters: the ventilated room convection strength E , the ventilated air changes F , and the plume buoyancy flux strength G , defined, respectively, as

$$E = \frac{h_+ \tau}{\rho_{\text{air}} C_{\text{air}} l_{\text{room}}}, \quad F = \frac{A^* g^{1/2} \beta^{1/2} u_0^{1/2} \tau}{S l_{\text{room}}^{1/2}}, \quad \text{and} \quad G = \frac{B_0^{2/3}}{g \beta \frac{6}{5} \alpha \left(\frac{9}{10}\alpha\right)^{1/3} \pi^{2/3} l_{\text{room}}^{5/3} u_0}. \quad (2.38)$$

Physically, E compares the energy crossing the ceiling surface over time τ with the heat capacity of the air, F is the number of air changes in time τ in a well mixed room that is u_0 hotter than the outside, and G compares the buoyancy flux through the plume at the ceiling height with the buoyancy ventilated out of the room.

These expressions involve the convection coefficient h_+ , the density of air ρ_{air} , the specific heat capacity of air C_{air} , the acceleration due to gravity g , the thermal expansion

coefficient β , and the entrainment coefficient α . The energy balance is then

$$(1 - \zeta) \frac{dU_r}{dT} = E (U|_{X=0} - U_r) + F (U_r - U_e)^{1/2} (1 - \zeta)^{1/2} \left[G\zeta^{-5/3} + U_e - U_r \right]. \quad (2.39)$$

The height of the interface is found using conservation of volume. The volume flux through the plume at the interface height q_p must be equal to the volume flux through the space (given by equation (2.4a) of Linden et al. (1990)),

$$q_p = \frac{6}{5} \alpha \left(\frac{9}{10} \alpha \right)^{1/3} \pi^{2/3} B_0^{1/3} (\zeta l_{\text{room}})^{5/3} = A^* [g' l_{\text{room}} (1 - \zeta)]^{1/2}, \quad (2.40)$$

with reduced gravity $g' = g\beta u_0 (U_r - U_e)$. It is assumed that the hot upper layer is well mixed, and that its temperature evolves slower than the plume evolves, i.e. quasi-steadiness is assumed. Equation (2.40) yields

$$J (U_r - U_e)^{1/2} = \zeta^{5/3} (1 - \zeta)^{-1/2}, \quad \text{with} \quad J = \frac{A^* g^{1/2} \beta^{1/2} u_0^{1/2}}{\frac{6}{5} \alpha \left(\frac{9}{10} \alpha \right)^{1/3} \pi^{2/3} B_0^{1/3} l_{\text{room}}^{7/6}}. \quad (2.41)$$

which involves one new dimensionless parameter, the plume volume flux strength J . Physically, J compares the volume flux through a well mixed room that is u_0 hotter than the outside, with the volume flux through the plume at the ceiling height. The conservation of volume equation, (2.41), is the same, with zero flux of lower layer air into the upper layer $V_c = 0$, as equation (3.1) from Livermore and Woods (2008), combined with their equations (3.3) and (3.5). The energy balance (2.39) and conservation of volume (2.41) give the temperature and height of the hot upper layer. The heat equation (2.11) is solved (numerically) with interior surface boundary condition (2.15) and the cooled exterior surface boundary condition (2.31) to find temperatures in the PCM ceiling.

The results are presented in figure 2.7, which shows that the interface between the hot layer and the ambient air fluctuates slightly, but remains approximately halfway up the room, for a particular A^* (via F, J). For a room without PCM thermal mass, and with no cooling above the ceiling, the dimensionless interface height ζ_n and upper layer temperature U_{rn} are given by equations (2.11a) and (2.11b) of Linden et al. (1990) respectively, which, in the notation of this chapter, are

$$G^{1/2} J = \left(\zeta_n^5 / (1 - \zeta_n) \right)^{1/2} \quad \text{and} \quad U_{rn} = U_e + G\zeta_n^{-5/3}. \quad (2.42)$$

Taking $G = 4.0$, $J = 0.5$, and $U_e = 3.5$, as used to obtain figure 2.7, gives that $\zeta_n \approx 0.75$ and $U_{rn} \approx 9.9$. The cooling at the PCM ceiling reduces both the dimensionless interface height

ζ and the dimensionless temperature of the hot layer U_r significantly. With a chilled PCM ceiling, the temperature U_r of the hot layer and the temperature of the ceiling fluctuate over the course of a day, but these fluctuations are much less than the fluctuations in cooling – the PCM thermal mass evens out temperatures over the course of a day, which is likely to enhance occupant comfort.

2.4.3 A period of hot weather

Heretofore, it has been assumed that the room temperature has had the same minimum and maximum each day, but this is clearly not realistic. Therefore, the model is extended to include a more physically realistic case of a period of relatively hot weather by using the model from section 2.2, but with a new room temperature distribution,

$$U_r = \begin{cases} U_0 \cos T, & T < T_{\text{hot_start}} \\ U_0 \cos T + U_{\text{hot}}, & T_{\text{hot_start}} \leq T \leq T_{\text{hot_end}} \\ U_0 \cos T, & T > T_{\text{hot_end}} \end{cases} \quad (2.43)$$

This room temperature distribution, for simplicity, approximates a large increase in temperature over a short period of time by a (physically unrealistic) jump in temperature at $T = T_{\text{hot_start}}$. The dot-dashed line in figure 2.8a shows the new room temperature distribution, with $T_{\text{hot_start}} = 2$ days and $T_{\text{hot_end}} = 4$ days.

The results plotted in figure 2.8a are obtained using the model from section 2.2, with this new room temperature distribution (2.43). It is clear that, during the period of hot weather, the daily maximum temperature increases by a factor of 1.5 from the first to the last day of the hot period, but it quickly recovers after the period of hot weather. The PCM still reduces the fluctuations to 75% of the room temperature variations (on the last day of the hot period), but this is not as good as outside of the hot period, when fluctuations are reduced to 50% of the room temperature variations. This suggests that using two PCMs, tailored to the different operating conditions (“normal” and “hot”), might well improve the performance of the PCM thermal mass during relatively hot periods.

As an example, consider a situation with two different PCMs with different, and distinct, melting ranges (U_{min_1} to U_{max_1} , U_{min_2} to U_{max_2}), different mass fractions ϕ_1, ϕ_2 , and different

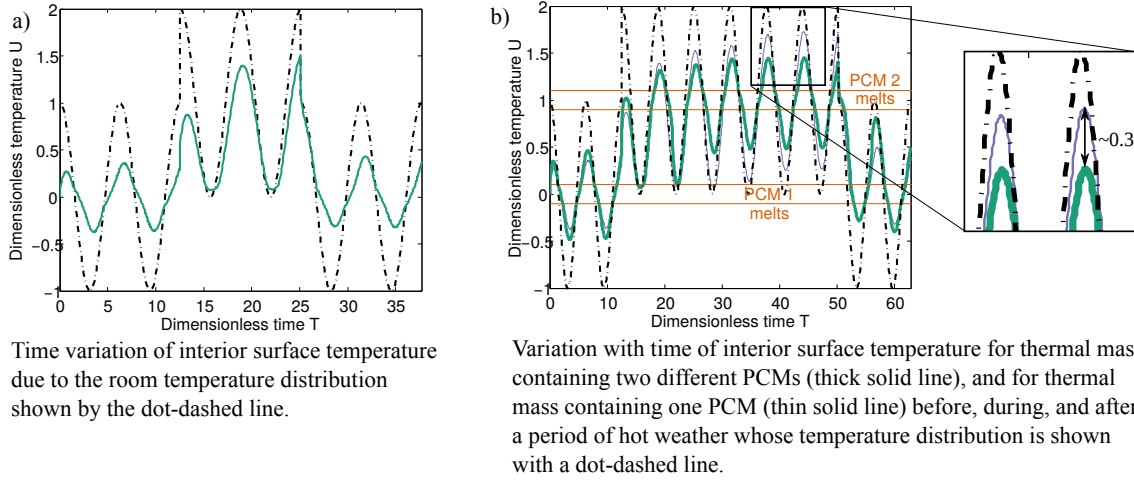


Fig. 2.8 Time variation of interior surface temperature with a) one PCM and parameters $H_+ = 1.06, \Omega = 0.2, U_{\min} = -0.1, U_{\max} = 0.1, s = 5$. For b), two PCMs are used, with parameters $H_+ = 1.06, \Omega = 0.2, U_{\min_1} = -0.1, U_{\max_1} = 0.1, U_{\min_2} = 0.9, U_{\max_2} = 1.1$, and for the two PCMs, $s_1 = 2.5, s_2 = 2.5$ (as defined in (2.44)), whilst for the one PCM $s = 5$ with the melting range $U_{\min_1} = -0.1$ to $U_{\max_1} = 0.1$.

latent heats L_1, L_2 . Then, the effective diffusivity $\bar{\Omega}$ is

$$\bar{\Omega} = \begin{cases} \Omega, & U < U_{\min_1}, \\ \Omega \left(1 + \frac{2s_1}{U_{\max_1} - U_{\min_1}}\right)^{-1}, & U_{\min_1} < U < U_{\max_1}, \\ \Omega, & U_{\max_1} < U < U_{\min_2}, \\ \Omega \left(1 + \frac{2s_2}{U_{\max_2} - U_{\min_2}}\right)^{-1}, & U_{\min_2} < U < U_{\max_2}, \\ \Omega, & U_{\max_2} < U. \end{cases} \quad \text{where } s_1 = \frac{\phi_1 L_1}{2Cu_0} \quad (2.44)$$

The results plotted in figure 2.8b are obtained using the expression (2.44) for $\bar{\Omega}$ in the equations and the method as described in section 2.2. The daily maximum interior surface temperature is below the room temperature in both normal and hot conditions. Specifically, during the latter part of the period of hot weather, as shown in the inset, the maximum temperature for the 2 PCMs case is $0.3u_0$ smaller – which for a minimum normal temperature of 20°C and a maximum normal temperature of 25°C is 0.75°C smaller – than for the single PCM case. The ideal proportion of the two PCMs depends on the desired conditions – is it better to be comfortable most of the time, with occasional temperature peaks, or to never have temperatures above some value? Of course the model presented in section 2.2 can be used to choose how much of each PCM to use to give the desired reduction in temperature fluctuations, and figure 2.8b is just a specific demonstration of the utility of the method that

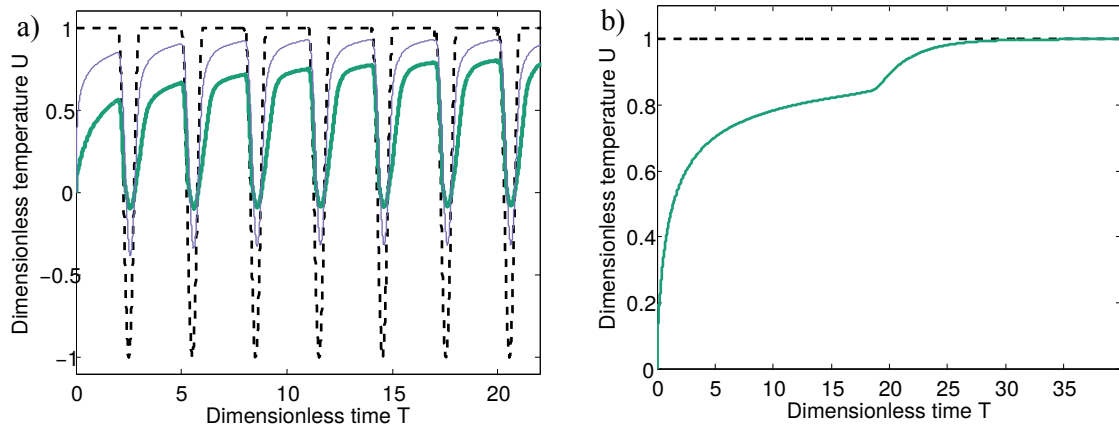
has been described in this chapter. Using a chilled ceiling, with the appropriate amount of cooling, would ensure comfortable conditions all the time, but would also use more energy than the passive PCM ceiling described here.

2.4.4 Long hot days with short cool nights

Up to this point, a sinusoidally varying room temperature has been used, but in practice, particularly during summer, the hot days are often longer than the cool nights. How PCM thermal mass responds to long hot days with short cool nights can be investigated, by using the room temperature distribution shown by the dashed line in figure 2.9a. Equations (2.11), (2.12), (2.14), and (2.15), with the new room temperature replacing equation (2.13), are solved and, for particular parameter values, the temperature profile shown in figure 2.9a is found. While, initially, the reduction in temperature fluctuations gets smaller with time, even after 7 diurnal cycles the temperature fluctuations for PCM thermal mass are smaller than those for thermal mass without PCM – the PCM is still beneficial. At some time, PCM in a constant temperature hot room completely melts (there will be a kink in the graph of temperature against time at this point) and then heats up towards room temperature. When it reaches room temperature, it is no longer effective. For example, in figure 2.9b the wall surface temperature has reached the room temperature by $T = 31$, or about 5 days. Before this time, the PCM remains beneficial. The amount and properties of PCM can be carefully selected so that PCM remains beneficial during hot weather for some desired time, for example, the working week. It is also important to consider typical room temperatures when choosing a PCM. The PCM melting range should be such that there is typically enough time – which may be less than half of the total time – when room temperatures are below the melting range, allowing the PCM to resolidify.

2.5 Discussion and Conclusions

This chapter has demonstrated that phase change material thermal mass can reduce temperature fluctuations. It has also demonstrated that it is possible to identify wall thicknesses and PCM mass fractions that balance the benefit of reducing the daily maximum interior surface temperature with the cost of extra PCM. The location of the PCM within the thermal mass is clearly important, so three different distributions of PCM through the thermal mass have also been considered. It was found that a “step” distribution – having PCM evenly distributed up to some depth into the wall, then having no PCM – appears to be best operationally, and the



Variation with time of interior surface temperature for PCM thermal mass, shown by the thick solid line, and thermal mass with no PCM, shown by the thin solid line. The room temperature, shown by the dashed line, has longer hot periods than cool periods.

Variation with time of interior surface temperature for PCM thermal mass, shown by the solid line, in response to a constant room temperature, shown by the dashed line.

Fig. 2.9 Variation with time of interior surface temperature. Parameters are $H_+ = 1.06$, $\Omega = 0.2$, $U_{\min} = -0.1$, $U_{\max} = 0.1$, with $s = 5$ for the PCM thermal mass and $s = 0$ for the thermal mass with no PCM.

best depth – the penetration depth – for PCM inclusion was estimated, in terms of known parameters.

The Richardson and Woods (2008) PCM thermal mass model was extended to include cooling at the exterior surface of the thermal mass, motivated by using waste “coolth” from an exhaust air heat pump to provide additional, free cooling. The appropriate values of the wall thickness and PCM mass fraction that were found are different from in the case without cooling, since the thermal mass must be sufficiently thin for the cooling at the exterior surface to affect the room temperature. Since real buildings are ventilated, natural ventilation was also included, in a room with a point source of buoyancy on the floor, and a PCM ceiling with cooling at the exterior surface, to explore how ventilation interacts with the PCM thermal mass. Understanding this problem helps to develop design guidelines for using PCM thermal mass in naturally ventilated rooms. In a room with stack-driven displacement ventilation, a hot layer forms at the top of the room and a model was developed that identifies the temperature and thickness of this hot layer. The fluctuations in the room and the interior surface temperatures were shown to be smaller than the fluctuations in cooling at the exterior surface, so PCM is clearly effective at reducing temperature fluctuations.

Because real weather contains hot periods, and in an effort to develop general design principles for PCM thermal mass that are effective under a range of realistic conditions,

non-uniform thermal forcing was also considered. During a period of relatively hot weather, it was found that the daily maximum surface temperature of PCM thermal mass increases, but, after such a period of hot weather, it quickly recovers to its behaviour before the hot period. The model was extended to include two PCMs – one that is effective during normal conditions, and another that is effective during a period of hot weather. It was found that, during the latter part of the period of hot weather, daily maximum interior surface temperatures were smaller (by about $0.3u_0$, as in figure 2.8b, which is 0.75°C when normal temperatures vary between 20°C and 25°C) with two PCMs than with one normal PCM. Outside of the period of hot weather, since there was less normal PCM when two PCMs were used, daily maximum surface temperatures were greater with two PCMs than with one normal PCM. The proportion of the two PCMs that should be used will depend on the desired outcome. Essentially, the key issue to consider is whether it is better to be comfortable most of the time and very uncomfortable occasionally, or to be not optimally comfortable most of the time. Since, during summer, the hot days may be longer than the cool nights, thermal forcing that mimicked such a diurnal cycle was considered. It was found that, for periods of cooling that allow the PCM to resolidify, PCM can still be effective in reducing temperature fluctuations. The response of PCM to a constant temperature hot room was considered, and it was found that the PCM is effective for some time before it completely melts and heats up to the constant room temperature.

Overall, this chapter has developed and used mathematical models to show that, in a range of realistic situations, phase change material thermal mass does reduce temperature fluctuations, but that it is important to select the “best” wall thickness and PCM mass fraction. What is “best” depends on the desired outcome, but this chapter has presented general, yet relatively simple, models, and used them in examples with commercially realistic parameters, that can be used straightforwardly for such design decisions.

Chapter 3

Detrainment of plumes from vertically distributed sources

3.1 Introduction

Vertically distributed buoyancy sources, for example, radiators and walls heated by the sun, are commonly found in buildings. The comfort of occupants is affected by the temperature stratification that develops in the building. Different buoyancy sources drive different flows and result in different temperature stratifications. Buoyancy sources usually drive turbulent plumes, which can be simply described using the Morton et al. (1956) plume model. There are three key assumptions in this model:

1. Profiles of density and vertical velocity across the plume are self-similar with height - in this chapter, we initially assume top hat profiles (constant across the plume, and zero outside).
2. Ambient fluid is entrained into the plume at a rate proportional, via an entrainment coefficient α , to the characteristic vertical velocity at that height.
3. Changes in density are small compared with a reference density (the Boussinesq approximation).

This plume model has been applied, by many authors, to a variety of situations in the built environment. See, for example, Linden (1999).

The plume model may be applied to a filling box with a point source or with a horizontal line source. In a filling box, the space is sealed, and there is an initial transient as the buoyant plume rises to the ceiling, where it spreads out, forming a stratified region, which grows deeper in time. The interface between this stratified region and the initial ambient

fluid is called the first front. Baines and Turner (1969) find an expression for the position of the first front with time, and use their experimental data to find a value of $\alpha = 0.10$ for the entrainment coefficient. Worster and Huppert (1983) consider the time-dependent ambient buoyancy profile, and find good agreement between the numerical solution of their governing equations and their approximate analytic expression for the ambient buoyancy profile. Section 3.3.1 discusses this horizontal line source model, and compares a series of experiments with the theoretical model. Cooper and Hunt (2010) present a model, which is discussed in section 3.3.2, for a filling box containing a buoyancy source that is vertically distributed over the full height of a wall. In this chapter, such a source is referred to as a full wall source. In a ventilated room with a full wall source, the plume fluid may reach its neutral buoyancy height at an intermediate height and spread horizontally in the room. Cooper and Hunt (2010) find that, if the plume is assumed uniform across its width, meaning that the intrusion occurs at a single height, the resulting ambient stratification is unstable with respect to small perturbations in either the plume flow or the ambient stratification. To solve this problem, they assume that the plume has a linear buoyancy profile across its width. However, in the unventilated case, they do not include this variation in buoyancy profile across the width of the plume, and so, in their model for the unventilated room, the plume can never detrain. Caudwell et al. (2016) also consider a vertically distributed source, but their source is held at a constant temperature, rather than providing a constant flux. In their experiments, the plume remained laminar for some distance, leading them to develop a hybrid model, combining a laminar part with a Cooper and Hunt-like turbulent part. While this hybrid model better describes the ambient buoyancy profile at small heights, it fails to capture the shape of the profile at the top of the space.

Cooper and Hunt (2010), Linden et al. (1990), and Chen et al. (2001) all consider a ventilated room with a vertically distributed, constant flux source. In this case, the plume can reach its neutral buoyancy height at an intermediate height within the room, where it intrudes into the ambient. Linden et al. (1990) assume that the intrusion depth is negligible, with the result that the model predicts layers of different density in the ambient, although in their experiments these layers are not seen. Cooper and Hunt (2010) show that this layered stratification is unstable to small perturbations in plume flow or ambient stratification, thus it is not expected to be physically realised. Instead, they allow intrusions to have a finite depth. Chen et al. (2001) also observe intrusions in experiments with a vertically distributed buoyancy source in a naturally ventilated space. They suggest that these intrusions smooth out the layered profile predicted by Linden et al. (1990). Both Cooper and Hunt (2010) and Linden et al. (1990) predict intrusions only for a ventilated space, they do not allow for detrainment of the plume in a unventilated space, despite Cooper and Hunt (2010) proposing

a linear buoyancy profile across the width of the plume for the ventilated space, which allows for detrainment in both ventilated and unventilated spaces.

Detrainment, however, may be important for vertically distributed sources. In experiments with a vertical line source, Gladstone and Woods (2014) observe detrainment, that is, plume fluid intruding into the ambient at intermediate heights. If, rather than being entrained into a plume and flushed quickly out of the room, contaminants are repeatedly detrained from and entrained into a plume, air quality may be affected. In experiments with a vertical ice wall as a source, McConnochie and Kerr (2016) find that, in the stratified region below the first front, ambient buoyancy profiles are approximately linear. They suggest that this disagreement between the profiles from their experiments and the profiles predicted by the models of Cooper and Hunt (2010) and Linden et al. (1990) is due to detrainment. When detrainment has a significant effect, a peeling plume model, such as that of Hogg et al. (2015) may be appropriate – here, density and vertical velocity are assumed to vary linearly across the plume, allowing parts of the plume to “peel” off into the ambient as outer parts of the plume reach their neutral buoyancy height at intermediate heights. We extend this peeling plume model, applying it to a vertically distributed buoyancy source, and find that the peeling plume model captures the shape of the ambient buoyancy profile more accurately than the model of Cooper and Hunt (2010).

In this chapter, we consider three sources in a sealed space: a horizontal line source, a full wall source, and a half wall source (a source that is vertically distributed, but over only half of the height of a wall). We wish to know whether they have one-way-entrainment, as is conventionally assumed, or whether they also have detrainment. First, in section 3.2, the results of experiments with each of the three sources are presented. Then, in section 3.3, theoretical models are presented for each source, which are then compared with the experimental results. We compare the measurements of the buoyancy profiles produced by a line source with the model of Worster and Huppert (1983) in section 3.3.1. With the full wall source, section 3.3.2 shows that the experimental results of section 3.2 disagree with the Cooper and Hunt (2010) model, so we compare the experimental results with a peeling plume model. The natural question, having considered both a horizontal line source and a full wall source, is to consider a half wall source. Section 3.3.3 shows that the half wall experiments can be described by an extension of the Cooper and Hunt (2010) one-way-entrainment model. Finally, section 3.4 contains the conclusions of this work.

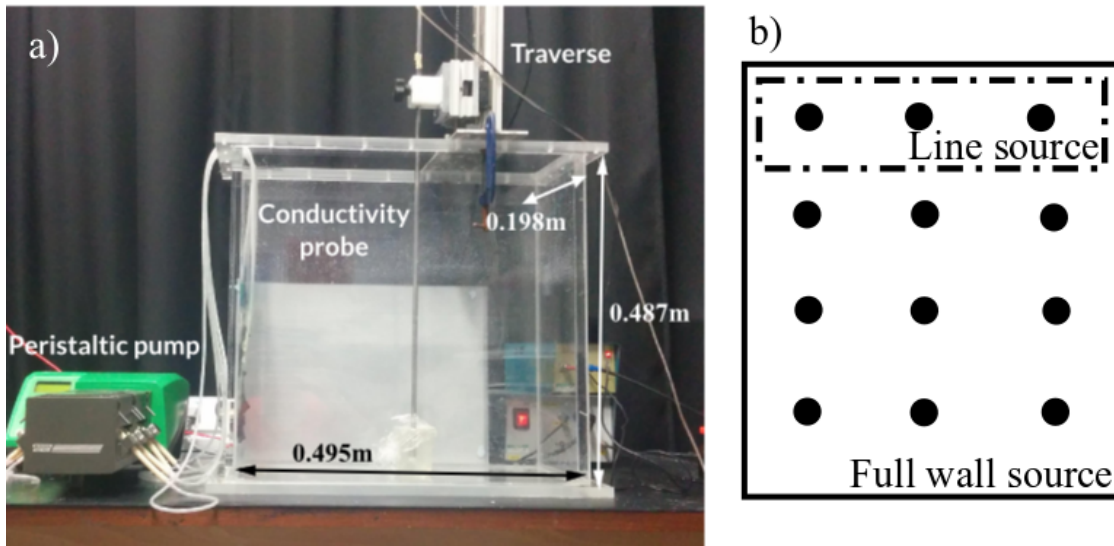


Fig. 3.1 The experimental setup (left), including details of the source (right).

3.2 Experiments

3.2.1 Methods

Experiments with each of the three sources are performed, to investigate whether detrainment occurs. In these experiments, salt provides the density differences. Figure 3.1 shows the experimental setup: the tank is 0.487m tall, and is filled to approximately 0.3m with fresh water. A source (described below) covers one wall of the tank, and this wall is 0.198m wide. The wall perpendicular to the source is 0.495m long.

To approximate a line source, salt water is pumped through three tubes, which are distributed (in a line) over the width of the tank wall. The spacing of these sources is kept the same in each experiment. Figure 3.1 shows the source setup for the full wall source of section 3.2.3; using just the top row of tubes, shown by the dashed box, gives a line source. The end of each tube is covered with a fine mesh fabric to ensure that the fluid leaving the source is turbulent. Two Watson Marlow 520Du peristaltic pumps with 505L and 505LX pumpheads pump salt water through the tubes. A total of 6 tubes run through the pumpheads and are then split into two, giving 12 tubes which make up the full wall source. The spacing between these tubes is kept the same in each experiment, and was chosen so that the sources are evenly distributed across the wall. The half wall source is spread over the top half of the wall only. The half wall source, shown in figure 3.6, has the same number of tubes as are used for the full wall source, but the tubes are distributed over only the top half of the wall.

A conductivity probe, traversed vertically through the tank over a height of 0.25m every 2 minutes, measures the stratification. The conductivity probe is calibrated using a range of samples of salt water whose densities are measured using a density meter. The measured stratification is used to calculate the dimensionless ambient buoyancy, defined as $\alpha^{2/3} f_0^{-2/3} H g \frac{(\rho_a - \rho_1)}{\rho_1}$ for the line source, where α is the entrainment coefficient, f_0 is the source buoyancy flux per unit source width, H is the tank height, g is gravitational acceleration, ρ_1 is the initial ambient density, and ρ_a is the ambient density. For the full wall and half wall sources, f_0 is replaced by $b_{s_0} H$, where b_{s_0} is the source buoyancy flux per unit area. The resulting experimental ambient buoyancy profiles, such as those presented in figure 3.2, show scatter of approximately 1 dimensionless ambient buoyancy unit, compared with a maximum dimensionless ambient buoyancy of about 2-9 (i.e. 11%-50% scatter). The source fluid is dyed with food colouring, using different colours at different times during the experiment, to visualise the flow. When the plume detrain, dyed fluid is observed to exit the plume and enter the ambient at an intermediate height.

3.2.2 Horizontal line source

A total of 20 experiments with a line source were performed, varying both the source density and the source volume flux; these experiments are listed in table 3.1. While the dimensionless density differences $\Delta\rho = (\rho_a - \rho_1) / \rho_1$ between the source and the initial ambient for experiments E_{line} , J_{line} , O_{line} , and T_{line} are large compared with those for experiments A_{line} , F_{line} , K_{line} , and P_{line} , entrainment rapidly reduces the density, and so the Boussinesq approximation works well soon after the fluid leaves the source. The density profiles from a typical experiment (N_{line} , which, as listed in table 3.1, has a flow rate of 0.9ml/s and a dimensionless density difference $\Delta\rho = 0.13$) at 4 different times (375s, 855s, 1335s, and 1815s after starting) are shown in figure 3.2. In each of the profiles shown, near the bottom of the tank (dimensionless height zero), the profile is close to vertical. In all of these line source experiments the dye descended to the floor of the tank in the plume, rather than intruding into the ambient, suggesting that detrainment did not occur. In section 3.3.1, we will compare these experimental results with the one-way-entrainment model of Worster and Huppert (1983), showing that the experimental results agree with the theory, and so producing a line source using several individual sources is appropriate.

3.2.3 Full wall source

The experiments are set up as in section 3.2.2, but using the full wall source, shown by the solid line box in figure 3.1. A total of 20 experiments with a full wall source were performed,

Flow rate	Approximate amount, by volume, of saturated salt water				
	20%	40%	60%	80%	100%
0.4 ml/s	A _{line} , $\Delta\rho = 0.04$	B _{line} , $\Delta\rho = 0.04$	C _{line} , $\Delta\rho = 0.07$	D _{line} , $\Delta\rho = 0.10$	E _{line} , $\Delta\rho = 0.12$
0.6 ml/s	F _{line} , $\Delta\rho = 0.02$	G _{line} , $\Delta\rho = 0.06$	H _{line} , $\Delta\rho = 0.09$	I _{line} , $\Delta\rho = 0.12$	J _{line} , $\Delta\rho = 0.18$
0.9 ml/s	K _{line} , $\Delta\rho = 0.02$	L _{line} , $\Delta\rho = 0.05$	M _{line} , $\Delta\rho = 0.10$	N _{line} , $\Delta\rho = 0.13$	O _{line} , $\Delta\rho = 0.17$
1.1 ml/s	P _{line} , $\Delta\rho = 0.03$	Q _{line} , $\Delta\rho = 0.06$	R _{line} , $\Delta\rho = 0.10$	S _{line} , $\Delta\rho = 0.14$	T _{line} , $\Delta\rho = 0.18$

Table 3.1 The 20 line source experiments, including the dimensionless density difference $\Delta\rho$ between the source and the initial ambient. These give the source buoyancy fluxes listed in table 3.2.

Experiment	Source buoyancy flux		
	($\times 10^{-6} \text{ms}^{-3}$) Line source	($\times 10^{-6} \text{m}^2 \text{s}^{-3}$) Full wall source Half wall source	
A	0.8	6.3	9.5
B	0.8	12.7	12.7
C	1.4	19.0	22.2
D	2.0	25.3	38.0
E	2.4	34.8	44.3
F	0.6	10.7	20.6
G	1.8	21.4	25.7
H	2.7	32.1	46.3
I	3.6	53.5	56.6
J	5.3	64.1	77.2
K	0.9	15.0	28.5
L	2.2	37.6	35.6
M	4.5	52.7	71.3
N	5.8	75.2	99.8
O	7.6	90.3	114.0
P	1.6	19.0	28.5
Q	3.3	47.5	47.5
R	5.4	76.0	66.5
S	7.6	95.0	114.0
T	9.8	133.0	142.5

Table 3.2 The source buoyancy flux per unit source width (line source) or source area (full wall and half wall sources), $g\Delta\rho$, multiplied by the volume flux (in $\text{m}^3 \text{s}^{-1}$), divided by the source width (line source) or source area (full wall and half wall sources).

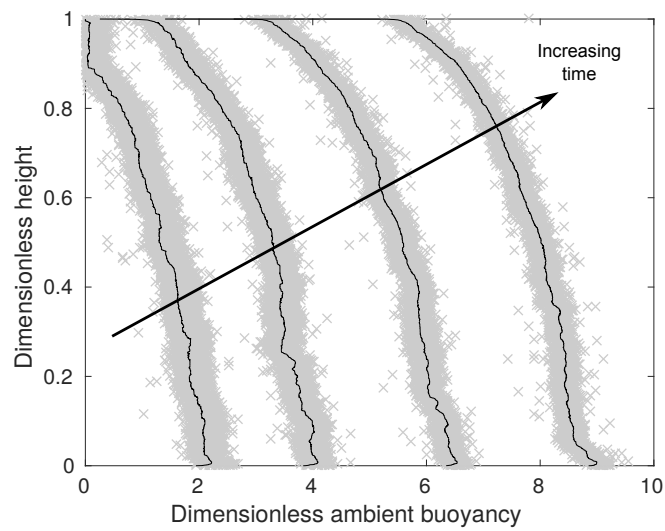


Fig. 3.2 Dimensionless ambient buoyancy profiles for line source experiment N_{line} (which has a flow rate of 0.9ml/s and a dimensionless density difference $\Delta\rho = 0.13$). The four subplots show the experimental results at four different times: 375s, 855s, 1335s, and 1815s after starting. When nondimensionalised by the timescale $W\alpha^{-2/3}f_0^{-1/3}$, where α is the entrainment coefficient, f_0 is the source buoyancy flux per unit source width, and W is the tank width, these times are 1.6, 3.7, 5.7, and 7.8. Grey crosses show the original data and a black line shows the filtered data (filtered using a median filter).

Flow rate	Approximate amount, by volume, of saturated salt water				
	20%	40%	60%	80%	100%
1.6 ml/s	A _{full} , $\Delta\rho = 0.02$	B _{full} , $\Delta\rho = 0.04$	C _{full} , $\Delta\rho = 0.06$	D _{full} , $\Delta\rho = 0.08$	E _{full} , $\Delta\rho = 0.11$
2.7 ml/s	F _{full} , $\Delta\rho = 0.02$	G _{full} , $\Delta\rho = 0.04$	H _{full} , $\Delta\rho = 0.06$	I _{full} , $\Delta\rho = 0.10$	J _{full} , $\Delta\rho = 0.12$
3.8 ml/s	K _{full} , $\Delta\rho = 0.02$	L _{full} , $\Delta\rho = 0.05$	M _{full} , $\Delta\rho = 0.07$	N _{full} , $\Delta\rho = 0.10$	O _{full} , $\Delta\rho = 0.12$
4.8 ml/s	P _{full} , $\Delta\rho = 0.02$	Q _{full} , $\Delta\rho = 0.05$	R _{full} , $\Delta\rho = 0.08$	S _{full} , $\Delta\rho = 0.10$	T _{full} , $\Delta\rho = 0.14$

Table 3.3 The 20 full wall source experiments, including the dimensionless density difference $\Delta\rho$ between the source and initial ambient. These give the source buoyancy fluxes listed in table 3.2.

varying both the source density and source volume flux; these experiments are listed in table 3.3. The density profiles from a typical experiment (N_{full} , which, as listed in table 3.3, has a flow rate of 3.8ml/s and a dimensionless density difference $\Delta\rho = 0.10$) at 4 different times (120s, 360s, 600s, and 840s after starting) are shown in figure 3.3. These profiles are qualitatively different from those in figure 3.2, which was for a horizontal line source – the full wall source profiles, rather than being almost vertical near the bottom of the tank, have a different slope and a change of curvature near the bottom of the tank.

One reason for this difference in profile shape is, as in the vertical line source experiments of Gladstone and Woods (2014), detrainment occurs. This detrainment is shown in figure 3.4, where the left hand figure shows red dyed source fluid intruding into the undyed ambient at intermediate heights, and the right hand figure shows green dyed source fluid intruding into the red (at lower heights) and undyed (at larger heights) ambient at intermediate heights. This detrainment occurs in each of the full wall source experiments. The fluid intrudes into the ambient over a range of heights, with the bottom part of this range being the same in each experiment. An example of this is shown in figure 3.5 which shows, on the left, experiment C_{full} at 6 minutes into the experiment, and, on the right, experiment T_{full} at 4 minutes into the experiment. Both experiments have intrusions over approximately the same range of heights. Over time, the intrusions extend horizontally, further into the ambient, and occur over a wider range of heights. Figure 3.4 shows this happening in experiment T_{full} : the left hand figure is at 4 minutes into the experiment, and has (red) intrusions over approximately the bottom third of the height to which the tank was filled, whilst the right hand figure is at 10 minutes into the experiment and has (green) intrusions over approximately the bottom two thirds of the height to which the tank was filled. Detrainment suggests that a one-way-entrainment model will be unable to predict the density profiles observed in experiments, and, instead, a peeling plume

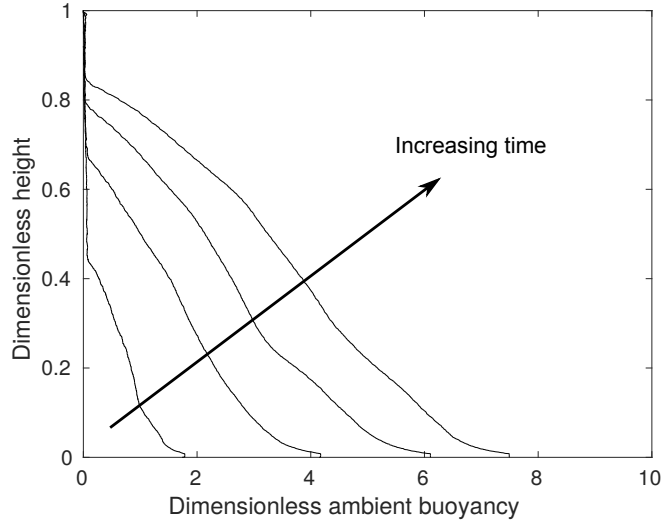


Fig. 3.3 Dimensionless ambient buoyancy profiles (median filtered data) for full wall source experiment N_{full} (which has a flow rate of 3.8ml/s and a dimensionless density difference $\Delta\rho = 0.10$). The four subplots show the experimental results at four different times: 120s, 360s, 600s, and 840s after starting. When nondimensionalised by the timescale $W\alpha^{-2/3}b_{s_0}^{-1/3}H^{-1/3}$, where α is the entrainment coefficient, b_{s_0} is the source buoyancy flux per unit source area, and W is the tank width, these times are 0.4, 1.3, 2.2, and 3.1.

model is needed. We compare the experimental results with both the one-way-entrainment model and a peeling plume model in section 3.3.2.

3.2.4 Half wall source

A line source and a full wall source give qualitatively different stratifications, so we now consider the stratification that develops with an intermediate case: a half wall source. The experiments are set up as in section 3.2.2, but using a half wall source. As in sections 3.2.2 and 3.2.3, 20 experiments were performed, varying both the source density and source volume flux; these experiments are listed in table 3.4.

The density profiles from a typical experiment (N_{half} , which, as listed in table 3.4, has a flow rate of 1.8ml/s and a dimensionless density difference $\Delta\rho = 0.14$) at 4 different times (375s, 855s, 1335s, and 1815s after starting) are shown in figure 3.7. At several times during each experiment, the source fluid was dyed a different colour. This dyed fluid descended to the floor of the tank in the plume, rather than intruding into the ambient. Since dyed fluid was not seen to intrude into the ambient, this suggests that detrainment did not occur in

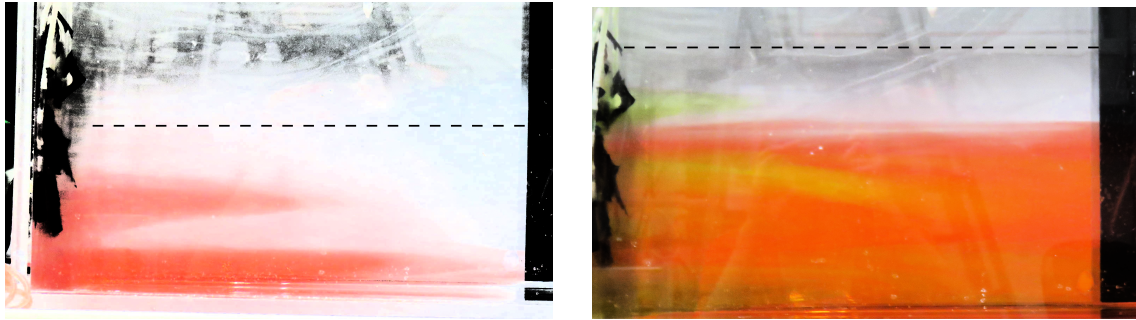


Fig. 3.4 Left: source fluid (dyed red 3 minutes into the experiment) detrainment – it intrudes into the ambient at intermediate heights. Shown at 4 minutes into experiment T_{full} . Right: source fluid (dyed green 7 minutes into the experiment) detrainment. Shown at 10 minutes into experiment T_{full} . The contrast has been enhanced, for clarity. The approximate location of the first front is shown by the dashed line.

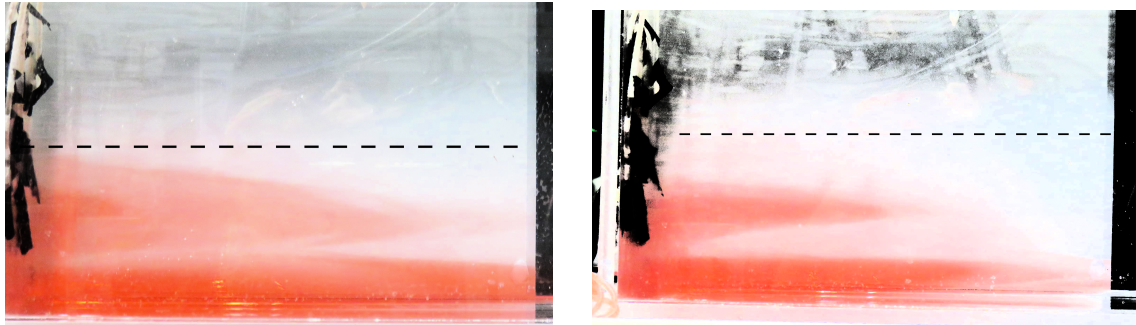


Fig. 3.5 Source fluid (dyed red 3 minutes into the experiment) detrainment at similar heights towards the bottom of the tank for each experiment. Experiment C_{full} at 6 minutes is shown on the left, and experiment T_{full} at 4 minutes is shown on the right. The contrast has been enhanced, for clarity. The approximate location of the first front is shown by the dashed line.

Flow rate	Approximate amount, by volume, of saturated salt water				
	20%	40%	60%	80%	100%
0.8 ml/s	$A_{half},$ $\Delta\rho = 0.03$	$B_{half},$ $\Delta\rho = 0.04$	$C_{half},$ $\Delta\rho = 0.07$	$D_{half},$ $\Delta\rho = 0.12$	$E_{half},$ $\Delta\rho = 0.14$
1.3 ml/s	$F_{half},$ $\Delta\rho = 0.04$	$G_{half},$ $\Delta\rho = 0.05$	$H_{half},$ $\Delta\rho = 0.09$	$I_{half},$ $\Delta\rho = 0.11$	$J_{half},$ $\Delta\rho = 0.15$
1.8 ml/s	$K_{half},$ $\Delta\rho = 0.04$	$L_{half},$ $\Delta\rho = 0.05$	$M_{half},$ $\Delta\rho = 0.10$	$N_{half},$ $\Delta\rho = 0.14$	$O_{half},$ $\Delta\rho = 0.16$
2.4 ml/s	$P_{half},$ $\Delta\rho = 0.03$	$Q_{half},$ $\Delta\rho = 0.05$	$R_{half},$ $\Delta\rho = 0.07$	$S_{half},$ $\Delta\rho = 0.12$	$T_{half},$ $\Delta\rho = 0.15$

Table 3.4 The 20 half wall source experiments, including the dimensionless density difference $\Delta\rho$ between the source and initial ambient. These give the source buoyancy fluxes listed in table 3.2.

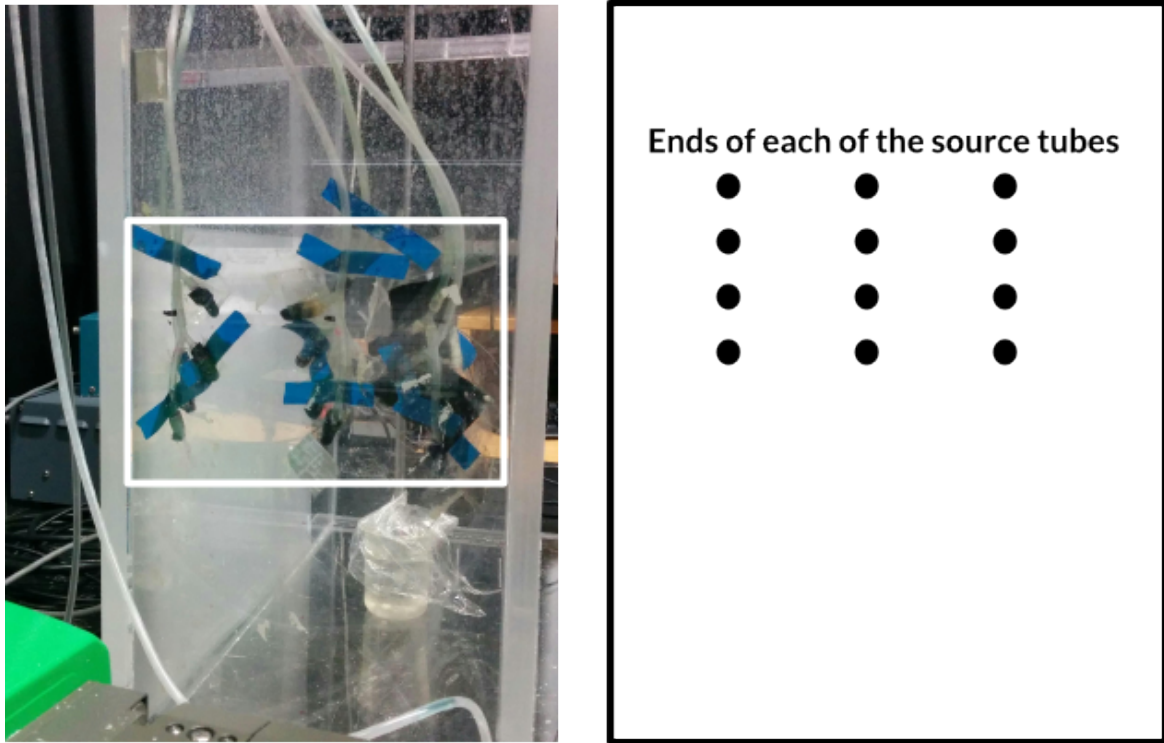


Fig. 3.6 The half wall source.

these experiments, so in section 3.3.3, we will compare these experimental results with a one-way-entrainment model.

3.3 Theoretical models

3.3.1 Horizontal line source

To confirm that the line source made up of several discrete source does indeed approximate a distributed source, we compare the line source experiments of section 3.2.2 with the well-established Worster and Huppert (1983) one-way-entrainment line source model.

Worster and Huppert (1983) use the Morton et al. (1956) plume model to describe an axisymmetric plume in a sealed, insulated room. For completeness, the horizontal line source version of this model is presented (changing notation) here.

The volume, momentum, and buoyancy fluxes per unit length through the plume are defined as

$$q = \int_0^\infty w dx, \quad m = \int_0^\infty w^2 dx, \quad \text{and} \quad f = \int_0^\infty wg \left(\frac{\rho_a - \rho}{\rho_1} \right) dx, \quad (3.1)$$

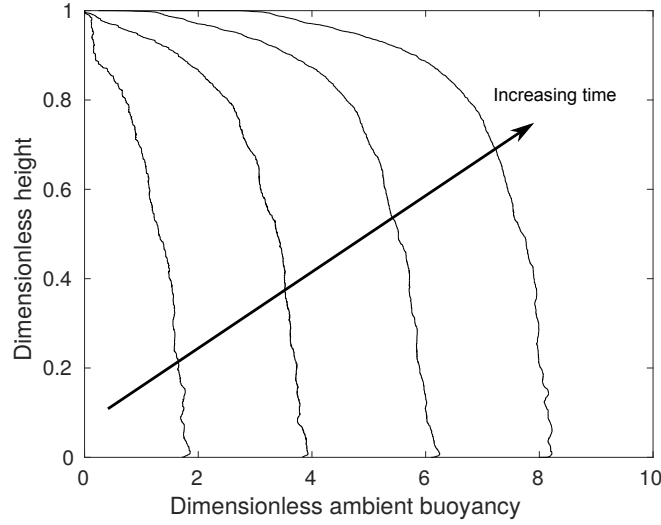


Fig. 3.7 Dimensionless ambient buoyancy profiles (median filtered data) for half wall source experiment N_{half} (which has a flow rate of 1.8ml/s and a dimensionless density difference $\Delta\rho = 0.14$). The four subplots show the experimental results at four different times: 375s, 855s, 1335s, and 1815s after starting.

where w is vertical velocity, x is distance (from the wall) across the plume, g is acceleration due to gravity, ρ_a is the ambient density, ρ is the plume density, and ρ_1 is the initial ambient density. Conservation of volume, momentum, and buoyancy fluxes give the plume equations:

$$\frac{dq}{dz} = \alpha \frac{m}{q}, \quad \frac{dm}{dz} = \frac{qf}{m}, \quad \text{and} \quad \frac{df}{dz} = -q \frac{\partial \delta_a}{\partial z}, \quad (3.2)$$

where z is vertical distance from the source, α is the entrainment coefficient, and $\delta_a = g(\rho_1 - \rho_a)/\rho_1$ is the ambient buoyancy. The boundary conditions are

$$q = m = 0 \quad \text{at} \quad z = 0, \quad \text{and} \quad f = f_0 \quad \text{at} \quad z = 0, \quad (3.3)$$

where f_0 is the source buoyancy flux per unit width. These boundary conditions are for a pure plume, and to account for the non-zero volume flux at the source, a virtual origin adjustment is required (as discussed by Morton et al. (1956)). This adjustment assumes that the theoretical source is some distance above the experimental source, so that, at the height of the experimental source, the plume has a non-zero volume flux. For the line source experiments of section 3.2.2, the adjustment is small (a dimensionless value of about 0.008), however, so we neglect it for the full wall and half wall models.

Experiment Timescale(s)	A _{line} 450	B _{line} 463	C _{line} 389	D _{line} 344	E _{line} 317	F _{line} 508	G _{line} 354	H _{line} 309	I _{line} 281	J _{line} 243
Experiment Timescale(s)	K _{line} 435	L _{line} 321	M _{line} 258	N _{line} 234	O _{line} 215	P _{line} 350	Q _{line} 281	R _{line} 241	S _{line} 217	T _{line} 199

Table 3.5 The timescales $W\alpha^{-2/3}f_0^{-1/3}$ for the 20 line source experiments.

Changes in ambient buoyancy are given by

$$\frac{\partial \delta_a}{\partial t} = \frac{q}{W} \frac{\partial \delta_a}{\partial z}, \quad (3.4)$$

where W is the width of the room outside the plume (we assume that the plume is thin) and t is time. This assumes that the aspect ratio of the box, H/W , is small, and that the time for the box to be filled with dense fluid is much greater than the time the plume takes to rise through the box.

We nondimensionalise, taking the height of the tank H as the natural length scale, and defining dimensionless variables

$$q = \alpha^{2/3} f_0^{1/3} H Q, \quad m = \alpha^{1/3} f_0^{2/3} H M, \quad f = f_0 F, \\ \delta_a = \alpha^{-2/3} f_0^{2/3} H^{-1} \Delta_a, \quad z = H Z, \quad \text{and} \quad t = W \alpha^{-2/3} f_0^{-1/3} T. \quad (3.5)$$

The particular value of α that we use for the line source is $\alpha = 0.04$, which is discussed further in section 3.3.1. On substituting these dimensionless variables into (3.2), we obtain the dimensionless plume equations

$$\frac{dQ}{dZ} = \frac{M}{Q}, \quad \frac{dM}{dZ} = \frac{QF}{M}, \quad \text{and} \quad \frac{dF}{dZ} = -Q \frac{\partial \Delta_a}{\partial Z}, \quad (3.6)$$

and on substituting the dimensionless variables (3.5) into (3.4), we obtain the dimensionless ambient buoyancy equation

$$\frac{\partial \Delta_a}{\partial T} = Q \frac{\partial \Delta_a}{\partial Z}. \quad (3.7)$$

The boundary conditions (3.3) become

$$Q = M = 0 \quad \text{at} \quad Z = 0, \quad \text{and} \quad F = 1 \quad \text{at} \quad Z = 0. \quad (3.8)$$

The timescale, $W\alpha^{-2/3}f_0^{-1/3}$, is given in table 3.5 for each of the 20 experiments performed, and varies between approximately 3 and 8 minutes.

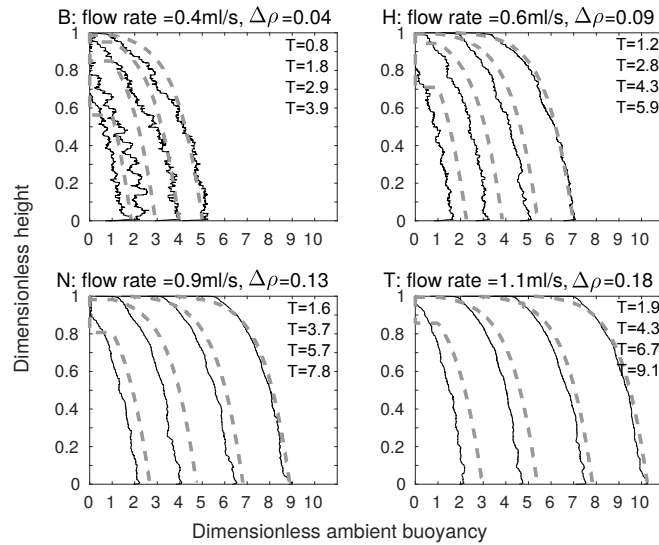


Fig. 3.8 Dimensionless ambient buoyancy profiles for line source experiments B_{line} , H_{line} , N_{line} , and T_{line} . Solid black lines show filtered experimental results, the dashed lines show the model results. Each subplot shows profiles at times 375s, 855s, 1335s, and 1815s after starting, as in figure 3.2. The corresponding dimensionless times are listed on each plot.

Equations (3.6) and (3.7), with boundary conditions (3.8), are solved numerically, using the method of Germeles (1975). This method assumes that, at $Z = 0$, the plume lays down layers of dense fluid. By tracking the position and thickness of these layers with time, we obtain the ambient stratification.

Comparing the model with experiments

Figure 3.8 shows qualitative agreement between the theoretical model and experimental results (representative experiments B_{line} , H_{line} , N_{line} , and T_{line} , which have different source buoyancy fluxes, as listed in table 3.2, are shown). Each subplot shows the ambient buoyancy profile at times 375s, 855s, 1335s, and 1815s after starting. The time used for the model is the time at which the probe has traversed through half of the height of the tank.

For a more quantitative measure of the agreement between the theoretical and experimental profiles, we calculate the root mean square (RMS) error by calculating, point by point, the square of the difference between the theoretical and experimental profiles, then taking the average over the tank height, and finally, taking the square root. The results of these calculations are shown in figure 3.9, where each subplot shows a different source flow rate. On each subplot, the five different lines correspond to the five different source densities used at that source flow rate, with darker lines for larger source densities. The RMS error

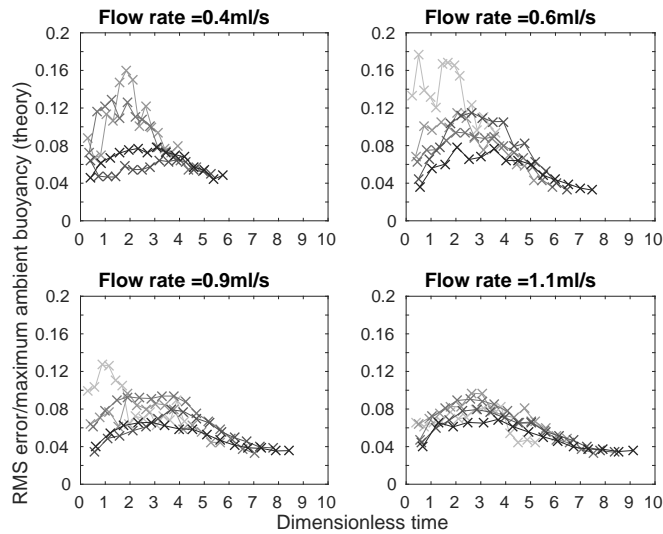


Fig. 3.9 RMS error between theoretical and experimental dimensionless ambient buoyancy profiles, divided by maximum theoretical dimensionless ambient buoyancy, against dimensionless time, for each of the 20 line source experiments listed in table 3.1, apart from experiment A which has a large RMS error, and is not shown.

was calculated at each time that a density profile was measured during an experiment - the crosses on each line correspond to these calculations. The error is smaller at larger times, in agreement with visual comparison of the profiles in figure 3.8. Apart from at the lowest source volume flux and density, in each experiment, the RMS error in dimensionless ambient buoyancy at late times is typically below 4% of the maximum theoretical dimensionless ambient buoyancy in that experiment. The RMS error is thus relatively small compared with the scatter in the original experimental data, leading to the conclusion that the theoretical model provides a good description of the experimental profiles. In these experiments, the value of the entrainment coefficient that gives a low RMS value at late times (the RMS error does vary with α) and a good visual fit between theoretical and experimental dimensionless ambient buoyancy profiles is $\alpha = 0.04$. This value is lower than other works on line sources (Baines (2002) took $\alpha = 0.073$), but we expect the value to be lower for the experiments described in this chapter because the source entrains only over part of the width of the tank, as it is made up of discrete sources.

To ensure that the three sources are, together, acting as a line source, rather than as three independent half axisymmetric plumes, the experimental first front heights from a representative experiment, N_{line} , are compared with the theoretical first front heights for a line source and an axisymmetric source (from Worster and Huppert (1983), adjusted to be for a half source) in figure 3.10. The crosses are the experimental results, the solid line is the line

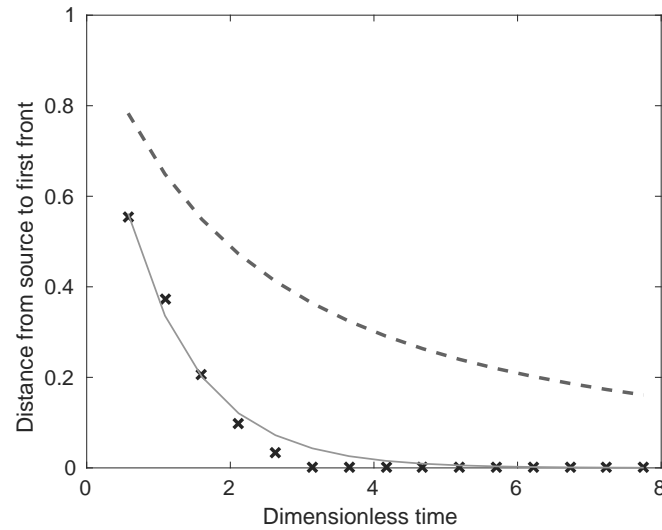


Fig. 3.10 The distance from the source to the first front for experiment N_{line} (crosses), from line source theory (solid line), and from half axisymmetric source theory (dashed line), with $\alpha = 0.04$ for both. The line source theory and the half axisymmetric source theory give very different first front speeds.

source theory, and the dashed line is the half axisymmetric source theory. The line source theory gives much better agreement with the experimental results than the axisymmetric source gives, and so we conclude that the line of discrete sources used in the experiments of section 3.2.2 do indeed act as a line source. In this section, we have seen that the line source experimental results of section 3.2.2 agree with the Worster and Huppert (1983) one-way-entrainment line source model, confirming that producing a distributed source using several discrete sources is appropriate.

3.3.2 Full wall source

Having confirmed that producing a distributed source using several individual sources is appropriate, we now consider a full wall source. Cooper and Hunt (2010) present a model, based on the Morton et al. (1956) one-way-entrainment plume model, for a filling box with a full wall source. For completeness, their model is presented here (changing notation) then, in section 3.3.2, we compare the experimental results of section 3.2.3 with the model, showing it to be an inadequate model when detrainment occurs. As in section 3.3.1, conservation of volume, momentum, and buoyancy fluxes give the plume equations. The volume and momentum flux equations are as in (3.2), but, in the buoyancy flux equation, an extra term, the source buoyancy flux per unit source area $b_s(z)$, accounts for the vertically distributed

Experiment	A _{full}	B _{full}	C _{full}	D _{full}	E _{full}	F _{full}	G _{full}	H _{full}	I _{full}	J _{full}
Timescale(s)	638	490	425	388	348	549	411	353	308	284
Experiment	K _{full}	L _{full}	M _{full}	N _{full}	O _{full}	P _{full}	Q _{full}	R _{full}	S _{full}	T _{full}
Timescale(s)	452	349	306	270	252	411	318	274	250	227

Table 3.6 The timescales $W\alpha^{-2/3}b_{s0}^{-1/3}H^{-1/3}$ for the 20 full wall source experiments, with $\alpha = 0.018$.

buoyancy source,

$$\frac{df}{dz} = -q\frac{\partial\delta_a}{\partial z} + b_s(z). \quad (3.9)$$

We nondimensionalise as in (3.5), but replacing f_0 by $b_{s0}H$, where $b_{s0} = b_s(0)$ is the source buoyancy flux per unit area at $z = 0$. The dimensionless plume equations with one-way-entrainment are then

$$\frac{dQ}{dZ} = \frac{M}{Q}, \quad \frac{dM}{dZ} = \frac{QF}{M}, \quad \text{and} \quad \frac{dF}{dZ} = -Q\frac{\partial\Delta_a}{\partial Z} + B(Z), \quad (3.10)$$

where $B(Z) = b_s(z)/b_{s0}$ is the nondimensional source buoyancy flux per unit area. For the full wall source $B(Z) = 1$. Boundary conditions are now

$$Q = M = F = 0 \quad \text{at} \quad Z = 0. \quad (3.11)$$

Equation (3.7) remains the appropriate equation for the ambient buoyancy. The timescale, $W\alpha^{-2/3}b_{s0}^{-1/3}H^{-1/3}$, is given in table 3.6 for each of the 20 experiments performed, and varies between approximately 4 and 11 minutes. Equations (3.10) and (3.7), with boundary conditions (3.11), are solved numerically, using the method of Germeles (1975), as described in section 3.3.1.

Comparing the model with experiments

Some representative experimental results are shown in figure 3.11, along with the Cooper and Hunt (2010) one-way-entrainment model, but, as expected, the experimental results and the model disagree. The experimental and theoretical profiles are qualitatively different near $Z = 0$ (the base of the tank). Cooper and Hunt's model, which is without detrainment, is inadequate for describing the experiments of section 3.2.3. This is further highlighted by considering the RMS error between the theoretical and experimental dimensionless ambient buoyancy profiles, as shown in figure 3.12. Unlike with the line source, shown in figure 3.9, the RMS error is larger than 8% of the maximum theoretical dimensionless ambient buoyancy, and appears to be increasing with time for all but the largest flow rate. Both the

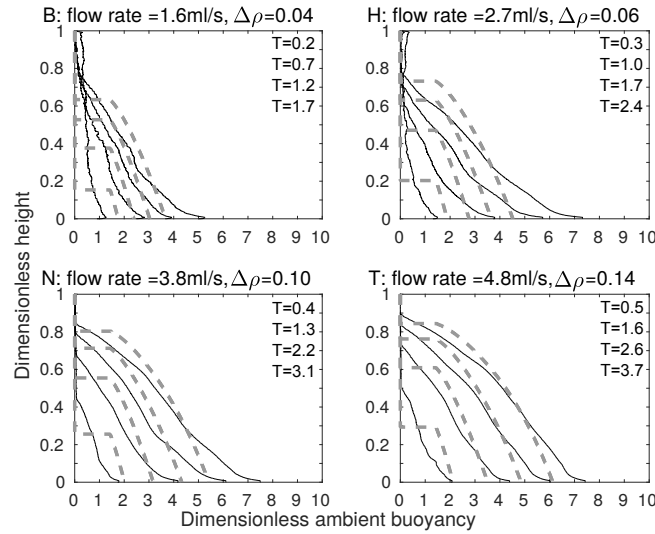


Fig. 3.11 Dimensionless ambient buoyancy profiles for full wall source experiments B_{full} , H_{full} , N_{full} , and T_{full} . Solid black lines show filtered experimental results, the dashed lines show the model results. Each subplot shows profiles at times 120s, 360s, 600s, and 840s after starting. The corresponding dimensionless times are listed on each plot.

RMS error and visually comparing the shapes of the profiles indicate that the Cooper and Hunt (2010) one-way-entrainment model is inadequate for describing the full wall source experiments.

Following Wells and Worster (2008), we add in a drag term D , to account for the effect of the wall on the flow. The momentum flux equation becomes

$$\frac{dM}{dZ} = \frac{QF}{M} - D. \quad (3.12)$$

Whilst adding this drag term does change the first front location, as shown in figure 3.13, it does not qualitatively change the shape of the ambient buoyancy profile. In particular, we do not see the distinctive “flick” (the change in curvature) near the base of the tank that is seen in the experimental profiles, in figure 3.11. We thus deduce that wall drag is not the reason for the disagreement between the theoretical and experimental profiles in figure 3.11. It would appear that detrainment, observed in experiments, must be included in the model, which we do using a peeling plume model. We see in the following section that a peeling plume model, which allows for intrusions of plume fluid into the ambient at intermediate heights, captures the experimentally observed change in curvature in the ambient buoyancy profile near the base of the tank.

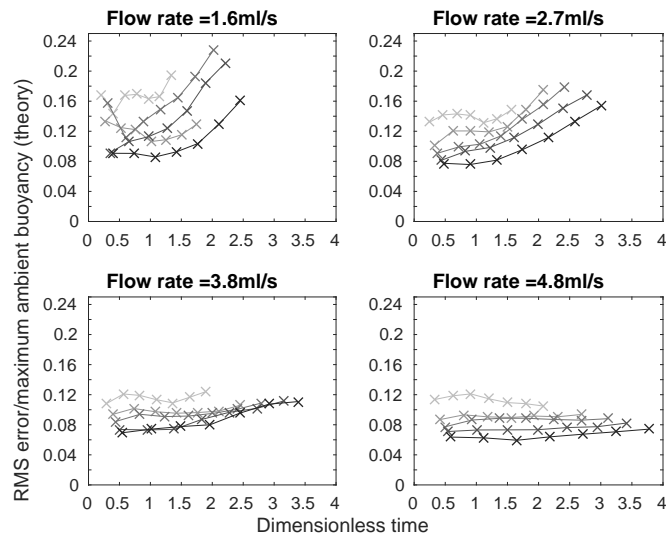


Fig. 3.12 RMS error between theoretical (Cooper and Hunt (2010) one-way-entrainment model, with $\alpha = 0.018$, chosen to give a low RMS error over all the experiments) and experimental dimensionless ambient buoyancy profiles, divided by the maximum theoretical dimensionless ambient buoyancy, against dimensionless time for each of the 20 full wall source experiments listed in table 3.3.

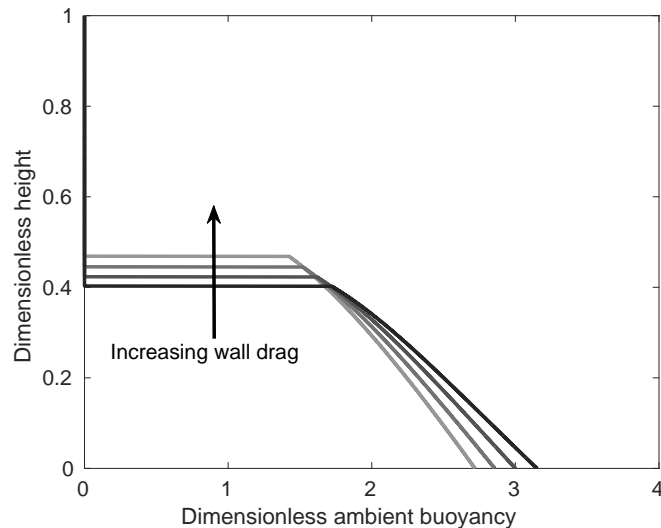


Fig. 3.13 Numerical solutions to the full wall source plume equations with wall drag. Dimensionless ambient buoyancy profiles are shown for four different values of dimensionless wall drag D : 0, 0.1, 0.2, and 0.3. Changing the value of D does not qualitatively change the shape of the ambient buoyancy profile.

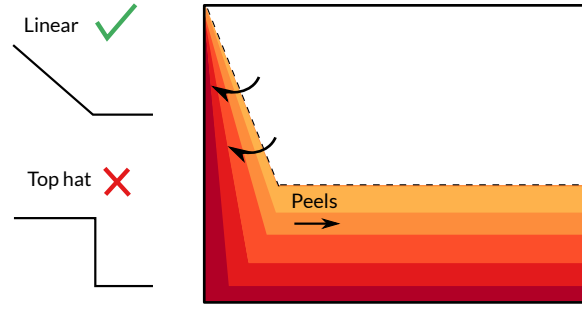


Fig. 3.14 In the peeling plume model, density and vertical velocity vary linearly across the width of the plume, allowing parts of the plume to peel off into the ambient at intermediate heights.

Peeling plume

The detrainment observed in experiments suggests that some plume fluid reaches its neutral buoyancy height at intermediate heights. The assumption of top hat profiles across the width of the plume rules out this possibility in the model. So, we relax the top hat profile assumption and instead consider linear profiles for vertical velocity and density. Linear profiles allow parts of the plume to peel off at intermediate heights where the density in the plume matches that in the environment, as shown in figure 3.14. This peeling plume model was developed by Hogg et al. (2015) to look at the flow of rivers into lakes. In this section their model is presented, but we extend it from a line source to a full wall source, which has different governing equations (3.10) from those used by Hogg et al. (2015).

To allow the plume to peel at intermediate heights, we now assume, as Hogg et al. (2015) assume, that vertical velocity and density vary linearly across the plume:

$$w = \begin{cases} w_m(z)(b-x)/b, & x < b, \\ 0, & x > b \end{cases} \quad \text{and} \quad \rho = \begin{cases} \rho_1 + \rho_m(z)(b-x)/b, & x < b, \\ \rho_1, & x > b, \end{cases} \quad (3.13)$$

where x is the distance across the plume (from the source wall), b is the plume width, $w_m(z)$ is the maximum vertical velocity in the plume at height z , and $\rho_m(z)$ is the maximum density in the plume at height z . Note that we ignore the viscous boundary layer near the wall. On substituting these expressions for vertical velocity and density into (3.1), we obtain

$$q = \frac{w_m b}{2} = Q \alpha^{2/3} b_{s_0}^{1/3} H^{4/3}, \quad m = \frac{w_m^2 b}{3} = M \alpha^{1/3} b_{s_0}^{2/3} H^{5/3}, \quad f = \frac{g \rho_m w_m b}{3 \rho_1} = F b_{s_0} H, \quad (3.14)$$

and equation (3.10) still holds, with boundary conditions (3.11).

The plume evolves as in the Cooper and Hunt (2010) one-way-entrainment model described in section 3.3.2 until it reaches the first front (the interface between the initial ambient and the stratified part of the ambient). The ambient buoyancy before reaching the first front is $\Delta_a = 0$, and there is a similarity solution

$$Q = \frac{3}{4} \left(\frac{4}{5}\right)^{1/3} Z^{4/3}, \quad M = \frac{3}{4} \left(\frac{4}{5}\right)^{2/3} Z^{5/3}, \quad \text{and} \quad F = Z. \quad (3.15)$$

(This similarity solution is a rescaled version of that found by Cooper and Hunt (2010).) By conservation of volume, the first front height Z_0 is given by

$$\frac{dZ_0}{dT} = -Q|_{Z_0, T}. \quad (3.16)$$

This equation may be integrated, together with $Z_0 = 1$ at $T = 0$, to give the first front height, as found by Cooper and Hunt (2010),

$$Z_0 = \left(1 + \frac{1}{4} \left(\frac{4}{5}\right)^{1/3} T\right)^{-3}. \quad (3.17)$$

After the plume reaches the first front height, we assume that the plume fluid peels and moves to its neutral buoyancy height. The dimensionless buoyancy in the plume varies from zero at the edge of the plume, where plume fluid peels, to the dimensionless maximum buoyancy in the plume,

$$\Delta_m = \frac{3F}{2Q} = 2 \left(\frac{4}{5}\right)^{-1/3} Z^{-1/3}. \quad (3.18)$$

Fluid of buoyancy Δ_i may only begin to peel and enter the stratified part of the tank when the dimensionless maximum buoyancy in the plume at the first front height, $\Delta_m(Z_0(T))$, is equal to Δ_i , i.e. when

$$2 \left(\frac{4}{5}\right)^{-1/3} + \frac{T}{2} = \Delta_i. \quad (3.19)$$

On rearranging this equation, we obtain the time at which fluid of buoyancy Δ_i begins to peel,

$$T_i = \begin{cases} 2\Delta_i - 4 \left(\frac{4}{5}\right)^{-1/3}, & \text{for } \Delta_i > 2 \left(\frac{4}{5}\right)^{-1/3} \\ 0, & \text{for } \Delta_i < 2 \left(\frac{4}{5}\right)^{-1/3}. \end{cases} \quad (3.20)$$

This peeling time is different from that found by Hogg et al. (2015), because the full wall source plume governing equations are different from their line source plume governing equations.

Fluid with dimensionless buoyancy Δ_i is located at a distance

$$x_i = b \left(1 - \frac{\Delta_i}{\Delta_m} \right) \quad (3.21)$$

from the wall. This expression was obtained by rearranging (3.13). Nondimensionalising using αH , the length scale in the x direction, the dimensionless plume width is

$$\frac{b}{\alpha H} = \frac{1}{\alpha H} \left(\frac{4q^2}{3m} \right) = \frac{4Q^2}{3M} = Z. \quad (3.22)$$

On substituting this expression for the dimensionless plume width into (3.21), we find that fluid with dimensionless buoyancy Δ_i is located at a dimensionless distance

$$X_i = \frac{x_i}{\alpha H} = Z \left(1 - \frac{\Delta_i}{\Delta_m} \right) \quad (3.23)$$

from the wall.

The dimensionless vertical velocity, calculated by using the similarity solutions (3.15) and definitions of q, m, f in (3.14), is

$$W = \begin{cases} \frac{3}{2} \left(\frac{4}{5} \right)^{1/3} Z^{1/3} \left(1 - \frac{X}{Z} \right), & X < Z \\ 0, & X > Z. \end{cases} \quad (3.24)$$

To find the volume flux $Q_i(\Delta_i, Z)$ in the plume of fluid with buoyancy greater than Δ_i , we integrate the vertical velocity (up to X_i),

$$Q_i(\Delta_i, Z) = \int_0^{X_i} W dX = \frac{3}{4} \left(\frac{4}{5} \right)^{1/3} Z^{4/3} \left(1 - \frac{1}{4} \left(\frac{4}{5} \right)^{2/3} Z^{2/3} \Delta_i^2 \right). \quad (3.25)$$

The depth at which fluid of buoyancy Δ_i is located is calculated by summing the volume of fluid of each buoyancy arriving at the stratified part of the tank:

$$Z_i(\Delta_i, T) = 1 - \int_{T_i}^T Q_i|_{Z_0} dT, \quad (3.26)$$

where T_i is given by (3.20). Fluid of buoyancy Δ_i is found to be at height

$$Z_i = \begin{cases} Z_0 + \frac{3}{20} \left(\frac{4}{5} \right)^{2/3} \Delta_i^2 \left(1 - Z_0^{5/3} \right), & \Delta_i < 2 \left(\frac{4}{5} \right)^{-1/3}, \\ 1 + Z_0 - \frac{3}{20} \left(\frac{4}{5} \right)^{2/3} Z_0^{5/3} \Delta_i^2 - \frac{4}{\Delta_i^3}, & \Delta_i > 2 \left(\frac{4}{5} \right)^{-1/3}. \end{cases} \quad (3.27)$$

Since the full wall plume governing equations are different from the line source plume governing equations used by Hogg et al. (2015), the heights Z_i , at which fluid of buoyancy Δ_i is found, are also different.

Unlike the line source considered by Hogg et al. (2015), with a full wall source, buoyancy is added by the source in the stratified part of the tank. At each height, we account for this extra buoyancy by adding the (as yet unattributed) buoyancy output by the source at that height to Δ_i . Since the first front passes height Z at $T = 4 \left(\frac{4}{5}\right)^{-1/3} \left(Z^{-1/3} - 1\right)$, the new buoyancy is

$$\Delta_i^{\text{new}} = \Delta_i^{\text{old}} + T - 4 \left(\frac{4}{5}\right)^{-1/3} \left(Z_i^{-1/3} - 1\right). \quad (3.28)$$

The distribution Z_i then gives the ambient stratification.

The theoretical profiles given by the peeling plume model, shown in figure 3.15, capture the shape of the ambient buoyancy profiles measured in experiments, whereas the Cooper and Hunt (2010) model, shown in figure 3.11, does not – the peeling plume model is better at capturing the behaviour near $Z = 0$. The agreement is not perfect, however. In particular, in experiments there is more dense fluid near $Z = 0$ than there is in the model. This difference is because, in the theoretical model, the extra buoyancy from the source is just added at each height. In practice, however, a plume will form at the lower sources and some of the extra buoyancy will be added to the ambient at a depth nearer to $Z = 0$.

We calculate the RMS error between the experimental and the peeling plume theoretical dimensionless ambient buoyancy profiles, shown in figure 3.16. The peeling model is shown by thick orange lines marked with circles, with the Cooper and Hunt (2010) one-way-entrainment model shown by thin grey lines marked with crosses. While at the two smaller flow rates, the peeling plume model with $\alpha = 0.018$ makes only a little difference to the RMS error (compared with the Cooper and Hunt (2010) one-way-entrainment model in figure 3.12), at the two larger flow rates, the RMS error is smaller at late times with the peeling plume model than with the Cooper and Hunt (2010) one-way-entrainment model.

To improve the agreement between the peeling plume model and experiments at smaller flow rates, we can use different values of the entrainment coefficient α for the different flow rates. To select the appropriate α , we compare, by considering the RMS error, the first front height predicted by theory (note that this height is the same for both the peeling plume model and the Cooper and Hunt (2010) one-way-entrainment model) with that measured in experiments, for a range of values of α . In the experiments, there is no sharp first front, rather it is continuous, so we use the height at which the ambient density reaches some value (the somewhat arbitrary value of 0.65 is used because, looking at the ambient density profiles, this marks out a plausible first front height). We select, for each flow rate, the α that

minimises the total RMS error for all experiments at that flow rate. This gives $\alpha = 0.011$ for experiments A_{full} to E_{full} , $\alpha = 0.011$ for experiments F_{full} to J_{full} , $\alpha = 0.018$ for experiments K_{full} to O_{full} , and $\alpha = 0.020$ for experiments P_{full} to T_{full} . The RMS error between theory and experiment using these values of α for both the peeling plume model and the Cooper and Hunt (2010) one-way-entrainment model is shown in figure 3.17. Whilst the difference between the peeling plume model and Cooper and Hunt (2010) one-way-entrainment model is small, the RMS error is now decreasing with time, so the model is getting better at larger times, rather than worse, as it was for the two lowest flow rates in figure 3.16. At the two larger flow rates, the peeling plume model still gives smaller RMS error at late times than the Cooper and Hunt (2010) one-way-entrainment model.

The agreement between the peeling plume model and experiments is better for larger flow rates than for smaller flow rates because the peeling plume model assumes variation in vertical velocity and in density across the width of the plume. This variation differs with source flow rate, as shown by the schematic in figure 3.18. For large source flow rates, source fluid is added with some velocity near the wall, whilst fluid is at rest in the ambient, so we expect variation in vertical velocity between these two extremes, across the width of the plume. For smaller flow rates, however, there is only a small variation in vertical velocity across the width of the plume, and so there can only be a small amount of peeling. Thus, the peeling plume model shows the best improvement over the Cooper and Hunt (2010) one-way-entrainment model at larger flow rates. The RMS error results, together with the better visual agreement between the profiles in figure 3.15, suggest that the peeling plume model is more appropriate than the Cooper and Hunt (2010) one-way-entrainment model for describing the dimensionless ambient buoyancy profiles that develop with a full wall source.

3.3.3 Half wall source

We extend the Cooper and Hunt (2010) one-way-entrainment model, presented in section 3.3.2, to a source distributed over only the upper part (in the experiments of section 3.2.4, the upper half) of a wall. In equation (3.10), $B(Z)$ is now given by

$$B(Z) = \begin{cases} 1, & \text{for } Z \leq Z_s \\ 0, & \text{for } Z > Z_s, \end{cases} \quad (3.29)$$

where Z_s is the nondimensional source height. For a half wall source, $Z_s = 0.5$. The remaining equations and boundary conditions are as in section 3.3.2. The timescale, $W\alpha^{-2/3}b_{s0}^{-1/3}H^{-1/3}$, is given in table 3.7 for each of the 20 half wall source experiments performed, and varies between approximately 2 and 5 minutes.

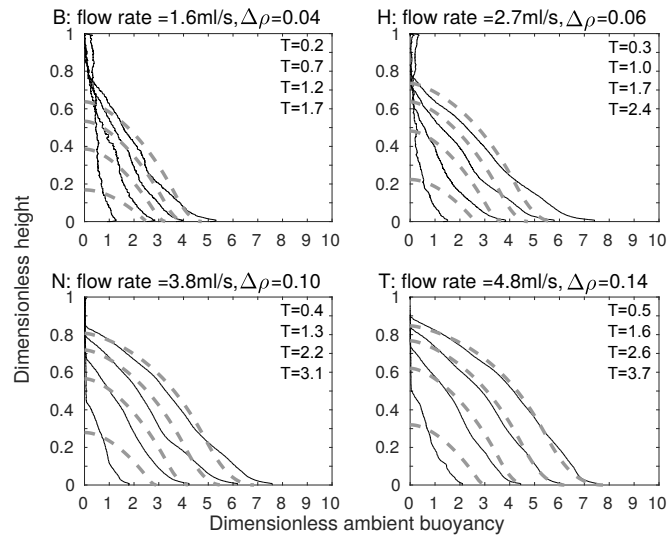


Fig. 3.15 Dimensionless ambient buoyancy profiles for full wall source experiments B_{full} , H_{full} , N_{full} , and T_{full} . Solid black lines show filtered experimental results, the dashed lines show the peeling plume model results with $\alpha = 0.018$. Each subplot shows profiles at times 120s, 360s, 600s, and 840s after starting. The corresponding dimensionless times are listed on each plot.

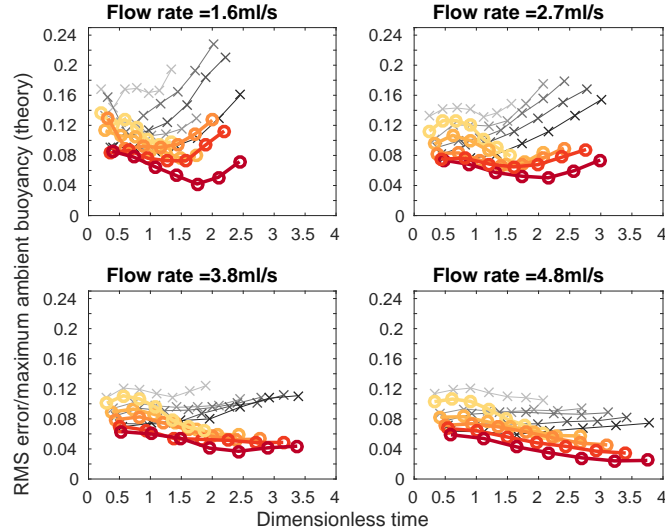


Fig. 3.16 RMS error between theoretical (peeling plume model shown by the thick orange lines marked with circles, and the Cooper and Hunt (2010) one-way-entrainment model shown by the thin grey lines marked with crosses, both models using $\alpha = 0.018$, which was chosen to give a low RMS error over all the experiments) and experimental dimensionless ambient buoyancy profiles, divided by the maximum theoretical dimensionless ambient buoyancy, against dimensionless time for each of the 20 full wall source experiments listed in table 3.3. Darker colours are experiments with larger source densities.

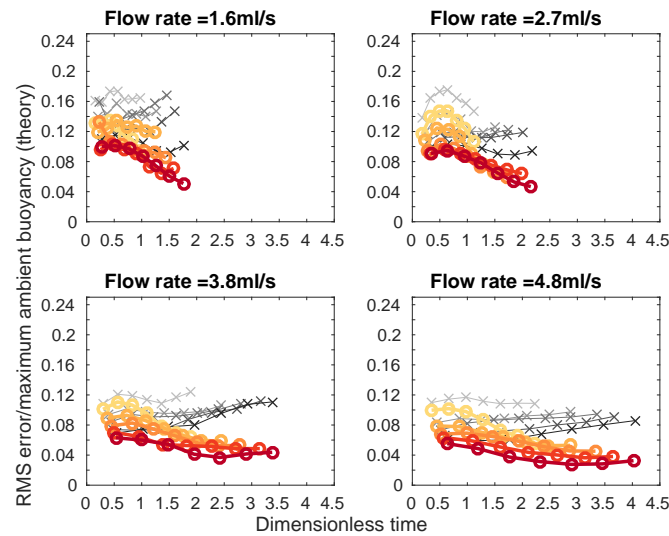


Fig. 3.17 RMS error between theoretical (peeling plume model shown in the thick orange lines marked with circles, and the Cooper and Hunt (2010) one-way-entrainment model shown in the thin grey lines marked with crosses) and experimental dimensionless ambient buoyancy profiles, divided by the maximum theoretical dimensionless ambient buoyancy, against dimensionless time for each of the 20 full wall source experiments listed in table 3.3. For a flow rate of 1.6ml/s, $\alpha = 0.011$, for a flow rate of 2.7ml/s, $\alpha = 0.011$, for a flow rate of 3.8ml/s, $\alpha = 0.018$, and for a flow rate of 4.8ml/s, $\alpha = 0.020$. Darker colours are experiments with larger source densities.

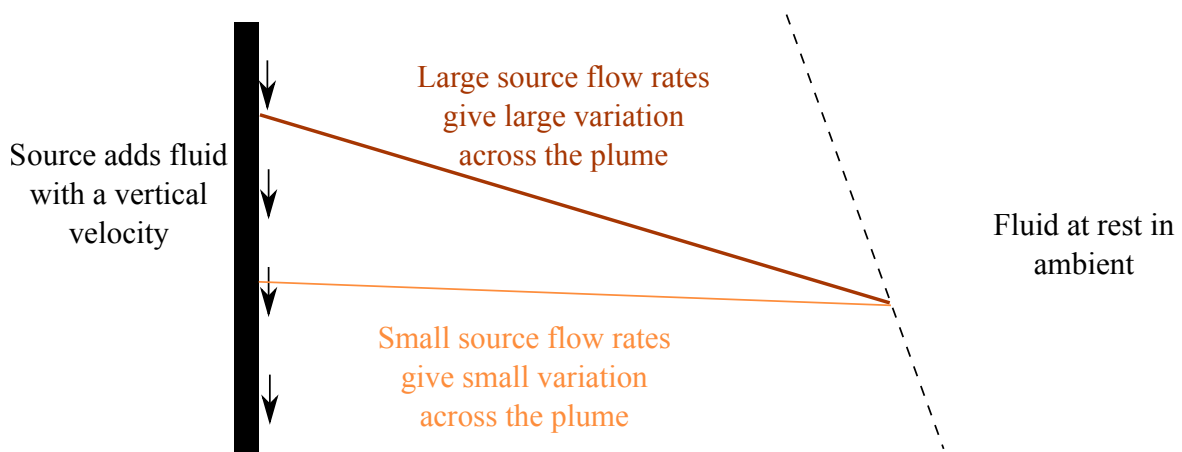


Fig. 3.18 Different source flow rates lead to different variations in vertical velocity across the width of the plume, leading to different amounts of peeling.

Experiment	A_{half}	B_{half}	C_{half}	D_{half}	E_{half}	F_{half}	G_{half}	H_{half}	I_{half}	J_{half}
Timescale(s)	270	248	207	174	164	221	200	160	152	136
Experiment	K_{half}	L_{half}	M_{half}	N_{half}	O_{half}	P_{half}	Q_{half}	R_{half}	S_{half}	T_{half}
Timescale(s)	195	171	143	126	120	187	162	142	118	110

Table 3.7 The timescales $W\alpha^{-2/3}b_{s0}^{-1/3}H^{-1/3}$ for the 20 half wall source experiments.

Comparing the model with experiments

In figure 3.19 we see that the extended Cooper and Hunt (2010) one-way-entrainment model captures the shape of the experimental profiles well. This agreement suggests that, for the half wall source, detrainment is unimportant. Indeed, detrainment was not observed in the experiments. A possible reason for this difference between a full wall source and a half wall source is that, with a half wall source, the plume is likely to be well mixed across its width (i.e. the plume buoyancy has a top hat profile across the plume), so the plume should not detrain. This is because, for a full wall source, dense fluid is added at the wall and less dense ambient fluid is entrained at the other side of the plume, so, as assumed in the peeling plume model of section 3.3.2, we expect the plume buoyancy profile to vary across the width of the plume. For the upper half of a half wall source, since the plume has had only a short distance over which to evolve, this change in density across the width of the plume is small. For the lower half of a half wall source, as for a line source, dense fluid is not being added at the wall, and we expect the plume to mix across its width and therefore to have only one-way-entrainment, with no detrainment.

As in the previous sections, we calculate the RMS error between the theoretical and experimental profiles, which is shown in figure 3.20. Whilst the RMS error is not as small as it was for the line source experiments in figure 3.9, it is still below 8% of the maximum theoretical dimensionless ambient buoyancy at late times for most experiments, which is small compared with the scatter in the experiments. This, together with the visual agreement between the profiles in figure 3.19, suggests that the extended Cooper and Hunt (2010) one-way-entrainment model is appropriate for the half wall source.

In this section, we have seen that detrainment is unimportant for a half wall source; an extension of the Cooper and Hunt (2010) model agrees with the experimental results.

3.4 Conclusions

Experimental results have shown that, unlike for a line source and a half wall source, detrainment is important for a full wall source. The existing models, which assume top

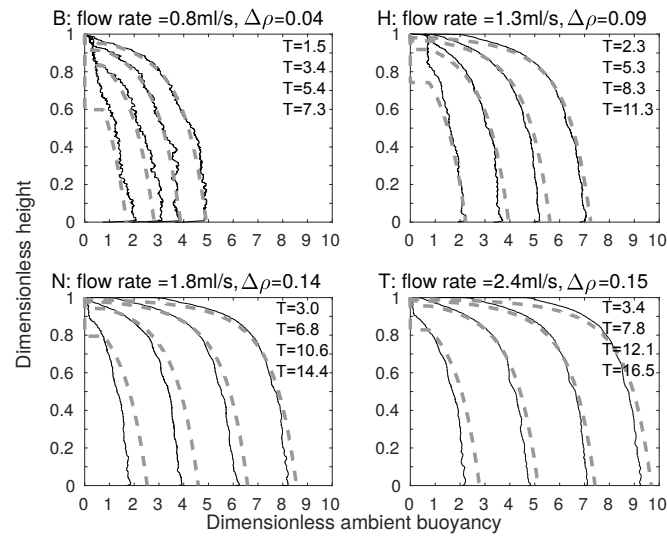


Fig. 3.19 Dimensionless ambient buoyancy profiles for half wall source experiments B_{half} , H_{half} , N_{half} , and T_{half} . Solid black lines show filtered experimental results, the dashed lines show the model results. Each subplot shows profiles at times 375s, 855s, 1335s, and 1815s after starting. The corresponding dimensionless times are listed on each plot.

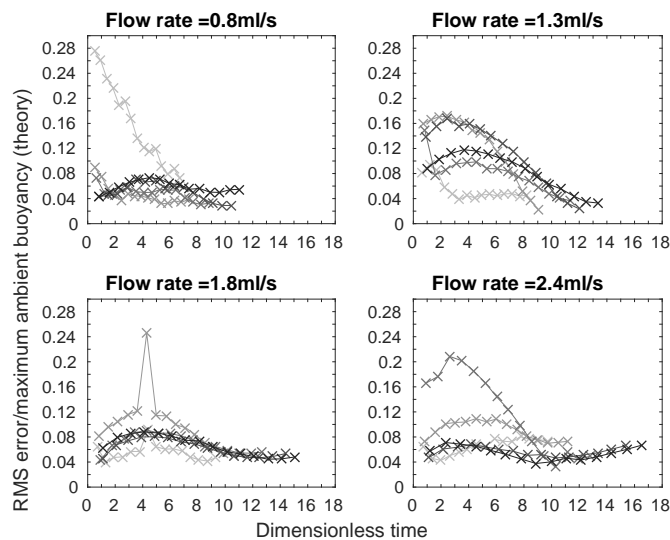


Fig. 3.20 RMS error between theoretical (extension of the Cooper and Hunt (2010) one-way-entrainment model) and experimental dimensionless ambient buoyancy profiles, divided by the maximum theoretical ambient buoyancy, against dimensionless time for each of the 20 half wall source experiments listed in table 3.4.

hat profiles for density and vertical velocity, ruling out the possibility of detrainment, are inadequate. The experimental results of section 3.2.3 show qualitatively different ambient buoyancy profiles from those predicted by one-way-entrainment models with top hat profiles. Instead, a peeling plume model, with linear profiles for density and vertical velocity across the width of the plume, is appropriate. Extending the peeling plume model of Hogg et al. (2015) to our situation gives a better explanation of the experimental results, capturing the shape of the dimensionless ambient buoyancy profiles more accurately. The peeling plume model is an oversimplification of what happens in experiments, however, as several discrete intrusions are observed in experiments (see figure 3.4), rather than intrusions occurring over the entire stratified region. This is potentially due to the discrete sources used in experiments, and, as such, the model is an oversimplification, but captures the physics better than one-way-entrainment models, which neglect the detrainment that is observed in experiments, do.

In experiments with a line source and with a half wall source, detrainment was not observed. The existing models, with top hat profiles for density and vertical velocity, agree with the experimental results. For the line source, the experiments agree with the Worster and Huppert (1983) line source model, confirming that approximating a distributed source using several individual sources is appropriate. For the half wall source, the experimental results agree with an extension, which allows the source to be spread over only part of the wall, of the Cooper and Hunt (2010) one-way-entrainment model. The agreement between this model and experiments suggests that detrainment is unimportant with a half wall source.

Through a series of experiments, we have observed that detrainment occurs with a vertically distributed full wall source. With such a source, a peeling plume model, with linear profiles for density and vertical velocity, is appropriate for describing the ambient buoyancy profiles. Detrainment and peeling should be included in models for full wall sources because such models give a qualitatively different ambient profile structure, which better captures profiles measured in experiments, than models with one-way-entrainment only.

Chapter 4

Time-varying vertically distributed buoyancy sources

4.1 Introduction

When PCM (phase change material) solidifies, it provides a time-varying source of buoyancy, and, when the PCM is contained in wallboard, this source is vertically distributed. Time-varying, vertically distributed buoyancy sources also appear as patches of wall heated by the sun, with the amount of sunlight varying over a day, for example. In this chapter, we seek to understand how time-varying, vertically distributed buoyancy sources affect the stratification that develops in a sealed space, and how the stratification differs from that produced by a constant buoyancy flux source.

Scase et al. (2006) extend the plume model of Morton et al. (1956) to a time-varying point source. They find that, following a decrease in source buoyancy flux, the plume has three regions: an upper region that behaves as a steady plume with the initial source buoyancy flux, a lower region that behaves as a steady plume with the final, lower source buoyancy flux, and, between the upper and lower regions, a transitional region, where the plume narrows. Scase and Hewitt (2012), however, find that the model of Scase et al. (2006) is ill-posed, and they introduce a velocity diffusion term to make the system of equations well-posed.

For unsteady plumes, Craske and van Reeuwijk (2016) find, guided by DNS (direct numerical simulation) of plumes with a step change in source buoyancy flux, that the form of the velocity profile across the plume (Gaussian or top-hat, for example) affects the response of the system. They develop a general framework for unsteady plumes which includes the previous, ill-posed models as degenerate cases in a large set of well-posed models. Three unsteady plume models, of varying complexity, are presented. The first model consists of

three coupled partial differential equations, and can be used for sources with independently-varying volume, momentum, and buoyancy fluxes. The second model is simpler, and consists of a single partial differential equation, derived by using the assumption that the plume is pure and straight-sided. The third model is a similarity solution that applies only for small changes in buoyancy flux (they consider a small step change in source buoyancy flux), and is valid far from the source. In each of the models, they assume that, in steady state, there is a Gaussian velocity profile across the plume.

In this chapter, in section 4.2, results from experiments with time-varying buoyancy sources are presented. Three types of time-varying, vertically distributed source are used: linear “ramps down” in source buoyancy flux, linear “ramps up” in source buoyancy flux, and a source buoyancy flux that mimics the solidification of PCM. In section 4.3 two theoretical models are presented: a top-hat plume model, with one-way-entrainment, and a peeling plume model, with both entrainment and detrainment. We compare the experiments with theory in section 4.4, and apply the theoretical model in section 4.5, determining a minimum wall thickness for a PCM wall to be effective, before drawing conclusions in section 4.6.

4.2 Experiments

4.2.1 Setup

The experimental setup is as in chapter 3; a tank filled with fresh water forms the ambient, and salt water pumped into the tank through tubes that are spread over one wall of the tank forms the source. Figure 4.1 (a copy of figure 3.1 but without the line source indicated) shows this experimental setup. The tank is 0.487m tall, and is filled with fresh water to approximately 0.3m. A source covers one wall of the tank, and this wall is 0.198m wide, with the wall perpendicular to the source being 0.495m wide. The source is made up of 6 tubes that run through the pumpheads of two Watson Marlow 520Du peristaltic pumps with 505L and 505LX pumpheads. These tubes are then split into two, giving a total of 12 tubes that make up the source. The ends of these tubes are covered with a fine mesh fabric, to ensure that the fluid leaving the source is turbulent, and the tubes are then attached to the wall of the tank, as shown in the right hand photograph in figure 4.1.

To provide a time-varying source, the flow rate from the pumps is adjusted over the course of an experiment. This change in flow rate is achieved by sending appropriate commands to the pumps, using MATLAB, over RS232 (a serial communication standard). The flow rate is decreased (for a “ramp down”) or increased (for a “ramp up”) every few seconds, as listed in table 4.1, by 0.1rpm (revolutions per minute), corresponding to a change in flow rate of

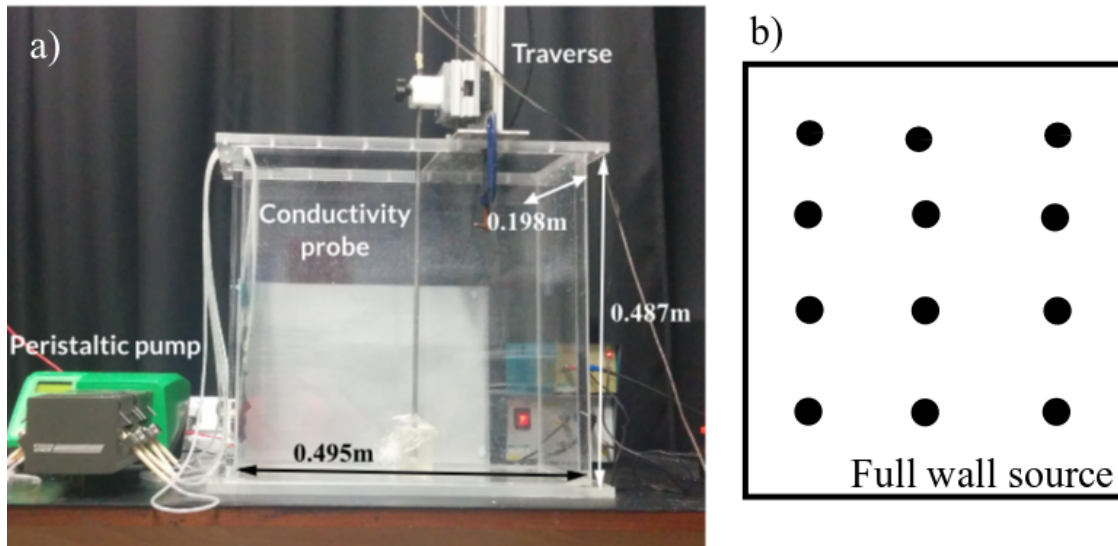


Fig. 4.1 The experimental setup (left), including details of the source (right).

Ramp	Initial flow rate (ml/s)	Seconds between decreases	Decrease in flow rate ($\times 10^{-3}$ ml/s ²)
Ramp 1	3.7	5	2.1
Ramp 2	6.3	3	3.5
Ramp 3	9.5	2	5.3

Table 4.1 The three ramps used for the “ramp down” experiments. The “ramp up” experiments start from zero flow rate and reach the values listed in the “Initial flow rate” column of the table after 30 minutes, so the magnitude of the slope of the ramp is the same as for the “ramp down” experiments, but with the opposite sign.

approximately 0.01ml/s, with an experiment lasting 30 minutes. Three different slopes of ramp are used for both the “ramp down” and the “ramp up” experiments, and these ramps are listed in table 4.1.

A conductivity probe is traversed vertically through the tank over a height of 0.25m (in the rest of this chapter, “tank height” refers to this height) to measure the stratification. The stratification is measured every 2 minutes. Dye is added to the source fluid (with different colours used at different times through the experiment) to visualise the flow, and to test for detrainment. When the plume detrains, dyed fluid exits the plume and enters the ambient at an intermediate height.

For each source type, 12 different experiments are carried out. These experiments use four different source densities and 3 different ramp slopes (the ramp slopes are listed in table 4.1). The source densities and ramps for each experiment are listed in table 4.2, and the corresponding maximum source buoyancy fluxes are listed in table 4.3. Note that the maximum source buoyancy flux occurs at the start of the “ramp down” experiments and

Experiment	Ramp	Dimensionless source density difference $\Delta\rho$	
		“Ramp down”	“Ramp up”
<i>A</i>	Ramp 1	0.07	0.05
<i>B</i>	Ramp 1	0.12	0.10
<i>C</i>	Ramp 1	0.16	0.16
<i>D</i>	Ramp 1	0.19	0.20
<i>E</i>	Ramp 2	0.06	0.06
<i>F</i>	Ramp 2	0.10	0.09
<i>G</i>	Ramp 2	0.14	0.14
<i>H</i>	Ramp 2	0.19	0.19
<i>I</i>	Ramp 3	0.06	0.06
<i>J</i>	Ramp 3	0.10	0.11
<i>K</i>	Ramp 3	0.14	0.13
<i>L</i>	Ramp 3	0.19	0.18

Table 4.2 The ramp and dimensionless source density difference for each of the 12 “ramp down” experiments and each of the 12 “ramp up” experiments.

at the end of the “ramp up” experiments. The dimensionless source density difference is $\Delta\rho = (\text{source density} - \text{ambient density})/\text{ambient density}$. The timescales for each of the experiments, $W\alpha^{-2/3}b_{s0\max}^{-1/3}H^{-1/3}$, where W is the tank width, α is the entrainment coefficient (listed in table 4.6 for the “ramp down” experiments and in table 4.7 for the “ramp up” experiments), $b_{s0\max}$ is the maximum source buoyancy flux per unit source area, and H is the tank height, are listed in table 4.4.

4.2.2 Selecting a source buoyancy flux that mimics the solidification of PCM

Together with the “ramp down” and “ramp up” experiments, experiments that mimic the solidification of PCM are also carried out. When the PCM solidifies, changing from liquid to solid, heat is released, so the PCM acts as a buoyancy source. When PCM is incorporated into wallboard, for example, PCM solidifying produces a time-varying, vertically distributed buoyancy source.

Measurements of PCM properties suggest that, outside of the PCM melting/solidifying range, a linear “ramp down” in source buoyancy flux is appropriate. These measurements, taken by Xie et al. (2013), Günther et al. (2006), Rady and Arquis (2010), and Kuznik et al. (2011), use the T-history method, where a sample and a reference are heated, and their temperature differences from the surroundings are measured. The measurements show that, outside of the melting/solidifying range, the temperature of a fully melted PCM being cooled

Experiment	Maximum source buoyancy flux ($\times 10^{-6} \text{m}^2 \text{s}^{-3}$)	
	“Ramp down”	“Ramp up”
<i>A</i>	52	34
<i>B</i>	89	73
<i>C</i>	115	116
<i>D</i>	136	149
<i>E</i>	78	78
<i>F</i>	123	118
<i>G</i>	179	170
<i>H</i>	243	232
<i>I</i>	122	118
<i>J</i>	188	202
<i>K</i>	259	243
<i>L</i>	354	345

Table 4.3 The maximum source buoyancy flux for each of the 12 “ramp down” experiments and each of the 12 “ramp up” experiments. Source buoyancy flux is $g\Delta\rho$ multiplied by the source flow rate, divided by the source area.

Experiment	Timescale (s)		
	“Ramp down”	“Ramp up”	
		One-way-entrainment	Peeling
<i>A</i>	454	609	459
<i>B</i>	379	404	359
<i>C</i>	404	348	308
<i>D</i>	382	449	371
<i>E</i>	317	396	351
<i>F</i>	272	400	344
<i>G</i>	266	355	306
<i>H</i>	240	320	276
<i>I</i>	231	401	306
<i>J</i>	216	289	256
<i>K</i>	212	271	241
<i>L</i>	212	241	214

Table 4.4 The timescale $W\alpha^{-2/3}b_{s0\max}^{-1/3}H^{-1/3}$ for each “ramp down” and “ramp up” experiment. Since the one-way-entrainment and peeling plume models have different values of α that minimise total RMS error, timescales calculated using both values of α are listed.

decreases linearly with time. Calling the temperature of the PCM (which varies as the PCM cools and solidifies) θ_{PCM} , we take the source buoyancy flux to be

$$\frac{g\beta}{\rho_{air}C_{air}}h(\theta_{PCM} - \theta_1), \quad (4.1)$$

where g is gravitational acceleration, ρ_{air} is the density of air, C_{air} is the specific heat capacity of air, β is the thermal expansion coefficient, h is the convection coefficient, and θ_1 is the room temperature (assumed constant). Since PCM temperatures decrease linearly with time, outside of the solidifying range, so too does the source buoyancy flux.

The solidifying range is narrow, we assume, compared with the change from the initial temperature down to the solidifying range, so we assume that the PCM solidifies at a single temperature, the maximum temperature θ_{max} in the solidifying range. When the PCM is solidifying, then, there is a constant source buoyancy flux, as the PCM temperature is constant. To mimic the solidification of PCM, we use a source buoyancy flux that “ramps down” in time, then is constant for some period of time, and finally “ramps down” in time again (potentially with a different slope from the first “ramp down” section, as found by Günther et al. (2006) and Rady and Arquis (2010)). An example of such a source buoyancy flux is shown in figure 4.2. In the figure, the times marked on the x-axis are the time t_{r1} over which the first ramp occurs, the time t_s that the source buoyancy flux is constant for (while the PCM is solidifying), and the time t_{r2} over which the second ramp occurs. The other labels indicate the initial source buoyancy flux b_{s0} , which includes the initial PCM temperature θ_{start} , and the constant buoyancy flux b_{s1} . This form of source buoyancy flux is written as

$$b_s = \begin{cases} b_{s0} \left(\frac{t_{r1} - \left(1 - \frac{b_{s1}}{b_{s0}}\right)t}{t_{r1}} \right), & t \leq t_{r1}, \\ b_{s1}, & t_{r1} < t \leq t_{r1} + t_s, \\ b_{s1} \left(\frac{t_{r1} + t_s + t_{r2} - t}{t_{r2}} \right), & t_{r1} + t_s < t \leq t_{r1} + t_s + t_{r2}. \end{cases} \quad (4.2)$$

To calculate the solidification time t_s , when the PCM is solidifying, and the source buoyancy flux is constant, we equate the energy transferred across the wall’s surface in the solidification time with the energy required to solidify the PCM. Equating these energies gives

$$h(\theta_{max} - \theta_1)t_s = \rho l_{pcm} \phi L, \quad (4.3)$$

where h is the convection coefficient, t_s is the solidification time, ρ is the thermal mass density, l_{pcm} is the thickness of the PCM thermal mass, ϕ is the PCM mass fraction (mass of PCM/mass of wall), and L is the latent heat. Rearranging this equation, we find that the

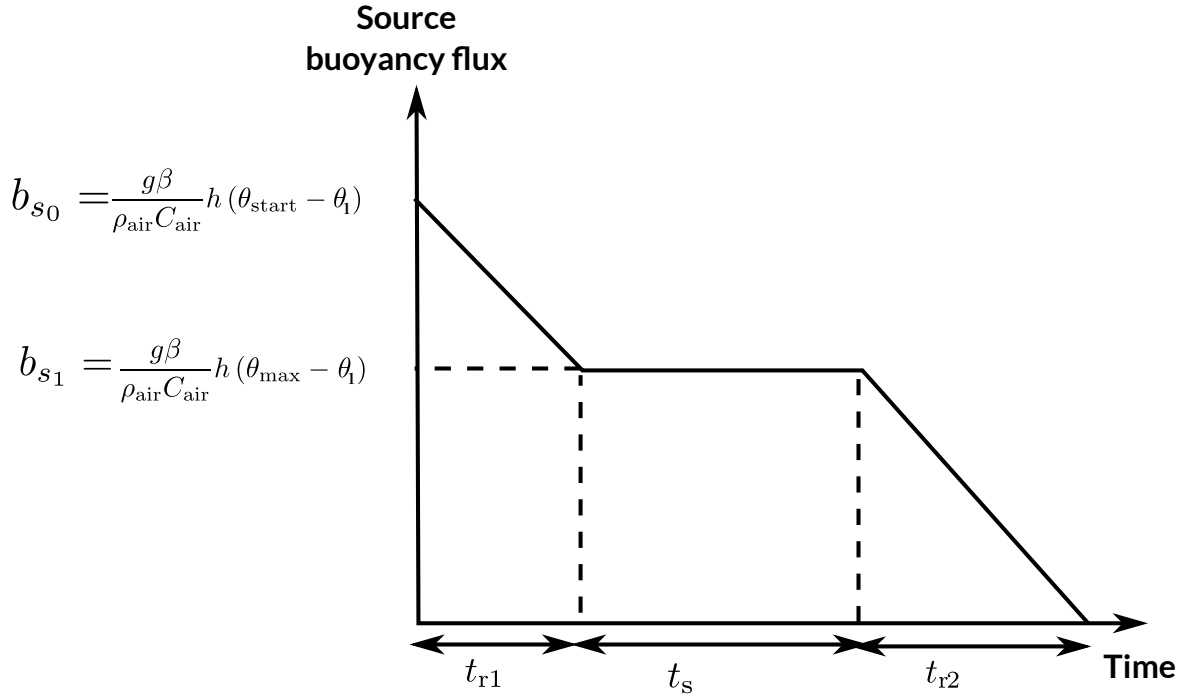


Fig. 4.2 The form of source buoyancy flux that mimics the solidification of PCM.

solidification time is

$$t_s = \frac{\rho l_{\text{pcm}} \phi L}{h(\theta_{\text{max}} - \theta_1)}. \quad (4.4)$$

Similarly, we find the time t_{r1} over which the PCM decreases from temperature θ_{start} to temperature θ_{max} (and the time t_{r2} over which the PCM decreases from temperature θ_{max} , after the PCM has solidified completely, to θ_1) by equating the energy transferred across the wall's surface in time t_{r1} with that released by the PCM during the time t_{r1} (during this time, only the sensible heat, rather than the latent heat, is relevant). Equating these two energies gives

$$\int_{t=0}^{t=t_{r1}} h(\theta - \theta_1) dt = \frac{\rho l_{\text{pcm}} C (\theta_{\text{start}} - \theta_{\text{max}})}{t_{r1}}, \quad (4.5)$$

where C is the specific heat capacity of the thermal mass. Since we are assuming a linear ramp in PCM temperature (see figure 4.2), for $0 \leq t \leq t_{r1}$, we write

$$h(\theta - \theta_1) = \frac{-h(\theta_{\text{start}} - \theta_{\text{max}})}{t_{r1}}t + h(\theta_{\text{start}} - \theta_1). \quad (4.6)$$

Substituting this expression into equation (4.5), then calculating the integral and rearranging, we find that

$$t_{r1} = \frac{\rho l_{\text{pcm}} C (\theta_{\text{start}} - \theta_{\text{max}})}{\frac{1}{2}h((\theta_{\text{start}} - \theta_1) + (\theta_{\text{max}} - \theta_1))}, \quad (4.7)$$

Quantity	Meaning	Value	Units
g	gravitational acceleration	10	ms^{-2}
h	convection coefficient	7	$\text{Wm}^{-2}\text{K}^{-1}$
β	thermal expansion coefficient	3.43×10^{-3}	K^{-1}
θ_{start}	starting temperature	26	$^{\circ}\text{C}$
θ_1	room temperature	20	$^{\circ}\text{C}$
θ_{max}	melting temperature	23	$^{\circ}\text{C}$
ρ	thermal mass density	880	kg m^{-3}
l_{pcm}	thermal mass thickness	0.0125	m
ϕL	latent heat in thermal mass	18182	J kg^{-1}
C	specific heat capacity	1182	$\text{J kg}^{-1} \text{K}^{-1}$
ρ_{air}	density of air	1.205	kg m^{-3}
C_{air}	specific heat capacity of air	1005	$\text{J kg}^{-1} \text{K}^{-1}$

Table 4.5 Parameter values for Knauf Comfortboard. Convection coefficient from Richardson and Woods (2008); thermal expansion coefficient, density of air, specific heat capacity of air from The Engineering ToolBox, and melting temperature, thermal mass density, thermal mass thickness, and latent heat from Knauf (2014).

and, similarly, that

$$t_{r2} = \frac{\rho l_{\text{pcm}} C}{\frac{1}{2}h}. \quad (4.8)$$

To ensure that our experiments are relevant to real PCM, we calculate the times and source buoyancy fluxes for two layers of Knauf Comfortboard, as used in the real life data collection described in appendix A. The appropriate parameter values are listed in table 4.5. Using the values from table 4.5, we find the following source buoyancy flux values between which the source ramps (as shown in figure 4.2):

$$\frac{g\beta}{\rho_{\text{air}}C_{\text{air}}}h(\theta_{\text{start}} - \theta_1) = 0.0012 \text{ m}^2\text{s}^{-3}, \quad (4.9)$$

and

$$\frac{g\beta}{\rho_{\text{air}}C_{\text{air}}}h(\theta_{\text{max}} - \theta_1) = 0.0006 \text{ m}^2\text{s}^{-3}. \quad (4.10)$$

The relevant times are

$$t_{r1} = 1238\text{s (about 20 minutes)}, \quad (4.11)$$

$$t_s = 9524\text{s (about 2 hours 40 minutes)}, \quad (4.12)$$

$$t_{r2} = 3715\text{s (about 1 hour)}, \quad (4.13)$$

For an analogue laboratory experiment, the Reynolds number UL/ν should be the same in the full scale room and in the lab scale experiment, which allows the ratio of source buoyancy flux in the full scale room to the source buoyancy flux for the analogue experiment to be found. We take U to be the plume vertical velocity, which scales as the scale for plume momentum flux m over the scale for plume volume flux q , which is (see scalings in chapter 3) $\alpha^{-1/3} b_{s_0}^{1/3} L^{1/3}$, where $L = 2.5\text{m}$, the height of the room, and T_{room} is a timescale associated with the full scale room. The kinematic viscosity ν is that of air, $15.11 \times 10^{-6} \text{m}^2 \text{s}^{-1}$ (The Engineering ToolBox). For the analogue experiments, $L = 0.3\text{m}$, the depth up to which the tank is filled, and $\nu = 1 \times 10^{-6}$ for water (The Engineering ToolBox). Equating these two Reynolds numbers gives the ratio of source buoyancy flux scales,

$$\frac{b_{s_{0\text{lab}}}}{b_{s_{0\text{room}}}} = 1.4. \quad (4.14)$$

The ratio of timescales between the full scale room and the analogue experiment is also required. From the scalings in chapter 3, the timescales are $W \alpha^{-2/3} b_{s_0}^{-1/3} H^{-1/3}$, where W is the room width, perpendicular to the source, b_{s_0} is the initial source buoyancy flux per unit area, and H is the room height. Knowing the ratio of source buoyancy fluxes, we find the ratio of timescales, using $W_{\text{lab}} = 0.5\text{m}$, $H_{\text{lab}} = 0.3\text{m}$, $W_{\text{room}} = 4\text{m}$, and $H_{\text{room}} = 2.5\text{m}$, which yields

$$\frac{T_{\text{lab}}}{T_{\text{room}}} = 0.23. \quad (4.15)$$

To find the appropriate source buoyancy fluxes and times for the analogue experiments, we multiply the source buoyancy fluxes from the full scale room by 1.4, and multiply times from the full scale room by 0.23. This scaling of source buoyancy fluxes and times gives a starting source buoyancy flux of $0.00168 \text{m}^2 \text{s}^{-3}$. In the analogue experiments, we obtain

$$b_s = \frac{g \frac{\rho_{\text{source}} - \rho_0}{\rho_0} \text{source flow rate}}{\text{source area}}. \quad (4.16)$$

The source buoyancy flux corresponds to, using a source density of $\rho_{\text{source}} = 1.14 \text{g cm}^{-3}$ (saturated salt water) and a reference density $\rho_0 = 1 \text{g cm}^{-3}$, a source flow rate of 8.8ml/s . To mimic PCM wallboard solidifying, the source flow rate is “ramped down” from 80rpm (8.5ml/s) to 40rpm (4.1ml/s) over 4 minutes, then kept at 40rpm for 36 minutes, then “ramped down” from 40rpm to 0rpm over 14 minutes. In the experiments, the dimensionless density difference is $\Delta\rho = 0.20$, which gives a source buoyancy flux of $331 \times 10^{-6} \text{m}^2 \text{s}^{-3}$. The entrainment coefficient used is $\alpha = 0.012$, which gives a timescale $W \alpha^{-2/3} b_{s_0}^{-1/3} H^{-1/3}$ of 217s .

4.2.3 Results: “ramp down” in source buoyancy flux

Results from a representative experiment with a “ramp down” in source buoyancy flux (experiment G_{down}) are shown in figure 4.3. Each subplot shows both the original data (grey) and the filtered (using a median filter) data (black solid line), with each subplot showing a different time during the experiment. The scatter in the data is over approximately 0.5 dimensionless ambient buoyancy units, compared with a maximum dimensionless ambient buoyancy of just over 5, giving an error of approximately 10%. Comparing with the constant flux profiles in figure 3.3, we see that, towards the bottom of the tank, the profile is roughly linear with both a “ramp down” and a constant flux source. At the very bottom of the tank, however, the constant flux experiments have a large change in curvature, a “flick”, where dimensionless ambient buoyancy increases rapidly over a short distance, whereas this change in curvature is absent in the “ramp down” experiments. This lack of a large change in curvature is consistent with a source whose strength is decreasing in time, since at later times there is less buoyancy to add, including at the bottom of the tank where the change in curvature occurs in the constant flux experiments. Having less buoyancy to add means that there is only a small increase in dimensionless ambient buoyancy (compared with the rest of the tank) at the bottom of the tank, and thus a much smaller change in curvature in the profile. In addition, just below the first front at later times, the profiles from the “ramp down” experiments have a kink, where the profile starts to flatten out before reaching the linear section. This kink is different from the constant flux experiments, where the profiles, rather than flattening out at an intermediate height, get steeper with decreasing dimensionless height (after passing the first front) until reaching the linear section and the large change in curvature near the bottom of the tank. We conclude that the constant flux and the “ramp down” sources give different ambient buoyancy profiles.

In the “ramp down” experiments, as shown in figure 4.4, we observe plume fluid detrainment into the ambient at a range of heights. This detrainment continues throughout the experiment: the photograph to the left of figure 4.4 shows the experiment 11 minutes after starting, and the photograph to the right of figure 4.4 shows the experiment 22 minutes after starting, with plume fluid intruding into the ambient at intermediate heights in both photographs. In the false-colour photographs, orange fluid (the fluid was dyed green in the experiments, but the photographs are false colour to improve the contrast) intrudes into the ambient in the left hand photograph, and in the later right hand photograph, these intrusions have extended farther horizontally into the ambient. Similar behaviour was seen in the other 11 “ramp down” experiments, with the plume detrainment over approximately the same range of heights in the 12 experiments, as seen in figure 4.5, where both experiment E_{down} and experiment J_{down} are shown.

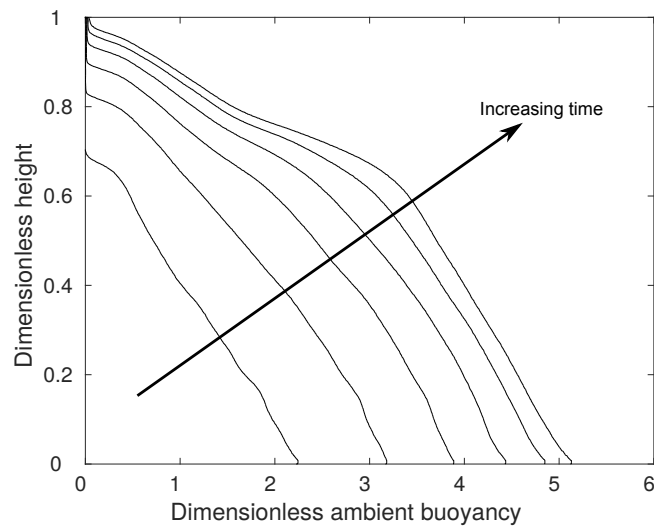


Fig. 4.3 Dimensionless ambient buoyancy profiles (median filtered data) for “ramp down” experiment G_{down} (which has an initial flow rate of 6.3ml/s and a dimensionless density difference $\Delta\rho = 0.14$). The six subplots show the experimental results at six different times: 235s, 475s, 715s, 955s, 1195s, and 1435s after starting, which correspond to dimensionless times of 0.9, 1.8, 2.7, 3.6, 4.5, and 5.4. A value of $\alpha = 0.012$ is used, consistent with table 4.6.

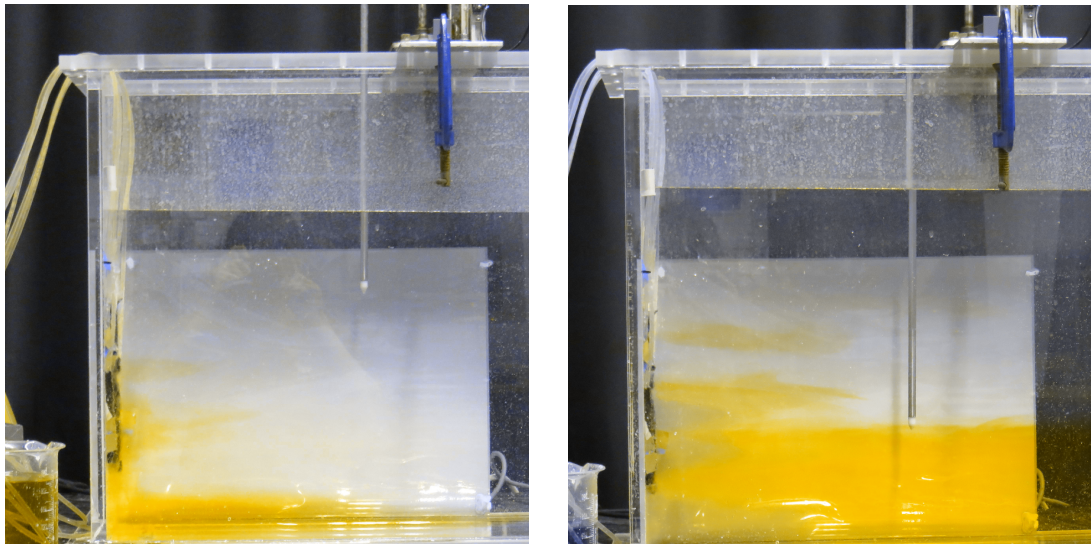


Fig. 4.4 False colour (enabling the intrusions to be more clearly seen) photographs of experiment J_{down} , taken 11 minutes (left) and 22 minutes (right) after the start of the experiment, showing dyed plume fluid (left: orange, right: blue) intruding into the ambient (left: undyed but stratified, right: orange at the bottom of the tank, undyed above) at several intermediate heights.

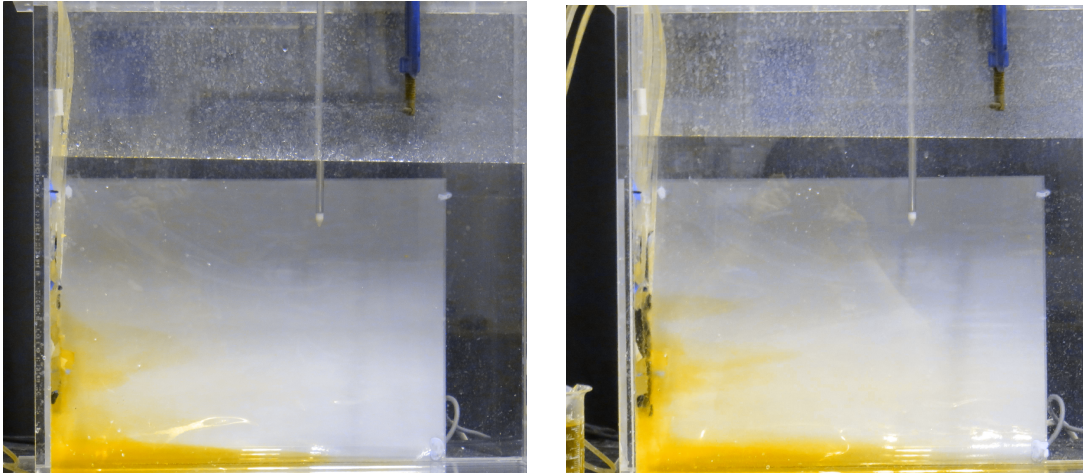


Fig. 4.5 False colour (enabling the intrusions to be more clearly seen) photographs of experiments E_{down} (left, taken at 11 minutes 40s after the start of the experiment) and J_{down} (right, taken at 11 minutes after the start of the experiment). In both photographs, plume fluid (orange) intrudes into the ambient over approximately the same range of heights.

4.2.4 Results: “ramp up” in source buoyancy flux

Results from a representative experiment with a “ramp up” in source buoyancy flux (experiment G_{up}) are shown in figure 4.6. Each subplot shows both the original data (grey) and the filtered (using a median filter) data (black solid line), with each subplot showing a different time through the experiment. Comparing the profiles in figure 4.6 with the constant flux profiles in figure 3.3, again we see that, at the very bottom of the tank, the constant flux experiments have a large “flick”, a change in curvature where dimensionless ambient buoyancy increases rapidly over a short distance, which is absent in the “ramp up” experiments. This lack of a “flick”, however, is inconsistent with a source whose strength is increasing in time, since, at later times, more buoyancy is available to be added to the ambient, including at the bottom of the tank where the “flick” occurs in the constant flux experiments, so we expect the “flick” to be larger, as more buoyancy is added there. A one-way-entrainment model, which gives profiles without a large change in curvature at the bottom of the tank, may be more appropriate than a peeling plume model. In section 4.4.2 we see that it is indeed the case that a one-way-entrainment model is more appropriate than a peeling plume model.

The difference between the constant flux, peeling plume theory profiles and the experimental profiles from the “ramp up” experiments suggests that, for a source that “ramps up” in time, a peeling plume model may be inappropriate, suggesting that detrainment (which nevertheless does still happen, as shown in figure 4.7) is less important than other physical processes, such as entrainment. Physically, it is plausible that entrainment remains important, since a source whose strength is ramping up in time produces an ever stronger plume that

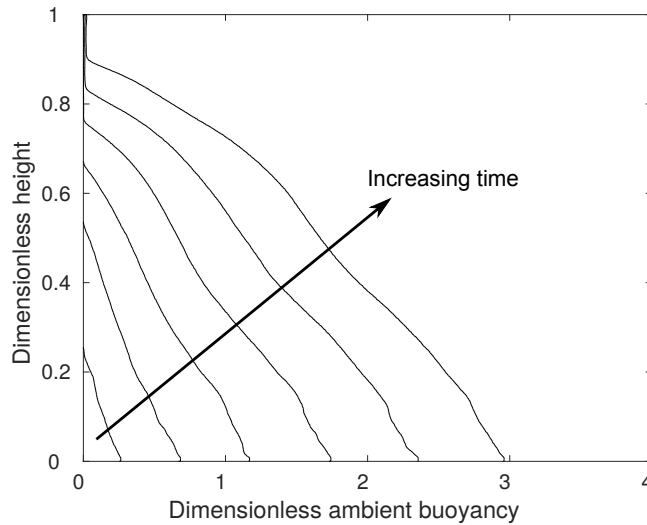


Fig. 4.6 Dimensionless ambient buoyancy profiles (median filtered data) for “ramp up” experiment G_{up} (which has an initial flow rate of 6.3ml/s and a dimensionless density difference $\Delta\rho = 0.14$). The six subplots show the experimental results at six different times: 235s, 475s, 715s, 955s, 1195s, and 1435s after starting, corresponding to dimensionless times of 0.7, 1.3, 2.0, 2.7, 3.4, and 4.0 (using the value of α for the one-way-entrainment model, $\alpha = 0.008$, from table 4.7). Note that, unlike the constant flux experiments of chapter 3, there is no “flick” – a large change in curvature – near dimensionless height 0.

is more able to “punch through” the ambient stratification to the very bottom of the tank, with little detrainment occurring as the plume descends. In addition, since the plume is driven by an increasingly large source buoyancy flux, it has a large vertical velocity, and remains turbulent when the first front has risen a significant distance through the tank. For a turbulent plume, entrainment is important, so entrainment in the stratified region below the first front remains important. The peeling plume model specifically neglects this entrainment.

In addition to both the “ramp down” and the “ramp up” experiments being different from the constant flux experiments, they are also different from each other. At later times, the part of the profile just below the first front has a significantly different shape (in the sense that the curvature is different) in the “ramp down” experiments compared with the “ramp up” experiments. This difference in shape is discussed further in section 4.4.1. Looking at the experimental results, we conclude that “ramp down”, sources that “ramp up”, and constant flux sources all give different ambient buoyancy profiles.

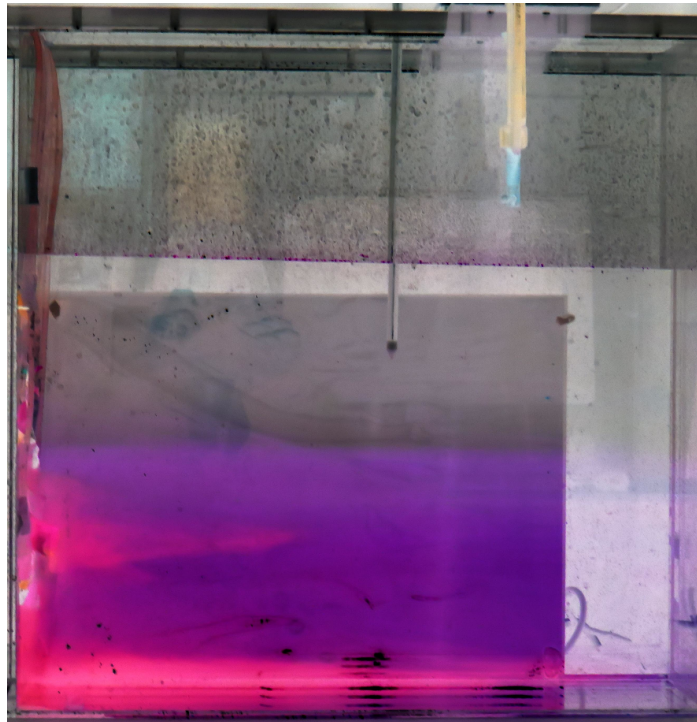


Fig. 4.7 A (false colour, to enable the intrusions to be clearly seen) photograph of experiment K_{up} , taken 21 minutes after the start of the experiment, showing dyed plume fluid (pink) detraining, that is, intruding into the ambient (purple at the bottom of the tank, and grey above that) at intermediate heights.

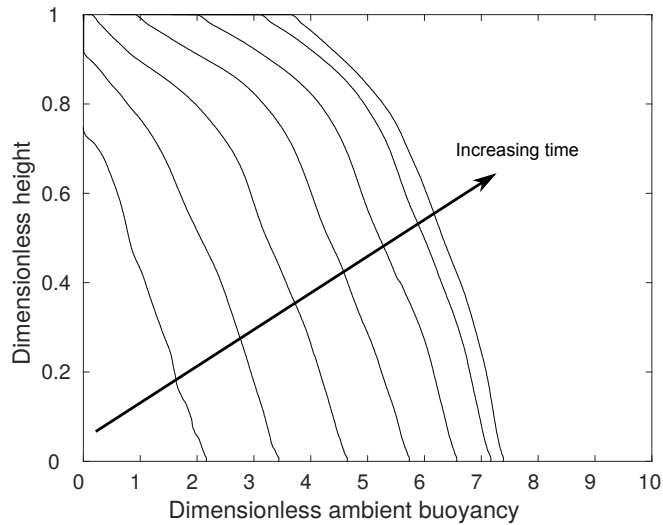


Fig. 4.8 Dimensionless ambient buoyancy profiles (median filtered data) for a PCM mimicking experiment, with the source buoyancy flux as described in section 4.2.2. The four subplots show the experimental results at four different times: 235s, 715s, 1195s, and 1675s after starting, which, when nondimensionalising by the timescale $\tau = 217s$, correspond to 1.1, 3.3, 5.5, 7.7, 9.9, 12.1, and 14.4.

4.2.5 Results: source buoyancy flux that mimics the solidification of PCM

Results from an experiment with a source buoyancy flux that mimics the solidification of PCM are shown in figure 4.8. Each subplot shows both the original data (grey) and the filtered (using a median filter) data (black solid line), with each subplot showing a different time through the experiment. The first front reaches the top of the tank after only a short time (between $715s=3.3\tau$ and $1195s=5.5\tau$). After that time, the shape of the profile only changes a little, and it is simply translated to the right, as more buoyancy is added from the source.

4.3 Theory

4.3.1 Top-hat plume with a vertically distributed, time varying source

To obtain the governing equations for a plume from a vertically distributed, time-varying source, we follow the approach of Scase et al. (2006) who considered a time-varying point source, together with the modification proposed by Scase and Hewitt (2012) to avoid the equations being ill-posed. We extend their work to, first, a 2D line source, and then to a

vertically distributed source (we assume that the problem is 2D). The starting point is the set of assumptions made by Morton et al. (1956), namely that profiles (across the width of the plume) of vertical velocity and buoyancy are self-similar with height (we take them to be top-hat profiles), that the plume entrains ambient fluid at a rate proportional, via an entrainment coefficient α , to the characteristic vertical velocity in the plume, and that changes in density are small compared with a reference density (the Boussinesq approximation).

To find an equation for plume volume flux, we begin with the equation for conservation of volume,

$$\frac{\partial u}{\partial x} + \frac{\partial w}{\partial z} = \frac{\alpha w}{b}, \quad (4.17)$$

where the x -direction is perpendicular to the vertical source, the z -direction is parallel to the vertical source, u is plume velocity in x -direction, w is plume velocity in z -direction (assumed constant across x -width of plume, i.e. a top-hat profile), b is the plume width, and α is the entrainment coefficient. Conservation of mass is given by

$$\frac{D\rho}{Dt} = \frac{(\rho_a - \rho)\alpha w}{b}, \quad (4.18)$$

where $\rho(z)$ is the plume density and $\rho_a(z, t)$ is the ambient density. Combining equations (4.17) and (4.18) gives

$$\frac{\partial \rho}{\partial t} + \frac{\partial}{\partial x}(\rho u) + \frac{\partial}{\partial z}(\rho w) = \frac{\rho_a \alpha w}{b}. \quad (4.19)$$

Integrating equation (4.19) over $[0, b]$ gives, for a top-hat plume,

$$\frac{\partial}{\partial t}(\rho b) - \rho \frac{\partial b}{\partial t} + \rho u|_{b^-} + \frac{\partial}{\partial z}(\rho w b) - \rho w \frac{\partial b}{\partial z} = \rho_a \alpha w. \quad (4.20)$$

At the edge of the plume, there is a kinematic boundary condition

$$u|_{x=b^-} = \frac{\partial b}{\partial t} + w \frac{\partial b}{\partial z}. \quad (4.21)$$

Now, using the kinematic boundary condition (4.21) in equation (4.20), we find that

$$\frac{\partial}{\partial t}(\rho b) + \frac{\partial}{\partial z}(\rho w b) = \rho_a \alpha w. \quad (4.22)$$

Since we are making the Boussinesq approximation, the density terms cancel. Defining the plume volume flux q , momentum flux m , and buoyancy flux f as

$$q = \int_0^\infty w dx, \quad m = \int_0^\infty w^2 dx, \quad \text{and} \quad f = \int_0^\infty w g \left(\frac{\rho_a - \rho}{\rho_1} \right) dx, \quad (4.23)$$

where ρ_1 is a reference density, equation (4.22) becomes

$$\frac{\partial}{\partial t} \left(\frac{q^2}{m} \right) + \frac{\partial q}{\partial z} = \alpha \frac{m}{q}. \quad (4.24)$$

To find an equation for plume momentum flux, we begin with the momentum equation, including the extra velocity diffusion term proposed by Scase and Hewitt (2012), which is

$$\frac{Dw}{Dt} = g \left(\frac{\rho_a - \rho}{\rho} \right) + \frac{\rho_a u_e w}{\rho b} + \frac{\varepsilon}{2\alpha} \frac{\partial}{\partial z} \left(bw \frac{\partial w}{\partial z} \right), \quad (4.25)$$

where ε is a dimensionless parameter, governing the strength of the velocity diffusion term. Equation (4.25) multiplied by ρ and rearranged gives

$$\begin{aligned} \frac{\partial}{\partial t} (\rho w) + \frac{\partial}{\partial z} (\rho w^2) + \frac{\partial}{\partial x} (\rho uw) - w \left[\frac{\partial \rho}{\partial t} + \frac{\partial}{\partial x} (\rho u) + \frac{\partial}{\partial z} (\rho w) \right] = g(\rho_a - \rho) + \\ \frac{\rho_a u_e w}{b} + \frac{\varepsilon}{2\alpha} \frac{\partial}{\partial z} \left(bw \frac{\partial w}{\partial z} \right). \end{aligned} \quad (4.26)$$

Using equation (4.19), we find that

$$\frac{\partial}{\partial t} (\rho w) + \frac{\partial}{\partial z} (\rho w^2) + \frac{\partial}{\partial x} (\rho uw) = g(\rho_a - \rho) + \frac{\varepsilon}{2\alpha} \frac{\partial}{\partial z} \left(bw \frac{\partial w}{\partial z} \right). \quad (4.27)$$

Integrating equation (4.27) over $[0, b]$, assuming a top-hat plume, and using the kinematic boundary condition (4.21) gives

$$\frac{\partial}{\partial t} (\rho w b) + \frac{\partial}{\partial z} (\rho w^2 b) = g(\rho_a - \rho) b + \frac{\varepsilon}{2\alpha} b \frac{\partial}{\partial z} \left(bw \frac{\partial w}{\partial z} \right), \quad (4.28)$$

which is rewritten as

$$\frac{\partial q}{\partial t} + \frac{\partial m}{\partial z} = \frac{qf}{m} + \frac{\varepsilon}{2\alpha} \frac{q^2}{m} \frac{\partial}{\partial z} \left(q \frac{\partial}{\partial z} \left(\frac{m}{q} \right) \right). \quad (4.29)$$

Now, to find an equation for plume buoyancy flux, we take equation (4.19) and add then subtract equal terms, to give

$$\frac{\partial}{\partial t} (\rho - \rho_a) + \frac{\partial \rho_a}{\partial t} + \frac{\partial}{\partial x} ((\rho - \rho_a)u) + \frac{\partial}{\partial x} (\rho_a u) + \frac{\partial}{\partial z} ((\rho - \rho_a)w) + \frac{\partial}{\partial z} (\rho_a w) = -\frac{\rho_a u_e}{b}, \quad (4.30)$$

which, using equation (4.17), simplifies to

$$\frac{\partial}{\partial t}(\rho - \rho_a) + \frac{\partial}{\partial x}((\rho - \rho_a)u) + \frac{\partial}{\partial z}((\rho - \rho_a)w) + \frac{\partial \rho_a}{\partial t} = -w \frac{\partial \rho_a}{\partial z}. \quad (4.31)$$

Integrating equation (4.31) over $[0, b]$, assuming a top-hat plume, and using the kinematic boundary condition (4.21), gives

$$\frac{\partial}{\partial t}((\rho - \rho_a)b) + \frac{\partial}{\partial z}((\rho - \rho_e)bw) + b \frac{\partial \rho_a}{\partial t} = -bw \frac{\partial \rho_a}{\partial z}, \quad (4.32)$$

which, since ρ_1 , a reference density, is constant, gives

$$\begin{aligned} b \frac{\partial}{\partial t} \left(g \left(\frac{\rho_a - \rho_1}{\rho_1} \right) \right) - \frac{\partial}{\partial t} \left(g \left(\frac{\rho - \rho_a}{\rho_1} \right) b \right) - \frac{\partial}{\partial z} \left(g \left(\frac{\rho - \rho_a}{\rho_1} \right) bw \right) \\ = bw \frac{\partial}{\partial z} \left(g \left(\frac{\rho_a - \rho_1}{\rho_1} \right) \right). \end{aligned} \quad (4.33)$$

Defining ambient buoyancy as

$$\delta_a = g \left(\frac{\rho_1 - \rho_a}{\rho_1} \right), \quad (4.34)$$

equation (4.33) becomes

$$\frac{\partial}{\partial t} \left(\frac{qf}{m} \right) + \frac{\partial f}{\partial z} = -q \frac{\partial \delta_a}{\partial z} - \frac{q^2}{m} \frac{\partial \delta_a}{\partial t}. \quad (4.35)$$

Equations (4.24), (4.29), and (4.35) are the governing equations for a time-varying, 2D line source. To change to a wall source, providing a source buoyancy flux of $b_s(z, t)$ per unit source area, we simply add the buoyancy source term into the buoyancy flux equation (4.35), yielding the following equations:

$$\frac{\partial}{\partial t} \left(\frac{q^2}{m} \right) + \frac{\partial q}{\partial z} = \alpha \frac{m}{q}, \quad (4.36)$$

$$\frac{\partial q}{\partial t} + \frac{\partial m}{\partial z} = \frac{qf}{m} + \frac{\varepsilon}{2\alpha} \frac{q^2}{m} \frac{\partial}{\partial z} \left(q \frac{\partial}{\partial z} \left(\frac{m}{q} \right) \right), \quad (4.37)$$

and

$$\frac{\partial}{\partial t} \left(\frac{qf}{m} \right) + \frac{\partial f}{\partial z} = b_s - q \frac{\partial \delta_a}{\partial z} - \frac{q^2}{m} \frac{\partial \delta_a}{\partial t}. \quad (4.38)$$

The steady version of equations (4.24), (4.29), and (4.38), with $\varepsilon = 0$, are exactly those used by Cooper and Hunt (2010) for a constant flux vertically distributed source.

We are interested in linear ramps both up and down in source buoyancy flux, as well as the combination of “ramps down” and a constant flux section that mimics the solidification of PCM. “Ramps up” are given by

$$b_{s\text{up}} = \frac{b_{s_0}}{t_{\text{ramp}}}t, \quad (4.39)$$

where b_{s_0} is the source buoyancy flux that is reached after ramping up for a time t_{ramp} . For “ramps down”,

$$b_{s\text{down}} = b_{s_0} \left(\frac{t_{\text{ramp}} - t}{t_{\text{ramp}}} \right), \quad (4.40)$$

where here b_{s_0} is the initial source buoyancy flux, and t_{ramp} is the time taken to “ramp down” from that initial source buoyancy flux to zero. For a PCM mimicking source,

$$b_s = \begin{cases} b_{s_0} \left(\frac{t_{r1} - \left(1 - \frac{b_{s1}}{b_{s0}}\right)t}{t_{r1}} \right), & t \leq t_{r1}, \\ b_{s1}, & t_{r1} < t \leq t_{r1} + t_s, \\ b_{s1} \left(\frac{t_{r1} + t_s + t_{r2} - t}{t_{r2}} \right), & t_{r1} + t_s < t \leq t_{r1} + t_s + T_{r2}, \end{cases} \quad (4.41)$$

where here b_{s_0} is the initial source buoyancy flux, b_{s1} is the source buoyancy flux during the constant flux section, t_{r1} is the time over which the first “ramp down” (from b_{s_0} to b_{s1}) occurs, t_s is the time over which the source provides a constant buoyancy flux, and t_{r2} is the time over which the second “ramp down” (from b_{s1} to zero) occurs.

These equations are nondimensionalised in the same way as in chapter 3. That is,

$$q = \alpha^{2/3} b_{s_0}^{1/3} H^{4/3} Q, \quad m = \alpha^{1/3} b_{s_0}^{2/3} H^{5/3} M, \quad f = b_{s_0} H F, \\ \delta_a = \alpha^{-2/3} b_{s_0}^{2/3} H^{-1/3} \Delta_a, \quad z = H Z, \quad t = W \alpha^{-2/3} b_{s_0}^{-1/3} H^{-1/3} T, \quad (4.42)$$

where W is the width of the tank (in the x-direction, perpendicular to the source). For neatness, we define ramp parameters a , a_1 and a_2 , together with the solidification time parameter a_s as

$$a_{(-,1,2,s)} = \frac{W}{t_{(\text{ramp},r1,r2,s)} \alpha^{2/3} b_{s_0}^{1/3} H^{1/3}}, \quad (4.43)$$

and the aspect ratio multiplied by the entrainment coefficient as λ ,

$$\lambda = \frac{\alpha H}{W}. \quad (4.44)$$

The plume equations (4.24), (4.29), and (4.38) then become

$$\lambda \frac{\partial}{\partial T} \left(\frac{Q^2}{M} \right) + \frac{\partial Q}{\partial Z} = \frac{M}{Q}, \quad (4.45)$$

$$\lambda \frac{\partial Q}{\partial T} + \frac{\partial M}{\partial Z} = \frac{QF}{M} + \frac{\varepsilon Q^2}{2M} \frac{\partial}{\partial Z} \left(Q \frac{\partial}{\partial Z} \left(\frac{M}{Q} \right) \right), \quad (4.46)$$

and,

$$\lambda \frac{\partial}{\partial T} \left(\frac{QF}{M} \right) + \frac{\partial F}{\partial Z} = \frac{b_s(aT)}{b_{s0}} - \lambda \frac{Q^2}{M} \frac{\partial \Delta_a}{\partial T} - Q \frac{\partial \Delta_a}{\partial Z}, \quad (4.47)$$

which for the ‘‘ramp down’’ is

$$\lambda \frac{\partial}{\partial T} \left(\frac{QF}{M} \right) + \frac{\partial F}{\partial Z} = 1 - aT - \lambda \frac{Q^2}{M} \frac{\partial \Delta_a}{\partial T} - Q \frac{\partial \Delta_a}{\partial Z}, \quad (4.48)$$

for the ‘‘ramp up’’ is

$$\lambda \frac{\partial}{\partial T} \left(\frac{QF}{M} \right) + \frac{\partial F}{\partial Z} = aT - \lambda \frac{Q^2}{M} \frac{\partial \Delta_a}{\partial T} - Q \frac{\partial \Delta_a}{\partial Z}, \quad (4.49)$$

and for the PCM mimicking source is

$$\begin{aligned} & \lambda \frac{\partial}{\partial T} \left(\frac{QF}{M} \right) + \frac{\partial F}{\partial Z} \\ &= -\lambda \frac{Q^2}{M} \frac{\partial \Delta_a}{\partial T} - Q \frac{\partial \Delta_a}{\partial Z} + \begin{cases} \left(1 - \left(1 - \frac{b_{s1}}{b_{s0}} \right) a_1 T \right), & T \leq \frac{1}{a_1}, \\ \frac{b_{s1}}{b_{s0}}, & \frac{1}{a_1} < T \leq \frac{1}{a_1} + \frac{1}{a_s}, \\ \frac{b_{s1}}{b_{s0}} \left(\frac{a_2}{a_1} + \frac{a_2}{a_s} + 1 - a_2 T \right), & \frac{1}{a_1} + \frac{1}{a_s} < T \leq \frac{1}{a_1} + \frac{1}{a_s} + \frac{1}{a_2}. \end{cases} \end{aligned} \quad (4.50)$$

The boundary conditions for all three types of source are

$$Q = M = F = 0 \text{ at } Z = 0. \quad (4.51)$$

The initial conditions for the ‘‘ramp down’’ and for the PCM mimicking source are the similarity solutions of Cooper and Hunt (2010) for a constant flux source with dimensionless

source buoyancy flux $b_s/b_{s0} = 1$,

$$Q = \frac{3}{4} \left(\frac{4}{5}\right)^{1/3} Z^{4/3}, \quad M = \frac{3}{4} \left(\frac{4}{5}\right)^{2/3} Z^{5/3}, \quad F = Z, \quad \text{at } T = 0 \quad (4.52)$$

while initial conditions for the “ramp up” (from zero) source are

$$Q = M = F = 0 \text{ at } T = 0. \quad (4.53)$$

Changes in ambient buoyancy δ_a are given by

$$\frac{\partial \delta_a}{\partial t} = \frac{q}{W} \frac{\partial \delta_a}{\partial z}, \quad (4.54)$$

which nondimensionalises to

$$\frac{\partial \Delta_a}{\partial T} = Q \frac{\partial \Delta_a}{\partial Z}. \quad (4.55)$$

In the constant flux experiments, we found $\alpha = 0.018$, and the aspect ratio of our tank is $H/W \approx 1/2$, so $\lambda \approx 0.009$, which is much smaller than 1. Since λ is small, we set $\lambda = 0$, for simplicity. We also set $\varepsilon = 0$, neglecting the velocity diffusion term. Scase and Hewitt (2012) include the velocity diffusion term to ensure that the system of equations is well posed. They note, however, that, it makes only a small difference for steady solutions and for power law sources such as the linear ramps that we are interested in. By setting $\lambda = 0$, eliminating the time derivatives, we ensure that perturbations cannot grow, as the only time dependence is through the time-varying source buoyancy flux, so the problem is well-posed. Thus, setting $\varepsilon = 0$ for simplicity is appropriate. With $\varepsilon = 0$, we are able to find simple analytic solutions, discussed in section 4.3.2, for the plume in a uniform, unconfined ambient with both a “ramp down” and a “ramp up” in source buoyancy flux, which are used in the peeling plume model.

To solve these equations numerically, which in section 4.4.2, we do for the “ramp up” source, the method of Germeles (1975) is used, which is shown schematically in figure 1.5 of chapter 1. To account for the extra volume added by the source in our experiments, however, we make an adjustment to the layer depth, as shown in figure 4.9. We add to the layer at the bottom of the tank, where the plume adds its fluid to the ambient, the extra volume added by the source in that timestep, and then multiply the buoyancy of that layer by the old layer thickness, divided by the new layer thickness, to ensure that only the total volume, rather than the total buoyancy, increases.

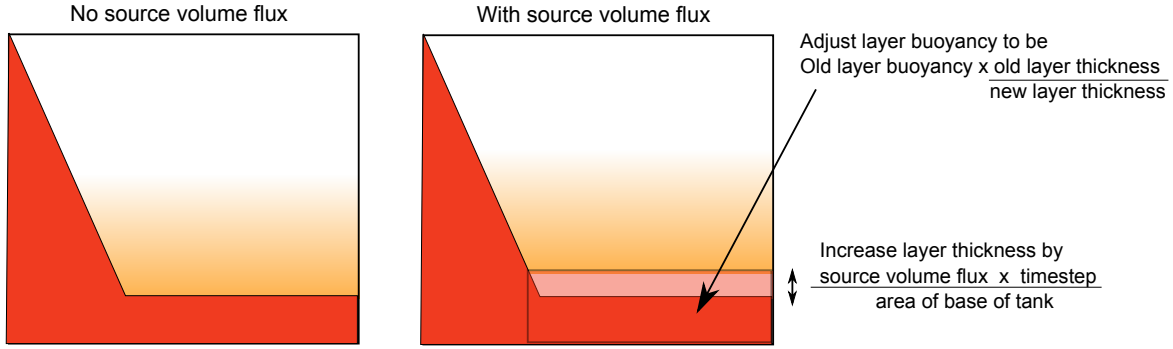


Fig. 4.9 Schematic showing how, in a modified version of the Germeles (1975) method, the layer thickness and buoyancy are adjusted to account for the non-zero source volume flux present in the experiments of section 4.2.

4.3.2 Analytic solutions for a plume in a uniform, unconfined ambient

For a uniform, unconfined ambient ($\Delta_a = 0$), the plume equations become

$$\frac{\partial Q}{\partial Z} = \frac{M}{Q}, \quad \frac{\partial M}{\partial Z} = \frac{QF}{M}, \quad \frac{\partial F}{\partial Z} = B_s(T), \quad (4.56)$$

where $B_s(T) = b_s(aT)/b_{s_0}$ is the dimensionless, time-varying source buoyancy flux per unit source area. The boundary conditions are $Q = M = F = 0$ at $Z = 0$, and the initial conditions are given by (4.52) for the “ramp down” and PCM mimicking sources, and by (4.53) for the “ramp up” source. The constant flux source, considered by Cooper and Hunt (2010), is a special case of the time varying source, with a constant source buoyancy flux B_s . A similarity solution exists for the constant flux case, given by Cooper and Hunt (2010), which, changed to notation consistent with the rest of this thesis, is

$$Q = \frac{3}{4} \left(\frac{4}{5} \right)^{1/3} B_s^{1/3} Z^{4/3}, \quad M = \frac{3}{4} \left(\frac{4}{5} \right)^{2/3} B_s^{2/3} Z^{5/3}, \quad F = B_s Z. \quad (4.57)$$

Since the only time dependence in (4.56) is from $B_s(T)$, this solution, with the constant B_s replaced by $B_s(T)$, is also a solution of (4.56). This can easily be verified by substituting the solution (4.57) into the plume equations (4.56). The solution has Q, M , and F varying as powers of Z , and so the boundary conditions $Q = M = F = 0$ at $Z = 0$ are clearly satisfied. For a “ramp down” source and a PCM mimicking source, the initial dimensionless source buoyancy flux is $B_s(T = 0) = 1$, so the initial conditions (4.52) for a “ramp down” or a PCM mimicking source are satisfied. For a “ramp up” source, the initial dimensionless source buoyancy flux is $B_s(T = 0) = 0$, so the initial conditions (4.53) for a “ramp up” source are satisfied.

Specifically, there is a simple, analytic solution to the plume equations (4.56), even when the source buoyancy flux varies in time as a “ramp down”, a “ramp up”, or a PCM mimicking source. For a “ramp down” in source buoyancy flux, this solution is

$$Q = \frac{3}{4} \left(\frac{4}{5}\right)^{1/3} (1 - aT)^{1/3} Z^{4/3}, \quad M = \frac{3}{4} \left(\frac{4}{5}\right)^{2/3} (1 - aT)^{2/3} Z^{5/3}, \quad F = (1 - aT)Z. \quad (4.58)$$

For a “ramp up” in source buoyancy flux, it is

$$Q = \frac{3}{4} \left(\frac{4}{5}\right)^{1/3} (aT)^{1/3} Z^{4/3}, \quad M = \frac{3}{4} \left(\frac{4}{5}\right)^{2/3} (aT)^{2/3} Z^{5/3}, \quad F = (aT)Z. \quad (4.59)$$

Finally, for a PCM mimicking source, it is

$$Q = \frac{3}{4} \left(\frac{4}{5}\right)^{1/3} (B_{sPCM(T)})^{1/3} Z^{4/3}, \quad M = \frac{3}{4} \left(\frac{4}{5}\right)^{2/3} (B_{sPCM(T)})^{2/3} Z^{5/3}, \quad F = (B_{sPCM(T)})Z, \quad (4.60)$$

where

$$B_{sPCM(T)} = \begin{cases} \left(1 - \left(1 - \frac{b_{s1}}{b_{s0}}\right) a_1 T\right), & T \leq \frac{1}{a_1}, \\ \frac{b_{s1}}{b_{s0}}, & \frac{1}{a_1} < T \leq \frac{1}{a_1} + \frac{1}{a_s}, \\ \frac{b_{s1}}{b_{s0}} \left(\frac{a_2}{a_1} + \frac{a_2}{a_s} + 1 - a_2 T\right), & \frac{1}{a_1} + \frac{1}{a_s} < T \leq \frac{1}{a_1} + \frac{1}{a_s} + \frac{1}{a_2}. \end{cases} \quad (4.61)$$

The width of the top-hat plume described by these similarity solutions is then given by

$$\frac{Q^2}{M} = \frac{\left(\frac{3}{4}\right)^2 \left(\frac{4}{5}\right)^{2/3} B_s^{2/3}(T) Z^{8/3}}{\frac{3}{4} \left(\frac{4}{5}\right)^{2/3} B_s^{2/3}(T) Z^{5/3}} = \frac{3}{4} Z, \quad (4.62)$$

provided that $B_s(T) > 0$. The plume is thus straight-sided, with a width that is independent of source strength, which is consistent with the results for a horizontal line source providing a constant source buoyancy flux. For a line source in a uniform, unconfined ambient, the equations are the 2D version of those used by Morton et al. (1956), which are, as given in section 3.3.1 of this thesis,

$$\frac{dQ}{dZ} = \frac{M}{Q}, \quad \frac{dM}{dZ} = \frac{QF}{M}, \quad \frac{dF}{dZ} = 0, \quad (4.63)$$

with $Q = M = 0$ and $F = F_0$ at $Z = 0$. This system of equations and boundary conditions has similarity solution

$$Q = F_0^{1/3}Z, \quad M = F_0^{2/3}Z, \quad F = F_0, \quad (4.64)$$

which gives a plume width of

$$\frac{Q^2}{M} = \frac{F_0^{2/3}Z^2}{F_0^{2/3}Z} = Z. \quad (4.65)$$

Thus, for both a horizontal, constant flux line source and a time-varying, vertically distributed source, the plume is straight sided (the plume width varies linearly with Z), and the width of the plume is independent of the source strength. The only difference between the plume width for the two cases is that, with a vertically distributed source, the resulting plume is narrower than for a horizontal line source.

For a vertical line source in a uniform environment, Gladstone and Woods (2014) present a solution to the horizontally averaged, quasi-steady plume equations, which are the axisymmetric versions of the plume equations above, but with the buoyancy flux equation changed to include, on the right hand side, the source buoyancy flux per unit source length. The solution to these equations that Gladstone and Woods (2014) find has a (dimensional) plume radius of $\alpha(z + z_0)$, where α is the entrainment coefficient, z is height, and z_0 is a virtual origin. This means that, as with the horizontal line source, the plume is straight-sided, with a radius that is independent of the source strength. One of the three models proposed by Craske and van Reeuwijk (2016) for an unsteady plume assumes that the plume remains straight sided. This assumption is consistent with observations from their DNS that, after a step change in source buoyancy, plume width remains mostly unchanged. Our similarity solution for the time-varying, vertically distributed source, which gives a straight-sided plume whose width is independent of the source strength, is thus consistent with previous work for horizontal and vertical line sources, as well as for unsteady point sources.

When the plume is within a sealed space, a stratified region forms, with an interface, the first front, between the stratified region and the initial ambient. The distance from the start of the source to the first front, Z_0 , obeys the following equation, because of volume conservation,

$$\frac{dZ_0}{dT} = -Q|_{Z_0, T}, \quad (4.66)$$

with the initial condition $Z_0 = 1$ at $T = 0$ (that is, $Z = 1$ is the ceiling of the room with a heated plume, or the floor of a tank with a salt plume). We find how the first front varies with time by integrating this equation, with $Q(Z_0, T)$ given by the similarity solution (4.57), and using the initial condition to determine the constant of integration. The similarity solution for a plume in a uniform, unconfined ambient is appropriate, since, until the first front is reached,

the plume is in a uniform ambient, with $\Delta_a = 0$, and the similarity solution describes the plume. For a “ramp down”, using Q given by equation (4.58), we find that

$$Z_{0\text{down}} = \left(1 + \frac{3}{16a} \left(\frac{4}{5} \right)^{1/3} \left(1 - (1 - aT)^{4/3} \right) \right)^{-3}. \quad (4.67)$$

For a “ramp up”, using Q from equation (4.59), we find that

$$Z_{0\text{up}} = \left(1 + \frac{3}{16a} \left(\frac{4}{5} \right)^{1/3} (aT)^{4/3} \right)^{-3}. \quad (4.68)$$

For a PCM mimicking source, using Q from equation (4.60), and ensuring that Z_0 is continuous at $T = 1/a_1$ and at $T = (1/a_1)(1 + \frac{t_s}{t_{r1}})$, we find that

$$Z_{0\text{PCM}} = \begin{cases} \left(1 + \frac{3}{16 \left(1 - \frac{b_{s1}}{b_{s0}} \right) a_1} \left(\frac{4}{5} \right)^{1/3} \left(1 - \left(1 - \left(1 - \frac{b_{s1}}{b_{s0}} \right) a_1 T \right)^{4/3} \right) \right)^{-3}, & T \leq \frac{1}{a_1}, \\ \left(1 + \frac{3}{16 \left(1 - \frac{b_{s1}}{b_{s0}} \right) a_1} \left(\frac{4}{5} \right)^{1/3} \left(1 - \left(\frac{b_{s1}}{b_{s0}} \right)^{4/3} \right) + \frac{1}{4} \left(\frac{4}{5} \right)^{1/3} \left(\frac{b_{s1}}{b_{s0}} \right)^{1/3} \left(T - \frac{1}{a_1} \right) \right)^{-3}, & \frac{1}{a_1} < T \leq \frac{1}{a_1} + \frac{1}{a_s}, \\ \left(1 + \frac{3}{16 \left(1 - \frac{b_{s1}}{b_{s0}} \right) a_1} \left(\frac{4}{5} \right)^{1/3} \left(1 - \left(\frac{b_{s1}}{b_{s0}} \right)^{4/3} \right) + \frac{1}{4} \left(\frac{4}{5} \right)^{1/3} \left(\frac{b_{s1}}{b_{s0}} \right)^{1/3} \frac{1}{a_s} + \frac{3}{16a_2} \left(\frac{4}{5} \right)^{1/3} \left(\frac{b_{s1}}{b_{s0}} \right)^{1/3} \left(1 - \left(\frac{a_2}{a_1} + \frac{a_2}{a_s} + 1 - a_2 T \right)^{4/3} \right) \right)^{-3}, & \frac{1}{a_1} + \frac{1}{a_s} < T \leq \frac{1}{a_1} + \frac{1}{a_s} + \frac{1}{a_2}. \end{cases} \quad (4.69)$$

For comparison, the first front with a constant flux source providing a source buoyancy flux of B_s per unit area, given by Cooper and Hunt (2010), but changed to our notation, is

$$Z_{0\text{constant}} = \left(1 + \frac{1}{4} \left(\frac{4}{5} \right)^{1/3} B_s^{1/3} T \right)^{-3}. \quad (4.70)$$

The first front height for the “ramp down”, given by (4.67), the “ramp up”, given by (4.68), the PCM mimicking source, given by (4.69), and the constant flux source, given by (4.70) are plotted in figure 4.10. The values of the parameter a , as defined in (4.43), are taken to be $a = 1/3$ for both the “ramp up” and “ramp down”, and $a_1 = a_2 = a_s = 1$ for the PCM mimicking source. The ratio of constant flux section source buoyancy flux to initial source buoyancy flux for the PCM mimicking source is $b_{s1}/b_{s0} = 1/2$, and dimensionless source buoyancy flux is $B_s = 1$ for the constant flux source. Both the “ramp down” and

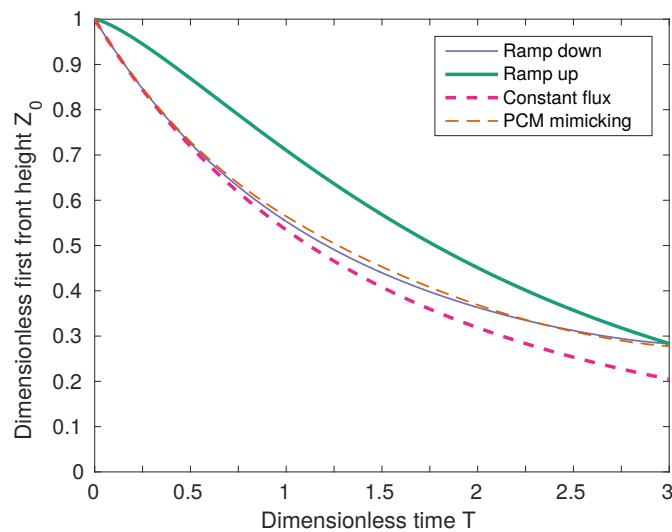


Fig. 4.10 The first front height, from theory, for 4 types of source: a “ramp down” in source buoyancy flux, a “ramp up” in source buoyancy flux, a constant source buoyancy flux, and a PCM mimicking source. All are shown up to a dimensionless time of 3, which is when the “ramp down” source and PCM mimicking source have reached zero source buoyancy flux, and so their first front height does not change beyond this point.

PCM mimicking source reach zero source buoyancy flux (and so their first front height then remains unchanged) at dimensionless time $T=3$, and so figure 4.10 shows the first front heights only up to this time. We see that the first front evolves differently with each of the four sources. For the “ramp down”, constant flux, and PCM mimicking sources, the rate at which the first front height changes decreases with time: figure 4.10 shows the thin purple line and the two dashed lines getting less steep with time for each of these three cases. The “ramp up”, however, behaves differently. At the start of the experiment, the rate at which the first front height changes increases with time: the thick green line in figure 4.10 initially gets steeper with time. Comparing the theoretical first front heights for the “ramp down” and the “ramp up” source shows that these two types of source behave differently, and will have a different effect on the stratification in a space. With the parameter values used, the PCM mimicking source, shown by the thin, dashed orange line, gives a first front height that varies in a similar way to the “ramp down” source, shown by the thin purple line. This is plausible since the PCM mimicking source is made up of two ramps and a constant flux section, and, with the parameters used to plot figure 4.10, two thirds of the total time was spent ramping down the source buoyancy flux.

The theoretical expressions for first front height are compared, in figures 4.11 and 4.12, with the experimental first front heights. Note that the dimensionless times that results are

shown up to are different from $T = 3$, used in figure 4.10, because the ramp sizes, and therefore times for the source to ramp down to zero, are different from the example used for figure 4.10. The experimental first front heights are calculated by finding the height at which the dimensionless ambient buoyancy is greater than 0.1 (note that 0.1 is used rather than zero because of scatter in the experimental data – looking for where dimensionless ambient buoyancy is first greater than zero would give an inaccurate first front height). Figure 4.11 shows the height of the first front from the tank floor in the “ramp down” experiments, divided by the corresponding theoretical height, $1 - Z_0$, with Z_0 given by (4.67). Apart from at early times (when the theory predicts that the first front is closer to the tank floor than is observed in experiments), the experimental first front height divided by the theoretical first front height is approximately 1 for each of the 12 “ramp down” experiments carried out. The theoretical expression for the first front height describes the experimental results for first front height well for the “ramp down” experiments. Similarly, figure 4.12 shows the height of the first front from the tank floor in the “ramp up” experiments, divided by the corresponding theoretical height, $1 - Z_0$, with Z_0 given by (4.68), and, again, apart from at early times (when, unlike for the “ramp down”, the theory predicts that the first front is further from the tank floor than observed in experiments), the data collapses, showing reasonable agreement between the theoretical and experimental first front heights for the “ramp up” experiments. In both the “ramp down” and the “ramp up” experiments, the first front is slightly further from the floor than the theory predicts (the data collapses onto a line slightly above 1), and this is because, in the experiments, extra volume is added by the source, whilst the theory assumes the source only adds buoyancy. In the numerical solutions, however, this extra volume is accounted for, as described at the end of section 4.3.1. The first front separates the initial ambient fluid from the stratified region, and to find the stratification in this region, we solve the plume equations (4.45), (4.46), and (4.47) numerically, as described at the end of section 4.3.1, for the one-way-entrainment model, or use the peeling plume model presented in the following section, 4.3.3. In both models, we account for the extra volume flux added by the source using a method such as that described in figure 4.9 for the one-way-entrainment model, or that described in section 4.3.3 for the peeling plume model.

4.3.3 Peeling plume with a vertically distributed, time varying source

The peeling plume model of Hogg et al. (2015), which, in section 3.3.2, we extended to a vertically distributed, constant flux source, we now extend further to a time-varying, vertically distributed source. Instead of assuming top-hat profiles for vertical velocity and density

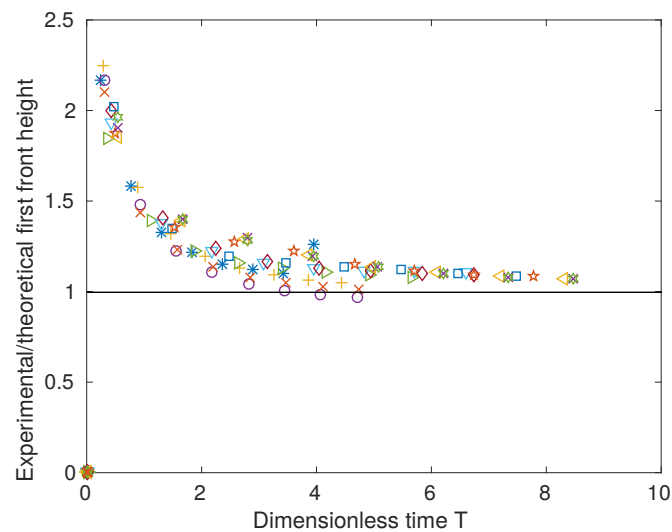


Fig. 4.11 The experimental first front height divided by the theoretical first front height from (4.67) for the 12 “ramp down” experiments. Each experiment is shown by a different marker shape. The experimental first front height (measured from the base of the tank upwards) is systematically slightly too large, compared with the theoretical first front height, because the theoretical first front height neglects the extra volume flux added by the source in experiments.

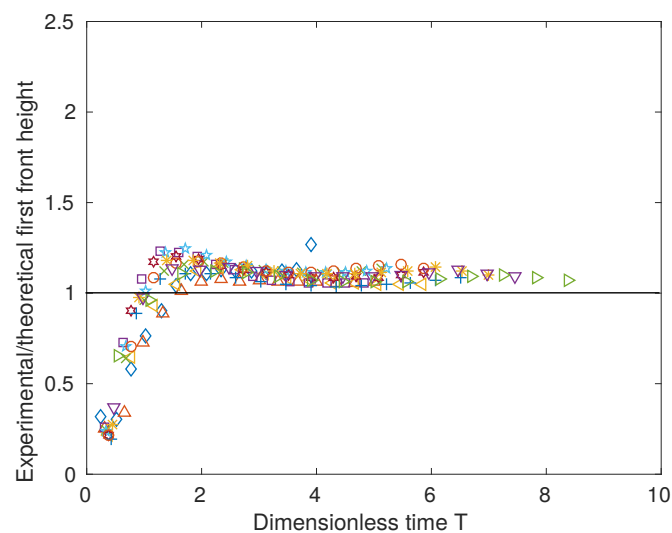


Fig. 4.12 The experimental first front height divided by the theoretical first front height from (4.68) for the 12 “ramp up” experiments. Each experiment is shown by a different marker shape. The experimental first front height (measured from the base of the tank upwards) is systematically slightly too large, compared with the theoretical first front height, because the theoretical first front height neglects the extra volume flux added by the source in experiments.

across the width of the plume, they now vary linearly,

$$w = \begin{cases} w_m(z)(b-x)/b, & x \leq b, \\ 0, & x > b \end{cases} \quad \text{and} \quad \rho = \begin{cases} \rho_1 + \rho_m(z)(b-x)/b, & x \leq b. \\ \rho_1, & x > b, \end{cases} \quad (4.71)$$

On substituting these expressions into the integral expressions for q, m , and f , we find that

$$q = \frac{w_m b}{2} = Q \alpha^{2/3} b_{s_0}^{1/3} H^{4/3}, \quad m = \frac{w_m^2 b}{3} = M \alpha^{1/3} b_{s_0}^{2/3} H^{5/3}, \quad f = \frac{g \rho_m w_m b}{3 \rho_1} = F b_{s_0} H, \quad (4.72)$$

and the equations for Q, M , and F are (4.45), (4.46), and (4.47), as for the top-hat plume. The plume evolves as in the top-hat plume model of section 4.3.1 until it reaches the first front. The first front height $Z_0(T)$ is given by

$$\frac{dZ_0}{dT} = -Q|_{Z_0(T)}, \quad (4.73)$$

with $Z_0 = 1$ at $T = 0$, which, for $\lambda = 0$, is given by equation (4.67) for a ‘‘ramp down’’, and by equation (4.68) for a ‘‘ramp up’’. Once the plume reaches the first front height, we assume that it peels, with plume fluid moving directly to its neutral buoyancy height. The dimensionless buoyancy in the plume varies (across the width of the plume) from zero at the edge of the plume, to the dimensionless maximum buoyancy in the plume (at height Z)

$$\Delta_m|_Z = \frac{3F}{2Q} \Big|_Z. \quad (4.74)$$

Fluid of buoyancy Δ_i begins to peel at time T_i , when the dimensionless maximum buoyancy in the plume at the first front height is equal to Δ_i . At height Z and time T , fluid with buoyancy Δ_i located at dimensionless distance from the wall

$$X_i = \frac{x_i}{\alpha H} = \frac{b}{\alpha H} \left(1 - \frac{\Delta_i}{\Delta_m(Z)} \right) = \frac{4Q^2}{3M} \left(1 - \frac{\Delta_i}{\Delta_m} \right). \quad (4.75)$$

The dimensionless vertical velocity, using the definitions of q, m , and f in equation (4.72), is given by

$$W = \begin{cases} \frac{3}{2} \frac{M}{Q} \left(1 - \frac{3M}{4Q^2} X \right), & X \leq \frac{4Q^2}{3M}, \\ 0, & X > \frac{4Q^2}{3M}. \end{cases} \quad (4.76)$$

The volume flux in the plume of fluid with buoyancy greater than Δ_i is found by integrating vertical velocity across the plume, from 0 to X_i ,

$$Q_i(\Delta_i, Z, T) = \begin{cases} \int_0^{X_i} W dX = \int_0^{\frac{4Q^2}{3M} \left(1 - \frac{\Delta_i}{\Delta_m(Z)}\right)} \frac{3M}{2Q} \left(1 - \frac{3M}{4Q^2} X\right) dX, & \text{if } X_i > 0 \implies \Delta_i < \Delta_m, \\ 0, & \text{if } X_i < 0, \implies \Delta_i > \Delta_m. \end{cases} \quad (4.77)$$

Calculating this integral, we find that

$$Q_i(\Delta_i, Z, T) = \begin{cases} Q(Z, T) \left(1 - \frac{\Delta_i^2}{\Delta_m(Z, T)^2}\right), & \text{if } \Delta_i < \Delta_m \\ 0, & \text{if } \Delta_i > \Delta_m. \end{cases} \quad (4.78)$$

The depth at which fluid of buoyancy Δ_i is located is calculated by summing the volume of fluid arriving at the stratified region with each buoyancy, giving

$$Z_i = 1 - \int_{T_i}^T Q_i|_{Z_0(\tilde{T})} d\tilde{T}, \quad (4.79)$$

which we calculate numerically. To account for the extra volume added by the source, we adjust this equation slightly, calculating,

$$Z_i = 1 - \left(\frac{\int_0^T Q_i(\Delta_i = 0) dT + \frac{1}{\alpha^{2/3} b_{s_0}^{1/3} H^{1/3}} \int_0^T v_s dT}{\int_0^T Q_i(\Delta_i = 0) dT} \right) \int_{T_i}^T Q_i|_{Z_0(\tilde{T})} d\tilde{T}, \quad (4.80)$$

where v_s is the (dimensional) source volume flux per unit source area. For the ‘‘ramp down’’ with initial source volume flux per unit source width v_{s_0} ,

$$\int_0^T v_s dT = v_{s_0} \left(T - \frac{aT^2}{2} \right) \quad (4.81)$$

for the ‘‘ramp up’’ with final source volume flux per unit source area v_{s_0} ,

$$\int_0^T v_s dT = \frac{av_{s_0}T^2}{2}, \quad (4.82)$$

and for the PCM mimicking source with initial source volume flux per unit source area v_{s_0} and source volume flux per unit source area v_{s_1} in the constant flux section,

$$\int_0^T v_s dT = \begin{cases} v_{s_0} \left(T - \frac{a_1 T^2}{2} \right) + \frac{v_{s_1} a_1 T^2}{2}, & T \leq \frac{1}{a_1}, \\ \frac{(v_{s_0} + v_{s_1})}{2a_1} + v_{s_1} \left(T - \frac{1}{a_1} \right), & \frac{1}{a_1} < T \leq \frac{1}{a_1} + \frac{1}{a_s}, \\ \frac{(v_{s_0} + v_{s_1})}{2a_1} + v_{s_1} \frac{1}{a_s} + v_{s_1} \left(\left(\frac{a_2}{a_1} + \frac{a_2}{a_s} + 1 \right) \left(T - \frac{1}{a_1} - \frac{1}{a_s} \right) \right) \\ \quad - \frac{v_{s_1} a_2}{2} \left(T^2 - \left(\frac{1}{a_1} + \frac{1}{a_s} \right)^2 \right), & \frac{1}{a_1} + \frac{1}{a_s} < T \leq \frac{1}{a_1} + \frac{1}{a_s} + \frac{1}{a_2}. \end{cases} \quad (4.83)$$

Then, just as the one-way-entrainment model is adjusted to account for the extra volume added by the source, we multiply the buoyancy of each layer by the old (before the adjustment) layer thickness, divided by the new layer thickness, so that the total buoyancy remains unchanged.

Finally, to account for the as yet unaccounted for buoyancy added from the wall after the first front, we must update the buoyancy at each height. We assume that the extra buoyancy to be added is simply added in to the ambient at the height from which it came, rather than forming a plume and descending deeper into the tank. The new buoyancy of each layer is

$$\Delta_i^{\text{new}} = \Delta_i^{\text{old}} + \int_{T_{ffi}}^T \frac{v_s}{v_{s_0}} \frac{1}{H_{\text{new}}} d\tilde{T}, \quad (4.84)$$

where T_{ffi} is the time the first front passes Z_i , which must be calculated numerically, and H_{new} is the new dimensionless box height. Before the first front reaches the top of the source, the new dimensionless box height is $H_{\text{new}}/H = 1$. After the first front reaches the top of the source, the new dimensionless box height is the height of the stratified region, divided by the source height, i.e. $H_{\text{new}}/H = 1 - Z_i$ ($i = 0, T$). With zero source volume flux, this height would also be $H_{\text{new}}/H = 1$, but with the extra volume added by the source, it is larger – we have $1 - Z_i > 1$, meaning that the stratified region extends beyond the source height, due to the extra volume flux added by the source. The heights Z_i with their corresponding Δ_i^{new} give the ambient stratification.

4.4 Comparing theory with experiments

4.4.1 “Ramp down” in source buoyancy flux

For a “ramp down” in source buoyancy flux, the peeling plume model is appropriate for describing the ambient buoyancy profile. Experimental ambient buoyancy profiles (thin,

solid, black lines) are shown together with the peeling plume theory ambient buoyancy profiles (thicker, dashed, grey lines) in figures 4.13, 4.14, and 4.15. Towards the bottom of the tank, there is reasonable agreement between the theoretical and experimental profiles, although there is a difference in the shape of the profiles near the first front height – a kink, discussed in section 4.2.3, appears in each of the experiments. A reason for this disagreement is discussed later in this section, and in figure 4.17. Away from this kink, the model captures the overall shape of the profile, and the rate at which the profiles evolve. At early times, when the source buoyancy flux is large, the spacing between consecutive profiles is large, which the model captures, and at late times, when the source buoyancy flux is small, the spacing between consecutive profiles is small, which the model also captures.

With a “ramp down” in source buoyancy flux, intrusions are inevitable. The plume has a higher source buoyancy flux at early times than at late times, so, as time goes on, the plume with a small source buoyancy flux enters a strongly stratified region, where it reaches its neutral buoyancy height, and intrudes into the ambient, before reaching the floor of the tank. Cooper and Hunt (2010) include such intrusions in their one-way-entrainment model for a vertically distributed source in a displacement ventilated space by, whenever the plume becomes neutrally buoyant, allowing an intrusion to occur over a finite depth, with a linearly varying buoyancy profile. They note that their arbitrary choice of the intrusion’s range of buoyancy does not capture the complex physics of detrainment. The peeling plume model avoids the need to select an arbitrary range of buoyancy – its profile varies from a maximum of the mean plume buoyancy near the source to a minimum of zero at the ambient, rather than a minimum of some arbitrary intermediate value. Since intrusions are inevitable for a “ramp down” in source buoyancy flux, and both the Cooper and Hunt (2010) one-way-entrainment model and peeling plume model use a linear buoyancy profile across the plume, we use only the peeling plume model, for simplicity. The peeling plume model requires the plume equations to be solved only in an unstratified ambient, and the stratification is found by simply calculating the volume of fluid of each density arriving at the stratified region.

We expect a peeling plume model to be appropriate when there is a “ramp down” in source buoyancy flux, because the plume strength is decreasing with time, so the plume is descending into relatively dense fluid that was added to the ambient when the plume was stronger and more dense. As the plume descends into the ambient, it reaches its neutral buoyancy height before reaching the floor of the tank, and then intrudes into the ambient. Since buoyancy continues to be added by the vertically distributed source below this height, a new plume forms, and the process repeats. As explained above, this intruding into the ambient is expected to happen even for a top-hat plume; for plumes with density and vertical velocity varying across their width, as is assumed in the peeling plume model, even more

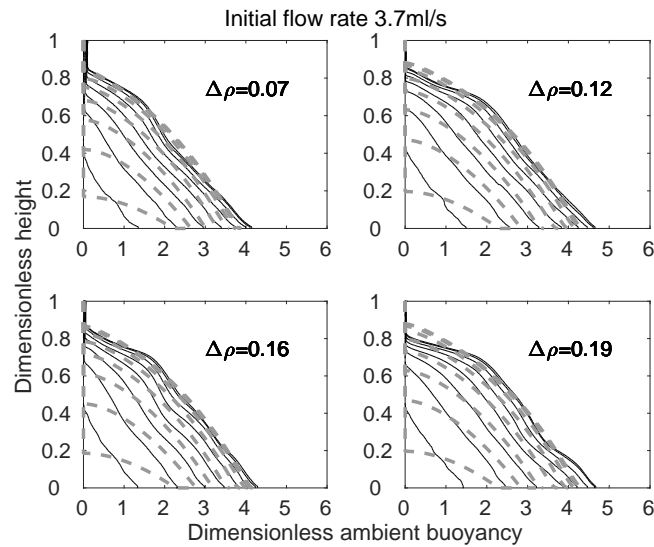


Fig. 4.13 Dimensionless ambient buoyancy profiles shown at 8 different times: 115s, 355s, 595s, 835s, 1075s, 1315s, 1555s, and 1795s (the 8 lines of each line style on each subplot) through each of 4 “ramp down” experiments (the 4 different subplots) with an initial flow rate of 3.7ml/s. Experimental profiles are shown by the thin, solid, black lines, and theoretical profiles using the peeling plume model are shown by the thicker, dashed, grey lines.

plume fluid is expected to leave the plume at intermediate heights. In experiments, we observe fluid leaving the plume and intruding into the ambient at intermediate heights: figure 4.4 shows plume fluid (orange) intruding into the undyed (but stratified) ambient at several heights. The peeling plume model includes both entrainment and detrainment, so we expect it to be appropriate.

The RMS error between the theoretical and experimental ambient buoyancy profiles is shown in figure 4.16. The entrainment coefficient α is selected, for each experiment, to be the value giving the lowest total (over all times a profile was taken) RMS error between the theoretical and experimental profiles. These values are listed in table 4.6. With these values of α , the RMS error at late times is low, less than 6% of the maximum theoretical dimensionless ambient buoyancy at each timestep, which is less than the scatter in the experimental data. We thus conclude that the peeling plume model is appropriate for describing the ambient buoyancy profile that develops in a sealed space with a vertically distributed buoyancy source, whose strength is decreasing linearly with time.

A possible reason for the difference between the theoretical and experimental profiles near the first front, the kink, is explained in the schematic in figure 4.17. In the peeling plume model, we assume that, once the first front has passed a particular height, the dense fluid added by the source at that height is added directly to the ambient at that height. In

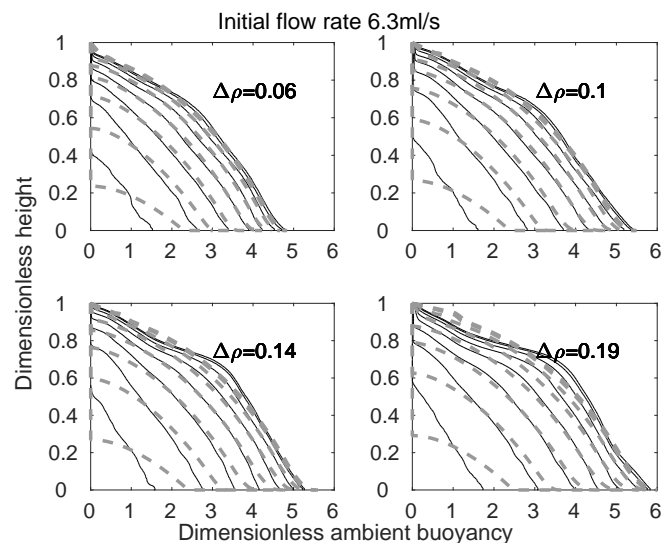


Fig. 4.14 Dimensionless ambient buoyancy profiles shown at 8 different times: 115s, 355s, 595s, 835s, 1075s, 1315s, 1555s, and 1795s (the 8 lines of each line style on each subplot) through each of 4 “ramp down” experiments (the 4 different subplots) with an initial flow rate of 6.3ml/s. Experimental profiles are shown by the thin, solid, black lines, and theoretical profiles using the peeling plume model are shown by the thicker, dashed, grey lines.

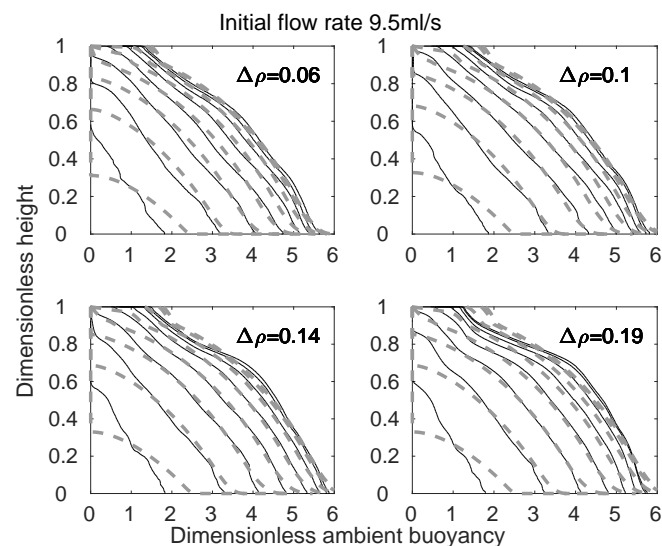


Fig. 4.15 Dimensionless ambient buoyancy profiles shown at 8 different times: 115s, 355s, 595s, 835s, 1075s, 1315s, 1555s, and 1795s (the 8 lines of each line style on each subplot) through each of 4 “ramp down” experiments (the 4 different subplots) with an initial flow rate of 9.5ml/s. Experimental profiles are shown by the thin, solid, black lines, and theoretical profiles using the peeling plume model are shown by the thicker, dashed, grey lines.

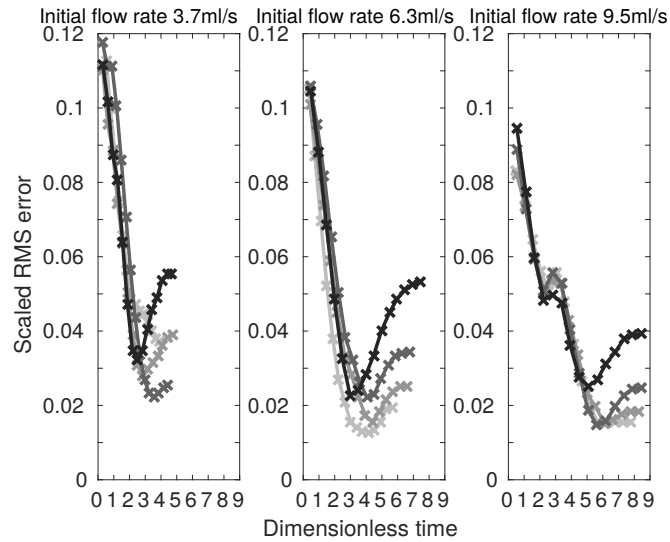


Fig. 4.16 RMS error between the theoretical and the experimental profiles, divided by the maximum dimensionless ambient buoyancy from theory at each timestep, for the “ramp down” experiments. Each subplot is for one slope of ramp, and each line is one experiment, with lighter coloured lines corresponding to experiments with smaller source densities. The crosses on each line are for each time that a profile is taken and compared.

Experiment	α
A_{down}	0.01
B_{down}	0.01
C_{down}	0.008
D_{down}	0.008
E_{down}	0.014
F_{down}	0.014
G_{down}	0.012
H_{down}	0.012
I_{down}	0.018
J_{down}	0.016
K_{down}	0.014
L_{down}	0.012

Table 4.6 The value of the entrainment coefficient α that minimises total RMS error between the experimental and theoretical (peeling plume) profiles, for each “ramp down” experiment.

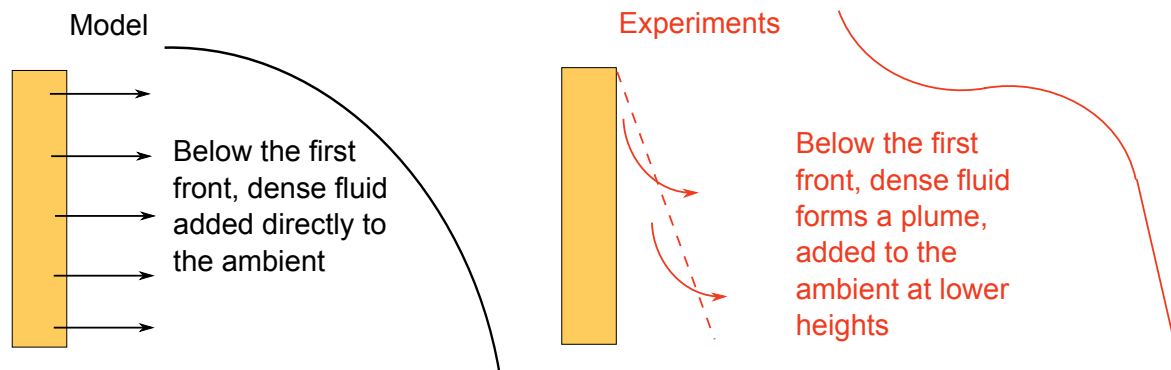


Fig. 4.17 Schematic showing why the model and experiments give different stratifications near the first front.

practice, however, we expect a plume to form, which descends and adds the dense fluid into the ambient at lower heights within the tank. This plume could explain the difference in the profile shapes between theory and experiments.

4.4.2 “Ramp up” in source buoyancy flux

For a “ramp up” in source buoyancy flux, a one-way-entrainment model better describes the ambient buoyancy profiles than the peeling plume model does. This difference between the models is seen by comparing figures 4.18, 4.19, and 4.20 which show experimental and peeling plume model ambient buoyancy profiles, with figures 4.21, 4.22, and 4.23, which show experimental and one-way-entrainment model ambient buoyancy profiles. In figures 4.18, 4.19, and 4.20, the peeling plume model fails to capture the experimental ambient buoyancy profile near the bottom of the tank accurately, in that there is a large change in curvature near the bottom of the tank in the theoretical profiles which is absent in the experimental profiles. The one-way-entrainment model, however, as shown in figures 4.21, 4.22, and 4.23, gives a better agreement between the experimental and theoretical profiles.

The entrainment coefficient α is selected, for each experiment, to have the value that gives the lowest total (over all times a profile was taken) RMS error between the theoretical and experimental profiles. These values of α are listed in table 4.7 for both the one-way-entrainment and peeling plume models.

The difference between the one-way-entrainment and peeling plume models is seen further by comparing the RMS error between theoretical and experimental profiles (divided by the maximum dimensionless ambient buoyancy from theory for each experiment), looking at the bottom tenth of the tank, for the two theoretical models. This comparison is shown in figure 4.24, where the grey lines are for the one-way-entrainment model, and the orange lines

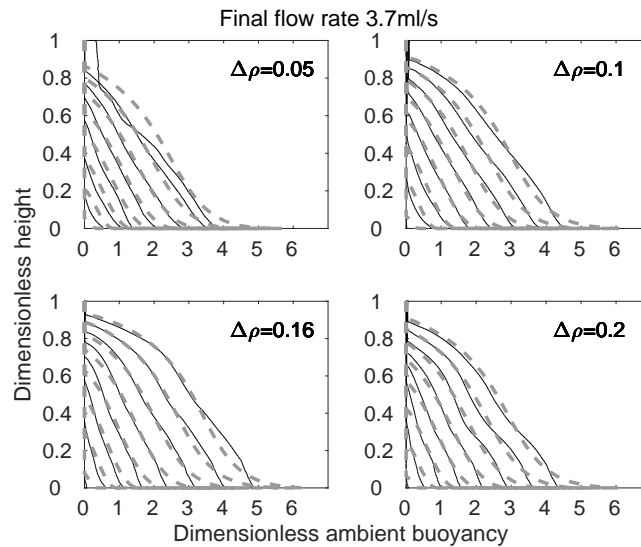


Fig. 4.18 Dimensionless ambient buoyancy profiles shown at 8 different times: 115s, 355s, 595s, 835s, 1075s, 1315s, 1555s, and 1795s through each of 4 “ramp up” experiments (one subplot for each experiment) with a final flow rate of 3.7ml/s. Experimental profiles are shown by the thin, solid, black lines, and theoretical profiles using the peeling plume model are shown by the thicker, dashed, grey lines.

are for the peeling plume model. In each subplot, the grey lines are below the corresponding orange lines at late times: the one-way-entrainment model gives lower RMS error between the theoretical and experimental profiles, so is the more appropriate model.

The one-way-entrainment model, as well as being better than the peeling plume model, also gives low RMS error over the whole profile. Figure 4.25 shows the RMS error between the dimensionless ambient buoyancy profiles from the one-way-entrainment model and from the experiments, divided by the maximum dimensionless ambient buoyancy from theory, at each timestep plotted. The scaled RMS error decreases, overall, with time, and is, with the exception of one experiment, below 6% of the maximum dimensionless ambient buoyancy at late times. During experiment A_{up} , shown by the lightest grey line on the left hand panel of figure 4.25, the RMS error increases by a large amount at the last time step because the source fluid ran out shortly before the end of the experiment, and so we expect experimental and theoretical profiles to differ there.

Physically, it makes sense that a one-way-entrainment model is more appropriate for describing ambient buoyancy profiles from a source that “ramps up” than a peeling plume model, because we expect entrainment to remain important. For a “ramp up” in source buoyancy flux, the plume is driven by an increasingly large source buoyancy flux, and is descending into a relatively weak stratification, made up of fluid added by the plume at earlier

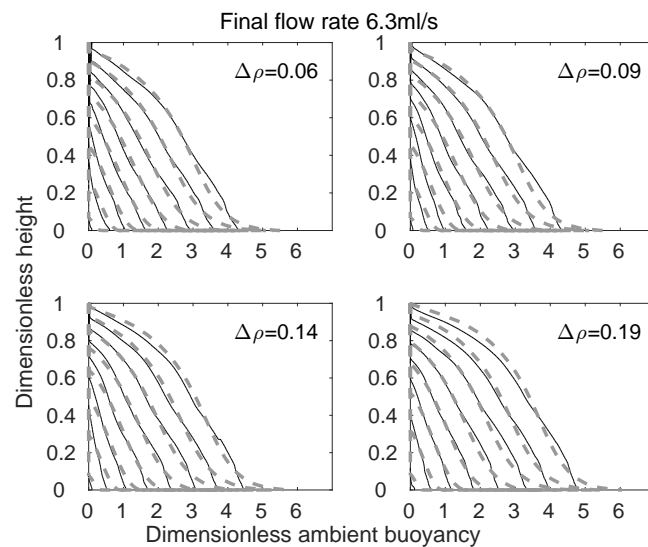


Fig. 4.19 Dimensionless ambient buoyancy profiles shown at 8 different times: 115s, 355s, 595s, 835s, 1075s, 1315s, 1555s, and 1795s through each of 4 “ramp up” experiments (one subplot for each experiment) with a final flow rate of 6.3ml/s. Experimental profiles are shown by the thin, solid, black lines, and theoretical profiles using the peeling plume model are shown by the thicker, dashed, grey lines.

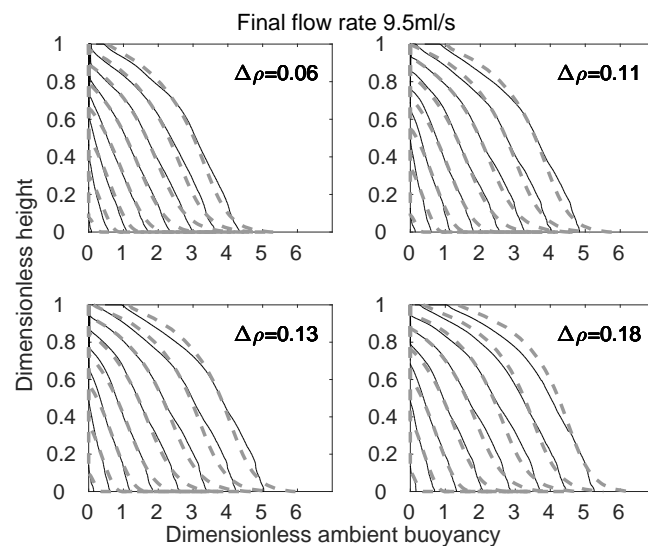


Fig. 4.20 Dimensionless ambient buoyancy profiles shown at 8 different times: 115s, 355s, 595s, 835s, 1075s, 1315s, 1555s, and 1795s through each of 4 “ramp up” experiments (one subplot for each experiment) with a final flow rate of 9.5ml/s. Experimental profiles are shown by the thin, solid, black lines, and theoretical profiles using the peeling plume model are shown by the thicker, dashed, grey lines.

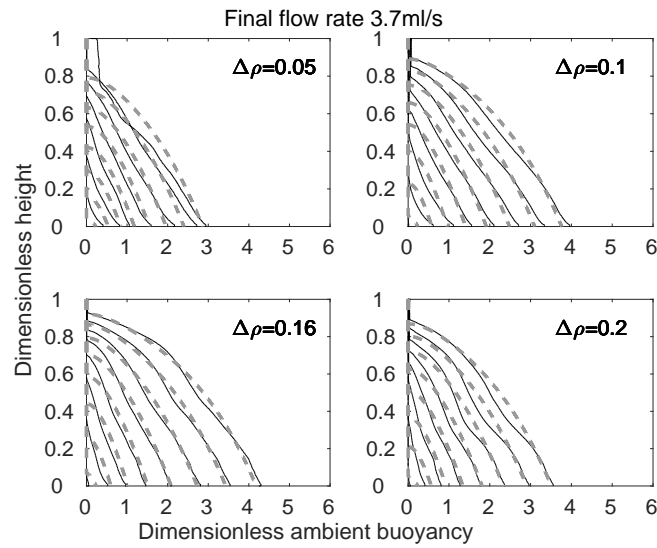


Fig. 4.21 Dimensionless ambient buoyancy profiles shown at 8 different times: 115s, 355s, 595s, 835s, 1075s, 1315s, 1555s, and 1795s through each of 4 “ramp up” experiments (one subplot for each experiment) with final source flow rate 3.7ml/s. Experimental profiles are shown by the thin, solid, black lines, and theoretical profiles using the one-way-entrainment model are shown by the thicker, dashed, grey lines.

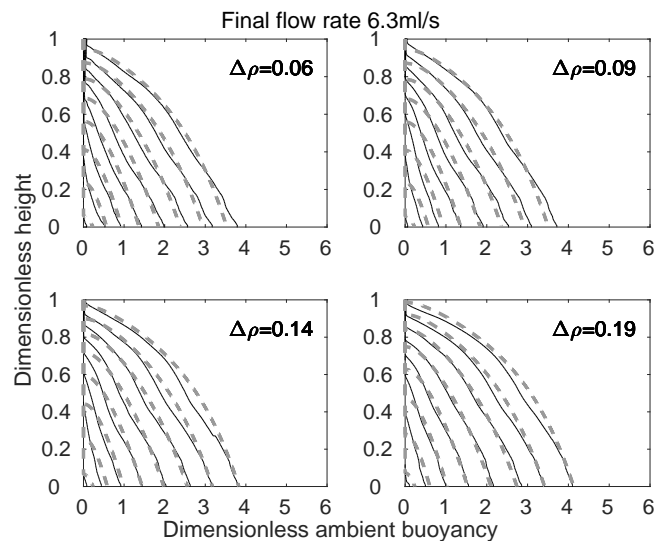


Fig. 4.22 Dimensionless ambient buoyancy profiles shown at 8 different times: 115s, 355s, 595s, 835s, 1075s, 1315s, 1555s, and 1795s through each of 4 “ramp up” experiments (one subplot for each experiment) with final source flow rate 6.3ml/s. Experimental profiles are shown by the thin, solid, black lines, and theoretical profiles using the one-way-entrainment model are shown by the thicker, dashed, grey lines.

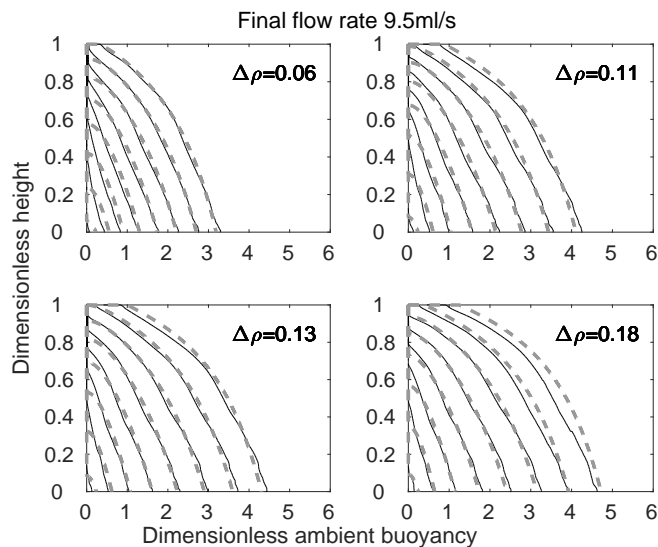


Fig. 4.23 Dimensionless ambient buoyancy profiles shown at 8 different times: 115s, 355s, 595s, 835s, 1075s, 1315s, 1555s, and 1795s through each of 4 “ramp up” experiments (one subplot for each experiment) with final source flow rate 9.5ml/s. Experimental profiles are shown by the thin, solid, black lines, and theoretical profiles using the one-way-entrainment model are shown by the thicker, dashed, grey lines.

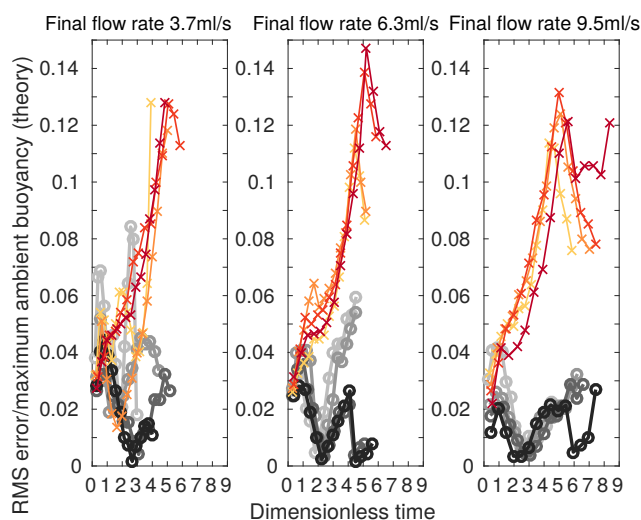


Fig. 4.24 RMS error between theoretical and experimental profiles for the “ramp up” experiments, looking at the bottom tenth of the tank, where the difference between the two models is located. The thick grey lines with circles are for the one-way-entrainment model, and the thin orange lines with crosses are for the peeling plume model. Each subplot is for one slope of ramp, and each line is one experiment. The crosses/circles on each line are for each time that a profile is taken and compared.

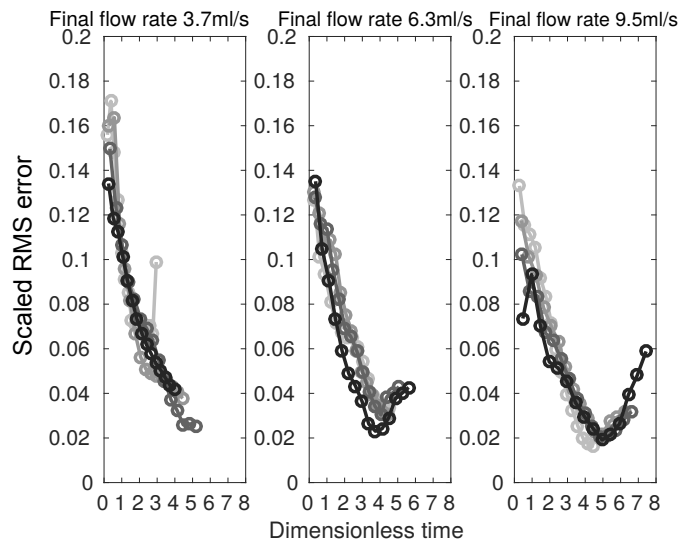


Fig. 4.25 RMS error between theoretical and experimental profiles for the “ramp up” experiments, divided by the maximum dimensionless ambient buoyancy from theory at each timestep - each circle - that a profile is taken and compared. Each subplot is for one slope of ramp, and each line is one experiment, with lighter shaded lines corresponding to smaller source densities. Values of the entrainment coefficient α are taken from table 4.7.

times, when the source buoyancy flux was smaller. We expect the plume, since it is driven by an increasingly large source buoyancy flux, to be able to “punch through” the ambient stratification to the bottom of the tank, with little detrainment occurring as the plume descends. The descending, turbulent plume is then expected to entrain fluid in the stratified region, as shown in the schematic in figure 4.26. The one-way-entrainment model, while neglecting the small amount of peeling, or detrainment, that happens, includes this entrainment in the stratified region, whereas the peeling plume model specifically neglects this entrainment. Some detrainment does occur, as seen in figure 4.7, where dyed plume fluid intrudes into the ambient at intermediate heights, but the ambient buoyancy profiles suggest that entrainment in the stratified region has a more significant effect on the ambient buoyancy profiles than detrainment does. In summary, therefore, a one-way-entrainment model is the appropriate model for describing ambient buoyancy profiles from our sources that “ramp up” in time.

4.4.3 A source buoyancy flux that mimics the solidification of PCM

The source buoyancy flux that mimics the solidification of PCM is made up of a “ramp down”, followed by a constant flux section, and finally another “ramp down”, as given by equation (4.2). Since a peeling plume model describes both “ramp down” and constant flux

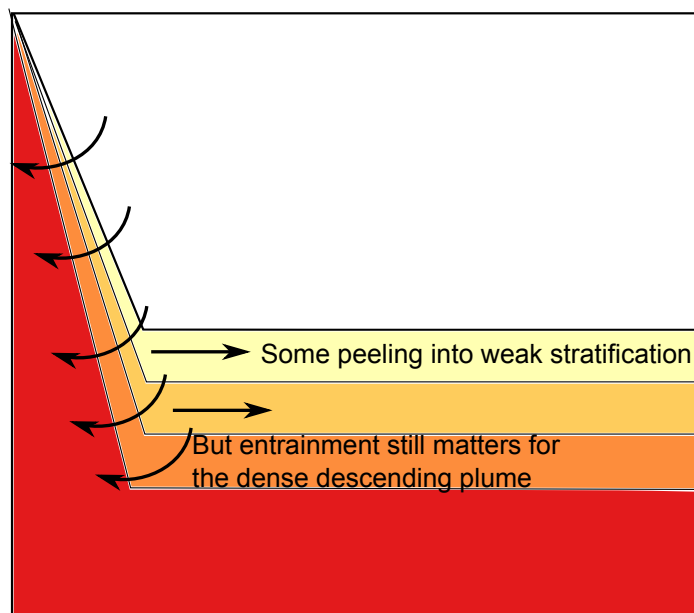


Fig. 4.26 Schematic showing that, although some peeling occurs, entrainment in the stratified region is still important.

Experiment	Entrainment coefficient, α	
	One-way-entrainment model	Peeling plume model
A_{up}	0.008	0.012
B_{up}	0.010	0.012
C_{up}	0.010	0.012
D_{up}	0.006	0.008
E_{up}	0.010	0.012
F_{up}	0.008	0.010
G_{up}	0.008	0.010
H_{up}	0.008	0.010
I_{up}	0.008	0.012
J_{up}	0.010	0.012
K_{up}	0.010	0.012
L_{up}	0.010	0.012

Table 4.7 The value of the entrainment coefficient that minimises total RMS error between the experimental and theoretical profiles, for each “ramp up” experiment, for both the one-way-entrainment model and the peeling plume model.

buoyancy sources, a peeling plume model is used to describe the stratification that develops with a source buoyancy flux that mimics the solidification of PCM. Theoretical (thick, dashed, grey lines) and experimental profiles (thin, solid, black lines) are shown in figure 4.27. The value of the entrainment coefficient chosen is $\alpha = 0.012$, which minimises the total RMS error between the theoretical and experimental profiles.

The peeling plume model for the PCM mimicking experiments, which combines the peeling plume model for a “ramp down” source and for a constant source, describes the shape of the ambient profiles well over most of the height of the tank. As observed in section 4.2.5, the first front rises quickly, and once it has reached the top of the tank, the shape of the profiles remains the same, as they are simply translated to the right as dense fluid is added by the source. Over most of the height of the tank, the peeling plume model describes the experimental profiles well, but at the bottom of the tank, the model and experiments differ. The model has a large change in curvature near to the bottom of the tank, whereas this change in curvature is absent from the experimental profiles. A possible reason for this difference is that, once the stratified region fills the whole tank, entrainment in the stratified region becomes of comparable importance to detrainment. The one-way-entrainment model includes entrainment in the stratified region, but neglects detrainment, whereas the peeling plume model neglects entrainment in the stratified region, but includes detrainment. The profiles would then be, we expect, somewhere between the shape of the one-way-entrainment profiles, with no large change in curvature at the bottom of the tank, and the peeling plume profiles, with a large change in curvature at the bottom of the tank. Away from the bottom of the tank, the shape of the profiles agrees well between theory and experiment, and the RMS error, scaled by the maximum theoretical dimensionless ambient buoyancy at each time step, is low (less than 2% at late times), as shown in figure 4.28.

4.5 Using the PCM mimicking source model to inform design decisions

The experiments have given us confidence that the PCM mimicking model describes the stratification that develops in a space with a vertically distributed source whose buoyancy flux “ramps down”, is constant, and then “ramps down” again. We now use this model to inform design decisions for the use of PCM in buildings. A key aspect of how effectively PCM walls perform is how long they take to completely solidify, since, during this time, they remain at an approximately constant temperature. To explore the effects of the solidification time on the stratification in a sealed space, we apply the PCM mimicking source model of section

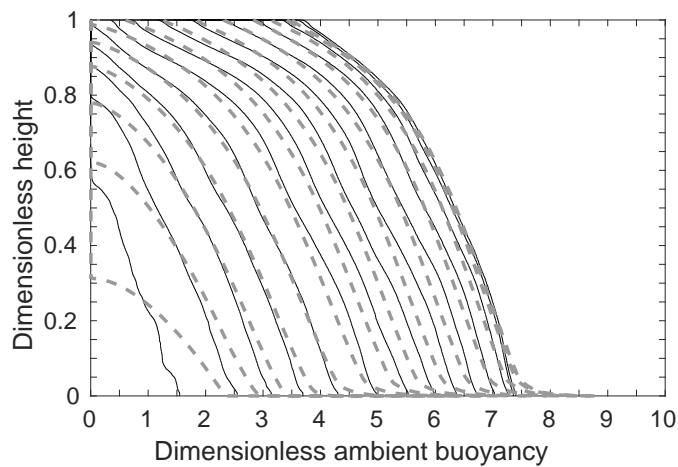


Fig. 4.27 Dimensionless ambient buoyancy profiles for the PCM mimicking experiment shown at 14 different times, starting at $115s = 0.5\tau$, and shown every $240s = 1.1\tau$. Experimental profiles are shown by the thin, solid, black lines, and theoretical profiles using the peeling plume model are shown by the thicker, dashed, grey lines. The entrainment coefficient used is $\alpha = 0.012$.

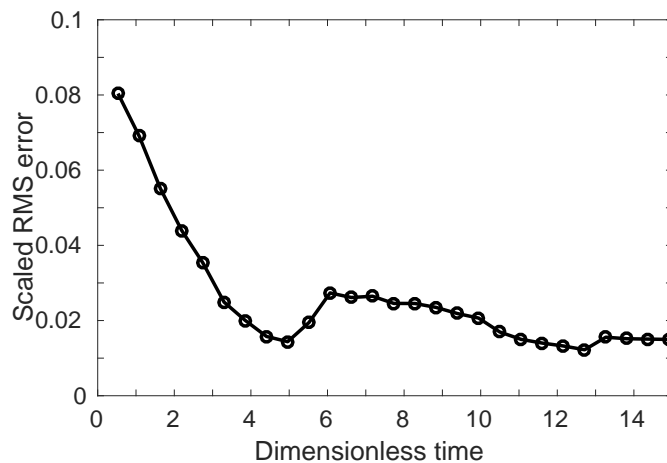


Fig. 4.28 RMS error between theoretical (peeling plume model) and experimental profiles, divided by maximum dimensionless ambient buoyancy at each time profiles were compared, for the PCM mimicking experiment. Each circle corresponds to a time at which a profile is measured and compared with the theory.

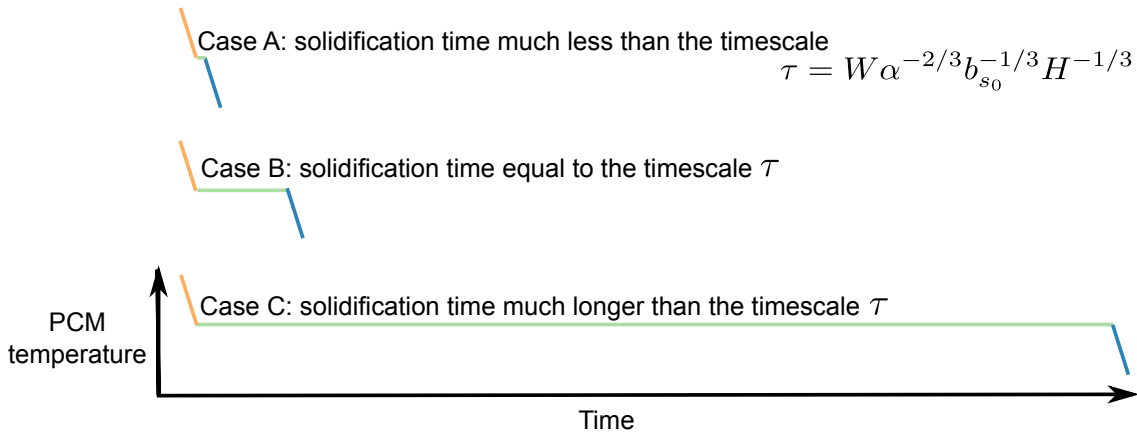


Fig. 4.29 Three cases to be studied using the PCM mimicking source model. Case A has solidification time $t_s \ll \tau$, case B has $t_s = \tau$, and case C has $t_s \gg \tau$.

4.4.3 to three cases: a room with little PCM, giving a solidification time t_s that is much less than the timescale $W \alpha^{-2/3} b_{s0}^{-1/3} H^{-1/3} = \tau$, a room with sufficient PCM that $t_s = \tau$, and a room with a large amount of PCM, so that $t_s \gg \tau$. These three cases are shown schematically in figure 4.29. In each of the cases, the two ramp times are taken, for simplicity, to be equal, with $a_1 = a_2 = 10$, which corresponds to $t_{r1} = t_{r2} = 0.1\tau$. The ramp times are taken to be much less than the timescale τ because we expect the amount of heat stored as sensible heat in the PCM, which gives rise to the ramp sections of the source buoyancy flux, to be less than the amount of heat stored as latent heat in the PCM. If the amount of latent heat, given in the right hand side of (4.3), is small compared with the amount of sensible heat, the sum of the right hand side of (4.5) and the equivalent expression for the second ramp down, the amount of PCM or the PCM melting temperature has been incorrectly selected. The ratio of the initial and constant source buoyancy fluxes is taken to be $b_{s1}/b_{s0} = 1/2$ in each case, for simplicity. In case A, $a_s = \tau/t_s = 10$, in case B, $a_s = \tau/t_s = 1$, and in case C, $a_s = \tau/t_s = 0.1$.

When the source buoyancy flux becomes zero, at time $t_{r1} + t_s + t_{r2}$, the dimensionless ambient buoyancy profiles from each of the three cases are as shown in figure 4.30. The dot-and-dash line shows case A, where $t_s \ll \tau$, the dashed line shows case B, where $t_s = \tau$, and the solid line shows case C, where $t_s \gg \tau$. In case A, most of the height of the room remains at the initial ambient temperature, with only the very top part of the room being stratified. In case B, the top half of the room is now stratified, but it is only in case C that the majority of the room has been heated by the PCM solidifying. When designing a room with PCM, we thus require the solidification time t_s to be much larger than the timescale τ . Combining the expression (4.4) for the solidification time t_s with the timescale $\tau = W \alpha^{-2/3} b_{s0}^{-1/3} H^{-1/3}$,

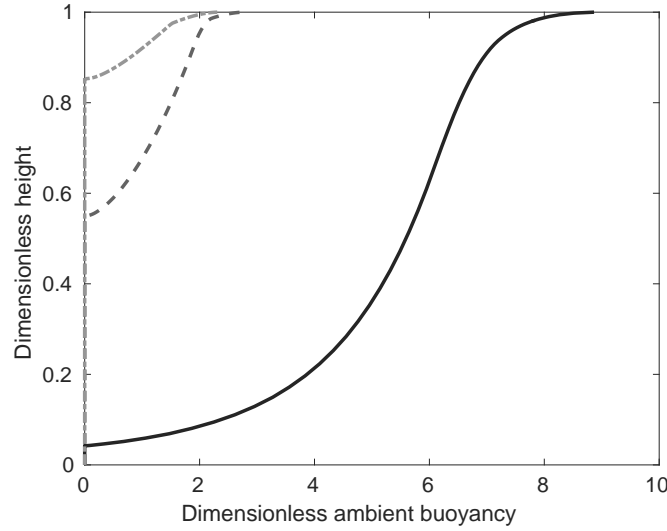


Fig. 4.30 The final dimensionless ambient buoyancy profiles for case A (dot-and-dash line), case B (dashed line), and case C (solid line).

this gives a restriction on the wall thickness l_{pcm} ,

$$l_{\text{pcm}} \gg \frac{Wh(\theta_{\text{max}} - \theta_1)}{\rho\alpha^{2/3}b_{s0}^{1/3}H^{1/3}\phi L}, \quad (4.85)$$

where W is the room width, h is the convection coefficient, θ_{max} is the maximum PCM melting/solidifying temperature, θ_1 is the initial ambient temperature, ρ is the wall density, α is the entrainment coefficient, $b_{s0} = \frac{g\beta}{\rho_{\text{air}}C_{\text{air}}}h(\theta_{\text{start}} - \theta_1)$ is the initial source buoyancy flux per unit source area, H is the room height, ϕ is the mass fraction of PCM, L is the PCM latent heat, g is gravitational acceleration, β is the thermal expansion coefficient, ρ_{air} is the density of air, C_{air} is the specific heat capacity of air, and θ_{start} is the initial PCM temperature. Using $W = 4\text{m}$ and $H = 2.5\text{m}$ (as used in section 4.2.2), with all the other parameter values as given in table 4.5 for Knauf Comfortboard, we find that we require $l_{\text{pcm}} \gg 0.0007\text{m}$. With $l_{\text{pcm}} = 0.0125\text{m}$ in the calculations of section 4.2.2 and the real life data collection of appendix A, this minimum wall thickness is exceeded, and we have $t_s = 17.9\tau \gg \tau$, as required.

The PCM mimicking model is a simplification of a real PCM wall, because, in the model, the source buoyancy flux is calculated using the PCM temperature and the initial ambient temperature, with no coupling between the developing ambient temperature profile and the source buoyancy flux. In a real room, however, the source buoyancy flux depends on the difference between the PCM temperature and the ambient temperature (which varies with

height and in time). To include this coupling between the ambient temperature and source buoyancy flux, we use a source buoyancy flux

$$b_s = \frac{g\beta h}{\rho_{\text{air}} C_{\text{air}}} (\theta_{\text{pcm}} - \theta_1 - (\theta_a(z, t) - \theta_1)), \quad (4.86)$$

where θ_a is the ambient temperature, which varies with height z and in time t . The difference between the PCM temperature θ_{pcm} and the initial ambient temperature θ_1 is

$$\theta_{\text{pcm}} - \theta_1 = \begin{cases} \theta_{\text{start}} - \theta_1 + \frac{(\theta_{\text{max}} - \theta_1 - (\theta_{\text{start}} - \theta_1))t}{t_{r1}}, & t \leq t_{r1}, \\ \theta_{\text{max}} - \theta_1, & t_{r1} < t \leq t_{r1} + t_s, \\ (\theta_{\text{max}} - \theta_1) \left(\frac{t_{r1} + t_s + t_{r2}}{t_{r2}} - \frac{t}{t_{r2}} \right), & t_{r1} + t_s < t \leq t_{r1} + t_s + t_{r2}. \end{cases} \quad (4.87)$$

Defining

$$b_{s0} = \frac{g\beta h}{\rho_{\text{air}} C_{\text{air}}} (\theta_{\text{start}} - \theta_1), \quad b_{s1} = \frac{g\beta h}{\rho_{\text{air}} C_{\text{air}}} (\theta_{\text{max}} - \theta_1), \quad (4.88)$$

we find that the dimensionless source buoyancy flux $B_s = b_s/b_{s0}$ is

$$B_s = \begin{cases} 1 - \left(1 - \frac{b_{s1}}{b_{s0}}\right) a_1 T - \frac{\theta_a - \theta_1}{\theta_{\text{start}} - \theta_1}, & T \leq \frac{1}{a_1}, \\ \frac{b_{s1}}{b_{s0}} \left(1 - \frac{\theta_a - \theta_1}{\theta_{\text{max}} - \theta_1}\right), & \frac{1}{a_1} < T \leq \frac{1}{a_1} + \frac{1}{a_s}, \\ \frac{b_{s1}}{b_{s0}} \left(\frac{a_2}{a_1} + \frac{a_2}{a_s} + 1 - a_2 T - \frac{\theta_a - \theta_1}{\theta_{\text{max}} - \theta_1}\right), & \frac{1}{a_1} + \frac{1}{a_s} < T \leq \frac{1}{a_1} + \frac{1}{a_s} + \frac{1}{a_2}. \end{cases} \quad (4.89)$$

Now, the change in ambient temperature can be written in terms of the ambient buoyancy, $(\theta_a - \theta_1) = (g\beta)^{-1} \delta_a = (g\beta)^{-1} \alpha^{-2/3} b_{s0}^{2/3} H^{-1/3} \Delta_a$, so

$$\frac{\theta_a - \theta_1}{\theta_{\text{start}} - \theta_1} = \frac{\delta_a}{g\beta (\theta_{\text{start}} - \theta_1)} = \left(\frac{g\beta (\theta_{\text{start}} - \theta_1) H}{\left(\frac{h}{\alpha \rho_{\text{air}} C_{\text{air}}}\right)^2} \right)^{-1/3} \Delta_a = \alpha^{-2/3} Ri_{\text{conv}}^{-1/3} \Delta_a, \quad (4.90)$$

where Ri_{conv} is a Richardson number with a velocity scale based on the convection coefficient and properties of air, $h/(\rho_{\text{air}} C_{\text{air}})$. Substituting (4.90) into (4.89) gives a dimensionless source buoyancy flux per unit source area of

$$B_s = \begin{cases} 1 - \left(1 - \frac{b_{s1}}{b_{s0}}\right) a_1 T - \alpha^{-2/3} Ri_{\text{conv}}^{-1/3} \Delta_a, & T \leq \frac{1}{a_1}, \\ \frac{b_{s1}}{b_{s0}} \left(1 - \alpha^{-2/3} Ri_{\text{conv}}^{-1/3} \Delta_a\right), & \frac{1}{a_1} < T \leq \frac{1}{a_1} + \frac{1}{a_s}, \\ \frac{b_{s1}}{b_{s0}} \left(\frac{a_2}{a_1} + \frac{a_2}{a_s} + 1 - a_2 T\right) - \alpha^{-2/3} Ri_{\text{conv}}^{-1/3} \Delta_a, & \frac{1}{a_1} + \frac{1}{a_s} < T \leq \frac{1}{a_1} + \frac{1}{a_s} + \frac{1}{a_2}. \end{cases} \quad (4.91)$$

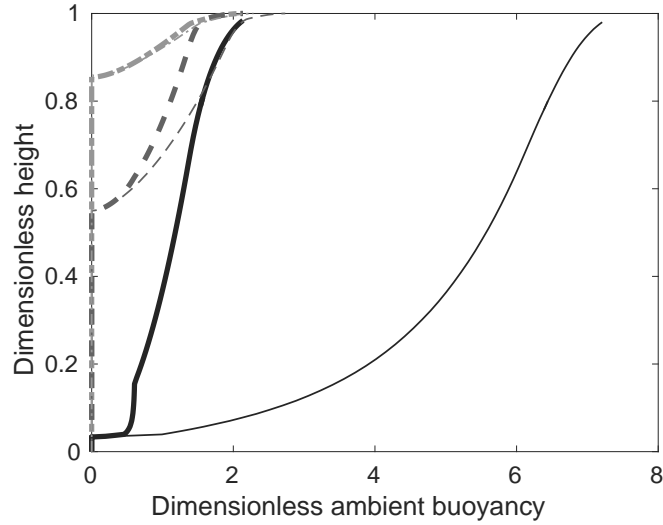


Fig. 4.31 The final dimensionless ambient buoyancy profiles for case A (dot-and-dash line), case B (dashed line), and case C (solid line). The new model, with the source buoyancy flux varying with the ambient temperature, is shown by the thick lines, while the old model, with a source buoyancy flux that depends on the initial ambient temperature only, is shown by the thin lines.

Since, in this section, we only consider PCM solidifying and acting as a heat source, if B_s as given in (4.91) becomes negative, we simply replace that value of B_s with zero. The peeling plume model is used as in section 4.3.3, but equation (4.84) becomes

$$\Delta_i^{\text{new}} = \Delta_i^{\text{old}} + \int_{T_{ff_i}}^T B_s(Z_i, T) dT. \quad (4.92)$$

The final ambient buoyancy profiles for cases A, B, and C when using this improved PCM mimicking model, which has a source buoyancy flux that depends on the difference between the PCM temperature and (time-and-height-varying) ambient temperature, are shown in figure 4.31. The thick lines show the new model, with the source buoyancy flux coupled to the ambient temperature, using $\alpha^{-2/3} Ri_{\text{conv}}^{-1/3} = 0.77$, calculated from the parameter values in table 4.5 with $H = 2.5\text{m}$. The thin lines show the old model, which has a source buoyancy flux that depends on the difference between the PCM temperature and the initial ambient temperature only. For case A, there is little difference between the two models, but for case C, the dimensionless ambient buoyancy is much lower with the new model than with the old model. In case C, the source heats the space for a long period of time, so the room heats up, and the temperature difference between the PCM and the room at later times is much smaller than it is initially, leading to a smaller source buoyancy flux at later times in

the new model. The new model is more physically realistic. When the ambient buoyancy profiles of figure 4.31 are converted to temperature profiles, using the parameter values from table 4.5, with $W = 4\text{m}$ and $H = 2.5\text{m}$, the resulting profiles are those shown in figure 4.32. The green rectangle indicates a temperature range of 1°C either side of the solidification temperature, which is a comfortable operative temperature within the room. For cases A and B, the part of the profile with temperatures within that comfortable range is towards the top of the room, away from where occupants are located. For case C, however, from a height of 0.1m up to 0.7m , which is within the occupied region of the room, temperatures are within the comfortable range of temperatures indicated by the green rectangle, including approximately 0.2m where temperatures are almost constant, at the PCM melting temperature of 23°C . The results of figure 4.32 strengthen the finding that, to use PCM effectively, we should select the PCM thickness so that the solidification time t_s is much longer than the timescale $\tau = W\alpha^{-2/3}b_{s0}^{-1/3}H^{-1/3}$, giving the restriction on how thin the wall can be,

$$l_{\text{pcm}} \gg \frac{Wh(\theta_{\text{max}} - \theta_1)}{\rho\alpha^{2/3}b_{s0}^{1/3}H^{1/3}\phi L}. \quad (4.93)$$

4.6 Conclusions

In this chapter, results from experiments with a time-varying, vertically distributed source are presented. Time-varying sources are relevant to the application of PCMs in buildings, since, when PCM solidifies, it provides a time-varying source buoyancy flux. Specifically, the solidification of PCM is approximated by a source buoyancy flux that “ramps down” in time, is then constant for some time, and finally “ramps down” to zero as the PCM wall temperature reaches the ambient temperature. Three types of time-varying source are considered: a “ramp down”, a “ramp up”, and a source that mimics the solidification of PCM.

With a “ramp down” in source buoyancy flux, the peeling plume model is appropriate for describing the stratification that forms in a sealed space with a vertically distributed buoyancy source. The peeling plume model captures the detrainment that occurs as plume fluid reaches its neutral buoyancy height at intermediate heights within the space. When comparing ambient buoyancy profiles from the peeling plume model with profiles from experiments, the RMS error between these profiles is low. At late times, it is less than 6% of the maximum theoretical dimensionless ambient buoyancy at each timestep.

For a “ramp up” in source buoyancy flux, however, a one-way-entrainment model is more appropriate than a peeling plume model. The RMS error between the theoretical and experimental ambient buoyancy profiles is lower at late times for the one-way-entrainment

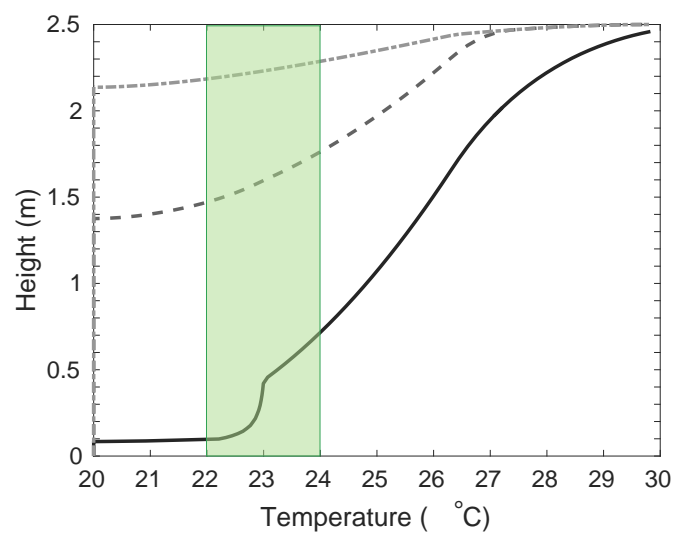


Fig. 4.32 The final temperature profiles for case A (dot-and-dash line), case B (dashed line), and case C (solid line). The green rectangle indicates temperature 1°C either side of the melting range. These temperatures are considered comfortable temperatures, and we aim to maintain temperatures in the occupied region of the room within this range. This is a preliminary result, and is by no means perfect. The wall thickness should be tuned to give comfortable temperatures over a wider range of heights in the room. This example shows, however, that the wall thickness needs to be such that the solidification time t_s is much greater than the timescale τ , as in case C, but just how much bigger is yet to be determined.

model than it is for the peeling plume model. The one-way-entrainment model being more appropriate makes sense physically, since a “ramp up” in source buoyancy flux gives an increasingly strong plume which is able to “punch through” the stratification, all the way to the bottom of the tank, with little detrainment, but with entrainment into the plume remaining important in the stratified region.

The stratification that develops in the PCM mimicking experiments is described by the peeling plume model, with a source buoyancy flux that “ramps down” to an intermediate value, then remains constant at that value for some time, and finally “ramps down” to zero. While the shapes of the experimental and theoretical profiles differ at the very bottom of the tank, the RMS error between the experimental and theoretical profiles, divided by the maximum theoretical dimensionless ambient buoyancy at each time profiles are compared, is less than 2% at late times, showing that the peeling plume model is appropriate. On applying the peeling plume model with a PCM mimicking source to three cases, each with a different solidification time, we find that, for the PCM to be effective, the solidification time should be much greater than the timescale τ , giving a restriction on how thin the PCM wall can be while remaining effective.

“Ramps down” and “ramps up” in source buoyancy flux from a vertically distributed source lead to different stratifications, and different models are required to describe them. For “ramps down” in source buoyancy flux, as for constant source buoyancy fluxes, the peeling plume model is appropriate, since it captures detrainment from the plume, which is important for a “ramp down” in source buoyancy flux. Once the stratified region fills the whole tank, however, the peeling plume model is only accurate away from the very bottom of the tank. For “ramps up” in source buoyancy flux, a one-way-entrainment model is more appropriate than a peeling plume model, since the one-way-entrainment model captures the entrainment by the plume in the stratified region, which the peeling plume model neglects. Indeed, this entrainment remains important for a “ramp up” in source buoyancy flux.

Chapter 5

Conclusions

In this thesis, three problems are presented that are motivated by the possibility of the use of phase change materials in buildings. In chapter 2, the temperature response of PCM wallboard to changes in room temperature is modelled, in a variety of realistic situations. In chapter 3, the stratification that develops in a space with a vertically distributed buoyancy source is considered, since PCM, included in a vertical wall, provides a vertically distributed buoyancy source when it solidifies. Detrainment is found to be important for a vertically distributed source. In chapter 4, the vertically distributed source now provides a source buoyancy flux that varies in time, since PCM solidification provides a time-varying vertically distributed buoyancy source. The results found in each of these chapters are summarised in section 5.1, and directions for future research are suggested in section 5.2.

5.1 Summary

5.1.1 PCM thermal mass reducing fluctuations in building temperature

The PCM thermal mass model of chapter 2 is used to calculate how temperatures in a wall containing PCM vary with both time and distance into the wall, in response to a room temperature that varies (typically sinusoidally) over the course of a day. To include the effect of the PCM's latent heat, an effective specific heat capacity is used. This effective specific heat capacity takes one value when the PCM temperature is within the range of temperatures at which the PCM melts and solidifies, and takes another value when the PCM temperature is outside this melting range. The model has five dimensionless parameters, which depend on properties of the PCM (its melting range and latent heat), properties of the wall (its density, specific heat capacity, thermal conductivity, and thickness), the amplitude

of room temperature variations, and a convection coefficient. These properties appear in five dimensionless parameters: the dimensionless convection rate, the dimensionless diffusivity, the Stefan number, the dimensionless minimum melting temperature, and the dimensionless maximum melting temperature.

Using the model, we find the “ideal” PCM mass fraction and wall thickness, defined as the smallest values still resulting in a $1 - 2^{\circ}\text{C}$ decrease in maximum interior wall surface temperature. The interior wall surface temperature is relevant because it affects occupant comfort. When parameter values for a salt hydrate PCM in a concrete wall are used, a PCM mass fraction of 0.4 with a wall thickness of 0.04m is ideal. These values give a reduction in maximum interior wall surface temperature of 1.7°C , but using extra PCM or a thicker wall has little effect. When parameter values for the same salt hydrate PCM, but in a wallboard wall, are used, a PCM mass fraction of 0.3 with a wall thickness of 0.03m, which reduces the maximum interior wall surface temperature by 1.3°C , is ideal.

Having found that the effectiveness of PCM varies with wall thickness, we consider three different distributions of PCM through the thermal mass, to find out which distribution is the most effective at reducing maximum interior wall surface temperatures. The three distributions considered are a uniform distribution (the PCM is distributed uniformly through the whole thickness of the thermal mass), a linear distribution (the amount of PCM varies linearly with depth into the thermal mass, with the largest amount of PCM at the interior wall surface, and no PCM at the external wall surface), and a step distribution (a uniform distribution of PCM from the interior wall surface up to some depth into the wall, and then no PCM beyond that point). We find that the linear distribution gives interior surface temperatures between those of the uniform and step distributions, so only the step and uniform (a step with PCM inclusion depth equal to the wall thickness) distributions are considered, as end cases. The penetration depth – the depth into the wall up to which PCM completely melts and solidifies over the course of a day – is key. If PCM is included far beyond this depth, the PCM at the back of the wall never completely melts and solidifies, and so is redundant. If, instead, PCM is only included up to a depth less than the penetration depth, the PCM melts before the excess heat is stored. The ideal step size for the step distribution is then the penetration depth.

We find an estimate of the penetration depth that depends only on known parameters. First, the variation of temperature with depth into the wall is approximated as linear until the temperature is within the melting range. The penetration depth is the depth into the wall at which the PCM temperature reaches this melting range. Beyond the penetration depth, we assume that the PCM temperature decays exponentially. With this approximate temperature profile, i.e. a linear variation from some temperature U_{hottest} (which we assume

varies sinusoidally in time, in phase with the room temperature) down to the melting range, and then exponential decay, we equate two ways of expressing the diurnal energy storage to calculate U_{hottest} in terms of known parameters. This U_{hottest} is then substituted into an expression for the penetration depth, giving an approximation to the penetration depth in terms of known parameters. This approximate value may be used to inform design decisions – PCM should be included to just beyond this penetration depth.

Some exterior wall surfaces are uninsulated, for example, surfaces cooled by cool air output by an exhaust air heat pump. In the model, this addition of cooling at the exterior surface simply requires a change in boundary condition at the exterior surface of the wall. Now, the heat flux through the exterior surface is proportional to the temperature difference between the wall and the cool air, whose temperature is specified and varies in time: a low temperature for 6 hours, then a higher temperature for 6 hours, and repeating. With cooling at the exterior, the “ideal” wall thickness changes – while a thick wall stores a large amount of heat, a thin wall allows the cooling at the exterior to influence temperatures in the room interior. We find that, for a wallboard wall containing a salt hydrate PCM, a PCM mass fraction of 0.3 with a wall thickness of 0.02m gives a substantial decrease in wall surface temperature, and larger values give little extra benefit. We also model a specified, sinusoidally varying, exterior temperature, with forced ventilation bringing exterior air into the room, and an additional power load (from, for example, a television, computer, or cooker), again allowing for time-varying cooling at the exterior wall surface. We solve for both the wall temperature and the room temperature, and find that, with a PCM mass fraction of 0.3 and a wall thickness of 0.02m, the interior surface temperature and interior air temperature both have smaller amplitude variations (by approximately 2°C) than the exterior air temperature has.

For PCM wallboard used on the ceiling of a naturally ventilated space, cooled above the ceiling, and with a localised heat source in the room, we extend the analysis of Livermore and Woods (2008) for a chilled ceiling to include PCM in the ceiling. Above the ceiling, the temperature is low for 6 hours, then higher for 6 hours, and this variation in temperature repeats. In a room with PCM and with cooling, the interface between the hot upper layer and the ambient air is at a lower height and the hot layer temperature and wall surface temperature are reduced by a large amount compared with a room without PCM and without cooling. Using cooling reduces temperatures overall, and using PCM smoothes out the variations in cooling temperature, both of which enhance occupant comfort.

Realistic room temperatures have different minima and maxima on different days, so we extend the model to include a more physically realistic period of hot weather in the middle of a period of normal weather. We find that, while the daily maximum surface temperature

increases (by a factor of 1.5) over the hot period, it is still reduced compared with the room temperature variations, and quickly recovers after the hot period. Using two PCMs with different melting temperatures, one for normal weather and another for hot weather, provides significant reduction of maximum interior surface temperatures during both normal weather and hot periods. The ideal proportion of each PCM depends on the desired conditions – are occasional temperature peaks acceptable, or must temperatures always be below some value?

In appendix A, temperature data collected in two real apartments, one containing PCM wallboard, and the other without PCM, is presented. Autumn data shows reduced temperatures in the apartment with PCM compared with the apartment without PCM, and winter data shows, as expected, little difference between the apartments. Unfortunately, summer data could not be collected, but the promising autumn results suggest that it is worthwhile collecting summer data, to strengthen the conclusion that PCM reduces summer overheating.

Overall, our theoretical model shows that PCM substantially reduces temperature fluctuations, in a range of realistic situations. It is important to select the “ideal” wall thickness and PCM mass fraction, and the general, but relatively simple, models presented in chapter 2 can be used to inform such decisions. Lower measured temperatures in an apartment containing PCM compared with an apartment without PCM (both measured in autumn) suggest that PCM is beneficial in reducing summer overheating, and further data collection is worthwhile.

5.1.2 Detrainment of plumes from vertical sources

The theoretical model of chapter 2 gives overall room temperatures, but to find the temperature stratification within the room, an alternative approach is needed. Chapter 3 is the first step in this approach. Since PCM in walls releases heat – and so acts as a buoyancy source – when it solidifies, we consider the stratification that develops in a sealed space containing a vertically distributed buoyancy source. We carry out analogue laboratory experiments, using a tank of fresh water to represent the room, and salt water to provide the density differences.

First, 20 experiments with a line source are carried out, each with a different combination of source density and source flow rate. The source consists of 3 tubes, through which salt water is pumped, that are spread in a horizontal line across one wall of the tank. The experimental ambient buoyancy profiles agree with established theory, suggesting that producing a distributed source by spreading out several individual sources works. In these line source experiments, plume fluid descends to the very bottom of the tank before spreading into the ambient.

With a vertically distributed source (a 4 x 3 grid of tubes spread across the tank wall), however, the plume fluid detrains in each of the 20 full wall source experiments, intruding into the ambient at intermediate heights. A one-way-entrainment model, which neglects this

detrainment, gives qualitatively different ambient buoyancy profiles from those measured in experiments. Instead, a peeling plume model is used, in which plume density and vertical velocity are assumed to vary linearly across the width of the plume. At intermediate heights, outer layers of the plume peel off into the ambient as they reach their neutral buoyancy height. The peeling plume model better describes the experimental ambient buoyancy profiles, with a lower RMS error between the theoretical and experimental profiles for the peeling plume model than for the one-way-entrainment model.

When the source is distributed over only half of the wall height, detrainment is no longer observed (in any of the 20 half wall source experiments), and a one-way-entrainment model is appropriate for describing the ambient buoyancy profiles. For a half wall source, since the plume has a smaller height over which dense fluid is being added at the wall, we expect the variation in density across the width of the plume to be small, with plume density almost constant across the width of the plume, so no peeling is expected. A one-way-entrainment model is thus appropriate, as shown by the low (compared with scatter in the experimental data) RMS error between the experimental and theoretical ambient buoyancy profiles for the one-way-entrainment model.

Overall, experiments with three types of buoyancy source: a line source, a full wall source, and a half wall source, in a sealed space, show that different physical processes govern the plumes produced by the three different sources, and so different models are used. For line sources and half wall sources, entrainment into the plume is one-way, with the plume descending all the way to the bottom of the tank before spreading into the ambient, and a one-way-entrainment model is appropriate for describing the ambient buoyancy profiles that develop in the space. For full wall sources, however, the plume detrains, intruding into the ambient at intermediate heights, and a peeling plume model, which includes this detrainment, is appropriate for describing the ambient buoyancy profiles that develop in the space.

5.1.3 Time-varying, vertically distributed buoyancy sources

Chapter 4 is the second part in our approach to describing the temperature stratification that develops in a space containing PCM wallboard. When PCM solidifies, its temperature varies in time, and so it acts as a time-varying buoyancy source. In chapter 4, experimental results and theoretical models are presented for the stratification that develops in a sealed space with a time-varying, vertically distributed buoyancy source. Experiments are carried out with a vertically distributed source, set up as in chapter 3, but now the source buoyancy flux is varied in time, by varying the source flow rate over the course of an experiment. Three types of source are used: linear “ramps down” to zero, linear “ramps up” from zero, and PCM mimicking sources, which consist of an initial “ramp down” to some non-zero value,

followed by a constant flux section at that non-zero value, and, finally, a second “ramp down” to zero.

For “ramp down” sources, we find that, apart from just below the first front, a peeling plume model describes the ambient buoyancy profiles well. Just below the first front, the experimental profiles flatten out, forming a “kink”, which the model fails to predict. A reason for this difference between the model and experiments is that the model assumes that, in the stratified region, dense fluid is added directly to the ambient, but in reality, this dense fluid descends some way as a plume, and is added to the ambient at a lower height. Apart from the kink, the experimental ambient buoyancy profiles are well described by the peeling plume model. Specifically, at late times, the RMS error between theoretical and experimental profiles is less than 6% of the maximum theoretical dimensionless ambient buoyancy at that time.

For “ramp up” sources, a one-way-entrainment model is used, since the peeling plume model predicts a large change in curvature near the bottom of the tank, which is inconsistent with experimental results. A one-way-entrainment model gives lower RMS error over the bottom tenth of the tank than the peeling plume model gives, and also has, at late times, an RMS error over the whole tank of less than 6% of the maximum theoretical dimensionless ambient buoyancy at that time. The good agreement between the experimental and one-way-entrainment model ambient buoyancy profiles suggests that detrainment, although observed in experiments, plays a less important role than entrainment plays in the stratified region. Physically, entrainment remaining important makes sense, since a plume from a source that “ramps up” in time gets stronger in time, and is better able to “punch through” the stratification, and descend to the bottom of the tank with little detrainment.

For a PCM mimicking source, made up of two “ramps down”, with a constant flux section in between, a peeling plume model describes the ambient buoyancy profiles well over the majority of the source height. Once the entire space is filled with dense fluid, the theoretical profiles show a large change in curvature near the bottom of the tank, which is absent in the experimental profiles. A reason for this difference in theoretical and experimental profiles is that, once the stratified region fills the whole space, entrainment in the stratified region becomes of comparable importance to detrainment, so we expect a profile between that of the peeling plume model and the one-way-entrainment model to be appropriate. Despite this difference at the very bottom of the tank, the peeling plume model captures the rest of the profile well. In both the peeling plume model and in experiments, the first front rises quickly through the space, so the stratified region fills the space for most of the experiment, and then the shape of the profiles changes very little, as they are simply translated to the right, i.e. to larger and larger average densities. We apply the peeling plume model with a

PCM mimicking source to three cases, with a different solidification time in each case, and find that, for PCM to be effective, the solidification time should be much greater than the timescale $\tau = W\alpha^{-2/3}b_{s_0}^{-1/3}H^{-1/3}$, as given in (4.42), which gives a restriction on how thin the PCM wall can be, whilst remaining effective.

In chapter 4, experiments with time-varying, vertically distributed buoyancy sources show that sources that “ramp down” in time and sources that “ramp up” in time give different stratifications. These different stratifications are captured by different models: a peeling plume model for “ramp down” sources, and a one-way-entrainment model for “ramp up” sources. To mimic PCM solidification, a “ramp down” to some non-zero value is followed by a constant flux section at that value, with a “ramp down” to zero at the end of the constant flux section. The ambient buoyancy profiles produced by such a source are well described, away from the very bottom of the tank, by a peeling plume model.

5.1.4 Overall key points of this thesis

This thesis adds to our understanding of the effect of PCM on building temperatures. Theoretical models show that PCM is beneficial at reducing temperature fluctuations, and those models provide a way to inform decisions on the appropriate quantities of PCM to use, and the appropriate locations at which to use it. Real life temperature data measured in two apartments, one with PCM and the other without PCM, strengthens this conclusion, showing that temperatures are reduced in the apartment with PCM. Summer data is required to strengthen this conclusion further. Solidifying PCM in walls produces a vertically distributed, time varying buoyancy source. Detrainment – plume fluid intruding into the ambient at intermediate heights – occurs for vertically distributed sources, and its importance relative to entrainment varies depending on the source. For sources with a “ramp down” in buoyancy flux, and constant flux sources, detrainment is important, and a peeling plume model describes the ambient buoyancy profiles. For a source with a “ramp up” in source buoyancy flux, however, entrainment in the stratified region has a more significant effect than detrainment has, and a one-way-entrainment model describes the ambient buoyancy profiles.

5.2 Future work

The work presented in this thesis suggests several directions for future research into the use of PCMs in low-energy buildings. Here, some such suggestions are presented for work following on from each of the three problems presented in this thesis.

5.2.1 PCM thermal mass reducing fluctuations in building temperature

Extending the model of chapter 2 into 2D, including a stratification in the room (based, for example, on the temperature stratification measured, in appendix A, in the apartment without PCM), is more physically realistic. The relevance of stratification is shown by the experiments of chapter 4 that mimic solidification in a PCM wall, together with the real temperature data collected in appendix A, which both show that a stratification is present in the space. This extended, 2D, model would then provide further insight into where PCM should be located in a room, in particular, whether it should be uniformly distributed with height, or should be placed only next to the stratified region.

For the model presented in this thesis to be of practical use, good communication with industry is essential, as is presenting the model in a user-friendly form. A GUI (graphical user interface) could be developed, for example, where users input their material types (for example, the wall material), and the climate type they are interested in, and have the GUI output the ideal wall thickness and amount of PCM. In addition, the model could be made compatible with popular modelling software, such as EnergyPlus. Rather than simply looking for a low maximum interior wall surface temperature, when selecting a wall thickness and an amount of PCM to use, the model could also be used to optimise based on meeting standards such as CIBSE guidelines for overheating, for the lowest cost. This alternative optimization would make the model even more relevant and attractive to industry.

As discussed in appendix A, summer data from the two apartments (one with PCM, the other without PCM) at Explore Industrial Park is needed to strengthen the conclusion that PCM reduces summer overheating. This summer data could be compared with the model of chapter 2 by forcing the model with the temperatures measured in the apartment without PCM, and comparing the wall temperatures that the model predicts with those measured in the apartment with PCM. Temperature measurements from rooms (with and without PCM) that are located in different climate types could be used with the model to optimise, for each climate type, properties of the PCM wall (PCM melting temperature, wall thickness, and amount of PCM). An ideal wall to use in each climate type could then be specified. Including the effect of insolation on the outside of the building would also allow us to design walls for different directions - a south-facing wall, for example, might be different from a north-facing wall, since they receive different amounts of insolation over the day.

5.2.2 Detrainment of plumes from vertical sources

The process of detrainment, observed in experiments in chapters 3 and 4, could be investigated more thoroughly. Such an investigation would involve using a wider range of experimental techniques, for example, PIV (particle image velocimetry) to investigate the flow in the space, and light attenuation to measure densities across the whole tank. These more detailed experiments could show where and when fluid detrains from the plume, and what the density of detraining fluid is, giving us more insight into the detrainment process. These experiments would allow us to determine when entrainment occurs, and when detrainment occurs – for example, does the plume only entrain up to a certain time, and then only detrain, or does it repeatedly change between entrainment and detrainment? A better understanding of the detrainment process will allow for better, more physically realistic, models of heating and ventilation in buildings.

Experiments with a heated wall would provide a more uniformly distributed source than our source, which is formed of a number of individual sources, spread over the wall of a tank. In such experiments, care must be taken to reduce, or account for, heat losses from the space, as well as to ensure that the wall is sufficiently hot for the plume it drives to be turbulent. In such experiments, we wish to know whether detrainment is observed, as it was in the salt water experiments. If detrainment is observed, the presence or absence in the ambient buoyancy profiles of the characteristic “flick”, i.e. the change in curvature at the bottom of the tank, associated with the peeling plume model would suggest whether the peeling plume model remains the appropriate model for a heated wall source.

Real rooms are ventilated so further work (both experimental and theoretical) could add ventilation to a space containing a vertically distributed source of buoyancy. These experiments could investigate the effect of ventilation on detrainment, finding out whether detrainment always occurs with a vertically distributed source, or whether it only occurs under certain ventilation regimes.

5.2.3 Time-varying, vertically distributed buoyancy sources

Motivated by the experiments suggested above, to investigate the detrainment process, the peeling plume model could be extended to include, in the stratified region, a descending plume that both entrains and detrains. The particular mechanism of this combination of entrainment and detrainment would be informed by the suggested experiments. For the “ramp up” experiments in chapter 4, entrainment remained a significant effect in the stratified region, whilst detrainment was also observed, so a model that includes both entrainment and detrainment may capture the physical situation more accurately. Experiments with a

wider range of slopes of “ramp up” could determine at what slope of “ramp up”, between the constant flux experiments of chapter 3 and the “ramp up” experiments of chapter 4, a one-way-entrainment model begins to be more appropriate than a peeling plume model.

Various assumptions were made in chapter 4, which could, in further work, be relaxed. For example, we set λ , defined in (4.44), to be $\lambda = 0$, neglecting the time derivatives in the plume equations (4.45) – (4.47), but the model could be implemented for $\lambda > 0$, to see whether, as expected, λ has only a small effect (for the values of λ that are relevant for the experiments). As in the suggested further work for chapter 3, ventilation could be included in both the experiments and the theoretical model, to approximate a realistic room better. Experiments designed to mimic a PCM source were carried out as part of this thesis, but experiments with actual PCM could also be carried out, to investigate how well the PCM-mimicking source captures the effect on the source buoyancy flux of PCM solidification. To investigate the effect of PCM over the course of several days or weeks, the PCM-mimicking source experiments, or experiments with real PCM, could be cycled to find out whether the stratification changes significantly over the course of several days.

The use of PCMs in low-energy buildings has the potential to reduce energy consumption, thus saving money on energy bills and reducing our contribution to climate change, and also suggests a wide range of interesting research problems, including the three problems studied in this thesis, and the future work discussed above.

References

- A. Abhat. Low temperature latent heat thermal energy storage: heat storage materials. *Solar Energy*, 30:313–332, 1983.
- M. Ahmad, A. Bontemps, H. Sallée, and D. Quenard. Thermal testing and numerical simulation of a prototype cell using light wallboards coupling vacuum isolation panels and phase change material. *Energy and Buildings*, 38:673–681, 2006.
- S. N. Al-Saadi and Z. Zhai. Modeling phase change materials embedded in building enclosure: A review. *Renew. Sust. Energy Rev.*, 21:659–673, 2013. doi: 10.1016/j.rser.2013.01.024.
- S. N. Al-Saadi and Z. Zhai. Systematic evaluation of mathematical models and numerical schemes for modeling PCM-enhanced building enclosure. *Energy Build.*, 92:374–388, 2015a. doi: 10.1016/j.enbuild.2015.01.044.
- S. N. Al-Saadi and Z. Zhai. A new validated TRNSYS module for simulating latent heat storage walls. *Energy Build.*, 109:274–290, 2015b. doi: 10.1016/j.enbuild.2015.10.013.
- R. Baetens, B. P. Jelle, and A. Gustavsen. Phase change materials for building applications: A state-of-the-art review. *Energy Build.*, 42(9):1361–1368, 2010.
- P. G. Baines. Two-dimensional plumes in stratified environments. *J. Fluid Mech.*, 471:315–337, 2002. doi: 10.1017/S0022112002002215.
- W. D. Baines and J. S. Turner. Turbulent buoyant convection from a source in a confined region. *J. Fluid Mech.*, 37:51–80, 1969. doi: 10.1017/S0022112069000413.
- C. Barreneche, A. Solé, L. Miró, I. Martorell, A. I. Fernández, and L. F. Cabeza. Study on differential scanning calorimetry analysis with two operation modes and organic and inorganic phase change material (PCM). *Thermochim. Acta*, 553(10):23–26, 2013.
- BASF. Micronal PCM. Website, 2015. URL http://www.micronal.de/portal/basf/ien/dt.jsp?setCursor=1_290798.
- A. Beizaee, K. J. Lomas, and S. K. Firth. National survey of summertime temperatures and overheating risk in English homes. *Build. Environ.*, 65:1–17, 2013.
- D. Bolster and C. P. Caulfield. Transients in natural ventilation – a time-periodically-varying source. *Building Serv. Eng. Res. Technol.*, 29(2):119–135, 2008.
- D. J. Bower, C. P. Caulfield, S. D. Fitzgerald, and A. W. Woods. Transient ventilation dynamics following a change in strength of a point source of heat. *J. Fluid Mech.*, 614:15–37, 2008.

- BRE. The Passivhaus Standard. website, 2011. URL <http://www.passivhaus.org.uk/standard.jsp?id=122>.
- L. F. Cabeza, A. Castell, C. Barreneche, A. de Gracia, and A. I. Fernández. Materials used as PCM in thermal energy storage in buildings: A review. *Renew. Sust. Energy Rev.*, 15: 1675–1695, 2011.
- S. S. S. Cardoso and A. W. Woods. Mixing by a turbulent plume in a confined stratified region. *J. Fluid Mech.*, 250:277–305, 1993. doi: 10.1017/S0022112093001466.
- C. Castellón, M. Medrano, J. Roca, L. F. Cabeza, M. E. Navarro, A. I. Fernández, A. Lázaro, and B. Zalba. Effect of microencapsulated phase change material in sandwich panels. *Renew. Energy*, 35:2370–2374, 2010. doi: 10.1016/j.renene.2010.03.030.
- T. Caudwell, M. E. Negretti, and J.-B. Flór. Convection at an isothermal wall in an enclosure and establishment of stratification. *J. Fluid Mech.*, 799:448–475, 2016. doi: 10.1017/jfm.2016.360.
- C. Cenedese and P. F. Linden. Entrainment in two coalescing axisymmetric turbulent plumes. *J. Fluid Mech.*, 752(R2), 2014.
- Z. D. Chen, Y. Li, and J. Mahoney. Natural ventilation in an enclosure induced by a heat source distributed uniformly over a vertical wall. *Build. Environ.*, 36:493–501, 2001.
- I.A. Coomaraswamy and C.P. Caulfield. Time-dependent ventilation flows driven by opposing wind and buoyancy. *J. Fluid Mech.*, 672:33–59, 2011.
- P Cooper and G.R. Hunt. The ventilated filling box containing a vertically distributed source of buoyancy. *J. Fluid Mech.*, 646:39–58, 2010. doi: 10.1017/S0022112009992734.
- P. F. Court, C. L. Pasquire, G. F. Gibb, and D. Bower. Modular assembly with postponement to improve health, safety and productivity in construction. *Practice Periodical on Structural Design and Construction*, 14(2):81–89, May 2009.
- J. Craske and M. van Reeuwijk. Generalised unsteady plume theory. *J. Fluid Mech.*, 792: 1013–1052, 2016. doi: 10.1017/jfm.2016.72.
- A. W. Date. A strong enthalpy formulation for the Stefan problem. *Int. J. Heat Mass Transfer*, 34:2231–2235, 1991.
- DECC. Energy consumption in the UK, 2012, updated in 2014. URL <https://www.gov.uk/government/publications/energy-consumption-in-the-uk>.
- Department for Communities and Local Government. 2012-based household projections - England: household types (stage 2) and national variants, December 2015. URL https://www.gov.uk/government/uploads/system/uploads/attachment_data/file/481704/2012-based_household_projections_England_2012_to_2037_Stage_2_household_types_and_national_variants.pdf.
- Department for Communities and Local Government. House building: December quarter 2015, England, February 2016. URL https://www.gov.uk/government/uploads/system/uploads/attachment_data/file/502930/House_Building_Release_Dec_Qtr_2015.pdf.

- Department of Energy & Climate Change. Annual fuel poverty statistics report, 2015, 2015. URL https://www.gov.uk/government/uploads/system/uploads/attachment_data/file/468011/Fuel_Poverty_Report_2015.pdf.
- DuPont. DuPont Energain energy-saving thermal mass systems, 2007. URL http://www.siginsulation.co.uk/Literature/duPont_energain_prod%20info.pdf.
- DuPont. DuPont Energain energy-saving thermal mass systems. Datasheet, 2011.
- A. F. Elmozughi, L. Solomon, A. Oztekin, and S. Neti. Encapsulated phase change material for high temperature thermal energy storage – heat transfer analysis. *Int. J. Heat Mass Transfer*, 78:1135–1144, 2014.
- A. Ezzamel, P. Salizzoni, and G. R. Hunt. Dynamical variability of axisymmetric buoyant plumes. *J. Fluid Mech.*, 765:576–611, 2015. doi: 10.1017/jfm.2014.694.
- H. E. Feustel and C. Stetiu. Thermal performance of phase change wallboard for residential cooling application. Technical Report LBL-38320, Lawrence Berkeley National Laboratory, 1997.
- M. Fiorentini, P. Cooper, and Z. Ma. Development and optimization of an innovative HVAC system with integrated PVT and PCM thermal storage for a net-zero energy retrofitted house. *Energy Build.*, 94:21–32, 2015. doi: 10.1016/j.enbuild.2015.02.018.
- S. D. Fitzgerald and A. W. Woods. Transient natural ventilation of a room with a distributed heat source. *J. Fluid Mech.*, 591:21–42, 2007.
- G. V. Fracastoro and M. Serraino. Energy analyses of buildings equipped with exhaust air heat pumps. *Energy Build.*, 42(8):1283–1289, 2010. doi: 10.1016/j.enbuild.2010.02.021.
- D. M. Gann. Construction as a manufacturing process? Similarities and differences between industrialized housing and car production in Japan. *Constr. Manag. Econ.*, 14:437–450, 1996.
- A. E. Germeles. Forced plumes and mixing of liquids in tanks. *J. Fluid Mech.*, 71:601–623, 1975. doi: 10.1017/S0022112075002765.
- A. G. F. Gibb. Standardization and pre-assembly – distinguishing myth from reality using case study research. *Constr. Manag. Econ.*, 19:307–315, 2001.
- C. Gladstone and A. W. Woods. On buoyancy-driven natural ventilation of a room with a heated floor. *J. Fluid Mech.*, 441:293–314, 2001.
- C. Gladstone and A. W. Woods. Detrainment from a turbulent plume produced by a vertical line source of buoyancy in a confined, ventilated space. *J. Fluid Mech.*, 742:35–49, 2014. doi: 10.1017/jfm.2013.640.
- C. I. Goodier and A. G. F. Gibb. Future opportunities for offsite in the UK. *Constr. Manag. Econ.*, 25(6):585–595, 2007.
- L. E. Goodrich. Efficient numerical technique for one-dimensional thermal problems with phase change. *Int. J. Heat Mass Transfer*, 21:615–621, 1978.

- B. L. Gowreesunker, S. A. Tassou, and M. Kolokotroni. Improved simulation of phase change processes in applications where conduction is the dominant heat transfer mode. *Energy and Buildings*, 47:353–359, 2012.
- S. Guichard, F. Miranville, D. Bigot, B. Malte-Damour, and H. Boyer. Experimental investigation on a complex roof incorporating phase-change material. *Energy Build.*, 108: 36–43, 2015. doi: 10.1016/j.enbuild.2015.09.055.
- E. Günther, S. Hiebler, and H. Mehling. Determination of the heat storage capacity of PCM and PCM-objects as a function of temperature. In *Proceedings of ECOSTOCK*, 2006.
- J. L. M. Hensen. Literature review on thermal comfort in transient conditions. *Build. Environ.*, 25(4):309–316, 1990. doi: 10.1016/0360-1323(90)90004-B.
- C. A. R. Hogg, S. B. Dalziel, H. E. Huppert, and J. Imberger. Inclined gravity currents filling basins: peeling detrainment and its implications for transport and vertical structure in basins. *J. Fluid Mech.*, 2015. submitted.
- J.M. Holford and A.W. Woods. On the thermal buffering of naturally ventilated buildings through internal thermal mass. *J. Fluid Mech.*, 580:3–29, 2007. doi: 10.1017/S0022112007005320.
- M. J. Hosseini, A. A. Ranjbar, M. Rahimi, and R. Bahrapoury. Experimental and numerical evaluation of longitudinally finned latent heat thermal storage systems. *Energy Build.*, 99: 263–272, 2015. doi: 10.1016/j.enbuild.2015.04.045.
- IPCC. Climate Change 2014: Synthesis Report. Contribution of Working Groups I, II, and III to the Fifth Assessment Report of the Intergovernmental Panel on Climate Change, 2014. URL <https://www.ipcc.ch/report/ar5/syr/>. Core Writing Team, R. K. Pachauri and L. A. Meyer (eds.).
- X. Jin, S. Zhang, X. Xu, and X. Zhang. Effects of PCM state on its phase change performance and the thermal performance of building walls. *Build. Environ.*, 81:334–339, 2014.
- E. Kaminski, S. Tait, and G. Carazzo. Turbulent entrainment in jets with arbitrary buoyancy. *J. Fluid Mech.*, 526:361–376, 2005.
- M. Karkri, M. Lachheb, F. Albouchi, S. B. Nasrallah, and I. Krupa. Thermal properties of smart microencapsulated paraffin/plaster composites for the thermal regulation of buildings. *Energy Build.*, 88:183–192, February 2015. doi: 10.1016/j.enbuild.2014.11.068.
- N. B. Kaye and G. R. Hunt. Time-dependent flows in an emptying filling box. *J. Fluid Mech.*, 520:135–156, 2004.
- N. B. Kaye and P. F. Linden. Coalescing axisymmetric turbulent plumes. *J. Fluid Mech.*, 502:41–63, 2004. doi: 10.1017/S0022112003007250.
- N. B. Kaye, M. R. Flynn, M. J. Cook, and Y. Ji. The role of diffusion on the interface thickness in a ventilated filling box. *J. Fluid Mech.*, 652:195–205, 2010.

- M. A. Khalifa. *Application of phase change materials as a solution for building over-heating: a case for the UK*. PhD thesis, University of Nottingham, March 2013. URL http://etheses.nottingham.ac.uk/3837/1/APPLICATION_OF_PHASE_CHANGE_MATERIALS_AS_A_SOLUTION_FOR_BUILDING_OVERHEATING.pdf.
- P. D. Killworth and J. S. Turner. Plumes with time-varying buoyancy in a confined region. *Geophys. Astrophys. Fluid Dynamics*, 20:265–291, 1982.
- Knauf. Knauf Comfortboard, 2014. URL <http://www.knauf.co.uk/files/download/comfortboardbrochurepdf/488>.
- Y. Konuklu, H. O. Paksoy, M. Unal, and S. Konuklu. Microencapsulation of a fatty acid with poly(melamine-urea-formaldehyde). *Energy Convers. Manage.*, 80:382–390, 2014.
- J. Kosny, N. Shukla, and A. Fallahi. Cost analysis of simple phase change material-enhanced building envelopes in southern U.S. climates. Technical report, Fraunhofer CSE, 2013. URL http://cse.fraunhofer.org/Portals/55819/docs/ba_pcm_enhanced_building_envelopes.pdf.
- M. Kumagai. Turbulent buoyant convection from a source in a confined two-layered region. *J. Fluid Mech.*, 147:105–131, 1984.
- F. Kuznik, D. David, K. Johnnes, and J. Roux. A review on phase change materials integrated in building walls. *Renew. Sust. Energy Rev.*, 15:379–391, 2011.
- Laing O’Rourke. Modular Manufacturing, 2016. URL <http://www.laingorourke.com/what-we-do/modular-manufacturing.aspx>.
- G.F. Lane-Serff and S.D. Sandbach. Emptying non-adiabatic filling boxes: the effects of heat transfers on the fluid dynamics of natural ventilation. *J. Fluid Mech.*, 701:386–406, 2012.
- T. Lecompte, P. Le Bideau, P. Glouannec, D. Northerhauser, and S. Le Masson. Mechanical and thermo-physical behaviour of concretes and mortars containing phase change material. *Energy Build.*, 94:52–60, 2015. doi: 10.1016/j.enbuild.2015.02.044.
- P.F. Linden. The fluid mechanics of natural ventilation. *Annu. Rev. Fluid Mech.*, 31:201–238, 1999.
- P.F. Linden, G.F. Lane-Serff, and D.A. Smeed. Emptying filling boxes: the fluid mechanics of natural ventilation. *J. Fluid Mech.*, 212:309–335, 1990. doi: 10.1017/S0022112090001987.
- B. Lishman and A. W. Woods. On transitions in natural ventilation flow driven by changes in the wind. *Build. Environ.*, 44:762–772, 2009.
- H. Liu and H. B. Awbi. Performance of phase change material boards under natural convection. *Build. Environ.*, 44:1788–1793, 2009.
- S. R. Livermore and A. W. Woods. On the effect of distributed cooling in natural ventilation. *J. Fluid Mech.*, 600:1–17, 2008. doi: 10.1017/S0022112007009809.
- K. J. Lomas and T. Kane. Summertime temperatures and thermal comfort in UK homes. *Build. Res. Inf.*, 41, 2013.

- C. D. McConnochie and R. C. Kerr. The turbulent wall plume from a vertically distributed source of buoyancy. *J. Fluid Mech.*, 787:237–253, 2016. doi: 10.1017/jfm.2015.691.
- Met Office. UK climate - historic station data. website. URL <http://www.metoffice.gov.uk/public/weather/climate-historic/#?tab=climateHistoric>.
- P. Moreno, A. Castell, C. Solé, G. Zsembinszki, and L. F. Cabeza. PCM thermal energy storage tanks in heat pump system for space cooling. *Energy Build.*, 82:399–405, 2014.
- B.R. Morton, G. Taylor, and J.S. Turner. Turbulent gravitational convection from maintained and instantaneous sources. *Proc. R. Soc. Lond. A*, 234:1–23, 1956. doi: 10.1098/rspa.1956.0011.
- R. W. Mott and A. W. Woods. On the mixing of a confined stratified fluid by a turbulent buoyant plume. *J. Fluid Mech.*, 623:149–165, 2009.
- L. Navarro, A. de Gracia, A. Castell, S. Álvarez, and L. F. Cabeza. PCM incorporation in a concrete core slab as a thermal storage and supply system: Proof of concept. *Energy Build.*, 103:70–82, September 2015. doi: 10.1016/j.enbuild.2015.06.028.
- D. A. Neeper. Thermal dynamics of wallboard with latent heat storage. *Sol. Energy*, 68(5): 393–403, 2000. doi: 10.1016/S0038-092X(00)00012-8.
- NIBE Energy Systems AB. NIBE F470 Exhaust Air Heat Pump. Brochure, 2012. URL <http://www.nibe.co.uk/nibedocuments/12093/639511-1.pdf>.
- R. M. Novais, G. Ascensão, M. P. Seabra, and J. A. Labrincha. Lightweight dense/porous PCM-ceramic tiles for indoor temperature control. *Energy Build.*, 108:205–214, 2015. doi: 10.1016/j.enbuild.2015.09.019.
- S. Noyé. Seasonal heat storage with phase change material. Master’s thesis, Department of Civil Engineering, Technical University of Denmark, 2011.
- S. Paillat and E. Kaminski. Entrainment in plane turbulent pure plumes. *J. Fluid Mech.*, 755 (R2), 2014.
- W. Pan, A. G. F. Gibb, and A. R. J. Dainty. Perspectives of UK housebuilders on the use of offsite modern methods of construction. *Constr. Manag. Econ.*, 25(2):183–194, 2007.
- A. Pasupathy, R. Velraj, and R. V. Seeniraj. Phase change material-based building architecture for thermal management in residential and commercial establishments. *Renew. Sust. Energy Rev.*, 12:39–64, 2008.
- Z. Pavlík, A. Trník, J. Ondruška, M. Keppert, M. Pavlíková, P. Volfová, V. Kaulich, and R. Černý. Apparent thermal properties of phase-change materials: An analysis using differential scanning calorimetry and impulse method. *Int. J. Thermophys.*, 34(5):851–864, 2013. doi: 10.1007/s10765-012-1169-1.
- K. Peippo, P. Kauranen, and P. D. Lund. A multicomponent PCM wall optimized for passive solar heating. *Energy Build.*, 17:259–270, 1991.

- N. Poudel and V. Y. Blouin. US map visualisation of optimal properties of phase change materials for building efficiency. In Chris Jarrett, Kyoung-Hee Kim, and Nick Senske, editors, *The Visibility of Research*, page 545. ARCC, University of North Carolina at Charlotte, March 2013.
- M. Rady and E. Arquis. A comparative study of phase changing characteristics of granular phase change materials using DSC and T-history methods. *FDMP*, 6(2):137–152, 2010.
- A. R. Rempel and A. W. Rempel. Rocks, clays, water, and salts: Highly durable, infinitely rechargeable, eminently controllable thermal batteries for buildings. *Geosciences*, 3:63–101, 2013. doi: 10.3390/geosciences3010063.
- M.J. Richardson and A.W. Woods. An analysis of phase change material as thermal mass. *Proc. R. Soc. A*, 464:1029–1056, 2008. doi: 10.1098/rspa.2007.0312.
- L. T. Rodrigues and M. Gillott. A novel low-carbon space conditioning system incorporating phase-change materials and earth-air heat exchangers. *Int. J. Low Carbon Tech.*, 2013.
- L. Royon, L. Karim, and A. Bontemps. Optimization of PCM embedded in a floor panel developed for thermal management of the lightweight envelope of buildings. *Energy Build.*, 82:385–390, 2014.
- R. F. Rupp, N. G. Vásquez, and R. Lamberts. A review of human thermal comfort in the built environment. *Energy Build.*, 105:178–205, 2015. doi: 10.1016/j.enbuild.2015.07.047.
- S. M. T. Sameni, M. Gaterell, A. Montazami, and A. Ahmed. Overheating investigation in UK social housing flats built to the Passivhaus standard. *Build. Environ.*, 92:222–235, 2015. doi: 10.1016/j.buildenv.2015.03.030.
- S. D. Sandbach and G. F. Lane-Serff. Transient buoyancy-driven ventilation: Part 1. Modelling advection. *Building and Environment*, 46:1578–1588, 2011a.
- S. D. Sandbach and G. F. Lane-Serff. Transient buoyancy-driven ventilation: Part 2. Modelling heat transfer. *Building and Environment*, 46:1589–1599, 2011b.
- M. M. Scase and R. E. Hewitt. Unsteady turbulent plume models. *J. Fluid Mech.*, 697:455–480, 2012.
- M. M. Scase, C. P. Caulfield, S. B. Dalziel, and J. C. B. Hunt. Time-dependent plumes and jets with decreasing source strengths. *J. Fluid Mech.*, 563:443–461, 2006.
- T. Schütz, R. Streblov, and D. Müller. A comparison of thermal energy storage models for building energy system optimization. *Energy Build.*, 93:23–31, April 2015. doi: 10.1016/j.enbuild.2015.02.031.
- S. Serrano, C. Barreneche, L. Rincón, D. Boer, and L. F. Cabeza. Stabilized rammed earth incorporating PCM: Optimization and improvement of thermal properties and life cycle assessment. *Energy Procedia*, 30:461–470, 2012.
- N. P. Sharifi and A. Sakulich. Application of phase change materials to improve the thermal performance of cementitious material. *Energy Build.*, 103:83–95, September 2015. doi: 10.1016/j.enbuild.2015.06.040.

- L. Shilei, F. Guohui, Z. Neng, and D. Li. Experimental study and evaluation of latent heat storage in phase change materials wallboards. *Energy Build.*, 39:1088–1091, 2007.
- A. B. Shrinivas and G. R. Hunt. Confined turbulent entrainment across density interfaces. *J. Fluid Mech.*, 779:116–143, 2015. doi: 10.1017/jfm.2015.366.
- X. Tang, M. Xu, W. Zhang, Z. Yang, Y. Zhang, G. Yin, D. He, H. Wei, and X. Zhai. Shape-stabilized phase change materials based on fatty acid eutectics/expanded graphite composites for thermal storage. *Energy Build.*, 109:353–360, 2015. doi: 10.1016/j.enbuild.2015.09.074.
- The Engineering ToolBox. The Engineering ToolBox. Website. URL <http://www.engineeringtoolbox.com>.
- A. Tokuç, T. Başaran, and S. C. Yesügey. An experimental and numerical investigation on the use of phase change materials in building elements: The case of a flat roof in Istanbul. *Energy Build.*, 102:91–104, 2015. doi: 10.1016/j.enbuild.2015.04.039.
- V. V. Tyagi and D. Buddhi. PCM thermal storage in buildings: A state of art. *Renew. Sust. Energy Rev.*, 11:1146–1166, 2007.
- V. Udra. How much does free cooling cost? Fourth-year undergraduate project, University of Cambridge, 2015.
- Z. Ure. Personal communication, June 2013.
- T. S. van den Bremer and G. R. Hunt. Two-dimensional planar plumes and fountains. *J. Fluid Mech.*, 750:210–244, 2014a. doi: 10.1017/jfm.2014.246.
- T. S. van den Bremer and G. R. Hunt. Two-dimensional planar plumes: non-Boussinesq effects. *J. Fluid Mech.*, 750:245–258, 2014b. doi: 10.1017/jfm.2014.252.
- M. van Reeuwijk and J. Craske. Energy-consistent entrainment relations for jets and plumes. *J. Fluid Mech.*, 782:333–355, 2015. doi: 10.1017/jfm.2015.534.
- V. Voller and M. Cross. Accurate solutions of moving boundary problems using the enthalpy method. *Int. J. Heat Mass Transfer*, 24:545–556, 1981.
- E. V. Votyakov and A. M. Bonanos. A perturbation model for stratified thermal energy storage tanks. *Int. J. Heat Mass Transfer*, 75:218–223, August 2014.
- H. Weinläder, W. Körner, and B. Strieder. A ventilated cooling ceiling with integrated latent heat storage – monitoring results. *Energy Build.*, 82:65–72, 2014.
- A. J. Wells and M. G. Worster. A geophysical-scale model of vertical natural convection boundary layers. *J. Fluid Mech.*, 609:111–137, 2008.
- T. R. Whiffen, G. Russell-Smith, and S. B. Riffat. Active thermal mass enhancement using phase change materials. *Energy Build.*, 111:1–11, 2016. doi: 10.1016/j.enbuild.2015.09.062.
- A. B. D. Wong, R. W. Griffiths, and G. O. Hughes. Shear layers driven by turbulent plumes. *J. Fluid Mech.*, 434:209–241, 2001.

-
- M. G. Worster and H. E. Huppert. Time-dependent density profiles in a filling box. *J. Fluid Mech.*, 132:457–466, 1983. doi: 10.1017/S002211208300172X.
- J. Xie, Y. Li, W. Wang, S. Pan, N. Cui, and J. Liu. Comments on thermal physical properties testing methods of phase change materials. *Advances in Mechanical Engineering*, 2013, 2013.
- D. Zhou, C. Y. Zhao, and Y. Tian. Review on thermal energy storage with phase change materials (PCMs) in building applications. *Appl. Energy*, 92:593–605, 2012. doi: 10.1016/j.apenergy.2011.08.025.
- D. Zhou, G. S. F. Shire, and Y. Tian. Parametric analysis of influence factors in phase change material wallboard (PCMW). *Appl. Energy*, 119:33–42, 2014.

Appendix A

PCM wallboard field tests

A.1 Motivation

Theory shows that PCMs smooth out temperature fluctuations, as seen in chapter 2. We wish to test whether PCMs are effective, particularly at reducing summer overheating, in real buildings. To test this, temperatures are monitored in two apartments: one apartment is fitted with PCM wallboard, whilst the other apartment has no PCM wallboard. Comparing temperature data, measured in September 2015, from the two apartments suggests that PCM may reduce overheating. To strengthen this conclusion, it is worthwhile collecting summer temperature data.

A.2 Review of studies that use PCM in walls

Several studies feature PCM in walls. In numerical simulations of a building in Sunnyvale, California, Feustel and Stetiu (1997) find that PCM wallboard adds thermal mass to lightweight buildings. Their simulations, using the building simulation program RADCOOL, take account of the additional load from television and lighting during occupied hours. Lower peak temperatures are observed in a test cell containing PCM, compared with a test cell without PCM, in the experiments of Ahmad et al. (2006). In their experiments, walls made of PCM-filled polyvinyl chloride (PVC) panels are placed between a vacuum isolation panel and a piece of plywood. These walls are then placed in a frame, along with a (south facing) window, forming test cells, which are placed outside in the summer. The authors find that at the hottest part of the day, the cell without PCM exceeds 60°C, whereas the cell with PCM reaches approximately 40°C. Simulations using the energy simulation software TRNSYS, with a new module representing PCM, show good agreement with the experiments. Liu and

Awbi (2009) use DuPont Energain PCM panels on a wall. Their experiments are carried out in a test chamber where temperatures are cycled to allow for a charging and releasing cycle (i.e. a day and a night). They find that, when heat is being absorbed, use of PCM reduces the interior wall surface temperature.

Motivated by these previous studies showing PCM's effectiveness when used in test chambers, we carry out field tests in two real apartments. Whilst Ahmad et al. (2006) use macroencapsulated PCM, and Liu and Awbi (2009) use DuPont Energain, where an aluminium-laminated panel contains PCM mixed with a polymer (DuPont, 2007), we use wallboard containing microencapsulated PCM. We use PCM wallboard because it can be retrofitted easily, so has applications in both new and existing buildings.

A.3 Setup

A.3.1 Apartments

The apartments used for the field tests are located at Explore Industrial Park in Steetley, near Worksop. Temperatures measured by the Met Office about 20 miles from Worksop, in Sheffield, varied between a minimum of 2.0°C and a maximum of 6.9°C in February 2015 and a minimum of 12°C and a maximum of 20.8°C in July 2015 (Met Office). Explore Industrial Park is where Laing O'Rourke's manufacturing facilities are located, which were used to construct the apartments using modular manufacturing techniques (see chapter 1, section 1.4 for a discussion of modular manufacturing). The apartments are shown in figure 1.4 of chapter 1, and in figures A.1 to A.3.

Each apartment contains a living area (shown in figure 1.4 of chapter 1), a bathroom, and a bedroom (shown in figure A.2). Temperatures are measured in the bedrooms of both apartments. The bedrooms are used for testing because the orientation of their windows is the same, so we expect them to receive the same amount of sunlight. The bedroom window is part of a "winter garden", shown in figure A.1, where doors open from the bedroom onto a small balcony, which is mostly enclosed with a glass wall, but a small gap allows fresh air to enter. Each bedroom contains some furniture: a double bed, a small table, two bedside chests of drawers, two lamps, a built in wardrobe, and a portable radiator. The two bedrooms are shown in figure A.2. Within the apartment block, the bedrooms are located on the first floor, and are back to back – the walls on which pictures are hung, shown in figure A.2, are back to back. The footprint of each bedroom is 3.85m by 2.93m.

Two apartments are used, giving both a test (the apartment with PCM wallboard) and a control (the apartment without PCM wallboard). Comparing the two apartments allows us to

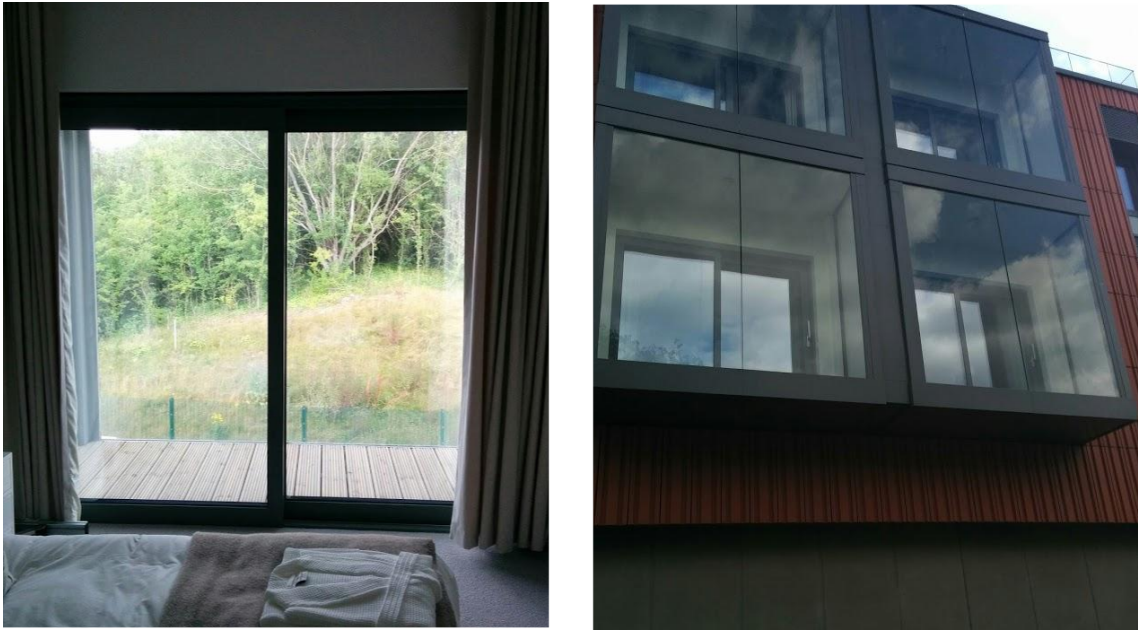


Fig. A.1 A winter garden, a space mostly enclosed by glass, apart from a small gap in the exterior glass wall, allowing for ventilation. Viewed from the bedroom of one of the test apartments (left), and from the exterior (right).



Fig. A.2 The two bedrooms: the apartment with PCM wallboard (left), and the apartment without PCM wallboard (right).



Fig. A.3 PCM wallboard mounted on the wall of one apartment. A double thickness of wallboard is used, as evident from the side view (right).

draw conclusions about whether PCM reduces summer overheating. The bedroom shown to the left of figure A.2 is fitted with PCM wallboard, whilst the bedroom shown to the right of figure A.2 contains no PCM.

A.3.2 PCM wallboard

PCM wallboard is mounted, as shown on the left of figure A.3, on the wall facing the bed in the left hand apartment. The wallboard is 2m high, 1.25m wide, and each sheet is 12.5mm thick. Two sheets are used, as shown on the right of figure A.3, giving a total thickness of 25mm. This double thickness is used because the model of chapter 2 suggests that a wall thickness of several centimetres is ideal.

Knauf Comfortboard, which is a plasterboard containing Micronal PCM (Knauf, 2014), is used. Micronal PCM is a wax PCM that is microencapsulated in a polymer film, with microcapsules measuring around $5\mu\text{m}$ (BASF, 2015). The Micronal PCM used in Knauf Comfortboard has a melting temperature of 23°C (Knauf, 2014). The board's density is $11/0.0125 = 880\text{kgm}^{-3}$, its latent heat capacity is $200000/11 = 18182\text{Jkg}^{-1}$, and its specific heat capacity is $13000/11 = 1182\text{Jkg}^{-1}\text{K}^{-1}$ (Knauf, 2014).

Parameter	Value
H_+ , dimensionless convection rate	3.7
Ω , dimensionless diffusivity	2.7
s , Stefan number	3.1
U_{\min} , dimensionless minimum melting temperature	0
U_{\max} , dimensionless maximum melting temperature	0.4

Table A.1 Dimensionless parameter values for Knauf Comfortboard.

Five key dimensionless parameters, for which values appropriate for Knauf Comfortboard will be found, are used in the model of chapter 2. These parameters are: the dimensionless convection rate H_+ , the dimensionless diffusivity Ω , the Stefan number s , the dimensionless minimum melting temperature U_{\min} , and the dimensionless maximum melting temperature U_{\max} . To calculate these parameters, properties listed on the Knauf Comfortboard datasheet (Knauf, 2014) are used: the wall density $\rho = 880\text{kg m}^{-3}$, the wall specific heat $C = 1182\text{J kg}^{-1}\text{K}^{-1}$, the wall thickness $l_{\text{tm}} = 0.025\text{m}$, and the latent heat in the PCM wall (the mass fraction of PCM multiplied by the PCM latent heat) $\phi L = 18182\text{J kg}^{-1}$. The melting temperature of the PCM is given as 23°C , although, in practice, PCMs have a range of melting temperatures. The minimum melting temperature is taken to be $\theta_{\min} = 22.5^\circ\text{C}$ and the maximum melting temperature to be $\theta_{\max} = 23.5^\circ\text{C}$. For thermal conductivity, the same value as Richardson and Woods (2008) use for wallboard is used: $K = 0.13\text{W m}^{-1}\text{K}^{-1}$. The same value as Richardson and Woods (2008) use is also used for the convection coefficient: $h_+ = 7\text{W m}^{-2}\text{K}^{-1}$. Assuming that, on a summer day, with additional heating load from a television and lighting, for example, room temperatures vary between 20°C and 25°C , giving a temperature scale of $u_0 = \frac{25-20}{2} = 2.5^\circ\text{C}$. Using these values, the values of the five dimensionless parameters, which are given in table A.1, may be calculated.

The PCM thermal mass model of chapter 2, with the five dimensionless parameters in table A.1, and a room temperature varying sinusoidally between 20°C and 25°C , gives the results shown in figure A.4. Maximum wall surface temperature with PCM (thick solid line) is lower than both maximum room temperature (thin dashed line) and maximum wall surface temperature without PCM (thin solid line). The amplitude of temperature oscillations is also smaller for wallboard with PCM than for wallboard without PCM. These theoretical results predict that Knauf Comfortboard will be effective at reducing summer overheating.

Two products other than Knauf Comfortboard were considered: DuPont Energain, and Armstrong CoolZone. Energain is a mixture of 60% paraffin wax with 40% ethylene based polymer, laminated on both sides with aluminium (DuPont, 2011). At only 5.2mm thick (DuPont, 2011), it is considerably thinner than the ideal thickness suggested by the PCM thermal mass model of chapter 2. Both for that reason, and because the aluminium lamination

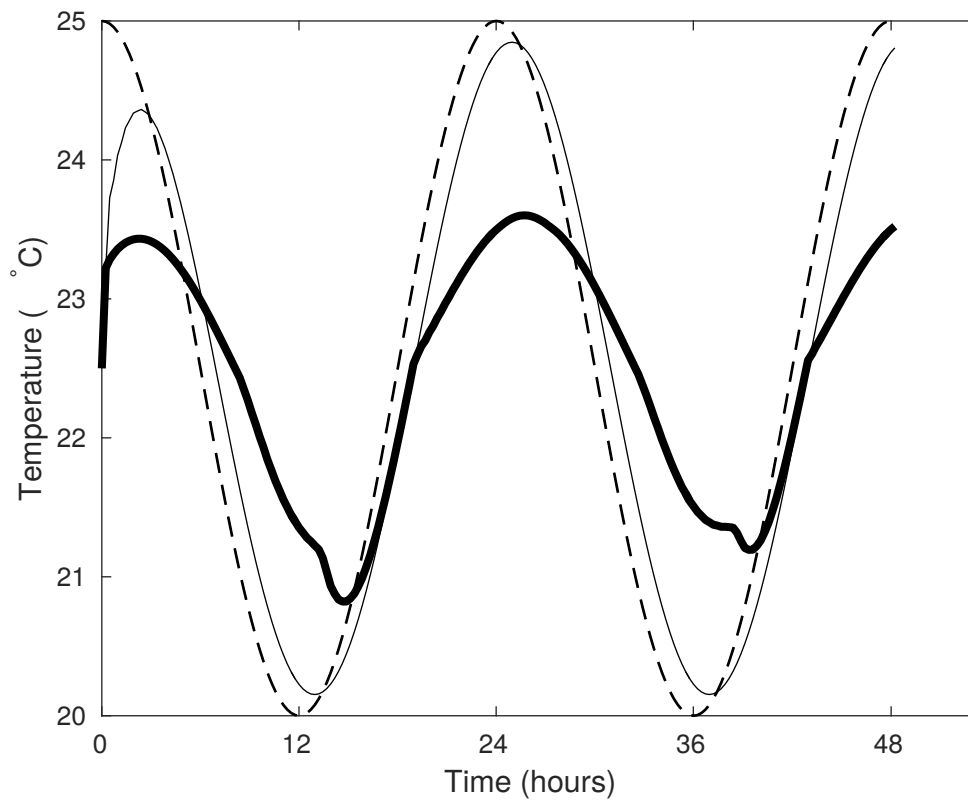


Fig. A.4 Wall surface temperature for PCM wallboard (thick solid line) and wallboard without PCM (thin solid line), responding to a sinusoidally varying room temperature (thin dashed line), using the five dimensionless parameter values listed in table A.1.

makes it different from conventional wallboard, Energain was not used in the tests. CoolZone is a ceiling based system, so, since we are interested in using PCM in walls, this was not used in the tests, instead, Knauf Comfortboard was used.

A.3.3 Equipment for measuring temperatures

Temperatures in each apartment are measured using T type thermocouples (HSTC-TT-TI-24S from Omega Engineering). In each apartment, 8 thermocouples measure wall temperatures and 8 thermocouples measure room temperatures. The thermocouples are located at a range of heights within the room: at 30, 53, 76, 100, 124, 148, 171, and 195 cm from the floor, for both the wall temperature and the room temperature measurements. Measuring temperatures at a range of heights reveals whether there is a stratification in the room. For wall temperatures, 5m long thermocouples are attached to the wall using masking tape and white tack, as shown in figure A.5. For room temperatures, 10m long thermocouples (the longer length allows the thermocouples to be connected to the same data acquisition box as the wall thermocouples are connected to) are placed on a free standing pole. This pole is located in a corner where the thermocouples are shaded from direct sunlight and away from where wall temperatures are measured, as shown in figure A.6.

In each apartment, the thermocouples are connected to a data acquisition (DAQ) box, which in turn is connected to a laptop running Signal Express to log the data. The DAQ box used is a 16-channel thermocouple module from National Instruments, NI 9213, in an NI cDAQ-9191 1-slot Wi-Fi chassis. A Wi-Fi chassis was selected because, if the laptop connected to the DAQ box wirelessly, the laptop could be placed out of sight, in a cupboard. The WiFi connection, however, proved unreliable, so instead an ethernet cable connects the DAQ box to the laptop. The laptop uploads data to a file share via Wi-Fi, allowing for remote access to the data. Temperatures are measured every 10s, and the data is stored in a text file, with a new file started every six hours. If errors stop Signal Express recording data, then since the laptops connected to the DAQ boxes can be accessed remotely (provided the laptops do not lose power, and have internet access – this was not always the case), the recording can be restarted easily.

A.4 Results and discussion

A.4.1 Autumn data

During September, temperatures in both apartments were measured over a 36 hour period (although technical problems resulted in a gap in the data). Temperature measurements



Fig. A.5 Thermocouples measuring temperatures of (left) PCM wallboard, and (right) a wall without PCM wallboard.

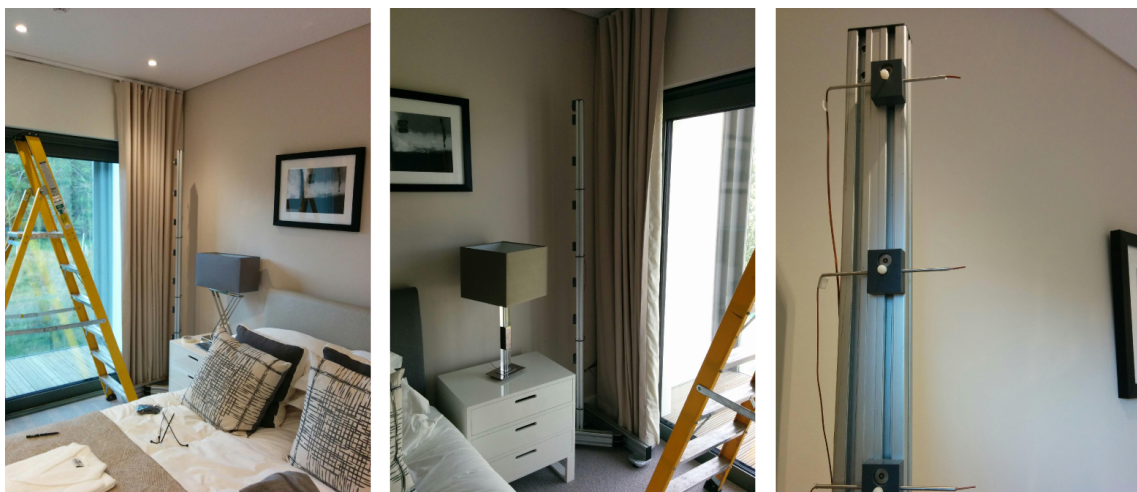


Fig. A.6 Thermocouples measuring room temperatures are placed on a free standing pole. The pole in the apartment with PCM (left), the pole in the apartment without PCM (centre), and detail of the thermocouple holders on the pole (right).

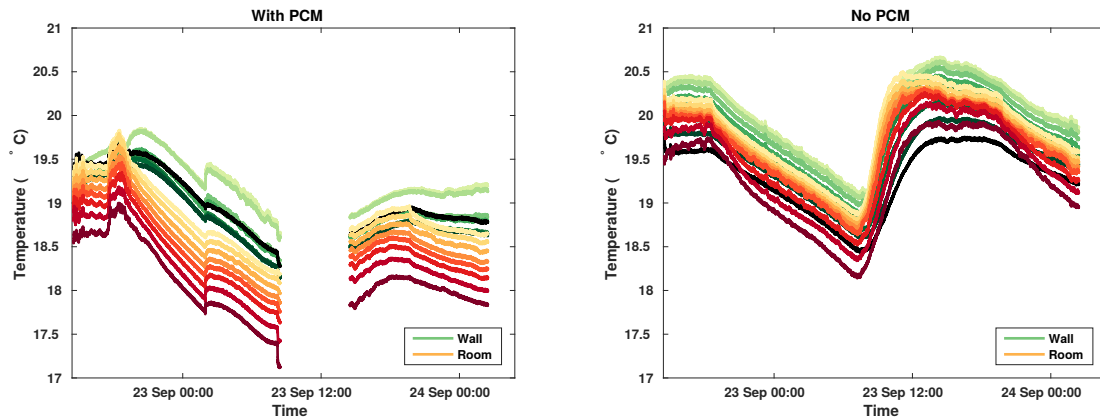


Fig. A.7 Wall (green lines) and room (orange lines) temperatures in the apartment with PCM wallboard (left) and in the apartment without PCM (right), measured during September 2015. Darker shades correspond to temperatures measured at lower heights.

started at 14:30 on September 22nd, 2015 and ended at 02:30 on September 24th, 2015. In the apartment with PCM, there is a gap in temperature measurements between 08:30 and 14:30 on September 23rd, since the file containing data from this period is corrupt. Despite considerable discussion with the manufacturer, this corrupt data file problem has remained unsolved. The temperature measurements that were taken are shown in figure A.7: the data from the apartment with PCM is on the left, and the data from the apartment without PCM is on the right.

Figure A.7 shows that wall temperatures (green lines) are higher than room temperatures (orange lines) in both apartments. Some stratification is present – typically, the darker the line (for either wall or room temperature), meaning the smaller the height the measurement was taken at, the cooler the temperature. Also, as assumed in chapter 2, temperatures vary over the course of a day.

The data suggests that PCM may reduce overheating. In the apartment with PCM, temperatures vary between 17 – 20°C, and in the apartment without PCM, temperatures vary between about 18 – 20.5°C over the period considered. Temperatures in the apartment with PCM were lower than those in the apartment without PCM, which may suggest that PCM is reducing overheating. This reduction in temperature happens despite measured temperatures being below the advertised melting temperature of the PCM, suggesting that the PCM melts over a range of temperatures (including 20.5°C, for example). Moreover, the apartment without PCM experiences a peak in temperature during the afternoon of the 23rd September, whereas the apartment with PCM has no such peak during that afternoon. These findings suggest that PCM may be able to reduce overheating in buildings.

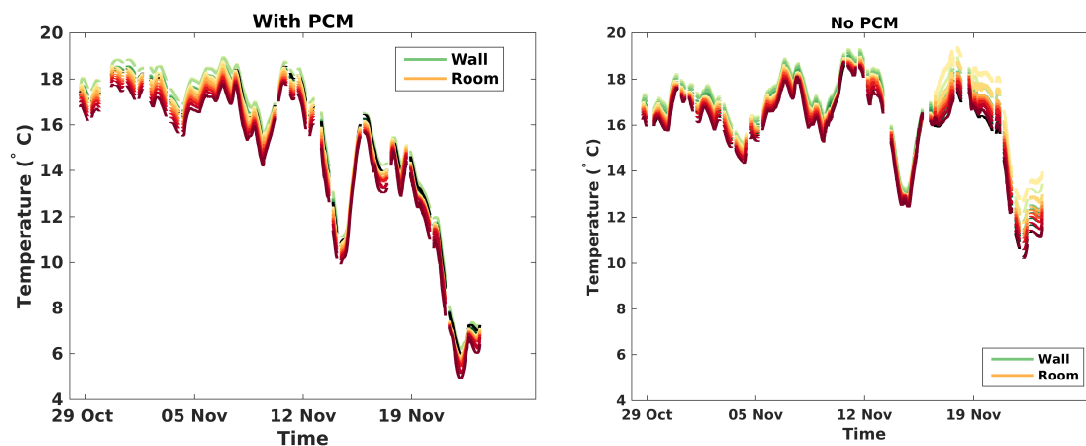


Fig. A.8 Wall (green lines) and room (orange lines) temperatures in the apartment with PCM wallboard (left) and the apartment without PCM (right), measured from the 28th October 2015 to the 23rd November 2015. Darker shades correspond to temperatures measured at lower heights.

Unfortunately, problems procuring the equipment and then technical problems meant that summer 2015 temperature data was not collected. The autumn data, collected on a warm day in September, suggests that PCM reduces overheating, but more data – particularly summer data, when overheating is most likely to be a problem – is required to strengthen this conclusion.

A.4.2 Winter data

During winter, temperatures in both apartments were measured over a period of almost a month (from 16:50 on the 28th October 2015 to 10:20 on the 23rd November 2015). As with the autumn data, there are gaps due to corrupt data files. The data collected is shown in figure A.8. Temperatures in both apartments are fairly similar until around 12th November. This is expected - during winter, temperatures are below the PCM melting range, so there should be little difference between the two apartments. After 19th November, there is a large drop in temperature in the apartment with PCM, with no corresponding drop in the other apartment. This large drop may be due to the heating in the apartment with PCM being switched off, whilst the heating in the other apartment remained switched on (this was the state the apartments were in after the period of data collection). This winter data confirms that, as expected, temperatures during the winter months are unaffected by the presence of PCM.

A.5 Conclusions

Temperature measurements from a field test of PCM wallboard in a real building suggest that PCM may be able to reduce summer overheating. Two apartments at Explore Industrial Park, in Steetley, near Worksop, were monitored. In each apartment, thermocouples and a data acquisition box measured temperatures at 8 heights, both on the wall and in the room. One apartment was fitted with a double thickness of Knauf Comfortboard – a wallboard containing microencapsulated PCM. The other apartment was left without PCM, as a control.

Data was collected over 36 hours in September 2015, and over almost a month during October and November 2015. Unfortunately, data from summer 2015 was not collected due to problems procuring the equipment and then technical problems. The September data shows that, in the apartment with PCM, temperatures are reduced compared with the apartment without PCM, and that, a temperature peak in the apartment without PCM is not present in the data from the apartment with PCM. The winter data shows that, as expected, during the winter (when temperatures are below the PCM melting range), there is little difference between the apartment with PCM and the apartment without PCM. The data collected suggests that PCM may reduce summer overheating, but more data – particularly summer data – is required to strengthen this conclusion.

